Experimental study of plasma parameters in nanosecond surface dielectric barrier filamentary discharge

Chenyang Ding

INSTITUT POLYTECHNIQUE DE PARIS

NNT : 2021IPPAX025

Thèse de doctorat

ÉCOLE POLYTECHNIQUE

IP PARIS

Experimental study of plasma parameters in nanosecond surface dielectric barrier filamentary discharge

Thèse de doctorat de l'Institut Polytechnique de Paris
préparée à l'École polytechnique

École doctorale n°626 Ecole Doctorale de l'Institut Polytechnique de Paris (EDIPP)
Spécialité de doctorat : Optique Lazer et Plasma

Thèse présentée et soutenue à Palaiseau, France, le 26/05/2021, par

M. CHENYANG DING

Composition du Jury :

Christophe Laux Professeur, École CentraleSupelec (EM2C), France	Président
Ronny Brandenburg Professeur, Leibniz Institute for Plasma Science and Technology (INP), Allemagne	Rapporteur
Thierry Belmonte Directeur de recherche, Université de Lorraine (IJL), France	Rapporteur
Jean-Marc Bauchire Professeur, Université d'Orléans (GREMI), France	Examinateur
David Pai Chargé de recherche 2, École polytechnique (LPP), France	Examinateur
Ivan Moralev Leading researcher, Joint Institute for High Temperatures (JIHT RAS), Russia	Examinateur
Yann Cressault Professeur, Université Toulouse III (LAPLACE), France	Examinateur
Svetlana Starikovskaia Directrice de recherche, École polytechnique (LPP), France	Directrice de thèse

To my parents, Mr. Yongbing DING and Mrs. Yafang CHEN

致我的父母，丁勇兵先生和陈亚芳女士

Contents

Acknowledgements

First and foremost I am extremely grateful to my supervisor, Prof. Svetlana M. Starikovskaia who is an expert in the field of plasma assisted combustion and low temperature plasma. It has really been a fantastic experience to do my PhD under her supervision. For sure, this candidate should be as fortunate as possible to be admitted as a member of her group. Unlike PhD supervisors who propose a research topic and focus on their own work, she has the ability to guide the student to conduct the research step–by–step and solve the problem together with the student. It is her hand-in-hand support and rich knowledge of physics that has driven me to finish my thesis. The most impressive point is that her work goes far beyond being a doctoral supervisor. She takes care and helps to solve each problem the students meet not only in research but also in their daily life. She is willing to bring students to the international plasma community. This has greatly broadened my horizons and helped me to get inspiring conversations and feedback from the world's top scientists in the community. In my opinion, she is the best female supervisor in the world. I am really grateful to be in her group.

I am also very thankful to the China Scholarship Council (CSC) for offering the 4-year full–time scholarship to support my PhD study in France. Thanks to Prof. Mousen Cheng in my domestic university for his firm and long term support to my study abroad.

A great deal of credit is due to my dissertation committee: Prof. Ronny Brandenburg, Dr. Thierry Belmonte, Prof. Christophe Laux, Prof. Jean-Marc Bauchire, Dr. David Pai, Dr. Ivan Moralev and Prof. Yann Cressault for serving on my committee.

Thanks to Dr. Yifei Zhu for his generous help in my research and personal life when I first came to France. Even though he has returned to China, he is still my half-supervisor in numerical modeling. Thanks to Xiang Fu and Dawei Guo for their help in administrative work in my domestic university.

I would like to express my thanks to Prof. Nicolay Popov for his guidance in understanding kinetics and kind help during my PhD. Thanks to Prof. Natalia

Babaeva, Prof. Ute Ebert and Prof. Ryo Ono for their valuable communication during conferences. Thanks to Dr. Anne Bourdon and Dr. Luca Perfetti to be in my follow–up committee.

Thanks to Dr. Sergey Shcherbanev, for his kind guidance and assistance when I started to do experiments in the lab. He provided me with a great headstart.

I wish to express my special thanks to my Russian colleagues in Joint Institute for High Temperatures of the Russian Academy of Sciences, Dr. Ivan Moralev and Dr. Igor Selivonin. I admire their positive work attitude and easy-going communication style. I appreciate their warm reception to my visit in Moscow. I had a very wonderful and impressive time in Russia.

Thanks to my first intern Jean Antonin who brought new ideas and new equipment to my experimental work. Thanks to Yerassyl Yerlanuly for bringing the electrode synthesized by carbon nanomaterials and doing the experiments with me.

Thanks to my current and former lab mates: Tat Loon Chng, Nikita Lepikhin, Inna Orel, Mhedine Alicherif, Georgy Pokrovskiy, Bo Liu, Xianjie Wang, Hang Yang, Yue Liu, Huan Xu and Melissa Menu for their company and encouragement.

In addition, I am thankful to our laboratory (LPP) for offering me a comfortable working environment. Thanks to the secretarial team for helping with all the administrative work and the informatic team for solving the technical problems. Thanks to the mechanical team for designing and manufacturing the experimental parts.

Thanks to Chinese Embassy in France for their support on my living abroad. Also great thanks to French government for offering me the housing allowance (CAF) and medical insurance (CSS).

Thanks to ParisTech for admitting me to study in France. Thanks to the French National Research Agency (ASPEN Project) and the French-Russian international laboratory LIA KaPPA 'Kinetics and physics of pulsed plasmas and their afterglow' (CNRS financial and organization support) project for covering my academic travel expenses. Thanks to Science Accueil for the reception service upon my arrival in France. Kind help and great effort offered by Mr. Guy Cassin, the justice conciliator of Palaiseau District Court, are gratefully appreciated.

Thanks to my two cats, Do-Do and Odin for being with me. They always brighten my emotions. The company and mutual understanding is a big treasure.

Finally, I would like to express my deep gratitude to my parents, grandparents and relatives for their long–term support and warm love throughout my life.

Abstract

Nanosecond surface dielectric barrier discharges (nSDBDs) at atmospheric pressure have been studied extensively over the last two decades for flow control. Synchronous start, within 0.2 ns, of the streamers from the edge of the high-voltage electrode and propagation along the dielectric provide a synchronous energy relaxation with generation of weak shock waves near the surface of the dielectric. About ten years ago, the nSDBD at high pressures was suggested as a source for plasma assisted ignition of combustible mixtures. During last six years, it was found that a severe transformation of a single-shot nanosecond surface streamer discharge is observed at increasing gas pressure and/or voltage. A regular structure of tens of filaments appears from the edge of the high-voltage electrode and propagates in the direction perpendicular to the edge of the high-voltage electrode, the number of filaments being $4-5$ times less than the number of streamers. There is no direct electrical connection between the channels of the filaments and the grounded electrode.

The present thesis is devoted to study of streamer-to-filament transition in a single shot high pressure surface nanosecond barrier discharge in non-reactive gases (N_2, O_2 and their mixtures). Literature review presents detailed analysis of streamer discharges and of transitory nanosecond sparks widely studied during last 4 years.

The results are presented in three parts. The first part shows the parameters of streamer-to-filament transition in the high pressure nSDBD for different gas mixture composition. For both negative and positive polarities, the transition is a function of pressure and of the voltage amplitude. For positive polarity, the effect of molecular oxygen addition on the transition is extremely strong. The influence of different dielectrics and different electrode materials of the start and development of the filaments is studied experimentally. The micro-images of discharge propagation on three electrode configurations at three different stages–streamer, transition to filament and filamentary regime–are compared.

In the second part, plasma properties in the filaments are studied with the help of the energy measurements, optical emission spectroscopy (OES) and Particle Im-

age Velocimetry (PIV). In the streamer and transition regime, the OES spectra mainly contains second positive system of molecular nitrogen while in the filamentary regime continuum (CW) emission and a few atomic lines are observed. The results of measured plasma parameters, namely synchronized in time specific deposited energy, electron temperature and electron density are included. The value of specific deposited energy in the filaments is as high as $6 - 8$ eV/particle; the electron density is in the range of $10^{18} - 10^{19}$ cm^{-3}, and the electron temperature stays at the level of $1.5 - 2$ eV in the near afterglow. Plasma at this stage is found to be close to local thermodynamic equilibrium (LTE) state demonstrating slow (tens of nanoseconds) electron density decay linked to the temperature relaxation. The results of the measurements are compared with the results of numerical modeling explaining the main experimentally observed features. In the model, stepwise ionization and dissociation from electronically excited states of molecular nitrogen leads to fast increase of the electron density, dissociation degree and gas heating at 6 bar on the time scale of parts of nanoseconds.

The third part is devoted to detailed study of streamer-to-filament transition in the micro-scale with the spatial resolution 7.6 μm/px. At a given time instant, the surface ionization wave front, composed from the merged streamers, is broken by a few plasma channels, moving with a higher velocity (we call them "protrusions"). Their radii are $10 - 20$ times smaller comparing to a typical streamer radius; they form, within a few nanoseconds, a regular structure of plasma channels around the high voltage electrode. Inside each of these channels, a backward emission of the second positive system of N_2 propagates from the "protrusion" head back to the high-voltage electrode. Continuous spectra, atomic lines and high electron density first appear when the backward emission approaches the high-voltage electrode, at the distance about 500 μm from the edge. The calculated results of emission intensity, electron density and electric field are given for studying the influence of oxygen admixtures on the transition.

Résumé de thèse

Les décharges nanosecondes, de surface, à barrière diélectrique (nSDBD) à la pression atmosphérique ont été étudiées de manière approfondie au cours des deux dernières décennies pour le contrôle du débit. Le démarrage synchrone, à 0,2 ns près, des streamers à partir du bord de l'électrode haute-tension et la propagation le long du diélectrique fournissent une relaxation d'énergie synchrone avec la génération d'ondes de choc faibles près de la surface du diélectrique. Il y a environ dix ans, les nSDBD à haute pression ont été suggérés comme source d'allumage pour la combustion assistée par plasma. Au cours des six dernières années, il a été constaté que pour une nSDBD de type streamer, une transformation radicale s'effectue pour une pression et/ou une tension de gaz croissante. Une structure régulière de dizaines de filaments apparaît à partir du bord de l'électrode haute tension et se propage dans la direction perpendiculaire au bord de l'électrode haute tension, le nombre de filaments étant 4 à 5 fois inférieur au nombre de streamers initiaux. Il n'y a pas de connexion électrique directe entre les canaux des filaments et l'électrode mise à la terre.

La présente thèse est consacrée à l'étude de la transition streamer–filament dans une nSDBD à haute pression pour des single-shots et dans des gaz non réactifs (azote, oxygène et leurs mélanges). La revue de la littérature présente une analyse détaillée des décharges de type streamers et des décharges transitoires nanosecondes largement étudiées au cours des 4 dernières années.

Les résultats sont présentés en trois parties. La première partie montre les paramètres de la transition streamer–filament dans les nSDBD haute-pressions pour différentes compositions de mélange gazeux. Pour des polarités négatives et positives, la transition est fonction de la pression et de l'amplitude de la tension. Pour une polarité positive, l'effet de l'addition d'oxygène moléculaire sur la transition est extrêmement fort. L'influence de différents diélectriques et de différents matériaux d'électrodes sur le début et le développement des filaments est étudiée expérimentalement. Les micro–images de propagation de décharge sur trois configurations d'électrodes à trois étapes différentes – streamers, transition vers filament

et régime filamentaire – sont comparées.

Dans la deuxième partie, les propriétés du plasma dans les filaments sont étudiées à l'aide de mesures d'énergie, de spectroscopie d'émission optique (OES) et de vélocimétrie par image de particules (PIV). Dans le régime streamers et de transition, les spectres OES contiennent principalement l'émission du deuxième système positif de l'azote moléculaire tandis que pour les filaments une émission continue (CW) ainsi que quelques raies atomiques sont observées. Les résultats de mesures des paramètres du plasma sont inclus, à savoir l'énergie déposée synchronisée dans le temps, la température électronique et la densité électronique. La valeur de l'énergie spécifique déposée dans les filaments est aussi élevée que $6 - 8$ eV/particule; la densité électronique est dans la gamme de $10^{18} - 10^{19}$ cm^{-3}, et la température électronique reste au niveau de $1,5 - 2$ eV dans l'afterglow. Le plasma à ce stade se révèle être proche de l'état d'équilibre thermodynamique local (LTE), présentant une lente décroissance de la densité électronique (dizaines de nanosecondes) liée à la relaxation de température. Les résultats des mesures sont comparés aux résultats de modélisations numériques expliquant les principales caractéristiques observées expérimentalement. Dans le modèle, l'ionisation et la dissociation par étapes des états excités électroniquement de l'azote moléculaire entraînent une augmentation rapide de la densité électronique, du degré de dissociation et du chauffage du gaz à 6 bar sur l'échelle de temps de la fraction de nanosecondes.

La troisième partie est consacrée à l'étude détaillée de la transition streamer-filament à l'échelle du micron avec une résolution spatiale de 7.6 μm/px. A un instant donné, le front d'onde d'ionisation de surface, composé de streamers fusionnées, est interrompu par quelques canaux de plasma, se déplaçant à une vitesse plus élevée (nous les appelons «protrusions»). Leurs rayons sont 10 à 20 fois plus petits par rapport à un rayon de streamer typique; ils forment, en quelques nanosecondes, une structure régulière de canaux plasma autour de l'électrode haute tension. A l'intérieur de chacun de ces canaux, une émission vers l'arrière du deuxième système positif de N_2 se propage de la tête «protrusions» vers l'électrode haute tension. Des spectres continus, des raies atomiques et une densité électronique élevée apparaissent pour la première fois lorsque l'émission vers l'arrière s'approche de l'électrode haute tension, à environ 500 μm du bord. Les résultats calculés de l'intensité d'émission, de la densité électronique et du champ électrique sont donnés pour étudier l'influence de l'ajout d'oxygène sur la transition.

Chapter 1

Literature review

In this chapter, typical dielectric barrier discharges at both atmospheric and elevated pressures are reviewed. Streamer–to–spark transition in nanosecond repetitive discharge is discussed in detail. Different diagnostic methods to measure plasma parameters are analysed. A few numerical models of nanosecond surface dielectric barrier discharges are discussed.

1.1 Dielectric barrier discharge at atmospheric pressure

Dielectric barrier discharges (DBDs) in atmospheric pressure have been widely studied over a few decades. Dielectric barrier discharge was known as "ozonizer discharge" from the beginning because it was first found that this kind of discharge can be used for ozone generation by W. Siemens in 1857 [1]. A scheme of the ozone discharge tube is shown in figure 1.1. The air or oxygen flows between the two coaxial glass tubes. The ozone was produced by the dielectric discharge in a small annular discharge gap between two coaxial external electrodes. DBD is also called "silent discharge" because it does not provide noticeable sound when operating [2].

In 1930s, K. Buss took the first image of micro–discharges traces in DBD and recorded the waveforms of applied voltage and current of the discharge [4]. He observed the luminous channel with a diameter of 100 μm caused by the appearance of the discharge. He found that the discharge must take place at the current amplitude decreases. Kogelschatz *et al.* also reported that the discharge happened on the rising

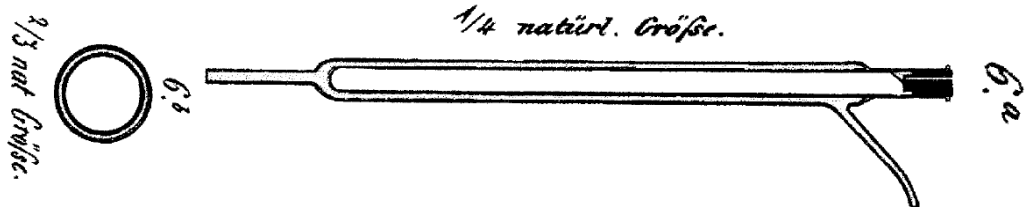

Figure 1.1: Ozone discharge tube of W. Siemens in 1857 [1]. "*natürl. Größe*" in the figure means natural size. The figure is taken from [3].

edge of applied voltage during their work on ozone generation [5] Strong disturbance was seen on the rising edge of voltage waveform as shown in figure 1.2(b).

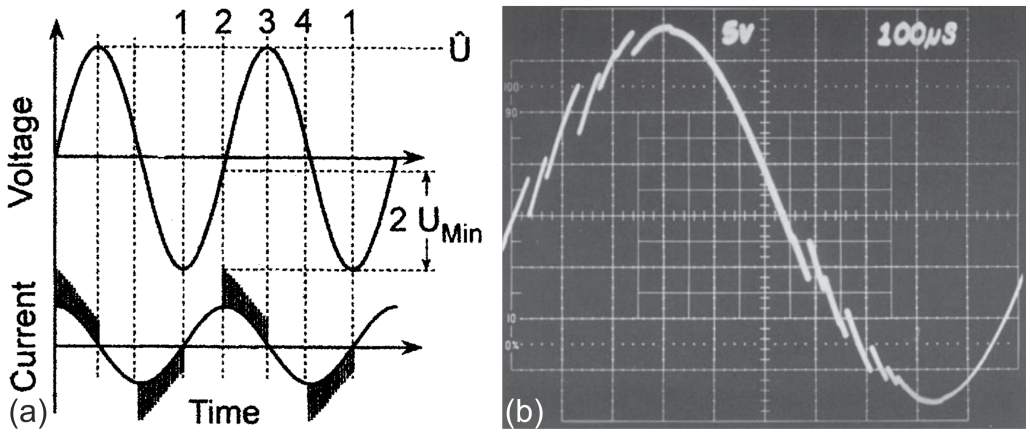

Figure 1.2: (a) Voltage and current diagram of micro–discharge activity. The plasma generation moments were indicated with black bands on current waveform. (b) Voltage recorded from the ozonizer discharge. Strong disturbance was shown on the rising edge of voltage. Figure (a) is taken from [3] and (b) from [5].

The name "Dielectric barrier discharges (DBDs)" comes from the electrode configuration of the discharge: one or both electrodes are covered with dielectric materials or the insulating material is put between the anode and cathode electrodes. According to different electrode configurations, DBDs can be divided into volume discharges, surface discharges and coplanar discharges [6]. Figure 1.3(a) shows the volume DBDs where the generated plasma fill the whole volume between two electrodes. In (a_1) both electrodes were covered by dielectric materials and the plasma was produced between two insulators. Only one insulator was used in (a_2) and (a_3) which helped decreasing the required voltage for launching the breakdown. However, these configurations may cause corrosion of the exposed electrode. Thus, they are not ideal for gas discharges where clean gas media is needed.

Surface DBDs are presented in figure 1.3(b_1) and (b_2); both electrodes were covered with insulator. In surface DBDs, the discharges were initiated from the edge of

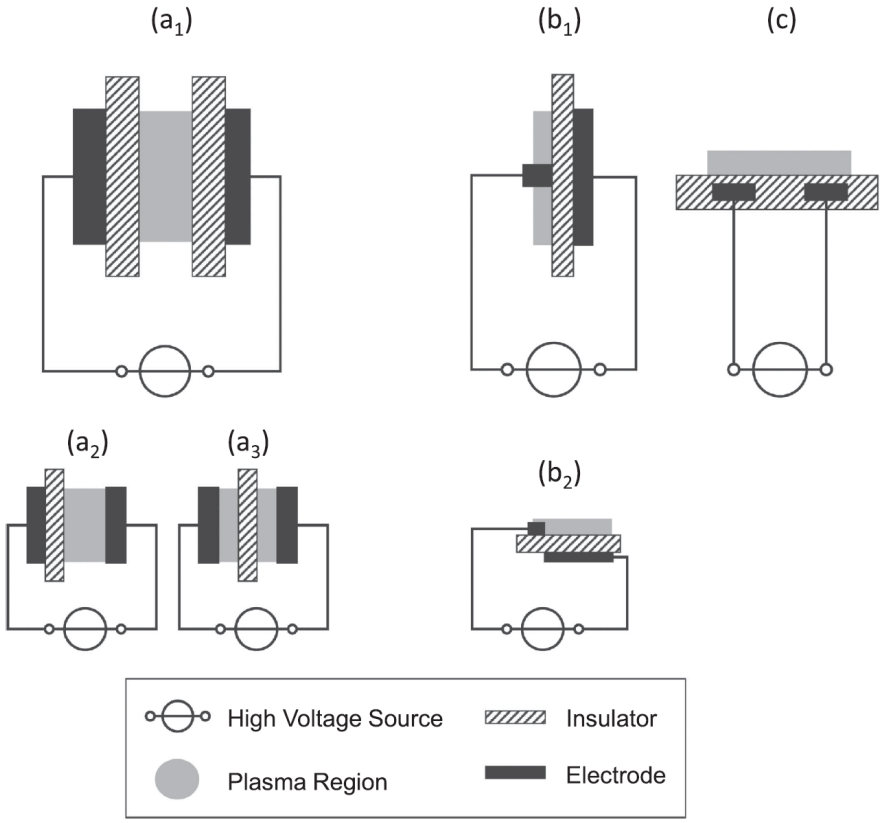

Figure 1.3: Different electrodes configurations of DBDs: (a) volume discharges, (b) surface discharges and (c) coplanar discharge. The figure is taken from [6].

one electrode and propagated along the surface of dielectric materials. One of the typical applications of surface DBDs is electro–hydrodynamic (EHD) actuator for the airflow controls [7–9]. The parameters, mainly the amplitude and frequency, of EHD force induced by the surface plasma are directly related to the applied electrical signal, providing enough sensitivity for parametric studies of the flow disturbances. Figure 1.3(c) is a coplanar DBD configuration where two strip–like metallic electrodes were embedded into the dielectric material (e.g. Al_2O_3 ceramics). Visually homogeneous plasma can be generated on the alumina surface at atmospheric pressure that is ideal for a large scale surface treatment [10].

Over a century, the research issues concerning with DBDs were dominated by the study of industrial ozone generation. Until 1990s, the major application of DBDs was still ozone generators which mainly used in water treatment [5, 11]. Benefiting from extensive research on ozone generators, a lot of diagnostic and modelling tools were developed in the modern research activities. A considerable amount of plasma physics and chemistry knowledge was also acquired and stored in the research of ozonizer discharges. Consequently, this resulted in generation and development of a great number of emerging dielectric barrier discharge applications, including plasma

catalysis [12], air pollution control [13–17], light source generation [18, 19], textile surface treatment [20,21], materials processing for microelectronics and photovoltaic cells [22], biological purification of packaging [23, 24], medical equipment disinfection [25], skin wound treatment and healing [26–28], plasma assisted ignition and combustion [29–31], etc.

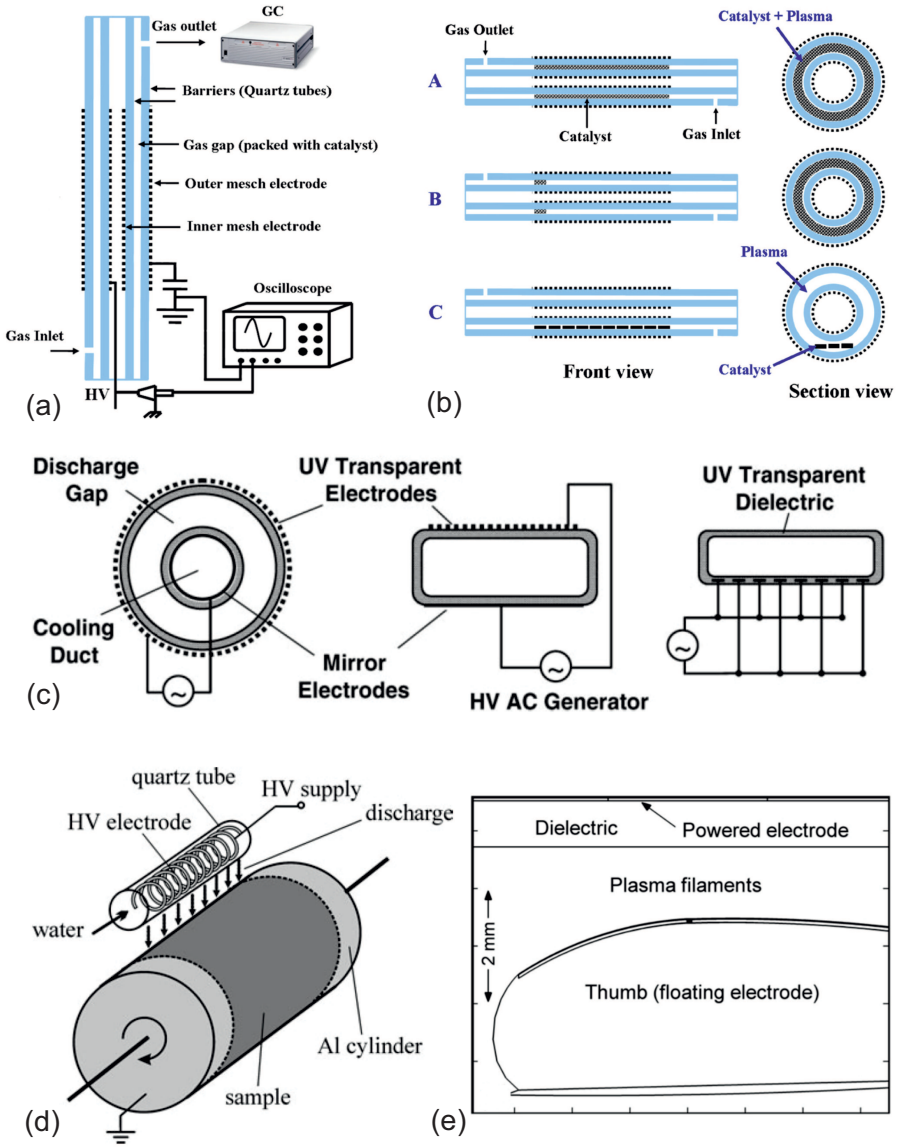

Figure 1.4: Schematic diagrams of electrode configurations for different applications of DBDs. (a) Discharge setup for plasma catalysis and (b) its front and section views, taken from [12]; (c) Electrode configuration of plasma UV and VUV light source, taken from [19]; (d) Experimental assembly of textiles surface treatments using DBDs, taken from [20]; (e) Electrode structure of plasma biological surface disinfection and sterilization, taken from [27].

In order to achieve the application purposes listed above, different electrode structures were designed. Figure 1.4(a) and (b) show the electrode configuration used in plasma catalysis at atmospheric dielectric barrier discharges. In some cases the electrodes are not made from solid metal but from the metallic films or foils. In [12], Tu *et al.* used the mesh stainless steel film on the inner surface of a coaxial quartz tube as the high–voltage (HV) electrode and covered on the outer surface acting as the ground electrode. The authors compared three types of catalyst packing methods and found that plasma generated in partially packed configurations (B&C) significantly increased the efficiency of chemical reactions of the catalyst. Due to the fact that the channel was filled by catalyst in the fully packing methods (A), the weak discharge limits the reaction efficiency of the catalyst. Figure 1.4(c) displays different cylindrical and planar electrode configurations for generating UV or VUV light using dielectric barrier discharges [19]. The mirror electrodes were used for the HV electrode and both the ground electrodes and the dielectric materials were UV transparent. The discharge gap is normally $0.1-3$ mm and the gas pressure in the sealed electrode can be $0.1-5$ bar. The UV light emitted by the discharge can be transformed to visible light using the phosphors.

There are a large number of applications of DBDs for the surface treatments, including the polymer films or the fabric materials, the purification and sterilization of packaging and even the surface of skin or body tissues. An example of treating the surface of textiles using DBDs is presented in figure 1.4(d). The textile material to be treated is rolled on an aluminum cylinder that works as the ground electrode. During the treatment process, the cylinder keeps rotating at a constant speed with the linear speed reaching up to 95 m/s [20]. The spiral stainless steel, placed inside a quartz tube, is connected to HV power supply. The micro–discharge channels, generated within a nanosecond time scale, are distributed randomly in the volume between both electrodes, which ensures a uniform treatment of the surface.

Figure 1.4(e) shows plasma treatment of the biological sample. Human thumb in this picture works as a floating electrode. The micro–discharge channels can be formed in the gap between the metallic electrode and living tissue. The current passed through the tissues in the form of displacement current rather than the motion of charges in the gas discharges. Experimental and numerical results show that the plasma generated in this way has the catalytic effect on blood coagulation without putting any thermal or chemical harm to the living tissues of human or animals [26, 27]. By physical nature, micro–discharges observed in DBDs, are streamers.

At high electron densities and high gas temperatures the discharges develop in the form of the arc discharge. Typically, arc discharge is observed between two open electrodes separated by a small gap less than 1 mm.

1.2 Nanosecond repetitive and single pulse discharges close to or reaching local thermodynamic equilibrium (LTE) state

Different to complete thermodynamic equilibrium (CTE), Local thermodynamic equilibrium (LTE) does not require the electromagnetic radiation to be in equilibrium, having the Plank distribution. But LTE, existing in the optically thin plasma, does require: (i) all plasma components follow Maxwell–Boltzmann translational energy distribution; (ii) excitations of all plasma components have a Boltzmann distribution; (iii) ionization equilibrium of all species in plasma follows Saha equation; (iv) the ratio of electric field and pressure (E/p) is small enough and the temperature is sufficiently high that the temperatures of electrons and heavy particles are equal ($T_e = T_h$); (v) The properties of the plasma tend to be balanced throughout the space [32–34].

Nanosecond pulsed discharges show different appearance at different experimental conditions (pressure, applied voltage and gas mixtures) in single or repetitive pulse regime. These discharges, including glow [35], corona [36], streamer [37–39], filament [40–42], spark [43–51] and even lightning [52–54] discharges, have been studied for a long period. The transitions can happen from non–thermal state to local thermodynamic equilibrium (LTE) state when one or more experimental conditions change.

In 1977, Stritzke *et al.* [43] made the spatial and temporal spectroscopy measurements on the streamer–to–spark transition in nitrogen (0.4 bar) on a plane–plane electrode system with 2 cm gap. They observed the second positive system of molecule nitrogen (SPS, $N_2\,(C^3\Pi_u \rightarrow B^3\Pi_g)$) in the emitted light. The electron density was found to be increasing from 10^{11} cm^{-3} to 10^{16} cm^{-3} with the heating of the plasma channel. A few nanoseconds after the avalanche, the dissociation and ionization took place, giving the strong continuum emission as well as a few atomic lines in the wavelength range of $300 - 860$ nm. At this stage, the electron temperature reached to $(5 - 6) \times 10^4$ K and the electron density increased up to 10^{18} cm^{-3}. Finally, the authors concluded that LTE state had been established in the ionized plasma channel. In the same year, Albrecht *et al.* [44] made a series of experiments of the spark discharges intended for studying the combustion of the fuel and air mixtures. They observed that the SPS emission peaking at 337.1 nm appeared only at the beginning of the ignition and disappeared rapidly with the dissociation of molecules. After rising of current, the atomic lines NII (N^+) peaking at 500.6 nm as well as the radiation of electrode material (MnII (Mn^+) peaking at

230.3 nm) generated within a few nanoseconds accompanied by the constriction of discharge channels. The time–resolved radial distribution of emission intensity for SPS of molecular nitrogen and N^+ atomic lines are shown in figure 1.5. It can be seen that the emission of SPS of molecular nitrogen had the highest intensity at 7 ns and disappeared from the core of discharge channel at 15 ns when N^+ atomic emission reached the peak intensity. The full ionized channel has the width of $50 - 100$ μm. The electron density at the thermodynamic equilibrium state was measured by the Stark broadening as high as 10^{19} cm^{-3}. Meanwhile, the electron temperature was seen from the Boltzmann plot of N^+ lines to be over 5 eV at the early phase of spark.

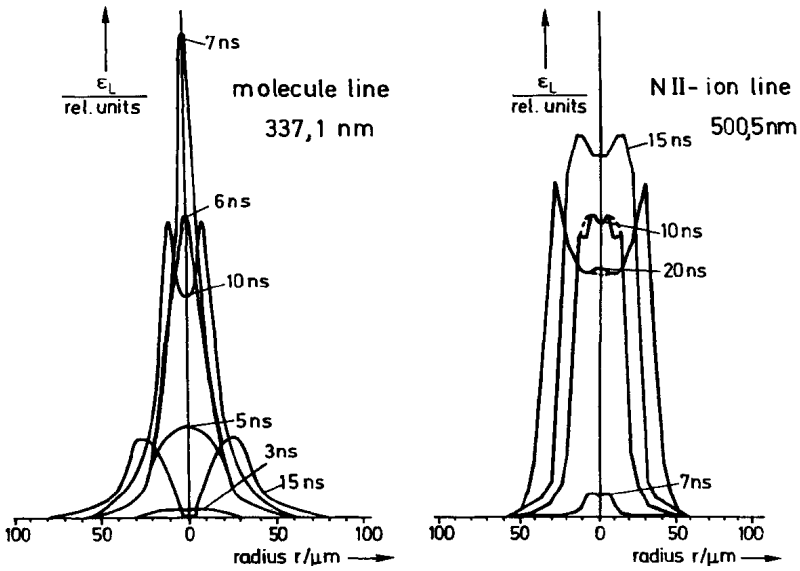

Figure 1.5: Radial distribution of emission intensity for molecular nitrogen (left) and N^+ atomic lines (right). The figure is taken from [44].

Lomaev *et al.* [45] observed the constriction of plasma channels when increasing the pressures from $0.1 - 4$ bar to over 5 bar. In their experiments, a steel tube, 6 mm in diameter and 50 μm thick, served as the cathode while a flat brass plat was used as the anode. The distance of the discharge gap was 12 mm. As shown in figure 1.6, the homogeneous diffuse plasma filled in the volume between tube cathode and anode at lower pressure conditions ($0.1 - 4$ bar). As the experiments were conducted in nitrogen with 5% of hydrogen, the strong emission of SPS of molecular nitrogen bands appeared during the homogeneous discharge regime. When pressure rose over 6 bar, a broadband continuum spectra in the wavelength range of $200 - 800$ nm appeared as well as NI (N atom) and NII atomic lines in the range of $400 - 800$ nm. With the continuous increase of pressure the emission intensity of atomic lines and continuum spectra grew significantly from 6 bar to 12 bar. The authors measured the electron density via the Stark broadening of H_α and H_β atomic lines. While the

electron density was determined from the ratio of intensity between first negative system (FNS, peaking at 391.4 nm) and SPS (peaking at 394.3 nm) of molecular nitrogen. The results indicated that the contraction of discharge channels happened with the significant rise of the electron density from 10^{15} cm^{-3} in diffuse mode to 10^{17} cm^{-3} in contacted discharge. High electron temperature, up to 3.5 eV, was observed after the breakdown happened in the gap and dropped rapidly to ~ 2 eV in a few nanoseconds.

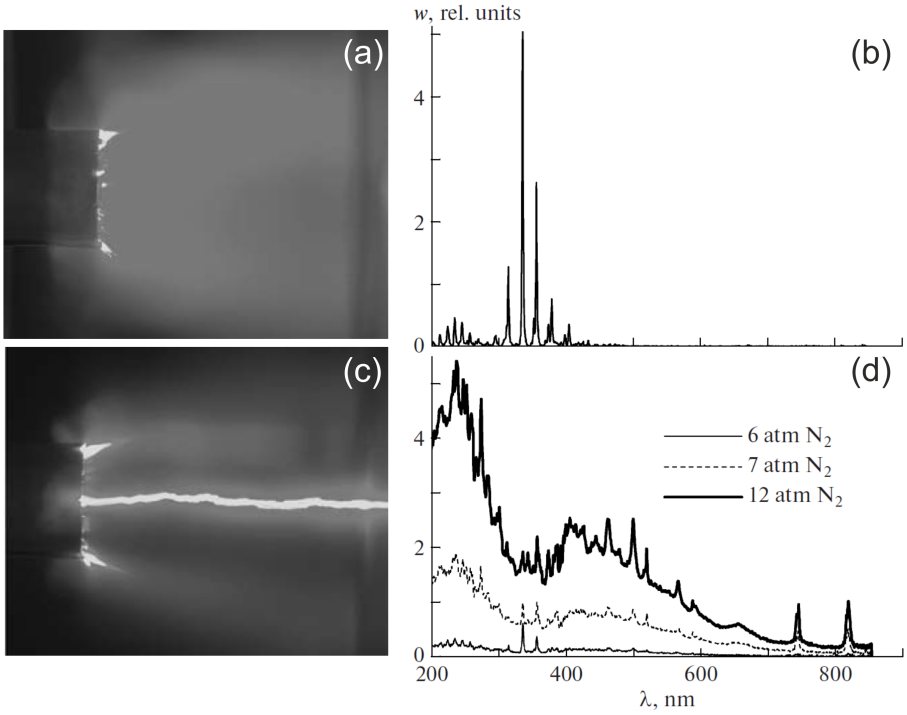

Figure 1.6: Images of the diffused and contracted discharges (a & c on the left) as well as the emission spectra for two modes (b & d on the right). The figure is collected from [45].

Similar formation of discharge channel contraction was reported by Shao *et al.* in [46] where a tube–plane electrode configuration was used. They saw the constriction of discharge channels when increasing the gas pressure or shortening the gap distances. In the initial stage before the ignition, there were a few spots on the cathode. A few nanoseconds later, the spark leaders first generated on the anode and propagated towards the middle of the gap. The authors believed that it was the propagation of the spark leaders from the anode that bridged the discharge gap. Analogously, the spectra before breakdown was dominated by SPS of molecular nitrogen while after the gap was bridged, mainly the continuum and NII, NI and OI (O atom) spectra as well as the atomic lines from electrode materials can be found.

Minesi *et al.* [47] very recently observed the formation of highly ionized plasma

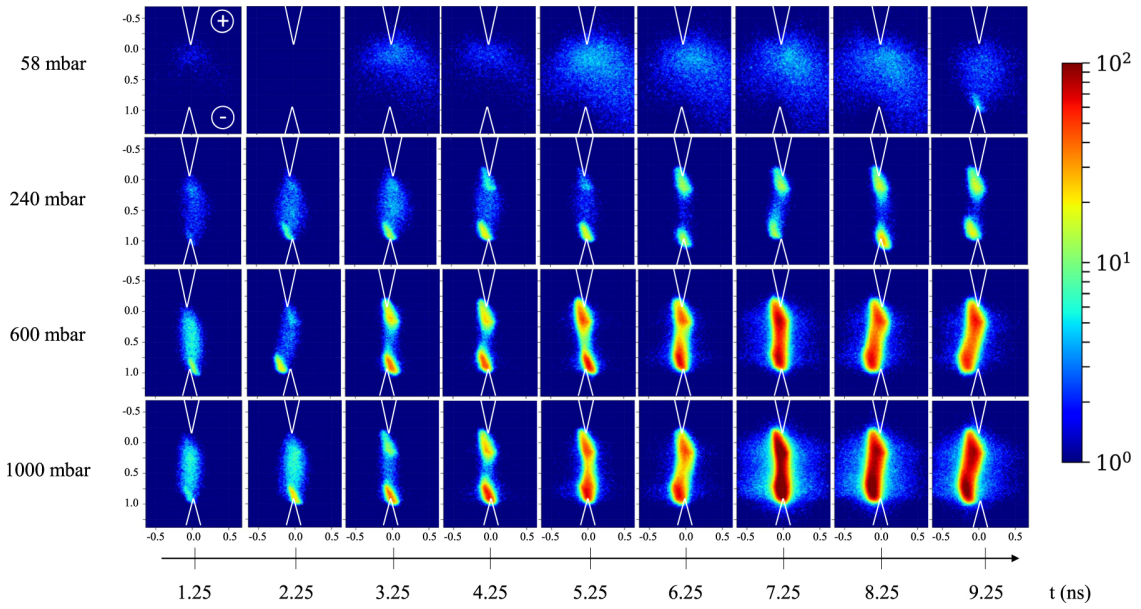

Figure 1.7: Comparison of discharge propagation on a pin–to–pin electrode at different pressures in the single shot regime. The upper electrode, marked by "⊕", is anode and the lower one is cathode marked by "⊖". The figure is taken from [47].

channels in the experiments at different pressures ranging from 58 mbar to 1 bar. As shown in figure 1.7, after the ignition of discharge, the diffuse plasma was generated between anode and cathode within 1.25 ns and first appeared near anode. Then, different from the generation of homogeneous plasma, the filament with higher emission intensity first exhibited on the edge of cathode within 1 ns. Due to the resolution limits of ICCD camera, the authors were not able to resolve the appearance of filaments. Immediately afterwards, the fully ionized filamentary discharge also appeared on the anode. Finally, as the continuous propagation of filaments from both cathode and anode to the middle of channel, the discharge channel closed a few nanoseconds after the ignition. When the breakdown happened in the gap, the electron temperature was as high as 4.1 eV and the peak electron density measured to be 4×10^{19} cm^{-3}. In figure 1.8 (a), both NII and OII (O^+) atomic lines in wavelength range of $400 - 600$ nm were well exhibited.

Van der Horst *et al.* [48] measured the time–resolved emission spectra of nanosecond pulsed discharges in N_2 with 0.9% H_2O at atmospheric pressure. They defined the discharge phase before closing the gap as the ignition mode where the emission consists mainly SPS of molecular nitrogen. The spark discharge mode was followed by the recombination phase. Both NII and NI atomic lines can be seen in the spark mode while only NI appeared on the spectra of recombination phase. The authors also detected the bands of first positive system (FPS) of molecular nitrogen ($N_2\,(B^3\Pi_g \rightarrow A^3\Sigma_u^+)$) as shown in figure 1.8 (b). It should be noted that one

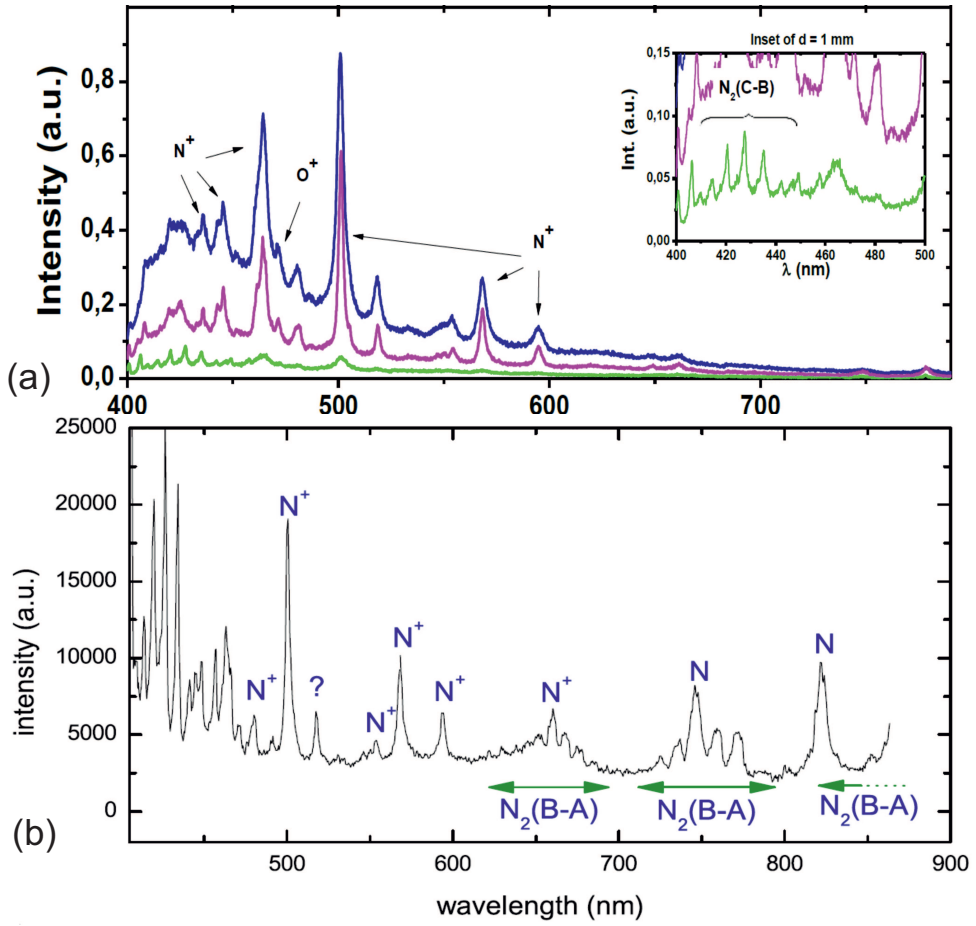

Figure 1.8: Emission spectra of the pin-to-pin discharges at atmospheric pressure with (a) gap $d = 1$ mm, voltage $U = 30$ kV and discharge frequency $f = 50$ Hz in air [55]; (b) gap $d = 2$ mm, voltage $U = 9$ kV and discharge frequency $f = 1$ kHz in N_2 [48].

atomic line that was not pointed out in both figure 1.8 (a) and (b) is N^+ spectrum ($^5F - ^5D^0$) peaking at $\lambda = 518$ nm (see figure 5.6 in chapter 5).

For better understanding the experimental spectra of the discharge close to LTE in nitrogen and air, the transition parameters of typical atomic lines in wavelength range of $440 - 600$ nm for NII and $700 - 900$ nm for NI and OI are displayed in table 1.1.

In addition to gaseous media, similar high values of electron density were also observed in liquid media, such as liquid nitrogen, transformer oil, deionized water and other electrolyte solutions. Belmonte *et al.* [57] observed the broad continuum emission in the discharge in liquid nitrogen on the pin–to–pin zinc electrodes with a $100 - \mu$m gap. The amplitude of applied voltage was 10 kV and the pulse duration was 200 ns. The spectra of the experiments with or without copper nanoparticles (Cu NPs) show significantly different results, as displayed in figure 1.9. Without Cu NPs,

Table 1.1: Typical atomic lines in wavelength range of $440 - 600$ nm for NII and $700 - 900$ nm for NI and OI. This is retrieved from NIST database [56].

	λ (nm)	Transition	$g_k A_k$ (10^8 s^{-1})	E_k (eV)
NII	444.7	$^1D^o - ^1P$	5.60	23.196
	463.1	$^3P - ^3P^0$	3.74	21.160
	464.3	$^3P - ^3P^0$	1.32	21.153
	478.8	$^3D^0 - ^3D$	1.25	23.242
	480.3	$^3D^0 - ^3D$	2.22	23.246
	500.5	$^3F^0 - ^3D$	10.3	23.142
	504.5	$^3S - ^3P^0$	1.01	20.940
	518.0	$^5F - ^5D^0$	2.14	30.127
	568.0	$^3D - ^3P^0$	3.47	20.666
	594.2	$^3D^0 - ^3P$	3.83	23.246
NI	746.8	$^4S^0 - ^4P$	0.78	11.996
	868.0	$^4D^0 - ^4P$	2.02	11.764
OI	777.2	$^5P - ^5S^0$	2.58	10.741
	822.1	$^3D - ^3D^0$	2.02	14.047

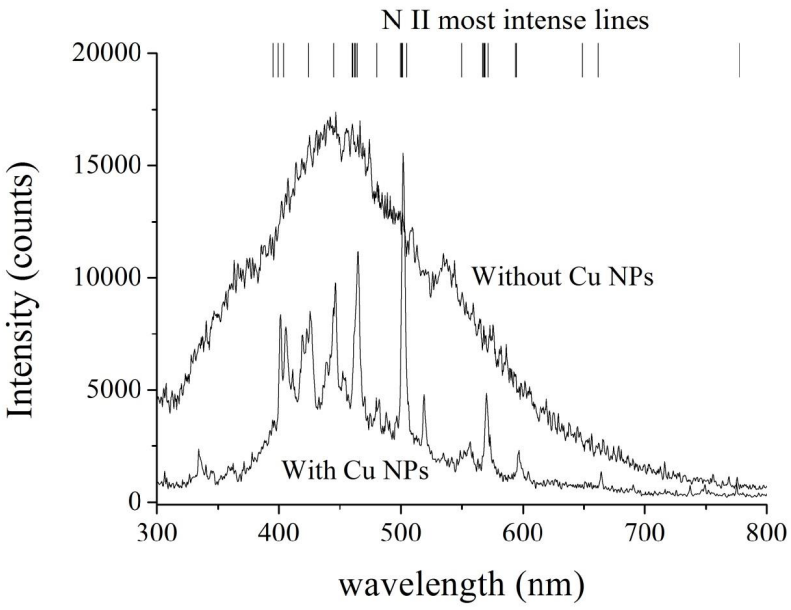

Figure 1.9: Emission spectra of discharges in liquid nitrogen with or without copper nanoparticles. Applied voltage $U = 10$ kV. Distance between two pin electrodes is 100 μm. The figure is taken from [57].

the spectra contains completely the continuum emission with high intensity while the spectra of experiments with Cu NPs show a series of N^+ atomic lines ranging from 400 nm to 600 nm accompanied by the cw emission with less intensity. The mechanism of copper nanoparticles that causes such a big difference is still unknown. The authors made the assumption that the presence of Cu NPs can promote the absorption of electrons in liquid nitrogen. The high intensity continuum emission and N^+ lines indicate strong dissociation and ionization process taken place during the discharge pulse. The authors derived the electron temperature of 0.9 eV and electron density up to 10^{17} cm^{-3}.

Bårmann *et al.* [58] measured the electron density up to 10^{19} cm^{-3} of the discharge between two hemispherical electrodes in transformer oil. During recent twenty years, a few groups reported identical high electron density ($10^{18} - 10^{20}$ cm^{-3}) with slow plasma decay (see figure 1.10) of the discharge on a pin–plane electrode in deionized water with solution conductivity of $2 - 800$ μScm^{-1} [59–64].

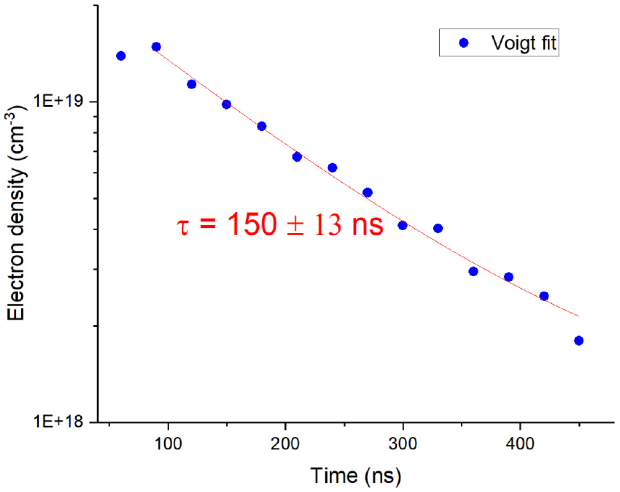

Figure 1.10: Electron density evolution of the discharge in water. Applied voltage $U = 100$ kV with pulse duration 6 ns. Distance between pin–plane electrodes is 5 mm. The figure is taken from [64].

Combining the examples and parameters talked above, we can arrive at the conclusion that the discharges reach local thermodynamic equilibrium (LTE) state generally accompanied by high electron density (in the order of $10^{17} - 10^{19}$ cm^{-3}) and high electron temperature. Their spectra mainly contains atomic lines (NII, OII, NI, OI and H_α) and continuum wavelength. These discharge results are in good agreement with the parameters of lightning in nature [52–54]. More detailed information concerning to plasma parameters of discharges close to or reaching local thermodynamic equilibrium (LTE) state are listed in table 1.2.

Table 1.2: Overview of discharges close to or reaching local thermodynamic equilibrium (LTE) state

Year	Ref.	Discharge name	Electrode & gap	Gas & pressure	Voltage (kV)	Pulse width	$T_{e,\,max}$ (eV)	$n_{e,\,max}$ (cm^{-3})	Energy (mJ)	Channel width (μm)	Frequency (Hz)
1977	Albrecht *et al.* [44]	spark	pin–plane 1 mm	N_2 1 bar	7	100 ns	5.2	10^{19}	–	50 – 80	single shot
1977	Stritzke *et al.* [43]	spark	plane–plane 2 cm	N_2 0.4 bar	28.8	–	4	10^{18}	–	–	single shot
2009	Lomaev *et al.* [45]	contracted discharge	tube–plane 12 mm	N_2 & He–H_2(5%) 0.1 – 12 bar	250	2 ns	3.5	3×10^{17}	–	–	single shot
2011	Bodrov *et al.* [65]	filament	laser–induced	air 1 bar	–	60 fs	3	10^{17}	4 – 7	120 – 150	10
2012	van der Horst *et al.* [48]	spark	pin–pin 2 mm	N_2/ N_2 & H_2O(0.9%) 1 bar	9	170 ns	–	4×10^{18}	–	–	1k
2012	Zhu *et al.* [66]	–	pin–pin 0.1 mm	Ar 1 bar	1	600 ns	–	10^{18}	–	–	1k
2012	Shao *et al.* [46]	spark	tube–plane 12 mm	N_2 & H_2(5%) 1 bar	250	2 ns	1.7	3×10^{17}	–	–	single shot
2012	Du *et al.* [49]	spark	SDBD	Ar & N_2(0.5%) 0.9 bar	0.7	560 μs	5	10^{17}	–	–	10
2013	Huang *et al.* [67,68]	–	pin–pin 0.4 mm	He&Ar& H_2(0.01%) 1 bar	2.5	40 ns	10	2×10^{17}	–	–	5k–667k

Continued on next page

Table 1.2 – *Continued from previous page*

Year	Ref.	Discharge name	Electrode & gap	Gas & pressure	Voltage (kV)	Pulse width	$T_{e,\,max}$ (eV)	$n_{e,\,max}$ (cm^{-3})	Energy (mJ)	Channel width (μm)	Frequency (Hz)
2014	Janda *et al.* [50,69]	transient spark	pin–plane 4 mm	air 1 bar	12.5	100 ns	–	7×10^{17}	0.1 – 1	< 100	1 – 10k
2016	Houpt *et al.* [70]	filament	flat SDBD	air 1 bar	15	50 μs	–	–	2 – 6	140	2k
2017	Lo *et al.* [51]	spark	pin–pin 3 mm	air 1 bar	35	25 ns	3.6	9.2×10^{18}	54	140	10
2018	Orrière *et al.* [71,72]	NRP spark	pin–pin 0.2 mm	air 1 bar	2.5	10 ns	6.2	1×10^{19}	0.1	30 – 70	8k
2019	Parkevich *et al.* [73,74]	filament/ spark	pin–plane 3 mm	air 1 bar	25	40 ns	–	5×10^{19}	80	10 – 50 for filaments 100 – 200 for sparks	single shot
2020	Minesi *et al.* [47]	thermal spark	pin–pin 0.9/2 mm	air/ air & H_2(1.6%) 0.05 – 1 bar	30	10 ns	4.1	4×10^{19}	2.5	250 at 58 mbar 140 at 1 bar	single shot
1964	Uman *et al.* [52,53]	lightning	cloud–ground	air 1 bar	10^5	0.5 s	2	4×10^{18}	–	–	single shot
2014	Xu *et al.* [54]	lightning	cloud–ground	air 1 bar	10^5	0.5 s	2.4	2×10^{18}	–	–	single shot
2018	Belmonte *et al.* [57]	spark	pin–pin 0.1 mm	Liquid nitrogen	10	200 ns	0.9	10^{17}	54	140	–

Continued on next page

Table 1.2 – *Continued from previous page*

Year	Ref.	Discharge name	Electrode & gap	Gas & pressure	Voltage (kV)	Pulse width	$T_{e,\,max}$ (eV)	$n_{e,\,max}$ (cm^{-3})	Energy (mJ)	Channel width (μm)	Frequency (Hz)
1996	Bårmann *et al.* [58]	streamer filaments	hemisphere–hemisphere 9 mm	transformer oil	65	–	–	10^{19}	–	–	single shot
2001	Šunka [59]	corona	pin-plane 28 mm	deionized water (300 μScm^{-1})	30	–	–	6×10^{18}	–	–	single shot
2007	Namihira *et al.* [60]	streamer	pin-plane 100 mm	tap water (250 μScm^{-1})	70	3 μs	1.3	8×10^{18}	–	–	single shot
2007	An *et al.* [61]	streamer/ filament	pin-plane 20 mm	deionized water ($2 - 800$ μScm^{-1})	25	–	–	$1.5{\times}10^{19}$	–	–	single shot
2012	Šimek *et al.* [62]	corona–like	pin-plane 28 mm	deionized water with NaH_2PO_4 (100/500 μScm^{-1})	25	2.5 μs	–	5×10^{18}	2000	–	50
2014	Marinov *et al.* [63]	–	pin-wire 2 mm	deionized water (5 μScm^{-1})	15	30 ns	–	$1.3{\times}10^{20}$	–	–	30
2018	Pongrác *et al.* [64]	corona–like	pin-plane 5 mm	deionized water (2 μScm^{-1})	100	6 ns	–	10^{19}	100	–	single shot

1.3 Optical diagnostic techniques for measuring plasma properties

The developing experimental techniques for plasma parameters diagnostics are essential for understanding the physical mechanism in the discharges. In general, the diagnostic techniques can be classified into two types: (a) the electrical methods for measuring the voltage and current in the circuit from which the physical properties of plasma in the discharge can then be derived; (b) the optical diagnostics for measuring plasma parameters, including gas temperature (T_g), electron density (n_e), electron temperature (T_e) and electron energy distributions.

Over a century, the Langmuir probe was one of the most widely used and basic electrical detection methods [75–80]. The working principle of Langmuir probe is as follows: a or multiple thin metal wires are put partially in contact with the plasma while the other part of the wire outside the plasma region, covered with insulating material, is connected to the electrode via an adjustable power supply. By measuring the relationship between the electrical current and the applied voltage, one can obtain the voltage–current characteristic curve of the probe. According to the special points on the curve, the electron density, electron temperature and electrical potential of plasma can be obtained. In spite of its low cost and ease of operation, the Langmuir probe has several experimental drawbacks, such as the poor time resolution and sometimes may disturb the plasma field. Consequently, some other experimental techniques, especially the optical diagnostics for plasma have been developed and implemented in the modern experiments and commercial plasma reactors.

In 1970s, Stritzke *et al.* [43] measured the nitrogen spectra of a spark discharge at low pressure (0.4 bar) with a time resolution of 5 ns and spatial resolution of 2 mm. The radial distribution of temperature along the plasma channel was determined from NI, NII, NIII, NIV and NV atomic lines. A broad band spectra in the wavelength range of $200-900$ nm of discharge in nitrogen was recorded by Sewraj *et al.* [81]. As shown in figure 1.11, second positive system (SPS, $N_2\,(C^3\Pi_u \rightarrow B^3\Pi_g)$) of molecular nitrogen can be clearly seen in UV and visible spectra. Besides, first negative system (FNS, $N_2\,(B^3\Pi_g \rightarrow A^3\Sigma_u^+)$) of N_2 at wavelength $\lambda = 391.4$ nm and in range of $650-670$ nm were also detected. The near IR spectrum was dominated by Herman IR system (HIR, $N_2\left(C'''^5\Pi_u \rightarrow A'^5\Sigma_g^+\right)$) in the wavelength range of $700-860$ nm. The authors also reported the Lyman-Birge-Hopfield system (LBH, $N_2\left(a^1\Pi_g \rightarrow X^1\Sigma_g^+\right)$) in VUV spectrum.

More detailed information about the emission produced by the radiative transitions between different energy levels of N_2 and N_2^+ are displayed in figure 1.12.

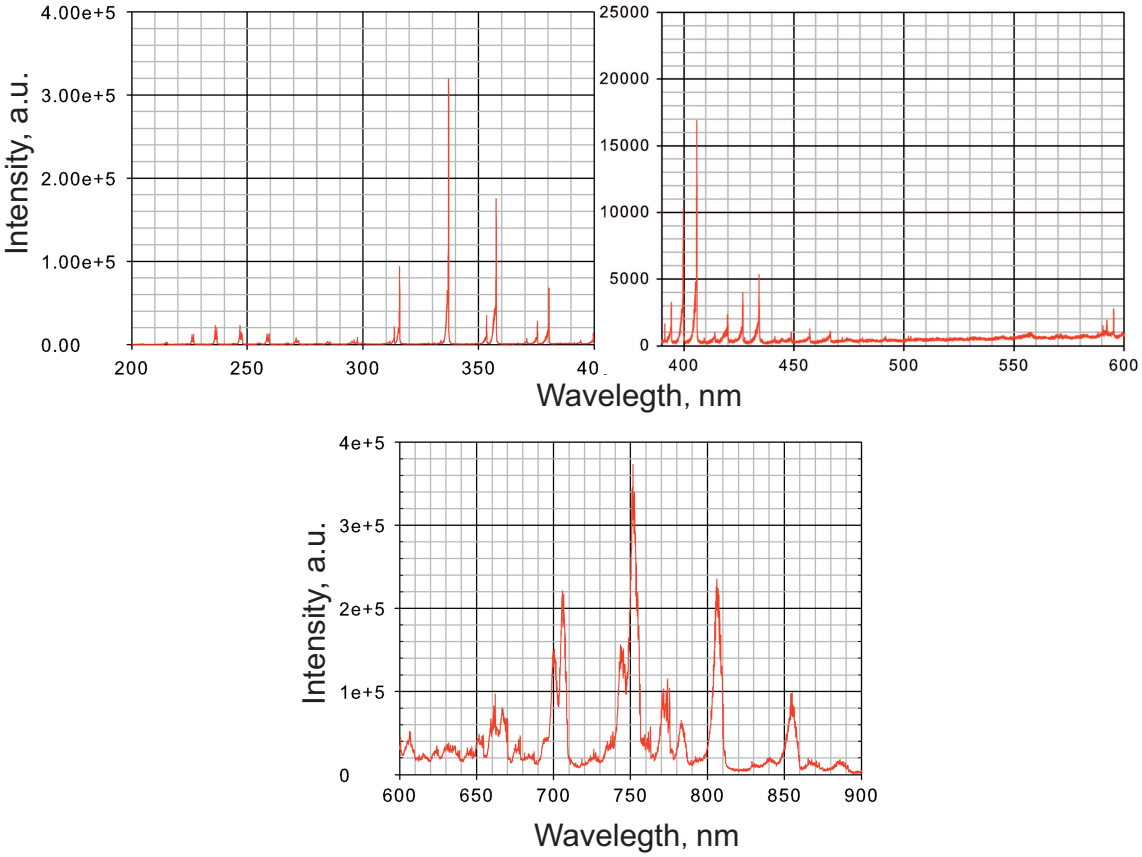

Figure 1.11: Emission spectra in wavelength range of $200 - 900$ nm of discharges in 1 bar nitrogen. The figure is taken from [81].

In addition to nitrogen being widely used in emission spectroscopy diagnosis, hydrogen (or water vapor) is also often used in the measurement of plasma parameters such as electron density and electron temperature. Babankova *et al.* [83] measured the excitation temperature from the emission of a series of hydrogen atomic lines in a high–power laser–induced dielectric discharge. The experiment was done in water vapor at low pressure (20 Torr). A single 1315.2 nm laser pulse with energy of a few hundreds Joules was used to launch the breakdown. Balmer series of hydrogen atoms (H_α, H_β, H_γ and H_δ) in the wavelength range of $400 - 700$ nm can be clearly seen from the figure 1.13 (a). The excitation temperature T_{exc} is determined from the Boltzmann plot of the relative emission intensity of Balmer series of hydrogen atoms.

The Balmer series of hydrogen atomic lines can also be used for determining the electron density n_e from the Stark broadening effects. Bruggeman *et al.* [84] compared the accuracy of the measured electron density from different Balmer series of hydrogen lines (H_α, H_β and H_γ) in a dc-excited discharge in water. It is found that the n_e results achieved from H_β line has higher precision than the results got

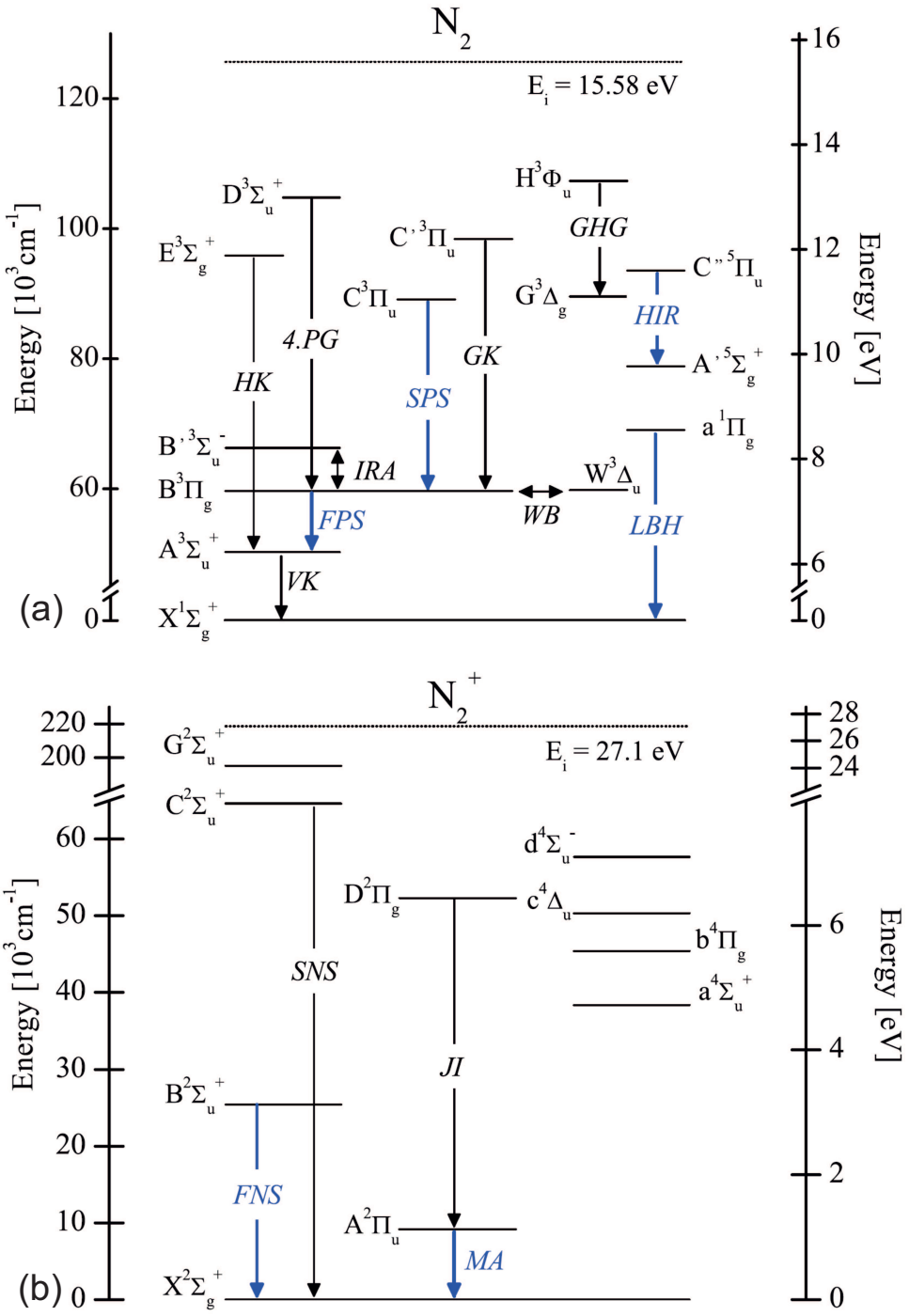

Figure 1.12: Common energy level diagram and radiative transition layout of (a) N_2 molecule and (b) N_2^+ ion. Abbreviations in (a): HK: Herman-Kaplan system, VK: Vegard-Kaplan system, 4PG: Fourth positive system, IRA: Infrared afterglow system, GK: Goldstein-Kaplan system, WB: Wu-Benesch system, GHG: Gaydon-Herman Green system; abbreviations in (B): SNS: Second negative system, JI: Janin-d'Incan system, MA: Meinel's auroral system. The figure is taken from [82].

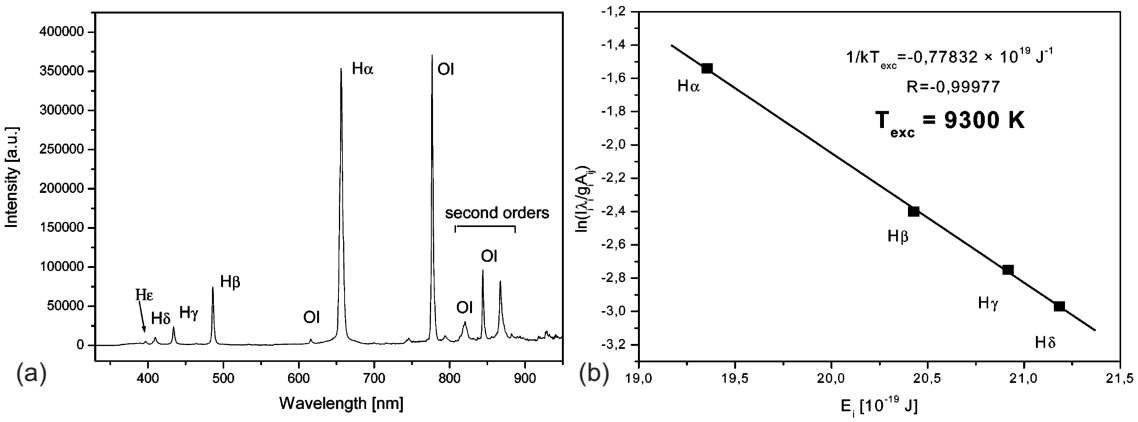

Figure 1.13: (a) Optical emission spectra of Balmer series of hydrogen atoms (H_α, H_β, H_γ, H_δ and H_ϵ) and (b) their Boltzmann plot. The figure is taken from [83].

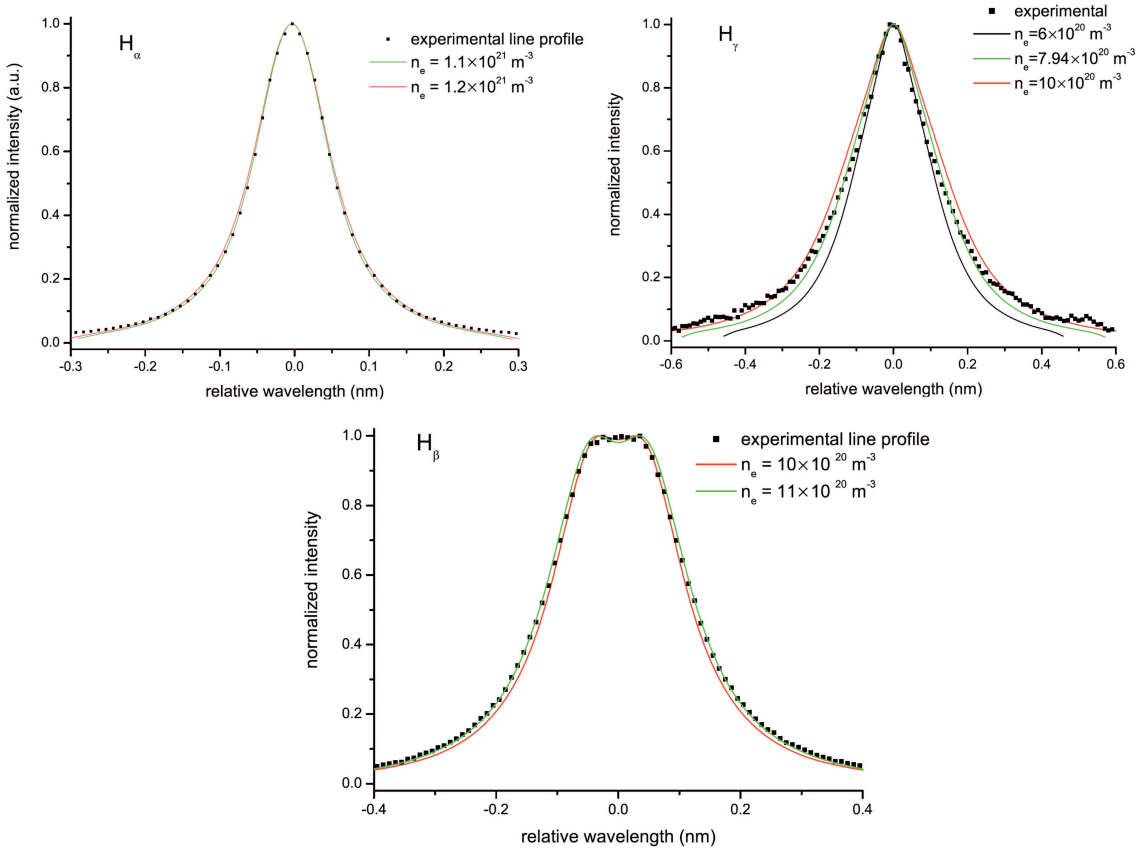

Figure 1.14: Fitting of the H_α, H_β and H_γ lines for determining the electron temperature of the plasma produced by a dc-excited discharge in water. The figure is taken from [84].

from both H_α and H_γ lines and the H_β line profile fitted better with the experimental data (see figure 1.14). The reason is that H_α line is not suitable for calculating the electron density in non–equilibrium plasma where electrons have significantly larger

translational energy than heavy particles. In most cases, the emission of H_γ line is rather weak.

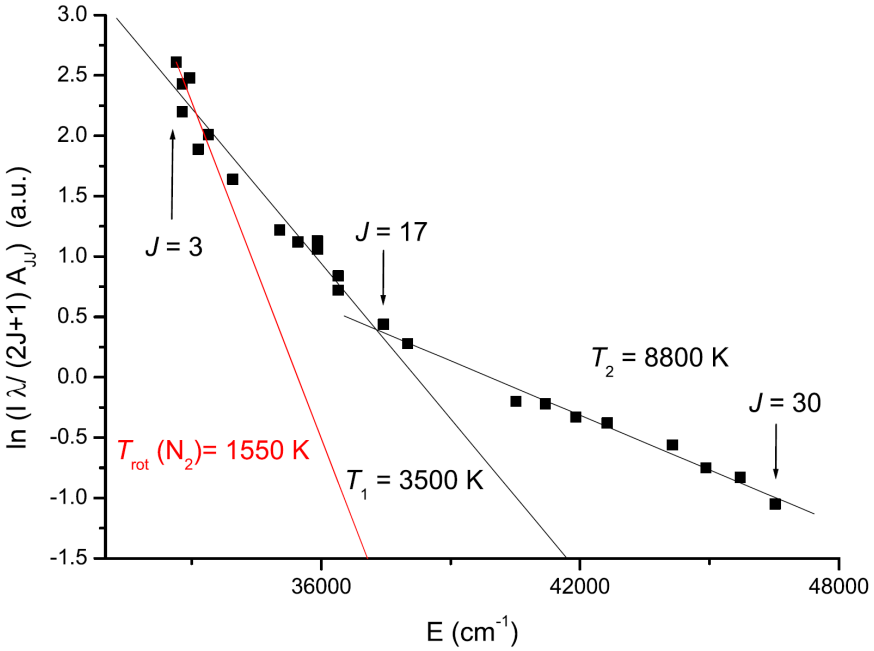

Figure 1.15: Boltzmann plot of OH(A-X) transition in the plasma produced by a dc-excited discharges in water. The figure is taken from [84].

In [84], the authors also measured the plasma temperatures of the discharge in vapor bubbles in water. The rotational temperature T_{rot} was calculated separately from both SPS of N_2 fitted by Specair [85] and the Boltzmann plot of OH($A^2\Sigma^+ \rightarrow X^2\Pi$, $\Delta\nu = 0$) transition bands. As shown in figure 1.15, the temperature results determined from two methods do not correspond to each other. The rotational temperature measured from SPS of N_2 ($T_{rot}(N_2)$=1550 K) is lower than measured from the Boltzmann distribution of OH(A-X) transition bands, T_1=3500 K from $J = 3 - 17$ and T_2=8800 K from $J = 17 - 30$. The appearance of two Boltzmann distribution comes from the different production mechanisms of OH($A^2\Sigma^+$).

1.4 Numerical modeling methods of surface dielectric barrier discharges

Numerical modeling method has been widely used for testing hypothetical suspicions, foreseeing the discharge behavior under certain conditions, explaining the phenomena observed in the experiments and optimizing the design of plasma actuators. Over a few decades, nanosecond surface dielectric barrier discharges (nSDBDs) were experimentally studied in atmospheric air for the applications of air flow control. With the development of computer technology, a series of numerical calculations were implemented for solving the problem of electrohydrodynamic (EHD) force generation [86] and control, plasma dynamics in the boundary layer as well as the kinetics involved in chemical reactions.

The first approximation of plasma kinetics influences on air dynamics was made by Roy with a basic 2D fluid model in [87] where the author concluded that the momentum transfer was caused by the charges accumulated on the dielectric surfaces. In the modeling of an asymmetric DBD actuator [88], Likhanskii *et al.* proposed a voltage waveform of the repetitive nanosecond pulses with dc bias that was found to be efficient for gas pushing by increasing the EHD forces. As shown in figure 1.16(b), the EHD forces in the vertical direction were significantly enhanced by applying a 3 kV positive nanosecond pulses with 4 ns pulse width and 1 kV positive bias.

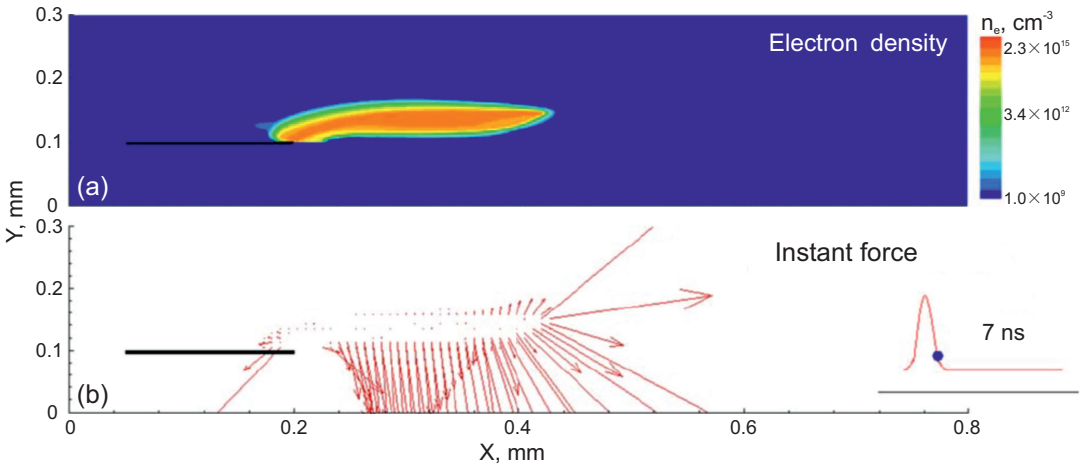

Figure 1.16: (a) Contour of electron density of a streamer ionization wave at positive polarity 3 kV in amplitude with 1 kV bias and (b) instantaneous EHD forces produced by discharges. The figure is taken from [88].

Later studies shown that SDBD can modify the dynamics of air flow via fast gas heating in the boundary layer with the absence of ion wind [89,90]. Unfer *et al.* used a 2D model, coupling the fluid discharge equations with compressible Navier–Stokes

equations, to simulate the plasma and flow interaction in the discharge boundary layer. The authors found that there was a micro shock wave generated near the tip of the electrode (see figure 1.17) caused by the fast energy deposition. Subsequently, the gas in the region of shock wave propagation was heated rapidly up to 1000 K when the vibrational–translational collisions were taken into account.

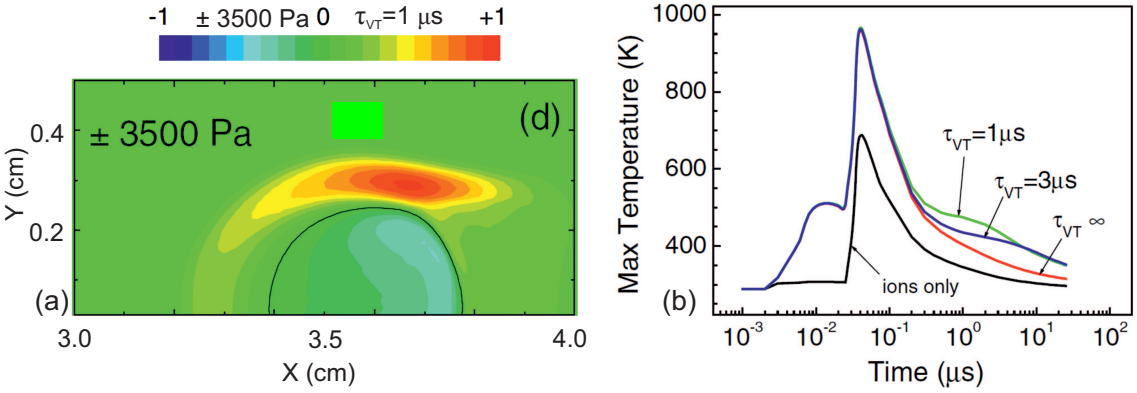

Figure 1.17: (a) Spatial distribution of the gas pressure perturbation at time t=8 μs with the relaxation time for vibrational–translational collisions $\tau_{VT} = 1$ μs and (b) The evolution of maximum gas temperature with different τ_{VT}. The figure is taken from [89].

Soloviev *et al.* calculated SDBD evolution at both discharge and afterglow phases with a 2D fluid model. The authors found that the air flow was mainly affected by the heat and momentum sources in the afterglow phase [91]. The plasma is redistributed shielding the external electric field when the discharge is off. In this period the ionization rate of air has been reduced to a very low value in the discharge region. The major processes in the afterglow phase, which lasts for many microseconds, are ion–electron and ion-ion recombination. The momentum and heat sources are promoted effectively in the afterglow period when the plasma diffuses outward to the surface of the dielectric. The thickness of the momentum source layer was found to depend on the amplitude of the applied voltage for both negative and positive polarities. Consequently, it is possible to achieve the maximum discharge interaction with air flow by optimizing the waveforms and amplitudes of applied voltages.

Similar model was used for simulating the streamer propagation of a SDBD ignited by a nanosecond negative high–voltage (HV) pulse at atmospheric air. In [92], the authors calculated the discharge development at both rising and trailing edges of the HV pulses. The differences between these two stages are significant. As shown in figure 1.18, at the rising edge of the HV pulse, the streamer is in contact with the dielectric surface when it propagates while at trailing edge, the plasma keeps a distance of $30 - 40$ μm from the surface when it travels. Additionally, the

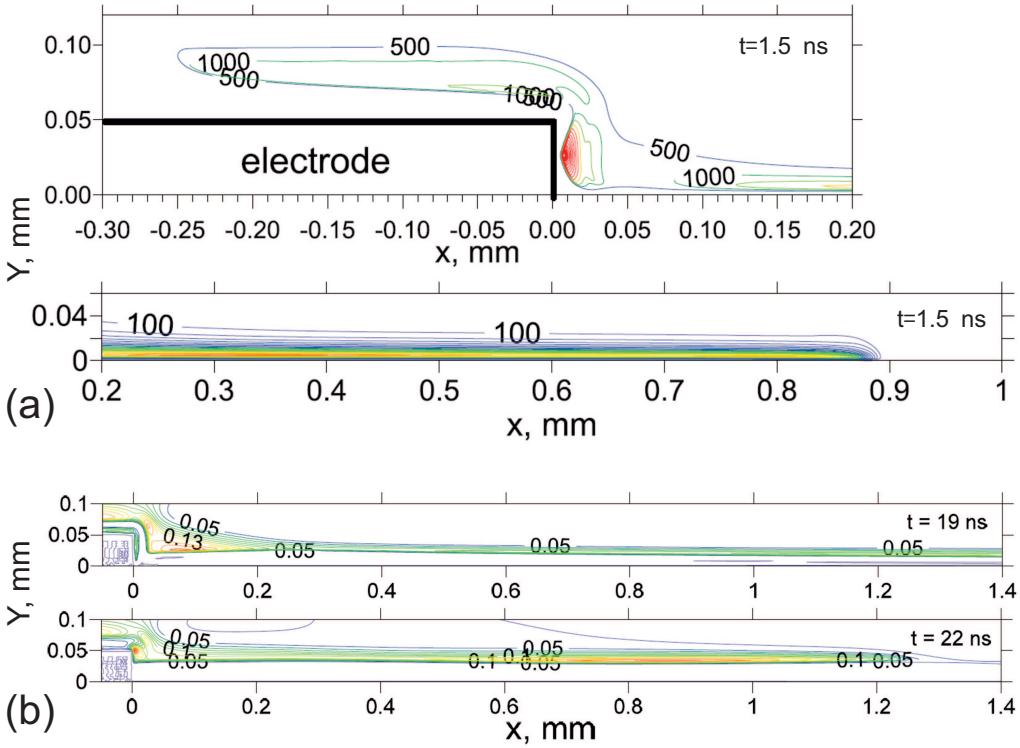

Figure 1.18: Map of electron density in unit of 10^{15} cm^{-3} of streamer propagation at negative polarity at (a) rising edge and (b) trailing edge of the high–voltage pulse. The value is shown on twenty scales. The figure is taken from [92].

major proportion of energy (over 90%) was deposited in the rising edge and plateau of HV pulse.

Since the fluid model were widely used due to its low computational cost for describing the essential plasma physics, several hybrid models that combine the fluid model with kinetic models are also implemented for preserving the accuracy of kinetics in the simulation. Meanwhile, hybrid model can reduce computational burden compared to the kinetic models.

A 2D hybrid model combining the conventional fluid model with Monte Carlo model was carried out by Babaeva *et al.* in [93] where the fluid equations were used to calculate the bulk electrons with low mean energy while the kinetics of secondary electrons with high energy were modeled by Monte Carlo simulation. The authors also did the pure fluid simulation to treat the dynamics of both bulk and secondary electrons for comparison.

The different outputs of these two models are shown in figure 1.19. In addition to the different velocities of streamer propagation under two models, the electron "needle" appearing at negative polarity is a distinguishing feature in the results of hybrid simulation. This feature was caused by the rapid generation and capture

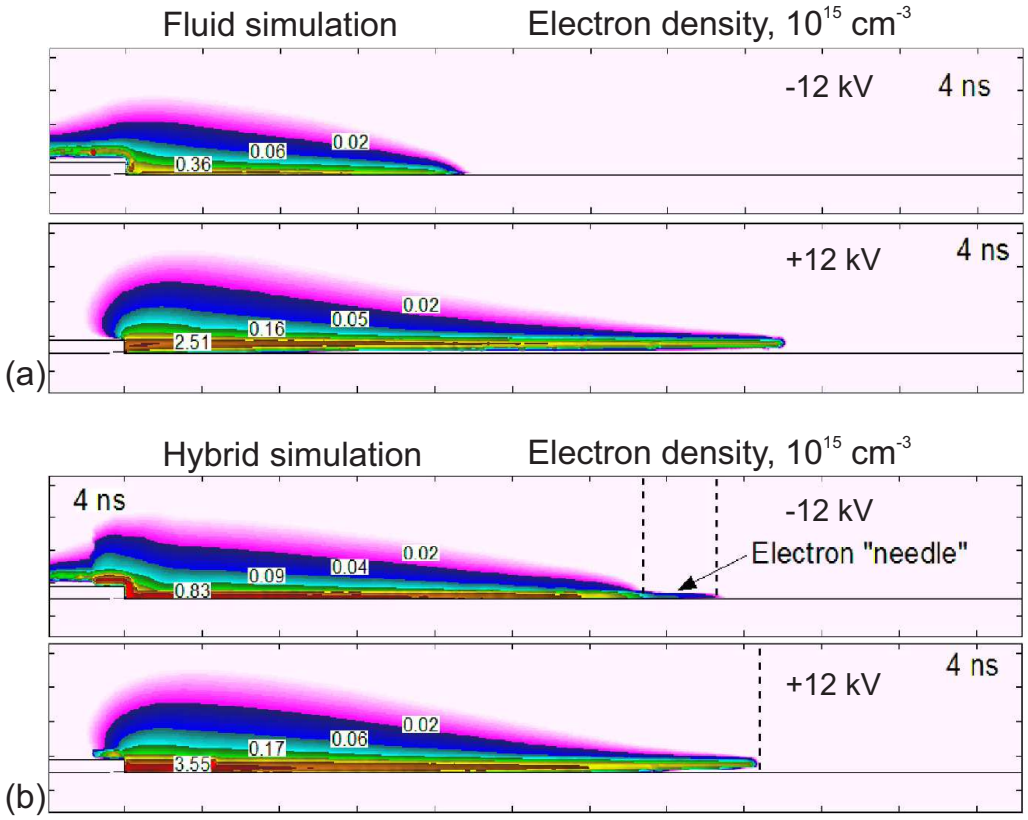

Figure 1.19: Electron density of streamer propagating at $t = 4$ ns at both negative and positive polarities by (a) fluid and (b) hybrid simulations. The value is shown on three decades log scales. The figure is taken from [93].

of secondary electrons in the narrow anode sheath area. The authors concluded that the "needle" indicated the high electric field in the negative streamer head with a typical length of 450 μm. The protrusion electrons and ions in the needle were produced by photoionization process.

The dynamics of nanosecond pulsed SDBDs at atmospheric pressure have been widely studied both experimentally and numerically over the past decades. However, there is few numerical study on the nSDBDs at elevated pressures, typically higher than 3 bar. The reason is that with the increase of gas pressure, the streamer discharge will transited to the filamentary mode from non-equilibrium plasma to local thermodynamic equilibrium plasma. This streamer–to–filament transition process is accompanied by the significant changes in plasma kinetics, including the ultrafast rise of electron density and gas heating. In addition, the high pressure condition will also enhance the collisions between electron and neutral particles and shorten their mean free path, thereby significantly decreasing the kinetic time scale. Furthermore, the reduced discharge channel width at high pressures requires finer mesh, accordingly leading to higher computational costs.

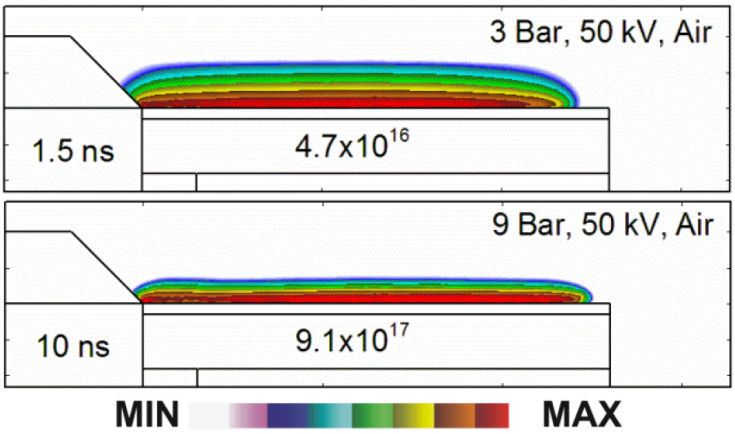

Figure 1.20: Electron density of streamer (filament) in unit of cm^{-3} at 3 and 9 bar at positive polarity 50 kV in air. The value is shown on four decades log scales. The figure is taken from [94].

Babaeva *et al.* in [94] made the attempt to calculate the morphology of a nS-DBD in air at elevated pressures and positive high voltage ($U = +50$ kV) by using nonPDPSIM model. The authors observed the dramatic increase of electron density up to 9.1×10^{17} cm^{-3} when the pressure grew from 3 bar to 9 bar (see figure 1.20). The shrunk of streamer channel and the slowing down propagation velocity at higher pressure were also reported.

Chapter 2

Problem formulation

As it was described in literature review, the dielectric barrier discharges (DBDs) at atmospheric pressure have been widely studied experimentally and numerically. Nanosecond DBDs in atmospheric pressure air came to the scene in the beginning of 21st century for the problem of flow control. Recent development of plasma technologies and high interest for plasma in adjacent fields, as aircraft industry ignition/combustion, demands fundamental study of gas discharges at elevated pressures and temperatures.

The advantage of a nanosecond DBD is a simultaneous initiation of hundreds of streamers propagating from the edge of the high–voltage electrode synchronously within 0.2 ns, and so producing a quasi–uniform plasma layer near the dielectric. The main challenge in initiation of combustion by nonequilibrium plasma is that the main energy input is directed to production of radicals and excitation of electronic levels of atoms and molecules. Then, due to radical recombination and relaxation of electronic excitation, the temperature increases rapidly, allowing development of chemical chains and, consequently, plasma assisted ignition (PAI). This process is relatively well described for moderate and low pressures. Only a few studies at elevated pressures, under conditions close to automotive engines, are known.

It has been recently shown [40, 95] that a single–shot nanosecond surface DBD changes dramatically with pressure increase. A system of synchronous streamers transforms in a single–shot regime, to the system of filaments. The filaments are plasma channels, originating in the vicinity of the edge of the high–voltage electrode and propagating, like streamers, in the direction perpendicular to the edge of the high–voltage electrode. The distance between adjacent filaments is $4 - 5$ times

greater than between the streamers.

Streamer–to–filament transition happens during a few nanoseconds, at this the electron density changes from $n_e^s \approx 10^{15}$ cm^{-3} to $n_e^f \approx 10^{19}$ cm^{-3} and optical emission spectra change from bands of molecular nitrogen to continuous wavelength (cw) and atomic lines, increasing in total intensity by a factor of ~ 50. It was also known [95] that streamer–to–filament transition can be observed in air and nitrogen for both negative and positive polarities of the high–voltage pulses.

The present work is focused on the following tasks:

1)To suggest and to develop another geometrical configuration of nanosecond surface dielectric barrier discharges, allowing observation of the streamers and filaments from the side.

2) Based on direct visualization of discharge using ICCD imaging combined with long distance microscope, electrical measurements (electrical current and deposited energy), optical emission spectroscopy and Particle Image Velocimetry (PIV) measurement, to obtain consistent plasma parameters of the filamentary nSDBD at elevated pressures in both nitrogen and air for both negative and positive polarities.

3) To study the experimental conditions and parameters of streamer–to–filament transition in N_2:O_2 gas mixtures with different oxygen fraction for both polarities of high–voltage pulses. To investigate the effects of modifications of material/structure of the high–voltage electrode (annealed or non–annealed, copper or copper covered with carbon nanomaterials) on the streamer–to–filament transition.

4) To find a method to visualize, with a high temporal resolution ($1 - 2$ ns), a zone of origin of a streamer–to–filament transition. To perform, for this zone, measurements with the high spatial resolution ($2 - 10$ μm/px). To study experimentally, the detailed morphology of streamer–to–filament transition; to find a point of origin of cw spectrum and high density of electrons. To analyse, with the help of numerical modeling, difference in development of high pressure streamers for different O_2 fractions.

Chapter 3

Experimental apparatus and numerical modelling methods

3.1 Scheme of the experimental setup

3.1.1 Electrode configurations

Two different electrode configurations were manufactured for the experiments. One is the electrode which has been developed for the applications related to plasma assisted combustion [40, 96]. This electrode is shown in figure 3.1. A metal disk, 20 mm in diameter, served as a high-voltage electrode. For the experiments that need to fix the starting position of discharge, the central metal disk was replaced by a gear wheel of the same diameter with 60 sawteeth. The high-voltage electrode, the metal disk or gear wheel, was fixed on the surface of the dielectric PVC film ($\epsilon \approx 3-3.5$) that was glued to the ground electrode by Geocel FIXER Mate silicon glue ($\epsilon \approx 3$). The thickness of both the PVC film and silicon glue was 0.3 mm, which gives the total thickness of the dielectric layer 0.6 mm. The inner diameter of the ground electrode was equal to the diameter of the high-voltage electrode, and the external diameter of the ground electrode was the same as the diameter of the PVC dielectric that is 50 mm. The discharge starts at the set of streamers from the high–voltage electrode. The streamers propagate in the radial direction. We will call this electrode system a radial electrode system.

To have a possibility to study the discharge development from the side, another electrode system has been developed. It is shown in figure 3.2. A base of the

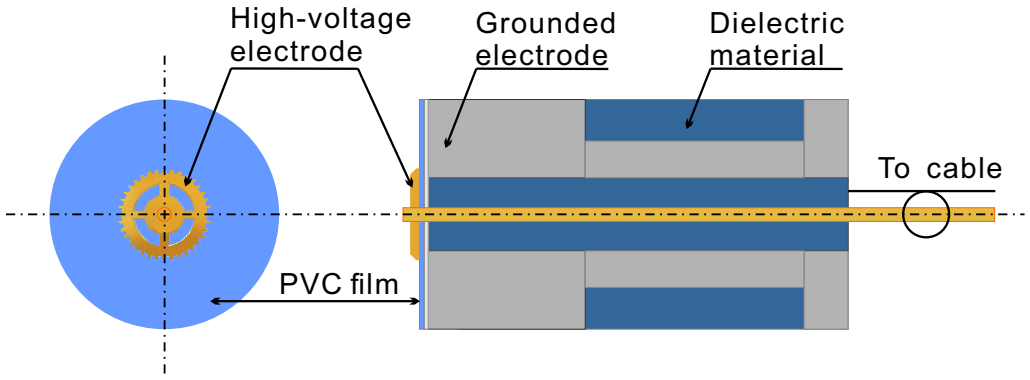

Figure 3.1: The radial electrode system.

cylinder, the metal disk of 30 mm in diameter, served as a high–voltage electrode. A few layers (8 to 9) of the dielectric PVC insulation tape ($\epsilon \approx 3$) were glued to the ground electrode, giving the total thickness of the dielectric layer equal to 1 mm. The external diameter of the ground electrode combined with the insulation tape was the same as the diameter of the high-voltage electrode, that is 24 mm. To produce, in controllable way, the discharge on the side surface of the cylinder, the adhesive copper tape with conductive adhesive layer and with the sawteeth on one side was glued around the metal disk. As described above, the sawteeth were used to fix the starting position of the discharge. The width of the copper tape was adjusted to ensure that the teeth edge stays at the same position as the interface of dielectric material and grounded electrode. We will call this electrode system a cylindrical electrode system.

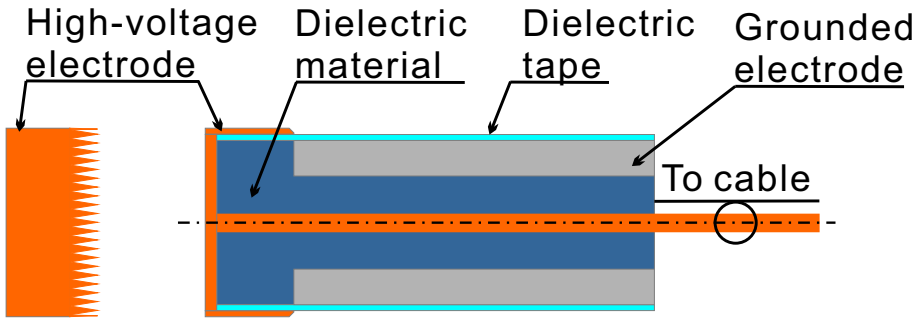

Figure 3.2: The cylindrical electrode system.

3.1.2 Surface dielectric barrier discharge cell and high pressure system

The high-pressure discharge cell is dedicated for studying the surface dielectric barrier discharge at high pressure conditions, up to 12 bar. The cubic shape constant

volume cell is made from stainless steel and acts as a part of the ground shield of the discharge system. The cell has three quartz optical windows 5 cm in diameter. One of the windows is situated in front of the electrode and used for the optical imaging and spectroscopy measurements in the radial electrode system. The other two windows are used for the optical measurements in the discharge cell equipped with the cylindrical electrode, as shown in figure 3.3.

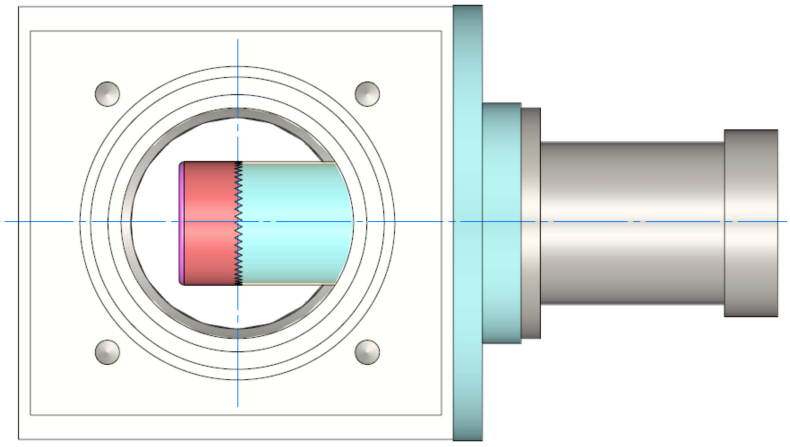

Figure 3.3: High-pressure chamber equipped with the cylindrical electrode system.

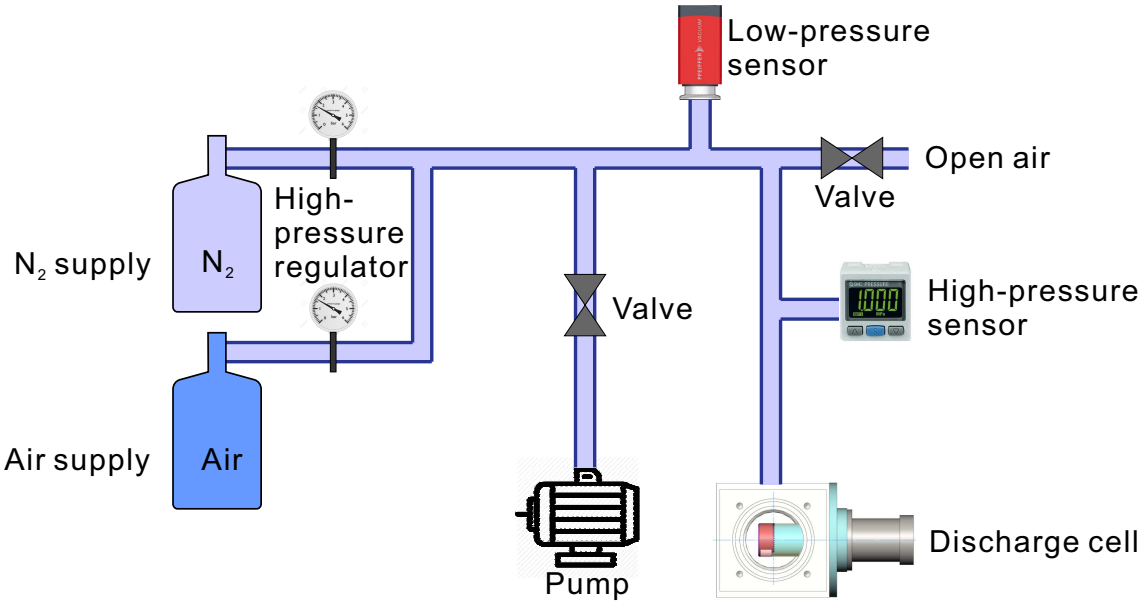

Figure 3.4: Schematic of the high-pressure controlling system.

The schematic of the high-pressure controlling system is shown in Figure 3.4. Before each set of the experiments, the high-pressure chamber was pumped down to about 100 Pa by the pump (Edwards XDS–10, A726-01-903). The low-pressure sensor (PKR 360, PFEIFFER VACUUM) was used to indicate the vacuum level

in the system. The chamber was then filled with the gas under study (nitrogen, nitrogen:oxygen mixtures and nitrogen:hydrogen mixtures, Air Liquide, impurities < 100 ppm). The high-pressure regulator (DHP 200-50-10, Air Liquide) was used to control the input gas pressure in the discharge chamber. The high-pressure sensor (ISE 30-01-65, SMC corporation) indicated the pressure above the atmospheric pressure in the discharge cell at the beginning of the experiment. After each set of the experiments, the valve to the open air was opened for exhausting the gas from the discharge chamber.

3.1.3 High voltage generator

In the past few decades, there are two ways for generating the nanosecond high–voltage pulses with kilovolts to megavolts amplitude based on the solid-state semiconductors. These two approaches are distinguished by the design of the switch part where the energy are stored. The "opening switch" design, also called inductive design, uses the inductive components to store the electromagnetic energy in the circuit. When the switch is opened suddenly, the energy can be released to the circuit, producing the high–voltage on the load. For the "closing switch" design, the high–voltage energy is stored in the capacitors. The pulse is generated by abruptly closing the switch in the circuit. The advantages of the "opening switch" design are as follows: The energy density stored in the inductive components is $1.5 - 2$ orders of magnitude higher than in the capacitors [97]. So the generator using "opening switch" has smaller size and lower cost. Apart from that, by opening the switch in the circuit, one can get the ideal pulse voltage on the load, which is much higher than the voltage in the intermediate stage of the pulse generation process. The disadvantage of the "opening switch" design is that a few kiloamperes breaking current could appear when the megavolts pulse voltage is generated. To solve this problem, I.V. Grekhov *et al.* from Ioffe Physical Technical Institute, Russian Academy of Sciences used a kind of semiconductor drift step recovery diodes (DSRDs) instead of injection thyratrons or exploding wires. The latters were usually used in laboratory and had very limited life time [98].

In our experiments, the commercial pulse generators FPG20–03PM and FPG20–03NM (FID Technology) are used. The high-voltage nanosecond pulse of positive or negative polarity has 2 ns rise time, 20 ns duration and $20 - 60$ kV amplitude on the electrode with jitters less than 20 ps. FID Technology uses the"opening switch" to design the high–voltage generators. These generators are able to work at high repetition rates, up to a few megahertz, by taking advantages of a semiconductor device called drift step recovery diodes (DSRD) [99–101] as the opening switch. As shown in figure 3.5(b), the low–voltage energy is stored in the inductive components

(L_1 to L_N). The number of the inductive components N depends on the amplitude of the intended high–voltage. By the abrupt opening of the DSRD, the high–voltage pulse can be generated on the load R_L.

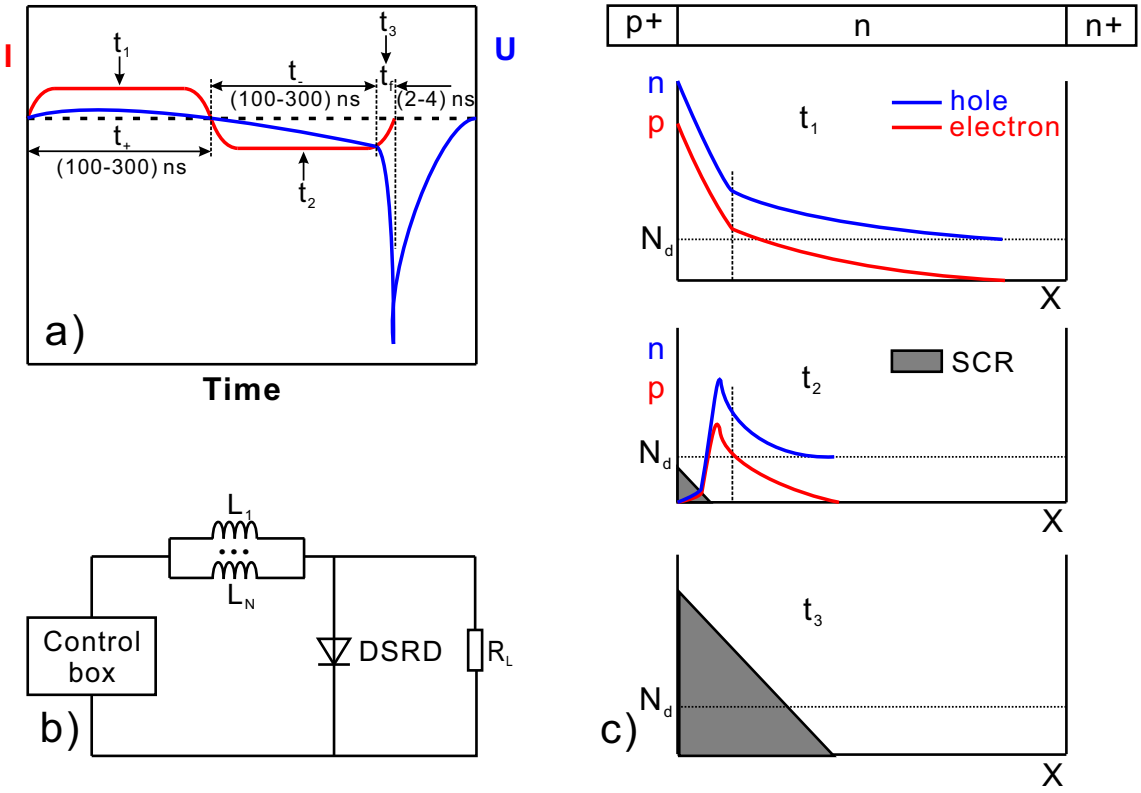

Figure 3.5: Working principle of the semiconductor device DSRD. (a) Diagram of current and voltage on DSRD; (b) Circuit diagram of the high-voltage generator where the DSRD works as a opening switch; (c) Carriers distribution during the pumping and recovery process of P–N junction. $N_d - N$ layer doping, SCR–Space charge region. This figure is redrawn from the works of Kardo et al [99, 101].

The drift step recovery diodes (DSRDs) have the advantages of ideally unlimited life time, low jitter (less than 100 ps) and high repetition rate (up to mega hertz). DSRD works at three stages, as shown in figure 3.5(a) and 3.5(c): first, during the time period of t_1 when the forward current pulse is applied to the semiconductor with "p+nn+" structure, the electrons are pumped to form a electron–hole diffusion area near the p+–n junction. At the second stage (time period of t_2) where the current changes to the reverse direction, the drift wave moves back towards the p+–n junction, compressing the diffusion region. In this region, a reverse distribution gradient of electrons and holes appears. As soon as the distribution gradient of electrons and holes reaches to zero, the space charge region (SCR) is formed. The propagating velocity of SCR border is inversely proportional to the electrons and holes' concentration in the diffusion region. At the second stage, the concentration

of carriers (electrons and holes) is high due to the compressed diffusion region. This causes that SCR propagates slowly in this period, leading the small voltage increase during the time period of t_2. At the beginning of period t_3 when the SCR border meets the head of the drift wave, the diffusion region collapses. After the collapses happens, the carriers (electrons and holes) will reach an equilibrium state in n layer and the conductive current will disappear from this region. In this case, the velocity and the voltage changing rate (dU/dt) increase sharply in $2-4$ ns because of the rapidly reduced carriers concentration. At the third stage, high voltage is generated from the self–induction in the drift step recovery diode circuit. After each opening operation, the charges accumulated on the P–N junction are removed completely giving the possibility to the next opening.

Due to the skin effect, the effective region of the drift step recovery diodes were limited under 40 cm^2, leading to the current density in DSRDs in the range of a few hundreds A/cm^2. To obtain the generator with high power performance (gigawatt power range), researchers from Russian Academy of Sciences developed another current breaker with silicon opening switch (SOS) effect. The most important progress of this switch is that the current density on the diode can reach up to 10^3-10^4 A/cm^2. The other differences between DSRDs and SOS are as follows: In DSRDs, the density of hole-electron plasma is relatively high in the P–N junction and weakly doped N region. These plasmas do not participate in the current breaking process. While in SOS process, the collapse caused by the confluence of hole-electron plasma front and space charge region (SCR) takes place at highly doped P region. Because of the ionization impact in SCR, the SOS diode donates more charges than the pumping of forward current.

3.1.4 Synchronization scheme and electrical measurements

The high-voltage generator was triggered by a triggering pulse generator (TGP110, Thurlby Thander Instruments), "TGP #1" shown in figure 3.6. The high-voltage pulse was transmitted to the electrode system via a 50 Ω high-voltage coaxial cable (RG 213). The cable is 30–meter long to separate the reflected signal from the incident one. The voltage signal was recorded by the back current shunt (BCS #1) in the middle of the coaxial cable and then sent to the oscilloscope. Detailed technology about back current shunt can be found in [102, 103]. Another triggering pulse generator (TGP #2) received the signal from BCS #2 that situated one meter from the high-voltage generator. This signal was used to trigger the spectrometer and ICCD camera.

The back current shunt (BCS) was made from a few resistances (normally 12 to 14) laying on the copper sheath of the coaxial cable (figure 3.7). It is an idea from

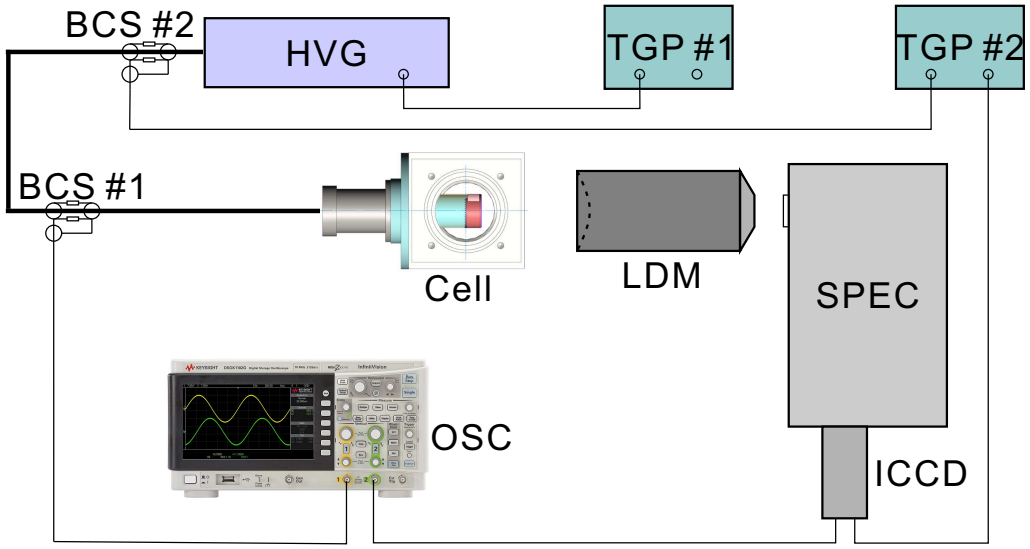

Figure 3.6: Schematic of the synchronization system. HVG–High-voltage generator, BCS–Back current shunt, TGP–Triggering pluser generator, LDM–Long distance microscope, SPEC–Spectrometer, ICCD–Intensified CCD camera, OSC–Oscilloscope.

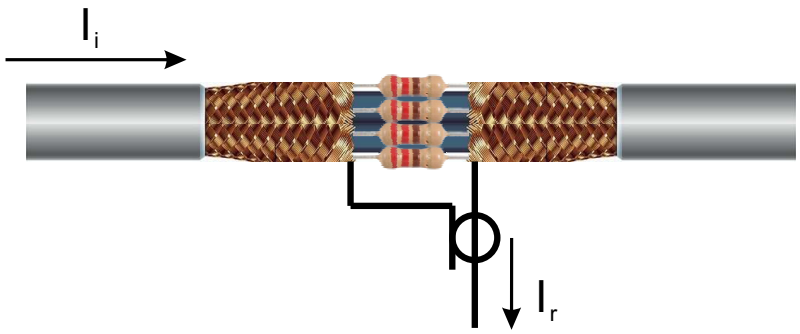

Figure 3.7: Schematic of the back current shunt (BCS)

the telegraph equations [104] that contains a pair of partial differential equations as follows:

$$\begin{aligned} \frac{\partial^2 V}{\partial x^2} &= LC\frac{\partial^2 V}{\partial t^2} + (RC + GL)\frac{\partial V}{\partial t} + GRV \\ \frac{\partial^2 I}{\partial x^2} &= LC\frac{\partial^2 I}{\partial t^2} + (RC + GL)\frac{\partial I}{\partial t} + GRI \end{aligned} \tag{3.1}$$

where L, C, R and G represent self–inductance, capacitance, series resistance and parallel conductance per unit length respectively. In a transmission lossless coaxial cable where $\omega L \gg R$ and $\omega C \gg G$, the equation 3.1 can be simplified as the wave propagation equations as follows:

$$\begin{aligned} u^2\frac{\partial^2 V}{\partial x^2} &= \frac{\partial^2 V}{\partial t^2} \\ u^2\frac{\partial^2 I}{\partial x^2} &= \frac{\partial^2 I}{\partial t^2} \end{aligned} \tag{3.2}$$

where $u = \frac{1}{\sqrt{LC}}$ is the wave propagation velocity (phase velocity). In the 50 Ω high-voltage coaxial cable (RG 213), the signal propagation velocity is about 0.2 m/ns. The equation 3.2 has the solution as follows:

$$\begin{aligned} V(x,t) &= f_1(x-ut) + f_2(x+ut) \\ I(x,t) &= \frac{f_1(x-ut)}{Z_c} - \frac{f_2(x+ut)}{Z_c} \end{aligned} \tag{3.3}$$

where $Z_c = \sqrt{L/C}$ is the characteristic impedance of the transmission cable. f_1 and f_2 are arbitrary functions and $f_1(x-ut)$ represents one transmission direction while $f_2(x+ut)$ presents the other. It can be seen that after the reflection, the voltage keeps the same polarity while the current changes the sign. Both voltage and current in equation 3.3 can be reconstructed by two parts, incident pulse V_i, I_i and reflected one V_r, I_r.

$$\begin{aligned} V(x,t) &= V_i + V_r = V_i(1+\Gamma_l) \\ I(x,t) &= I_i + I_r = I_i(1+\Gamma_l) \end{aligned} \tag{3.4}$$

where $\Gamma_l = \frac{Z_l - Z_c}{Z_l + Z_c}$ is the reflection coefficient and Z_l is the load impedance. If considering an open end where $Z_l \gg Z_c$, the reflection coefficient Γ_l is close to 1. In this case, the reflected current I_r has the same amplitude with the incident current I_i but changing the sign. Thus, the amplitude of both incident and reflected current can be measured from the potential difference of the parallel resistors in sheath of the coaxial cable which is called back current shunt (BCS). To achieve on the oscilloscope the same sign of the pulse as on the high-voltage generator, the central core of the BCS cable should be connected to the cooper sheath further to the incident pulse. In this work, 14 resistors (2.2 Ω for each) were soldered parallel in the sheath of the coaxial cable to make the BCS. BCS #1 was put in the middle of the 30 meter long coaxial cable to separate the incident and reflected pulse (see figure 3.8(a)). The voltage measured by the back current shunt U_{BCS} has the relation with the voltage in the central core of the coaxial cable U_c as follows:

$$U_c = \frac{Z_c}{R_{BCS}} U_{BCS} \tag{3.5}$$

where R_{BCS} is the total resistance of the set of 14 parallel resistors. Apart from that, the attenuation coefficient of the coaxial attenuators used to protect the oscilloscope should also be taken into consideration. For any coaxial cable with BCS used for the first time, the experimental calibration is essential.

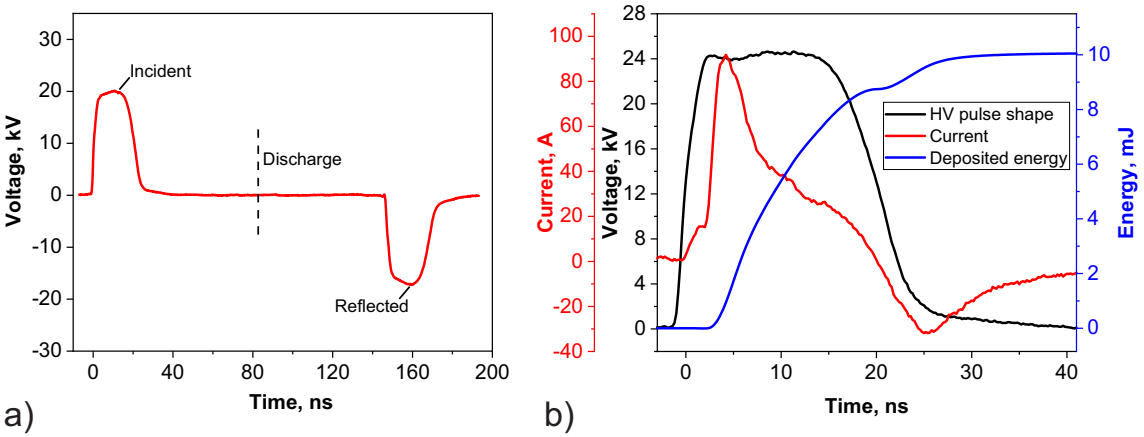

Figure 3.8: (a) Measured incident and reflected voltage waveform with BCS #1; (b) voltage, current and energy deposition.

The relation of the incident energy W_i and the reflected one W_r is as follows:

$$W_i = W_r + W_d + W_l \tag{3.6}$$

where W_d is the energy delivered to the discharge and W_l is the energy losses in the cable and for charging the capacitance of the electrode system. To measure the energy losses, it is necessary to modify the system in the way to avoid the discharge. One of the possible solutions is to cover the high–voltage electrode with the layer of silicon glue. In this case, the relation between energy would become:

$$W_i = W_{rg} + W_l \tag{3.7}$$

where W_{rg} is the energy reflected from the high–voltage electrode covered by glue. Consequently, the energy delivered to the discharge is the difference between two reflected energies. The electrical current I_d and the total deposited energy W_d (figure 3.8(b)) can be calculated as follows:

$$\begin{aligned} I_d &= \frac{|U_r - U_{rg}|}{Z_c} \\ W_d &= \frac{(U_r - U_{rg})^2}{Z_c} \end{aligned} \tag{3.8}$$

3.1.5 Long distance microscope

The QM 1 long distance microscope (Questar LaVision) (figure 3.9) is used in the experiments to study the discharge in the micrometer scale [105]. This microscope

is a catadioptric optical system that combines both the refraction and reflection components. The scheme of the QM 1 is similar to a typical scheme of Maksutov–Cassegrain telescope [106, 107]. The system contains a negative meniscus lens and two spherical mirrors. The lens at the entrance is called a correcting lens. It is intended for correcting the problems of chromatic and off-axis aberrations. The primary mirror is placed at the rear of the system for reflecting light. The secondary mirror is located centrally on the inner surface of the correcting lens, acting as a spherical mirror.

Figure 3.9: QM 1 long distance microscope. The figure is taken from [108].

The working principle of QM 1 long distance microscope is shown in figure 3.10. The light enters the optical system via the correcting lens in head of the microscope. After being refracted to the system, the light is reflected by the primary mirror locating at the rear of the microscope. This light is then sent back to the tube in the center of the primary mirror by the reflection of secondary mirror. This configuration gives the possibility of creating a long optical path in a mechanically short system, allowing the increase of the magnification. The prism is used for rotating the light path from horizontal position to vertical position. Instead of entering to the camera, the light would go directly to the eye piece (Questar, 16 mm focal length, 1.25 in in diameter) with the prism.

The QM 1 long distance microscope offers the option for adjusting the focal distance to achieve different magnifications. When the prism is put in the light path, the magnified image of the electrode can be viewed from the eye piece for adjusting. The eye piece can be replaced by a torch for finding the focal plane of the optical system. The focus rod at the rear of the long distance microscope is designed for adjusting the focal distance changing the distance between the primary and secondary mirrors. The focal distance of the QM 1 long distance microscope ranging between 52 cm and 180 cm with the measured depth of field 200 ± 30 μm and 1400 ± 30 μm respectively.

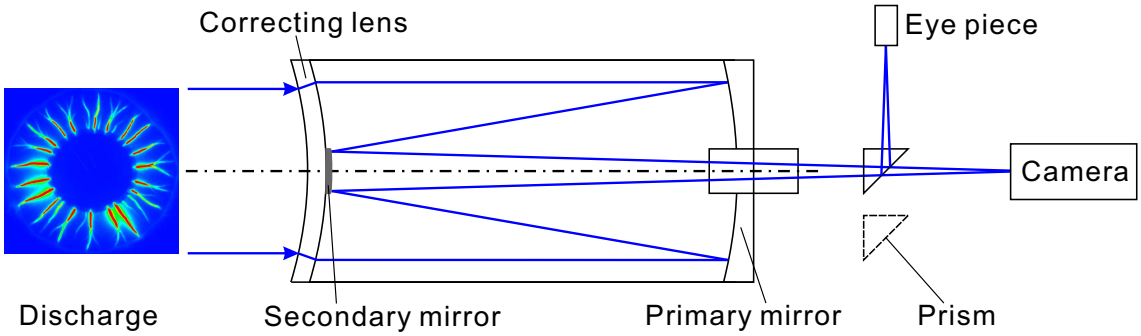

Figure 3.10: QM 1 long distance microscope working principle.

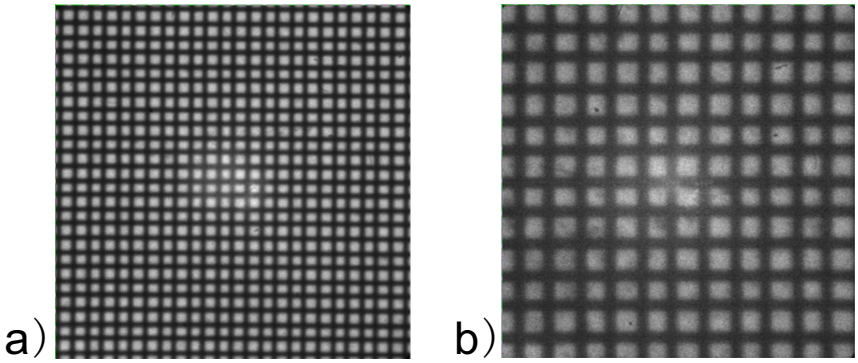

Figure 3.11: Image of the grids taken by LDM QM 1 with (a) 2 Barlow lenses (resolution of the optical system is 2.3 μm/px); (b) 3 Barlow lenses (resolution of the optical system is 1 μm/px). The focal distance of LDM is 0.5 m.

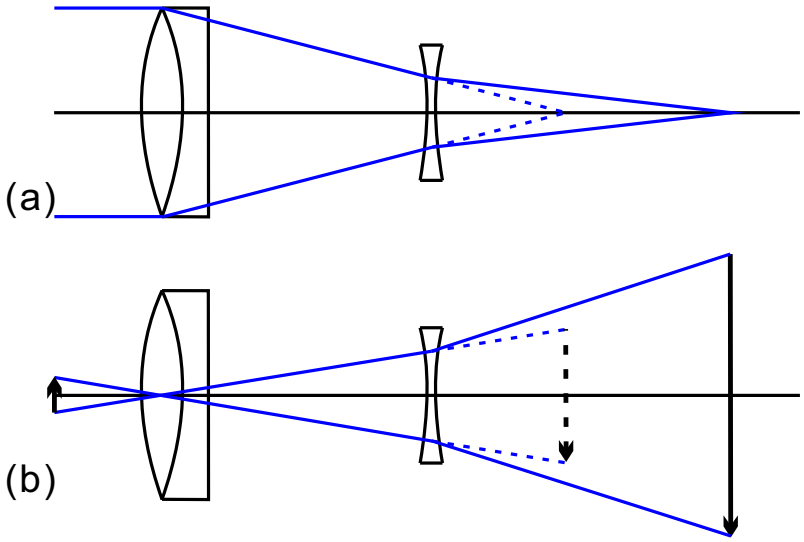

Figure 3.12: Scheme of the adoption of the Barlow lens after the achromatic doublet lens for (a) increasing the focal distance (b) amplifying the image.

The QM 1 long distance microscope was calibrated with a sheet fulling with 100 μm grids, as shown in figure 3.11. The central bright spot in both images was cause by the interference of the optical system, which was verified by the parallel beam. The Barlow lens (Questar) [109] was used to increase the magnification of the optical system by artificially extending the focal distance (see figure 3.12). It is a diverging lens, normally used with a set of optical lens, e.g. the achromatic doublet lens [110] that helps to reduce the optical aberration of the system.

Without the Barlow lens, the resolution of the QM 1 long distance microscope is 7.6 μm/px at the focal distance $f = 1$ m. With two and three Barlow lenses in the optical system, the resolution can increase to 3.6 μm/px and 2 μm/px at the same focal distance. Higher resolution can be achieved up to 1 μm/px when three Barlow lenses are put in the optical system at the focal distance $f = 0.5$ m. With the decrease of the working distance, the resolution of the system can increase due to the increased numerical aperture of the lenses. However, this is always accompanied by the decrease of the field of view and the drop of input light emission (see figure 3.13). This means the user should find the balance between optical resolution, working distance and the field of view.

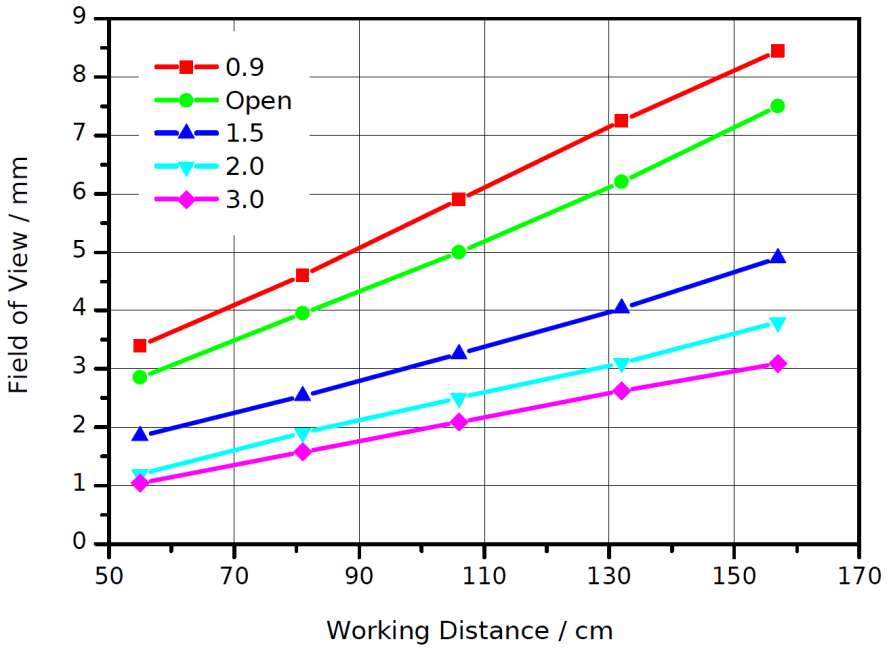

Figure 3.13: Field of view for the QM 1 LDM as a function of the working distance and optional lenses. The figure is taken from [108].

3.2 Experimental techniques

3.2.1 ICCD imaging and optical emission spectroscopy

A full–integrated intensified CCD camera (PI–MAX4: 1024i, Princeton Instruments) was used for all the imaging and spectroscopy experiments. It is a 16–bit digitization camera and the saturated limitation (maximum grey level) is 65535 counts for each frame. The ICCD camera is coupled fiber–optically with the Gen II filmless intensifiers which provides the sensitivity from UV to NIR (wavelength range from 170 to 900 nm) and ensures the required resolution that matches the CCD. The external synchronization allows camera to receive a TTL triggering signal (-5 to 5 V) from external devices. The monitor of the camera can output a TTL signal showing the shape of actual gate timing.

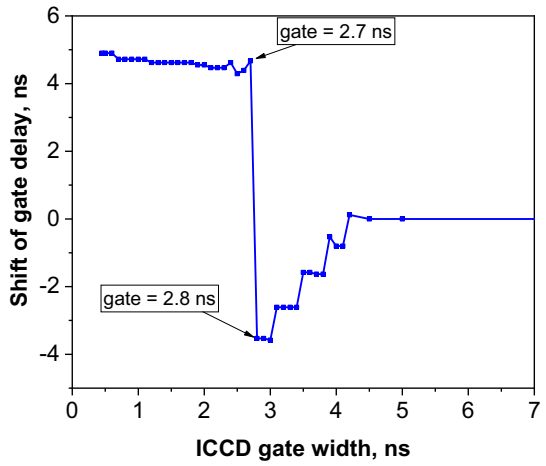

Figure 3.14: Calibrated ICCD camera delay on software WinSpec Princeton Instruments.

The ICCD camera can produce the frames with 1024 × 1024 pixel. It offers the minimum gate width (FWHM) less than 500 ps but it is only intended for the usage of Fast Gate tubes. For the time–resolved experiments, the ideal camera gate width can be setted as 1 to 2 ns for receiving enough light emission. The ICCD camera delay was calibrated with the help of LeCroy oscilloscope. The camera has the shift of time delay when the gate width decreases from higher than 4.5 ns to less than 4.5 ns (see figure 3.14). The shift of delay jumps from -3.5 ns to about 5 ns when the gate width decreasing from 2.8 ns to 2.7 ns. Practically, the camera delay also has a strong connection with the temperature of ICCD's internal sensor. The ICCD camera also has an internal delay (31.5 ns) between trigger in and opening the intensifier.

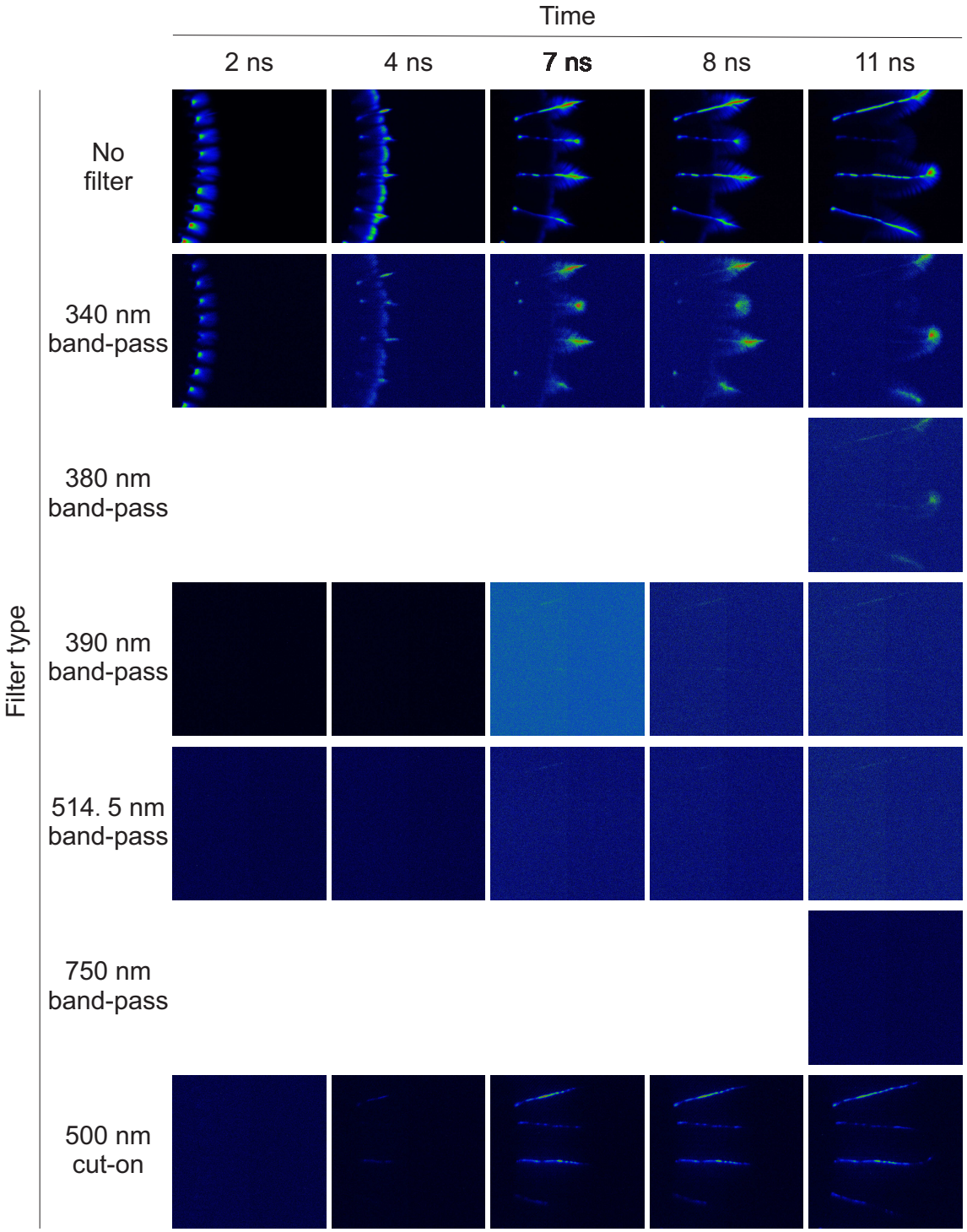

Figure 3.15: Preliminary results of filtered ICCD micro–images of the filamentary discharge in a single shot regime in 6 bar N_2 at negative polarity, $U = -24$ kV. The focal distance of LDM is 1 m. ICCD camera gate is 1 ns. Resolution of the optical system is 7.6 μm/px.

To analysis the spectral composition of the discharge, a set of UV/VIS bandpass filters (Thorlabs, FB340–10, FB380–10, FB390–10, FL514.5–10 and FB750–10) and longpass filters (Thorlabs, FEL0500) were used in the experiments. The filter was placed in a fast–change lens tube filter holder (Thorlabs, SM1QU) connecting with the Barlow lenses to ICCD camera. Figure 3.15 presents the preliminary experimental results showing the discharge spectral composition, which help for selecting working conditions.

A spectrograph (Acton 2500i, Princeton Instruments) was used in all the spectral analysis experiments combined with the ICCD camera. High efficiency optical coating craftsmanship (Acton #1900 Al+MgF_2) ensures 85% reflectance in the wavelength range from 200 to 700 nm. This spectrometer has the focal length of 500 mm. It has three gratings (600, 1200 and 2400 g/mm) mounted on an interchangeable triple grating turret. Gratings can be switched rapidly upon usage. All of these gratings have the same size (68×68 mm). It should be noted that different gratings have their own sensitive wavelength region. It is necessary to select the right grating to achieve the highest optical efficiency.

3.2.2 Using line broadening for determining the electron density at high pressures

In general, the broadening width in the spectra is the combination result of multiple effects that contain natural, resonance, Van der Waals and Stark broadening for Lorentzian part and Doppler and instrumental broadening for Gaussian part. The function of Lorentzian $L(\lambda-\lambda_0)$ and Gaussian profiles $G(\lambda-\lambda_0)$ can be given by the parameter full width at half maximum (FWHM) $\Delta\lambda_L$ and $\Delta\lambda_G$ respectively [111]:

$$L(\lambda-\lambda_0) = \frac{\frac{\Delta\lambda_L}{2\pi}}{(\lambda-\lambda_0)^2 + \left(\frac{\Delta\lambda_L}{2}\right)^2} \tag{3.9}$$

$$G(\lambda-\lambda_0) = \frac{2\sqrt{\ln 2}}{\sqrt{\pi}\Delta\lambda_G} \exp\left(-\frac{4\ln 2\,(\lambda-\lambda_0)^2}{\Delta\lambda_G^2}\right) \tag{3.10}$$

If we use half width at Half maximum (HWHM) l and g to replace full width at half maximum (FWHM) $\Delta\lambda_L$ and $\Delta\lambda_G$ and wavelength variable x to replace $\lambda-\lambda_0$, which are

$$l = \frac{\Delta\lambda_L}{2},\ g = \frac{\Delta\lambda_G}{2},\ x = \lambda-\lambda_0 \tag{3.11}$$

equation (3.9) and (3.10) can be written as

$$L(x) = \frac{1}{\pi}\cdot\frac{l}{x^2+l^2} \tag{3.12}$$

$$G(x) = \sqrt{\frac{\ln 2}{\pi}} \cdot \frac{1}{g} \cdot \exp\left(-\ln 2 \cdot \frac{x^2}{g^2}\right) \tag{3.13}$$

Normally, the overlay effect of two broadening effects are the convolution of their profile functions. The convolution of two functions $f(t)$ and $g(t)$ can be written as

$$f(t) * g(t) = \int_{-\infty}^{+\infty} f(\tau)g(t-\tau)d\tau = \int_{-\infty}^{+\infty} f(t-\tau)g(\tau)d\tau \tag{3.14}$$

In addition, the convolution can be operated in another way when it is difficult to integrate, according to the convolution theorem

$$f(t) * g(t) = F^{-1}[F(f(x))F(g(x))] \tag{3.15}$$

where F is the Fourier transform

$$F(f(x)) = \int_{-\infty}^{+\infty} f(x)e^{-2\pi ikx}dx \tag{3.16}$$

and F^{-1} is the inverse Fourier transform

$$F^{-1}(f(k)) = \int_{-\infty}^{+\infty} F(k)e^{2\pi ikx}dk \tag{3.17}$$

The convolution results of these different line broadening parts can be different according to their different distribution functions. When applying Fourier transform to the function of Lorentzian line profile equation (3.12), one can get that

$$F(L(x)) = \int_{-\infty}^{+\infty} \frac{1}{\pi} \cdot \frac{l}{x^2 + l^2} \cdot e^{-2\pi ikx}dx \tag{3.18}$$

Which can be modified by using Euler's formula $e^{ix} = \cos x + i \sin x$,

$$F(L(x)) = \frac{1}{\pi} \int_{-\infty}^{+\infty} \frac{l}{x^2 + l^2}(\cos(2\pi kx) - \sin(2\pi kx))dx \tag{3.19}$$

in which the term including $\sin x$ is an odd function, which is zero when integrated from $-\infty$ to $+\infty$, leaving

$$F(L(x)) = \frac{1}{\pi} \int_{-\infty}^{+\infty} \frac{l}{x^2 + l^2} \cos(2\pi kx)dx \tag{3.20}$$

the result can be easily achieved after the integration (3.20)

$$F(L(x)) = e^{-2\pi lk} \tag{3.21}$$

So the convolution of two Lorentzian functions $L_1(x)$ and $L_2(x)$ is as follow

$$F(L_1(x) * L_2(x)) = F(L_1(x))F(L_2(x)) = e^{-2\pi(l_1+l_2)k} \tag{3.22}$$

where l_1 and l_2 are the half width at half maximum (HWHM) of the two Lorentzian profiles. Then full width at half maximum (FWHM) of these two Lorentzian profiles in convolution case is

$$\Delta\lambda_L = \Delta\lambda_{L1} + \Delta\lambda_{L2} \tag{3.23}$$

For Gaussian function, by using Fourier transform

$$F(G(x)) = \int_{-\infty}^{+\infty} \sqrt{\frac{\ln 2}{\pi}} \cdot \frac{1}{g} \cdot \exp\left(-\ln 2 \cdot \frac{x^2}{g^2}\right) \cdot e^{-2\pi i k x} dx \tag{3.24}$$

and integrating the equation, one can get that

$$F(G(x)) = e^{-\frac{\pi^2 g^2 k^2}{\ln 2}} \tag{3.25}$$

the convolution of two Gaussian functions $G_1(x)$ and $G_2(x)$ can be formed as

$$F(G_1(x) * G_2(x)) = F(G_1(x))F(G_2(x)) = e^{-\frac{\pi^2 (g_1^2 + g_2^2) k^2}{\ln 2}} \tag{3.26}$$

where g_1 and g_2 are the half width at half maximum (HWHM) of the two Gaussian profiles. The full width at half maximum (FWHM) of these two Lorentzian profiles in convolution case is

$$\Delta\lambda_G = \sqrt{(\Delta\lambda_{G1})^2 + (\Delta\lambda_{G2})^2} \tag{3.27}$$

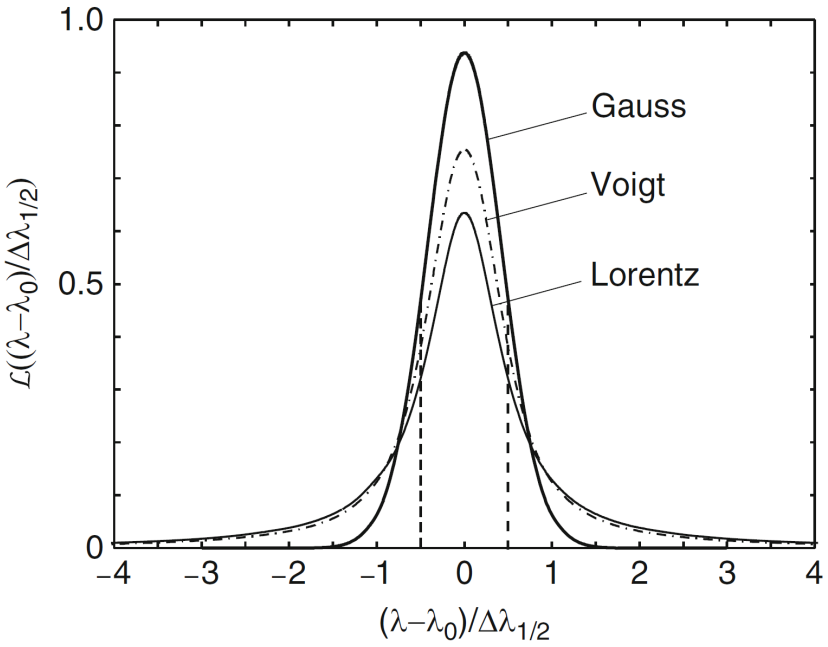

Figure 3.16: Scheme of Lorentzian, Gaussian and Voigt profiles with equal halfwidth $\Delta\lambda_{1/2}$. The figure is taken from [111].

In most cases, the real (experimental) spectrum is the convolution of two broadening parts (Lorentzian and Gaussian), although with different weights, also recognized as Voigt profile (see figure 3.16).

$$V(x) = L(x) * G(x) = \int_{-\infty}^{+\infty} L(x)G(t-x)dt \tag{3.28}$$

which is

$$V(x) = \sqrt{\frac{\ln 2}{\pi^3}} \cdot \frac{l}{g} \int_{-\infty}^{+\infty} \frac{e^{-\ln 2 \cdot (\frac{x-t}{g})^2}}{t^2 + l^2} dt \tag{3.29}$$

Although this equation is not integrable, it is still can be simplified by inducing a variable $a = l/g$ and normalized to half width at half maximum (HWHM) of Gaussian profile g.

$$V(x) = \sqrt{\frac{\ln 2}{\pi^3}} \cdot a \int_{-\infty}^{+\infty} \frac{e^{-\ln 2 \cdot (x-t)^2}}{t^2 + a^2} dt \tag{3.30}$$

where a is a shape factor representing the weights of Lorentzian and Gaussian profiles contributed in Voigt profile. And the FWHM ($\Delta\lambda_V$) in Voigt profile can be obtained only by numerical methods [112]:

$$\Delta\lambda_V \approx \sqrt{\left(\frac{\Delta\lambda_L}{2}\right)^2 + (\Delta\lambda_G)^2} + \frac{\Delta\lambda_L}{2} \tag{3.31}$$

This is an approximate Voigt non linear curve fitting equation with accuracy of 1% and could be miswritten in some papers [84]. The improvement of calculation methods can even produce an accuracy of 0.02% [113] on the following equation:

$$\Delta\lambda_V \approx \sqrt{0.2166\Delta\lambda_L^2 + (\Delta\lambda_G)^2} + 0.5346\Delta\lambda_L \tag{3.32}$$

In practical, when calculating electron density n_e from H_α spectra, only Stark effect was considered since other broadening width is negligible in our experimental spectra. However, when it comes to nitrogen atomic line (746 nm), Van der Waals and instrumental broadening affects cannot be ignored which in the same order as Stark effect. In addition, it is necessary to subtract molecular bands and cw spectra background before doing the calculation.

3.2.3 Particle Image Velocimetry (PIV)

Particle image velocity measurement (PIV) experiments were performed in Joint Institute for High Temperatures of the Russian Academy of Sciences (JIHT RAS) in Moscow (Russia) in the framework of collaboration within a Joint International Laboratory LIA KaPPA, "Kinetics and Physics of Pulsed Plasmas and their Afterglow". The experiments were performed with I. Selivonin under the supervision of Dr. I.Moralev.

Particle image velocity measurement (PIV) is a non–contact speckle image velocity measurement technology developed on the basis of flow display. PIV takes the advantages of the flow field information on one surface at a few specific moments to analyse the body motion. PIV measures the velocity of particles in the flow field by using the tracer particles with better following ability scattered in the fluid to represent the velocity of the flow field at the location. PIV can not only ensure the accuracy and resolution of a single-point measurement but also obtain the transient information and overall structure of the whole flow field. PIV technology has the ability to obtain small–scale structure vector diagrams. Thus it can be used for the analysis of the turbulence flow field that requires high spatial resolution in the small scale.

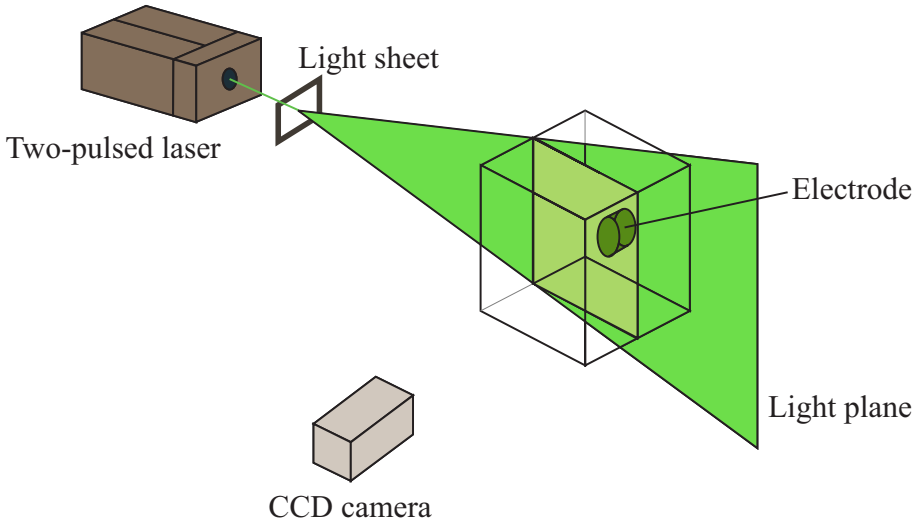

Figure 3.17: Composition of the Particle Image Velocimetry system.

As shown in figure 3.17, the particle image velocimetry system contains the following parts: a two–pulsed Nd–YAG laser with 532 nm wavelength as the light source, light sheet optics and CCD camera. The electrode was installed in the high–pressure chamber containing tracing particles. Tracer particles should generally be non–toxic, non–corrosive, chemically stable and clean.

For full–field PIV measurement, velocity can be calculated only when particles exist in the region of discretion. In the region where there is no particle, velocity cannot be obtained in this area. Therefore, particles are required to be uniformly distributed throughout the whole field to ensure velocity measurement in the entire flow field. Generally, there are three basic requirements in the PIV experiment: the particles should follow the fluid movement well; the particles should be good scatterers with good recording performance and high imaging visibility; the uniformity and concentration requirements of particle distribution. For the air flow condition,

smoke or oil mist (particle size can reach the order of 1 μm) are typically used as the tracing particles whose concentration can be easily adjusted. For PIV measurement, too high particle concentration will have a certain impact on the flow itself. The particle concentration should not be too low either because for each unit region there must be enough particle pairs. Only in this way can the correct displacement be obtained through statistical analysis. Because in principle, the more particle pairs in the interpretation area, the higher the signal–to–noise ratio.

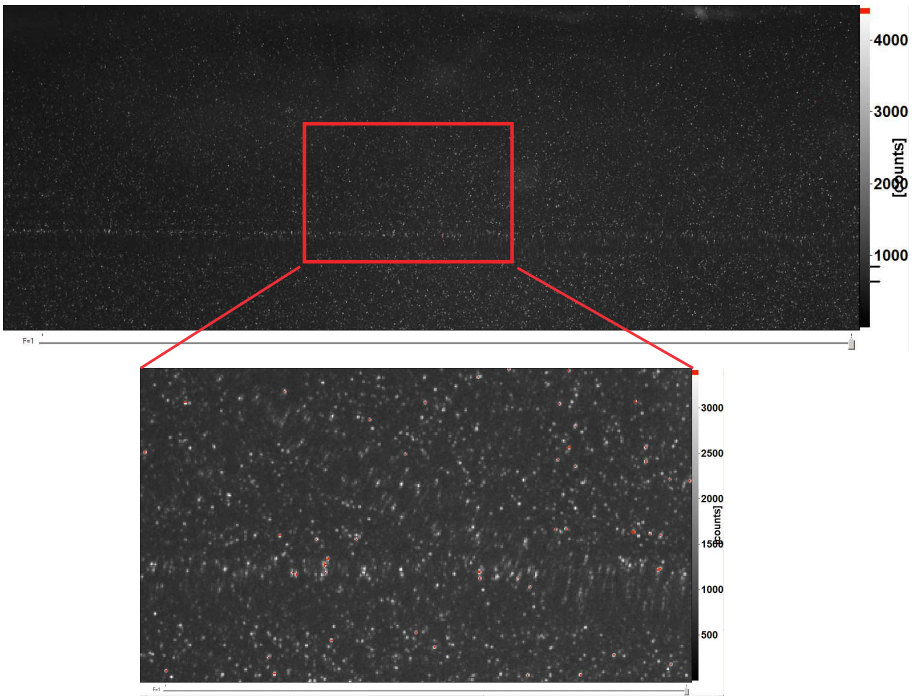

Figure 3.18: Recorded image of PIV particles.

The working principle of the Particle Image Velocimetry system is as follows: first, spreading the tracer particles (like oil) in the flow field. Then using a Nd YAG laser to illuminate the measured flow plane through two or more consecutive exposures. The images of the particles were recorded by the CCD camera, as shown in figure 3.18.

In order to analyse the motion and velocity of particles in the flow field, it is necessary to track the tracer particle positions in a certain area on the image. Since the tracer particles are small and densely distributed, it is difficult and inefficient to analyse the traces of a single particle independently. In order to avoid the disadvantages of single-point tracking analysis method, auto–correlation analysis method with higher precision can be used in most PIV flow field imaging analysis cases [114–116].

Suppose that two particle images of the same flow field are successively obtained within a short time interval Δt. The two images can be described as the function

$f(i,j,t)$ and $f(i+\Delta x, j+\Delta y, t+\Delta t)$, Δx and Δy represent the motion in x–axis and y–axis direction respectively. The size of the analysis window is $M \times N$. The auto–correlation function $r(k,l)$ of the two images can be defined as [114]:

$$r(k,l) = \sum_{i=0}^{M} \sum_{j=0}^{N} f(i,j,t) f(i+\Delta x+k, j+\Delta y+l, t+\Delta t) \tag{3.33}$$

Because of the small value of Δt, an assumption can be made that there is no drastic change in the flow field during this short period. According to the autocorrelation function is an even function and the maximum value is obtained at the origin, the inequality can be obtained as follows:

$$r(k,l) \leq r(-\Delta x, -\Delta y) \tag{3.34}$$

This means the maximum value of the auto–correlation function corresponds to the relative displacement between the flow fields. Therefore, the velocity of the flow field can be derived from the relevant maximum motion as the time interval Δt is known.

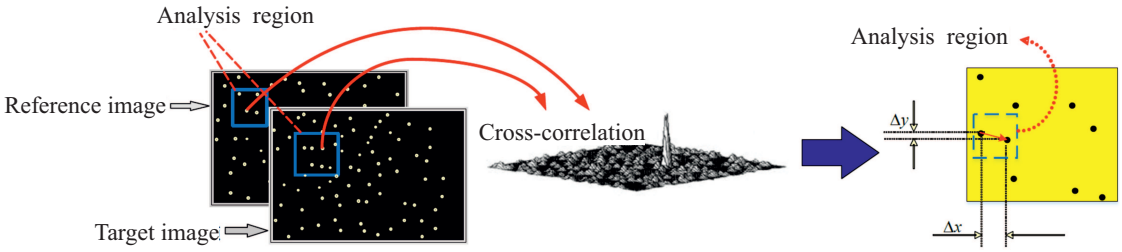

Figure 3.19: Process of the cross–correlation analysis method.

However, even with the auto–correlation matching analysis, the direction of the displacement vector on the image plane remains unknown. Practically, the cross–correlation analysis method is more widely adopted in PIV analysis. It takes a certain range on the first–pulse image as the template and searches within the same range on the target image. This step is aimed for finding the most similar position as the new position after the flow field movement. The difference between two positions is used as the displacement of the analysis node. The normalized covariance cross–correlation matching method is often used to evaluate the degree of similarity between two image regions in the process of analysing the changing of the position.

By calculating the difference between the reference template and the target image, one can get the displacement information of the selected region and then apply to the entire flow field. Then the flow field velocity vector diagram, velocity component diagram and the streamline diagram, etc. can be produced.

3.3 Numerical modelling

A modified 2D model based on PASSKEy (PArallel Streamer Solver with KinEtics) code, developed by Dr. Yifei Zhu in 2018 [117], has been used to calculate the plasma properties characters of nSDBD at high pressure conditions.

3.3.1 Elementary kinetics of 2D model for nSDBD at high pressures

The fluid models can be described by a series of Boltzmann equations and approximations listed below. In a system containing a large number of particles, the particle distribution $f(\boldsymbol{v}, \boldsymbol{r}, t)$ is governed by the following Boltzmann equation:

$$\frac{df}{dt} = \left(\frac{\partial f}{\partial t}\right)_{force} + \left(\frac{\partial f}{\partial t}\right)_{diff} + \left(\frac{\partial f}{\partial t}\right)_{coll} \tag{3.35}$$

which can also be written as:

$$\frac{\partial f}{\partial t} + \boldsymbol{u}\nabla_r f + \frac{\boldsymbol{F}}{m}\nabla_v f = \left(\frac{\partial f}{\partial t}\right)_{coll} \tag{3.36}$$

whereas $force$ ($\boldsymbol{F}$) is the force acted on the charged particles by an external influence rather than the internal force among particles, $diff$ represents the diffusion of the particles, $coll$ means collision between particles and $\boldsymbol{u}$ is the mean velocity of the group of particles.

Then the particle density $n(\boldsymbol{r}, t)$ can be defined as follows:

$$n(\boldsymbol{r}, t) = \int f(\boldsymbol{v}, \boldsymbol{r}, t) d^3v \tag{3.37}$$

whereas d^3v represents an infinitesimal element of three–dimensional velocity space.

Thus the mean flux $\boldsymbol{\Gamma} = n\boldsymbol{u}$ of the group of particles can be calculated as:

$$\boldsymbol{\Gamma} = n(\boldsymbol{r}, t)\boldsymbol{u}(\boldsymbol{r}, t) = \int \boldsymbol{v} f(\boldsymbol{v}, \boldsymbol{r}, t) d^3v \tag{3.38}$$

The momentum–transfer cross section σ_{tr} represents the mean transferred momentum among particles during the collision process. With the momentum–transfer cross section, one can define the characteristic frequencies $\boldsymbol{\nu}$ of the colliding particles:

$$\boldsymbol{\nu} = \frac{N}{n(\boldsymbol{r}, t)} \int \sigma_{tr} \boldsymbol{v} f(\boldsymbol{v}, \boldsymbol{r}, t) d^3v \tag{3.39}$$

whereas N is the neutral particle density.

The continuity equation can be achieved as follows by taking the zero moment of Boltzmann equation 3.36:

$$\frac{\partial n}{\partial t} + \nabla n\boldsymbol{u} = S_{coll} \tag{3.40}$$

in which S_{coll} is the source of particles coming from collisions.

The momentum balance equation can be derived from the first moment of Boltzmann equation 3.36:

$$\frac{\partial \boldsymbol{u}}{\partial t} + (\boldsymbol{u}\cdot\nabla)\boldsymbol{u} + \nu\boldsymbol{u} = -\frac{\nabla P}{nm} + \frac{\boldsymbol{F}}{m} \tag{3.41}$$

whereas the isotropic pressure $P = nk_bT$, n is the number density of particles, k_b is the Boltzmann constant and T is the gas temperature. T can be solved from the energy conservation equation by taking the second moment of Boltzmann equation 3.36:

$$\frac{\partial n_\epsilon}{\partial t} + eE\cdot\boldsymbol{\Gamma} + \nabla\boldsymbol{\Gamma_\epsilon} = S_\epsilon \tag{3.42}$$

in which $n_\epsilon = 3nT/2$, $\boldsymbol{\Gamma_\epsilon} = n_\epsilon\boldsymbol{u}$ is the energy flux. For equilibrium discharges, $\boldsymbol{\Gamma_\epsilon} = -k_T\nabla T$ while for the non-equilibrium cases, it is necessary to solve by the iterations based on the following approximations.

Since the characteristic time scale $\tau = \nu^{-1}$ is much smaller than the discharge propagation time, the velocity in time τ can be assumed as zero. In addition, at high pressure conditions, it can be approximated that $|(\boldsymbol{u}\cdot\nabla)\boldsymbol{u}| \ll \nu\boldsymbol{u}$. With the isotropic pressure equation $P = nk_bT$, the momentum balance equation 3.41 can be simplified as follows:

$$\boldsymbol{u} = -D\frac{\nabla n}{n} + \mu\frac{\boldsymbol{F}}{q} \tag{3.43}$$

whereas $D = k_bT/m\nu$ and $\mu = q/m\nu$ are the diffusion coefficient and mobility of particles. Then the energy flux can be written as:

$$\boldsymbol{\Gamma_\epsilon} = -D_\epsilon\nabla n_\epsilon + \mu_\epsilon\frac{\boldsymbol{F_\epsilon}n_\epsilon}{q} \tag{3.44}$$

3.3.2 PASSKEy code and governing equations

In the PASSKEy code, for charged particles, only the first moment of Boltzmann equation 3.36 is taken into consideration while the neutral species are assumed to keep still in the nanosecond time scale. Thus the continuity equation 3.40 and the conservation equation 3.42 can be rewritten as follows:

$$\frac{\partial n_i}{\partial t} - \nabla\cdot\boldsymbol{\Gamma_i} = S_i + S_{ph}, i = 1, 2, \ldots, N_{total} \tag{3.45}$$

$$\boldsymbol{\Gamma_i} = D_i \nabla n_i + \frac{q_i}{|q_i|} \mu_i n_i \nabla \Phi, i = 1, 2, \ldots, N_{charge} \tag{3.46}$$

whereas n_i and $\boldsymbol{\Gamma_i}$ are the number density and flux for species i, S_i is the source of species i due to gas phase reactions [118], S_{ph} is the source of electrons and oxygen ions due to photo–ionizations, N_{total} represents the number density of total species, D_i, q_i and μ_i are the diffusion coefficient, charge and diffusion mobility of charged species i respectively, Φ is the electrical potential and N_{charge} represents the number density of total species.

The photo–ionization rate S_{ph} is calculated based on the following Helmholtz equations that are verified by A. Bourdon et al [119] and A. Luque et al [120] in 2007:

$$S_{ph} = \sum_j S_{ph}^j \tag{3.47}$$

$$\nabla^2 S_{ph}^j - \left(\lambda_j p_{O_2}\right)^2 S_{ph}^j = -A_j p_{\mathrm{O_2}}^2 I \tag{3.48}$$

$$S_{\mathrm{ph}}^j = \iiint_V \frac{I A_j p_{\mathrm{O_2}}^2 \mathrm{e}^{-\lambda_j p_{\mathrm{O_2}} R}}{4\pi R} \, \mathrm{d}V \tag{3.49}$$

$$I = \xi \frac{p_q}{p + p_q} \alpha \mu E n_e \tag{3.50}$$

$$p_q = \frac{k_b T}{k_q \tau_0} \tag{3.51}$$

whereas j is the order of the exponentially fitted photo–ionization function, λ_j and A_j are the fitting coefficients [119], p_{O_2}, p_q and p are the partial pressure of oxygen, the quenching pressure of $\mathrm{C}^3\Pi_u$ and the ambient pressure respectively, V is the volume of the calculation domain, R is the distance between observation point and the source point, α is the Townsend ionization coefficient, μE represents the absolute drift velocity of electrons, n_e is the electron density, k_q is the collisional quenching rate constant and τ_0 is the radiative lifetime.

The Poisson equation is solved without considering the current in the material:

$$-\nabla^2(\epsilon\Phi) = \sum_{i=1}^{N_{charge}} q_i n_i + \rho \tag{3.52}$$

whereas ρ is the charge density on dielectric surfaces, which satisfies the continuity equations:

$$\frac{\partial \rho}{\partial t} = \sum_{j=1}^{n} q_j \frac{\partial n_i}{\partial t} \tag{3.53}$$

The Euler equation is given as follows:

$$\frac{\partial \boldsymbol{U}}{\partial t} + \frac{\partial \boldsymbol{F}}{\partial x} + \frac{\partial \boldsymbol{G}}{\partial y} = \boldsymbol{S} \tag{3.54}$$

$$[\boldsymbol{U}, \boldsymbol{F}, \boldsymbol{G}, \boldsymbol{S}] = \begin{bmatrix} \rho & \rho & \rho v & 0 \\ \rho u & p + \rho uu & \rho uv & 0 \\ \rho v & \rho uv & p + \rho vv & 0 \\ E & (E+p)u & (E+p)v & S_{heat} \end{bmatrix} \tag{3.55}$$

in which ρ is the air density, u and v are velocities in x and y directions respectively, E is the specific total deposited energy. p is given by the state equation:

$$p = \rho(\gamma - 1)(E - \frac{u^2 + v^2}{2}) \tag{3.56}$$

3.3.3 Calculation domain, boundary and initial values

A 5×5 cm calculation domain is divided by a few rectangular sub–domains, as shown in figure 3.20(a). The governing equations, including transport equations, Poisson equation, Helmholtz equations and Euler equations, are solved differently in different sub–domains. This approach is aimed for reducing the computational cost. A square mesh is distributed differently in different sub–domains and it is manually refined in sub–domains with higher interest 3.20(b).

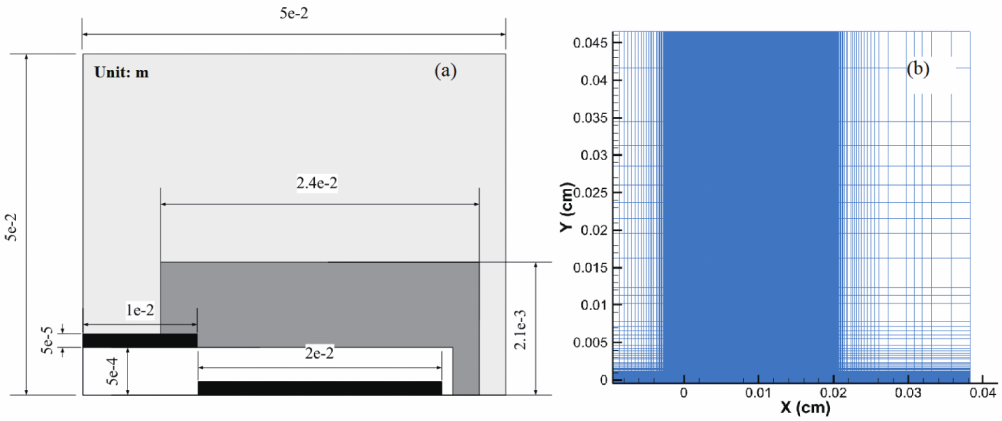

Figure 3.20: (a) Calculation domain and (b) structured mesh distribution, units are in meter. The figure is taken from [117].

Different boundary conditions are applied differently in each sub–domain and for different governing equations. For the transport equations of both electrons and ions, the flow towards boundary is set as $\partial \boldsymbol{j}/\partial n = 0$ while the flow away from boundary condition is set $\boldsymbol{j_e} = -\gamma \boldsymbol{j_i}$ for electrons and $\boldsymbol{j_i} = 0$ for ions. It is assumed that the secondary emission coefficient γ is set as zero on both metal and dielectric

boundaries [117]. For Helmholtz equations, the photo–ionization rate S_{ph} is set as zero on the boundary of the domain that is far from the discharge region.

For Poisson equation, first–type boundary condition $\phi = U(t)$ is applied on the metal boundaries while the second–type boundary condition $\partial\phi/\partial n$ is used on the non–metal boundaries. By collecting the charge flux flowing to the dielectric on the boundary of the plasma region, it is possible to accumulate surface charges on the surface of the dielectric in each time step. The accumulated charge is then stored on the edge of the finite–volume grid cell and taken into account as an additional charge when solving the Poisson equation. For Euler equations, no–slip boundary condition is set on all the fluid–solid surfaces. It assumes that the fluid velocity at all these boundaries is equal to zero.

An initial cloud of seed plasma is distributed in the region of ionization to ignite the discharge. The ionization region is calculated as the place where the electric field is higher than 32 kV/cm. The density of electrons n_e and ions n_i in the seed plasma cloud is given as follows (in unit of cm^{-3}):

$$n_e(x,y) = n_i(x,y) = \frac{10^{12}}{e^{(\frac{x}{0.002})^2+(\frac{y}{0.002})^2}} \tag{3.57}$$

x and y (in unit of cm) are the position coordinates in the calculation domain in figure 3.20(a).

Chapter 4

Streamer–to–filament transition of nanosecond surface dielectric barrier discharges: parameters of transition

Streamer-to-filament transition is a general feature of high pressure high voltage nanosecond surface dielectric barrier discharges (nSDBDs) for mixtures containing molecular gases. The transition is observed at high pressures and voltages in a single-shot experiment a few nanoseconds after the start of the discharge. A set of experimental results comparing streamer–to–filament transition for the identical high voltage pulses of negative and positive polarity is presented. The transition curves in voltage–pressure coordinates are obtained for N_2:O_2 mixtures on different dielectric surfaces and electrodes, at the pressure range 1-12 bar.

Streamer–to–filament transition happens in a similar way in all observed experimental conditions. In air at 1 bar and the applied voltage amplitude of 20 kV, a "regular" streamer nSDBD is observed. With the pressure increase, the discharge propagation length during the pulse decreases significantly: for example, in air at 5 bar the propagation length is 5 to 6 times smaller than at 1 bar. When voltage and/or pressure is increased, the discharge appearance changes and a filamentary nSDBD is observed. A regular structure of discharge channels, rarer than for streamers (typically one filament for $4-5$ streamers) and brighter (the light emission increases by a factor of 50 when passing to the filamentary mode) starts near the high voltage electrode, whatever the applied voltage polarity is, and propagates in a radial direction. The filament propagation length is a function of the applied voltage, its

polarity, the gas pressure and the gas mixture composition. Will underline that in all the experiments there is no closing on the open grounded electrode at the perimeter of the discharge system, that is no spark between the open electrodes is developed.

4.1 Micro–imaging of the discharge propagation

To study the development of a streamer–to–filament transition and to observe the changes of the general structure of the discharge with voltage, three different configurations of the high-voltage electrode were used. The behavior of streamer–to–filament transition was observed by the QM 1 long distance microscope accompanied with the ICCD camera. The long distance microscope was set between the high–voltage electrode and the objective of ICCD camera. All the experiments on micro–imaging were performed at both positive and negative polarities.

This section starts with the micro–imaging comparison of the streamer surface discharge propagation on three different high–voltage electrodes (gear, disc and cylindrical electrode) at atmospheric pressure. Then the micro–images of streamer–to–filament transition give the time-resolved information of discharge propagation with small camera gate (1 ns). The results show different behavior of the transition process in air and nitrogen at both positive and negative polarities with same amplitude. In the end, the discharge behavior changing with pressure and voltage are illustrated.

4.1.1 Micro–imaging of streamer propagation on different electrodes at atmospheric pressure

All experiments in this section were conducted in both air and nitrogen at both negative and positive polarities at atmospheric pressure. The voltage amplitude was fixed and equal to ± 20 kV. The camera gate was equal to 1 ns. The resolution of the optical system was 7.6 μm/px.

Dynamics of the discharge development on the gear–shape electrode are given by figure 4.1. The gear electrode was used to fix a position of each discharge channel in space. It is seen that for all conditions in figure 4.1(a)(b)(c)(d), the discharge starts as a set of streamers igniting at the same time (within 1 ns) from the high-voltage electrode. Every tooth provide one discharge channel and there is no distinctive difference between the channels.

At negative polarity, the surface streamer emission disappears earlier in air (at 8 ns) than in nitrogen. We comment this with the fact that quenching of $N_2(C^3\Pi_u)$,

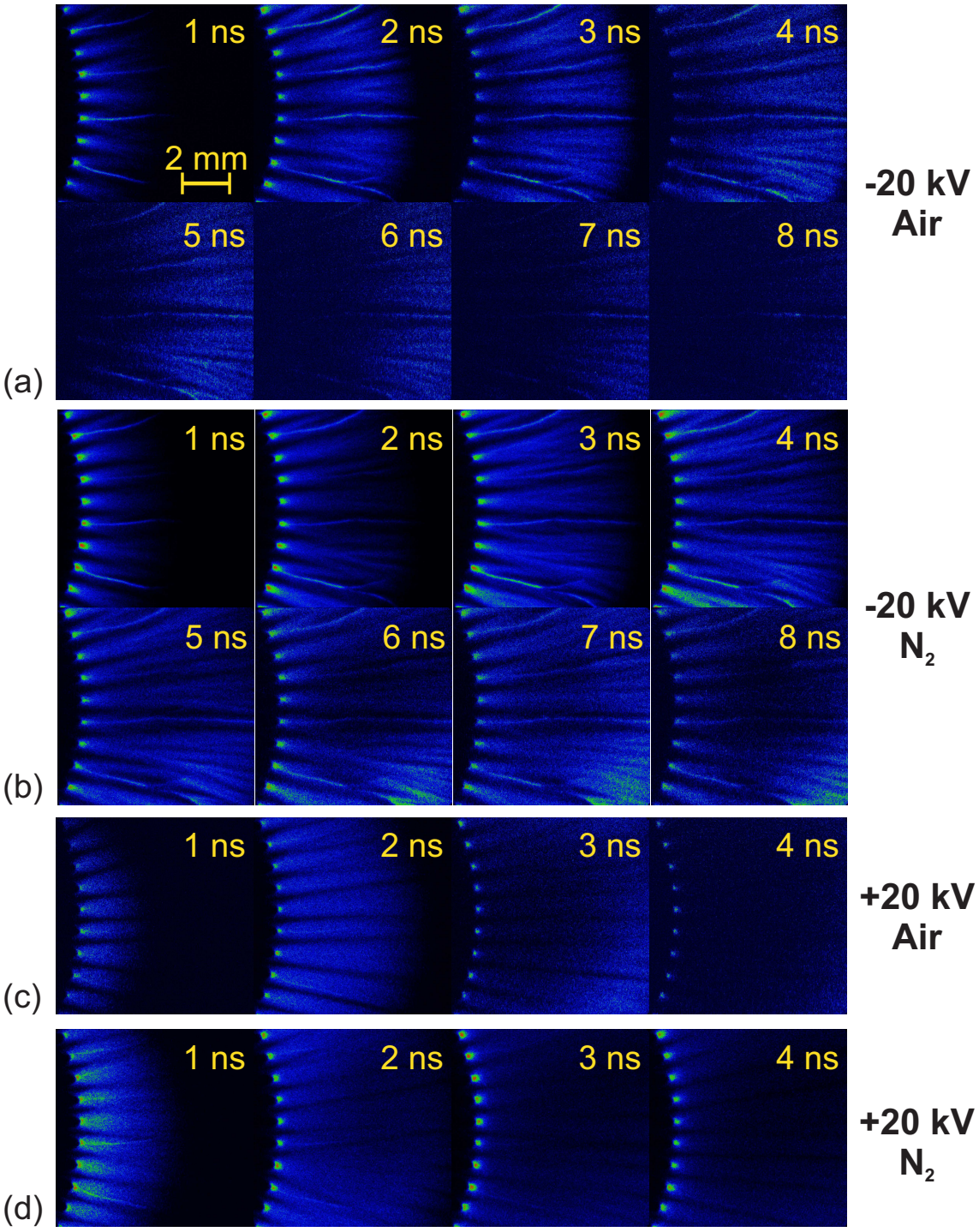

Figure 4.1: Micro–images of streamer surface discharge propagation at atmospheric pressure on the gear–shape electrode. (a) $U = -20$ kV, air; (b) $U = -20$ kV, nitrogen; (c) $U = +20$ kV, air; (d) $U = +20$ kV, nitrogen. Camera gate is 1 ns. Resolution of the optical system is 7.6 μm/px. Time instant is marked with yellow in each frame.

main emitting state during the discharge, by O_2 molecules is an order of magnitude stronger than by nitrogen [121]:

$$N_2\left(C^3\Pi_u\right) + N_2 \xrightarrow{k_q^{N_2}} \text{products}, \quad k_q^{N_2} = 0.09 \cdot 10^{-10}\ \text{cm}^3/\text{s} \tag{4.1}$$

$$N_2\left(C^3\Pi_u\right) + O_2 \xrightarrow{k_q^{O_2}} \text{products}, \quad k_q^{O_2} = 2.7 \cdot 10^{-10}\ \text{cm}^3/\text{s} \tag{4.2}$$

So at atmospheric pressure, a typical time of $N_2(C^3\Pi_u)$ quenching for molecular nitrogen is $\tau^{N_2} = 1/(k_q^{N_2}[N_2]) \approx 20.6$ ns, and for molecular oxygen is $\tau^{O_2} = 1/(k_q^{O_2}[O_2]) \approx 0.7$ ns. The streamer in air propagates and leaves the high–voltage electrode starting from 5 ns while in nitrogen, the streamer always "adheres" to the electrode during its propagation.

At positive polarity, the streamer discharge becomes more homogeneous than at negative polarity. Both streamers in air and nitrogen tend to adhere to the electrode. The discharge propagates and the emission disappears in a short time (less than 4 ns), leaving the bright spots near the high–voltage electrode.

Figure 4.2 presents the images taken in the system with the smooth edge electrode (a metal disc with diameter 20 mm) by long distance microscope at different experimental conditions. For both polarities, the streamers start homogeneously from the edge of the high–voltage electrode within 1 ns. The difference between the discharge in air and nitrogen is that for both polarities, the discharge in air vanishes much earlier than in nitrogen. For the streamer in nitrogen, there are more branches at negative polarity while at positive polarity, the streamer emission is more diffuse under the same conditions. The ICCD images for the side view taken with the cylindrical electrode system (figure 4.3) are focused so that the depth of field includes the only plasma channel, situated on the generatrix of the cylinder (the upper plasma filament at each frame of figure 4.3). The other streamers are deliberately out of focus. The edge of the high–voltage electrode is a sawtooth copper foil. The frequency of the teeth is similar to the frequency of the teeth in a flat electrode system with a gear–shaped high–voltage electrode.

The most important feature of these images is that it is possible to calculate the thickness of the emitting plasma channel. Significant increase of a streamer intensity is observed for all regimes between 1 ns and 2 ns. In air, for both polarities, a bright emission at the edge of the electrode is observed at 2 ns. Later, at $3-4$ ns, two maxima of emission intensity are observed, at the edge of the electrode and in the streamer head, the picture being in consistency with [117]. In nitrogen, maximum of emission always stages at the high–voltage electrode. It is possible that maximum of emission in the streamer head in air is due to active photoionization in the presence of O_2.

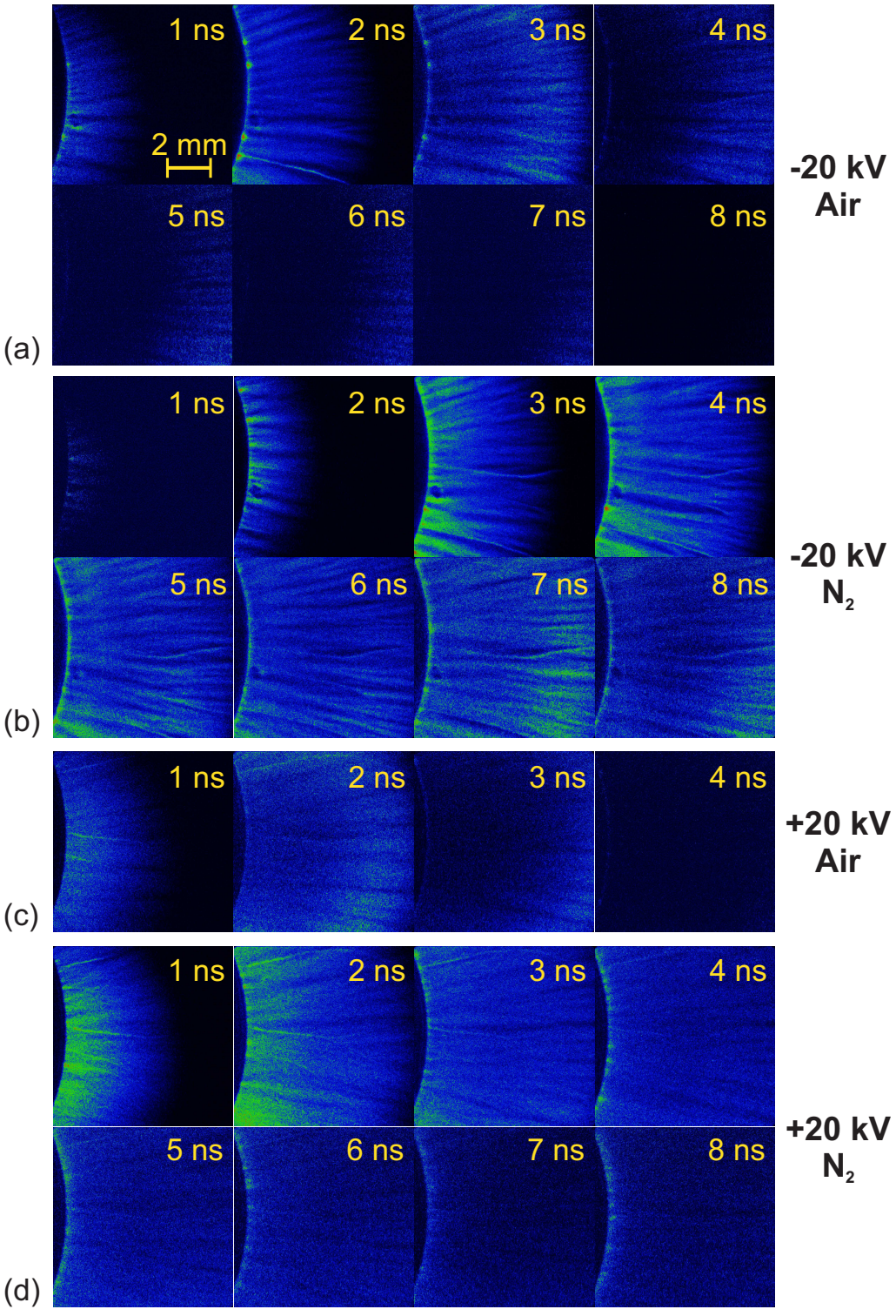

Figure 4.2: Micro–images of streamer surface discharge propagation at atmospheric pressure on the smooth electrode. (a) $U = -20$ kV, air; (b) $U = -20$ kV, nitrogen; (c) $U = +20$ kV, air; (d) $U = +20$ kV, nitrogen. Camera gate is 1 ns. Resolution of the optical system is 7.6 μm/px. Time instant is marked with yellow in each frame.

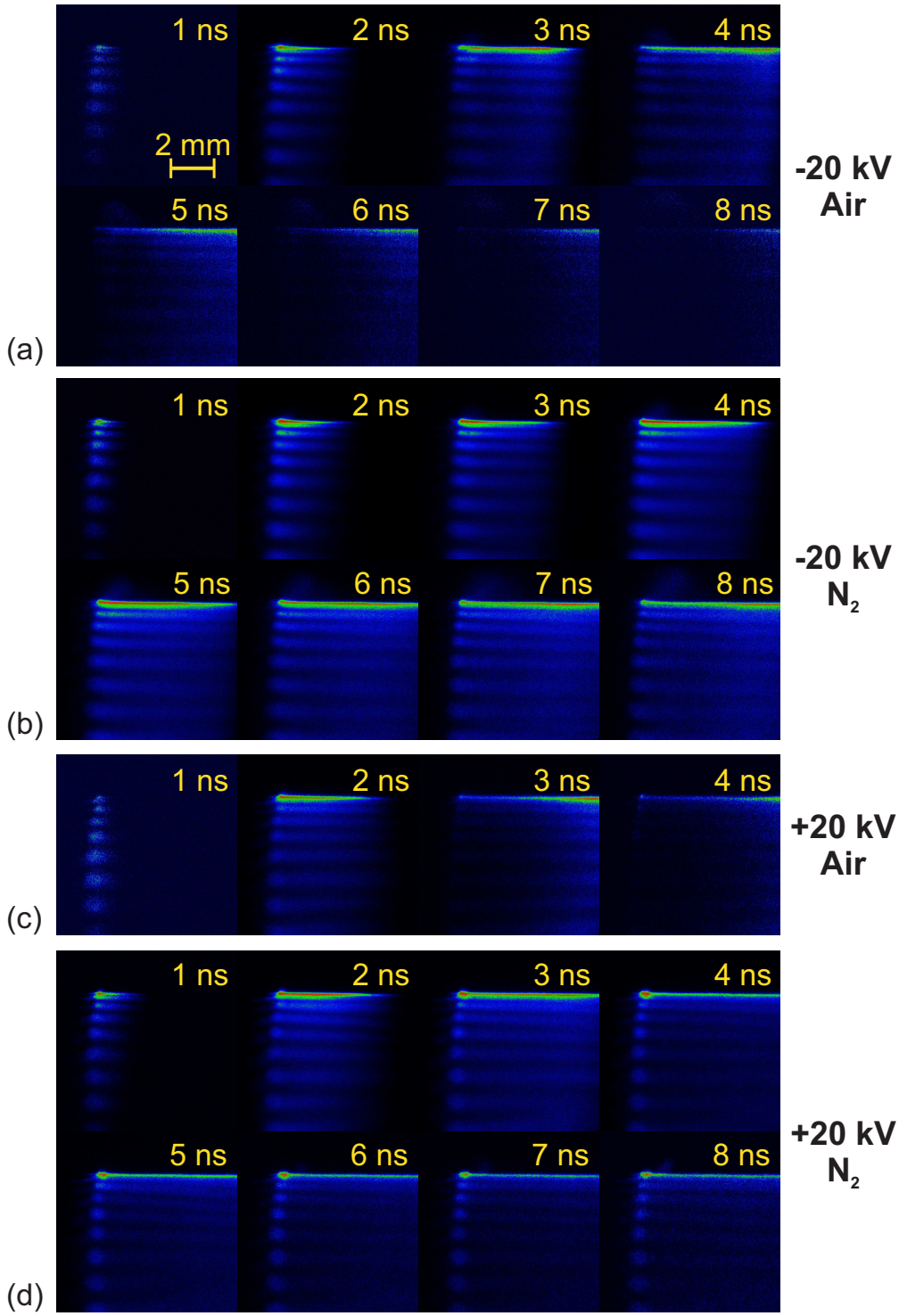

Figure 4.3: Micro–images of streamer surface discharge propagation at atmospheric pressure on the cylindrical electrode. (a) $U = -20$ kV, air; (b) $U = -20$ kV, nitrogen; (c) $U = +20$ kV, air; (d) $U = +20$ kV, nitrogen. Camera gate is 1 ns. Resolution of the optical system is 7.6 μm/px. Time instant is marked with yellow in each frame.

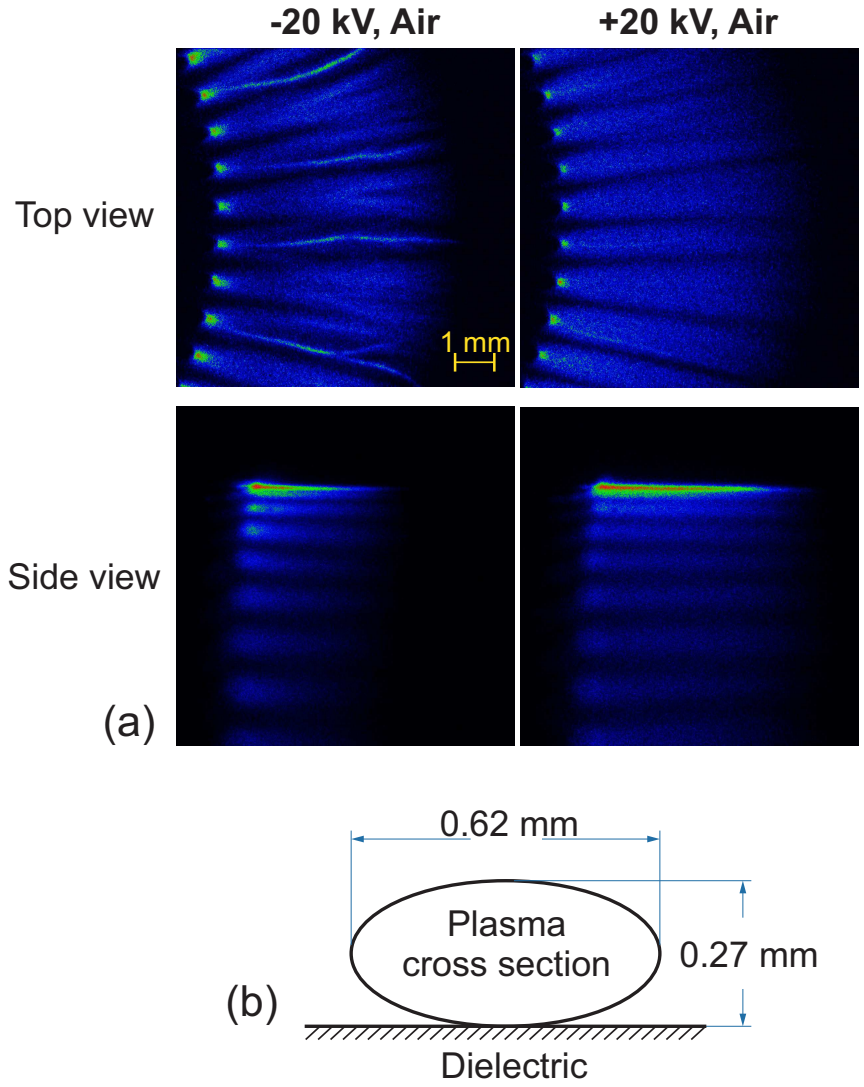

Figure 4.4: (a) Comparison of micro–images of streamer surface discharge propagation in ambient air at $U = \pm 20$ kV on gear–shape electrode (top view) and cylindrical electrode (side view) at time instant $t = 2$ ns; (b) Scheme of cross section of plasma channels at the position 1 mm from the high–voltage electrode. Camera gate is 1 ns. Resolution of the optical system is 7.6 μm/px.

If comparing two micro–images of the discharge on gear–shape and cylindrical electrodes at the same time instant (e.g. $t = 2$ ns as shown in figure 4.4(a)), we can find that in reality the cross section of the streamer channel is not a circle but an ellipse (see figure 4.4(b)). We measured the size of the cross section of plasma channel at the point 1 mm from the high–voltage electrode: the width of the streamer channel is 0.62 mm and the thickness is 0.27 mm. It should be noted that the sizes of the cross section of streamers in ambient air for both negative and positive polarities are identical.

4.1.2 Micro–imaging of temporary behavior of streamer–to–filament transition at different polarities

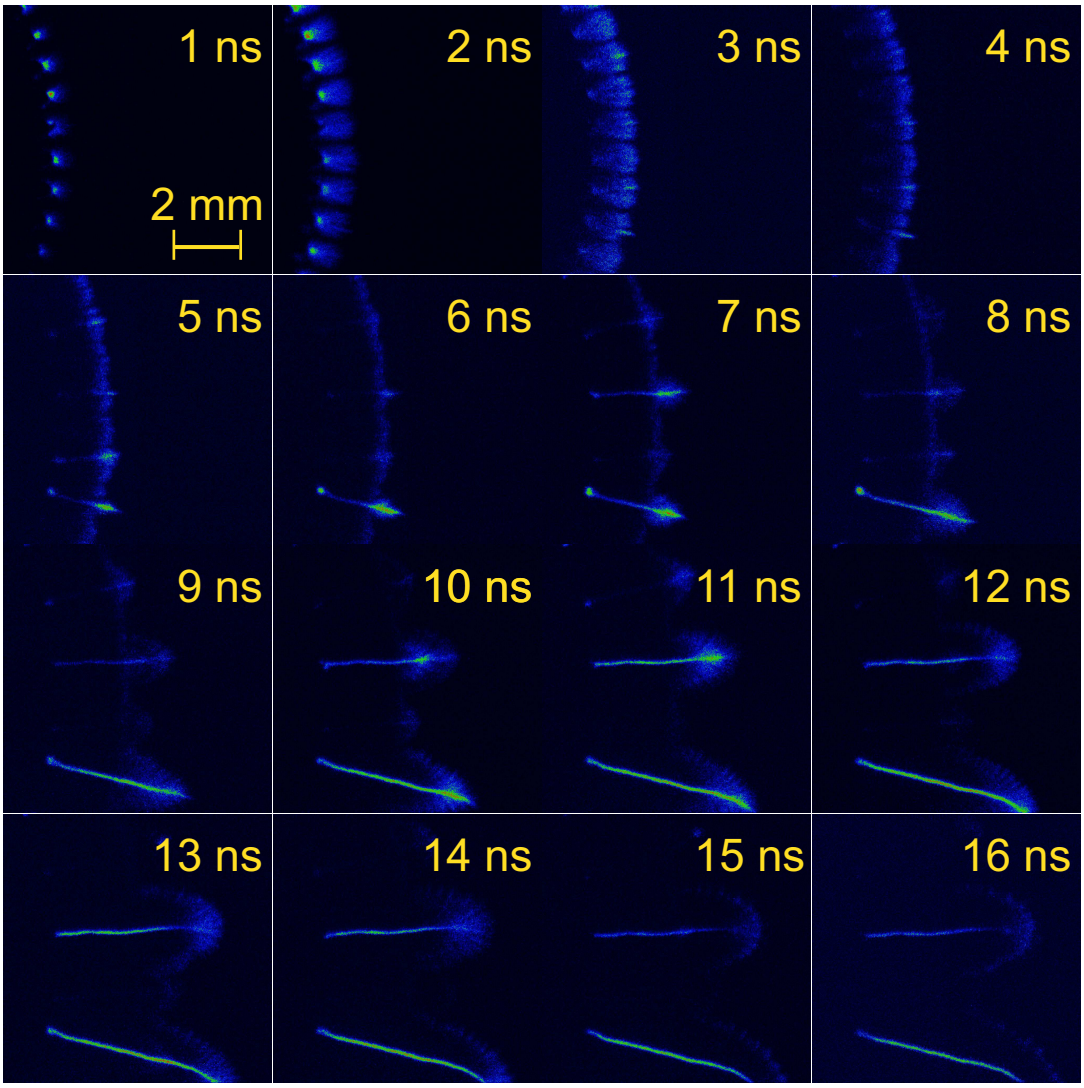

Figure 4.5: Micro–images of streamer–to–filament transition on gear electrode in 6 bar nitrogen at negative polarity. Voltage $U = -25$ kV. Camera gate is 1 ns. Resolution of the optical system is 7.6 μm/px. Time instant is marked with yellow in each frame.

When gas pressure and/or voltage amplitude increases, a streamer–to–filament transition is observed. Time–resolved streamer–to–filament transition and discharge propagation in 6 bar nitrogen at both negative and positive polarities are given by figure 4.5 and figure 4.6 respectively. The voltage amplitude was fixed and equal to ± 25 kV. The camera gate was equal to 1 ns. The resolution of the optical system is 7.6 μm/px. The gear electrode was used to fix a position of a streamer/filament in space; a few hours of training of the electrode system provided the filaments all the

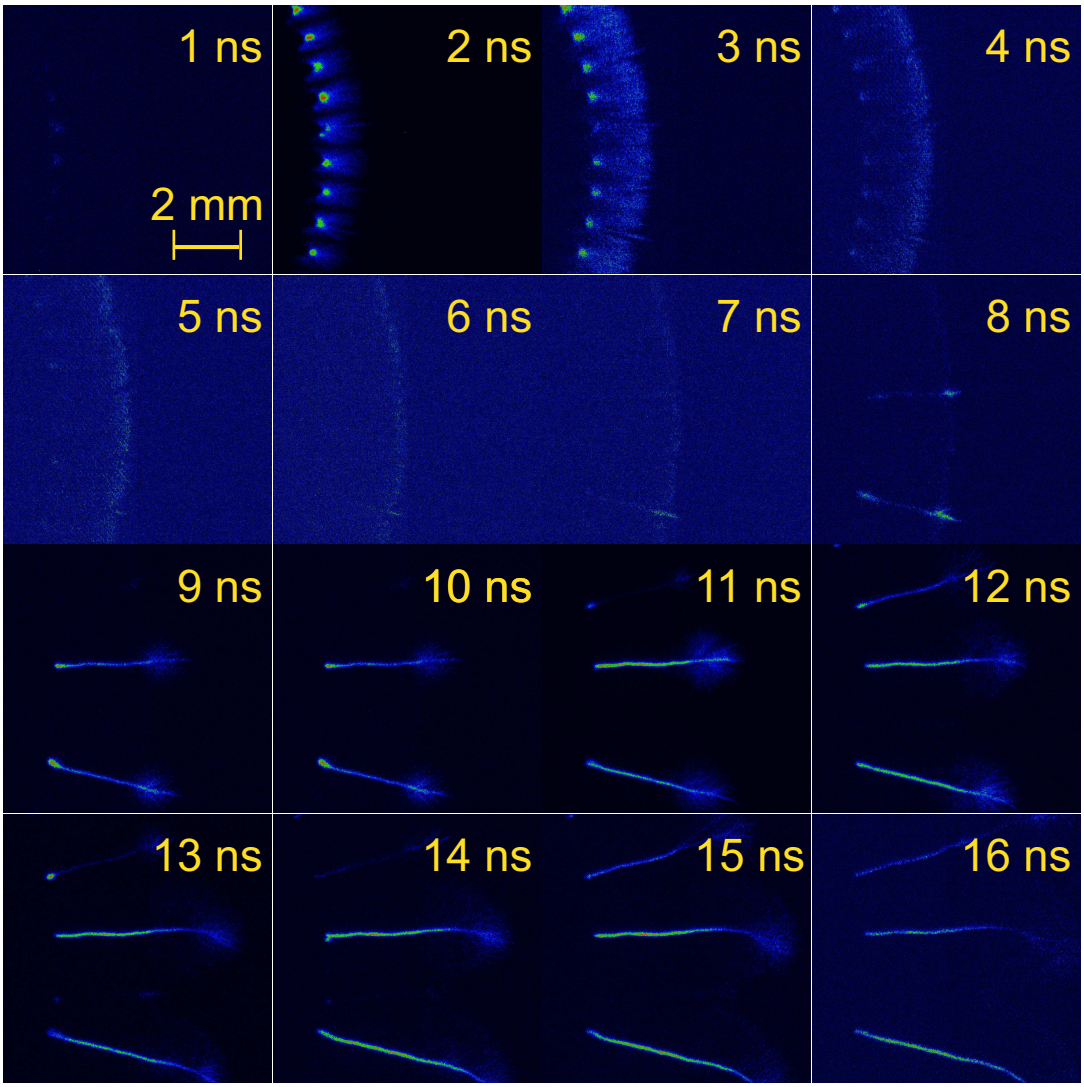

Figure 4.6: Micro–images of streamer–to–filament transition on gear electrode in 6 bar nitrogen at positive polarity. Voltage $U = +25$ kV. Camera gate is 1 ns. Resolution of the optical system is 7.6 μm/px. Time instant is marked with yellow in each frame.

time starting from the same points. As a result, it was possible to trace development of filaments changing the delay between the start of the pulse and the ICCD gate.

It is seen that for both polarities, the discharge starts as a set of streamers igniting at the same time (within 1 ns) from the high–voltage electrode. Starting from $3-5$ ns from the beginning of the pulse, a few protrusions can be clearly seen in the images.

For both polarities, the protrusions start from the emission in the streamer zone. Their propagation velocity is $2-3$ times faster than the streamer propagation velocity. There is a thin channel connecting the protrusion and the high–voltage electrode. At negative polarity, protrusions and streamers can be distinguished at

the same frames (see f.e., $4-8$ ns in figure 4.5), while at positive polarity, streamer emission intensity decays already at $4-7$ ns, and the first protrusions are clearly seen at $8-9$ ns (figure 4.6).

It can also be seen from both figures 4.5 and 4.6 that not all the streamer channels can produce the protrusion or filament and the distance between two adjacent filaments is $3-4$ times larger than between the streamers.

4.1.3 Parametric study of filamentary discharge in nitrogen at both polarities

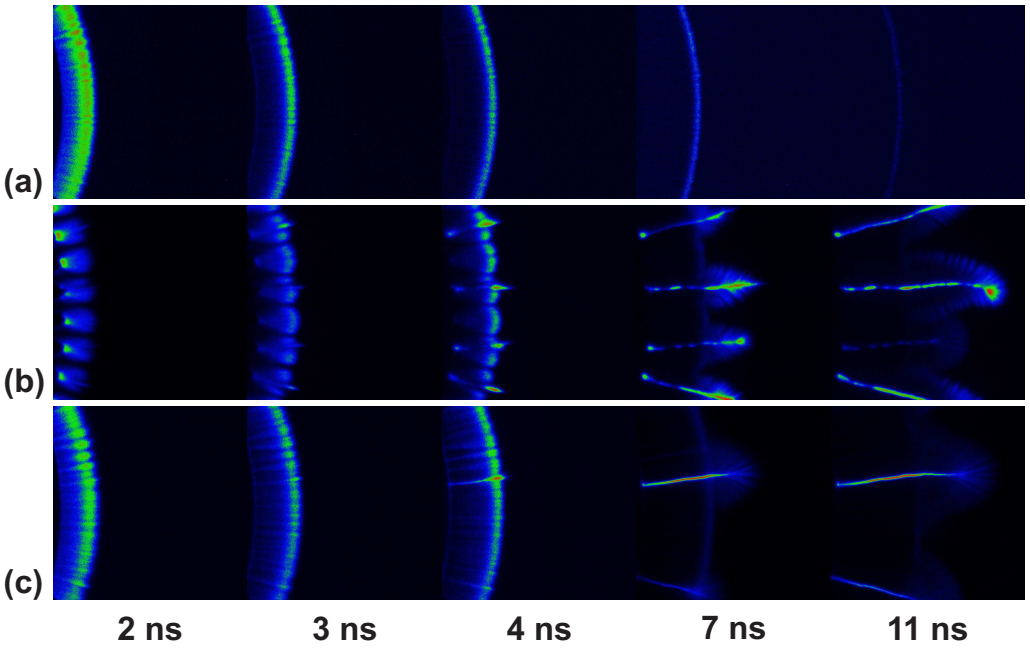

Figure 4.7: Micro–images of streamer–to–filament transition in 6 bar nitrogen at negative polarity. (a) $U = -25$ kV, on disc electrode; (b) $U = -25$ kV, on gear electrode; (c) $U = -32$ kV, on disc electrode. Camera gate is 1 ns with 50 accumulations. Resolution of the optical system is 7.6 μm/px. Time instants are indicated with black in the lower raw.

Figure 4.7 and 4.8 present the micro images taken in the system with the disc and gear electrodes by long distance microscope with the camera gate of 1 ns at ± 25 kV and ± 32 kV. For both negative and positive polarities, the streamers start from the edge of the high–voltage electrode simultaneously. The transition happens earlier at negative polarity ($t = 4$ ns) than at positive polarity ($t = 9$ ns).

For both polarities, at the same amplitude of the voltage (25 kV), the streamer–to–filament transition happens on the gear electrode rather than the disc electrode. This is due to the higher electric field generated in the region near the tip of gear

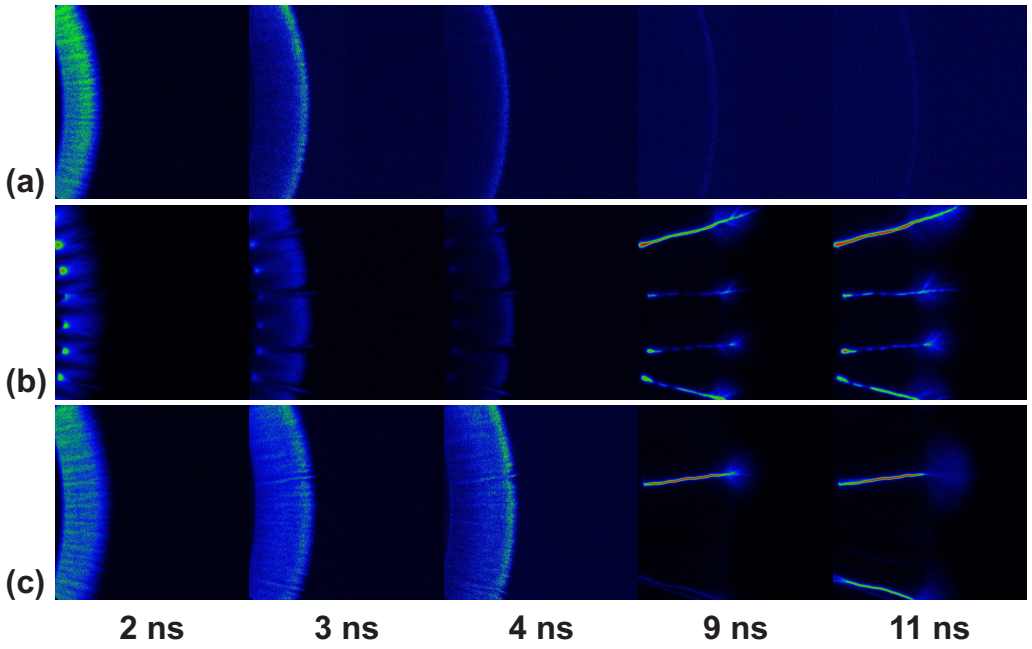

Figure 4.8: Micro–images of streamer–to–filament transition in 6 bar nitrogen at positive polarity. (a) $U = +25$ kV, on disc electrode; (b) $U = +25$ kV, on gear electrode; (c) $U = +32$ kV, on disc electrode. Camera gate is 1 ns with 50 accumulations. Resolution of the optical system is 7.6 μm/px. Time instants are indicated with black in the lower raw.

electrode. With the increasing amplitude of the voltage (from figure 4.7 and 4.8(a) 25 kV to (c)32 kV) on the disc electrode, the transition from streamer–to–filament happens at higher voltage conditions. When comparing figure 4.7 and 4.8(b) and (c), we can see that the distance between the filaments is smaller on the gear electrode than on the disc electrode.

Different morphology is observed for the emission from the tips of the filaments. For negative polarity, the emission appears as a "feather–like" structure (see figure 4.7(b)(c)) while at positive polarity the emission on the tip of the filament has almost a "ball–like" structure (see figure 4.8(b)(c)).

Figure 4.9 presents the micro–images taken by long distance microscope with a camera gate of 20 ns of the discharge on the disc electrode at different amplitudes of high voltage pulse. For both negative and positive polarities, the discharges are in the streamer regime at low voltage (±25 kV). With the increasing amplitude of the voltage (from ±25 kV to ±30 kV), a few thin channels are formed together with a previously homogeneous streamer zone. The emission intensity increases in these thin channels. The propagation velocity of these thin channels is slightly higher than the average propagation velocity of streamers.

With the continuous increase amplitude of the applied voltage (from ±30 kV

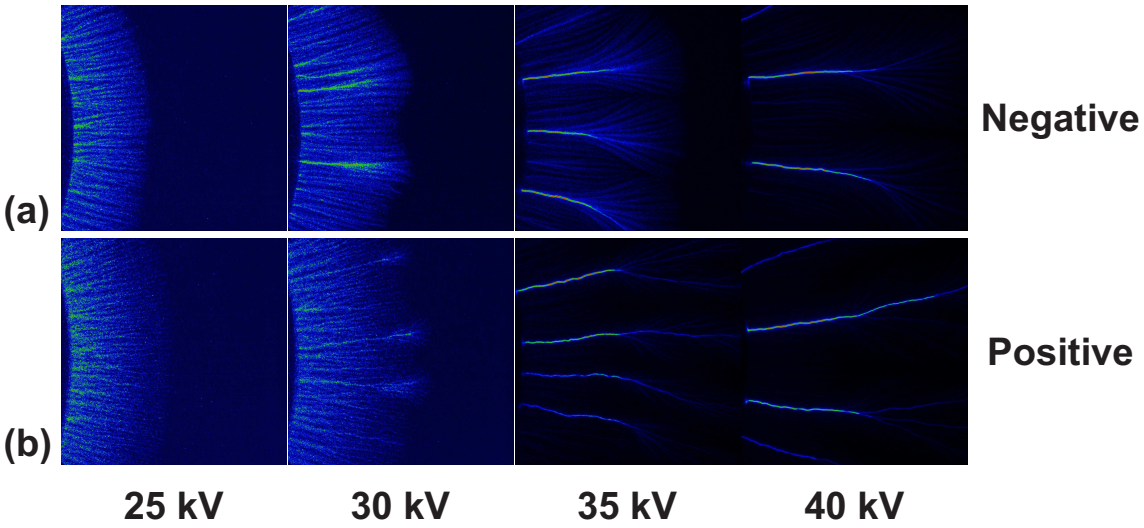

Figure 4.9: Comparison of streamer–to–filament transition in 6 bar nitrogen at both (a) negative and (b) positive polarities by varying the amplitude of applied voltage. Both sets of experiments were conducted on the disc electrode. Camera gate is 20 ns with 50 accumulations. Resolution of the optical system is 7.6 μm/px.

to $\pm$35 kV), previous constricted thin channels are well developed to the filaments with higher emission intensity. It should be noticed here that ICCD camera adjusts automatically the contrast of the images. Typically, the integrated over the ICCD sensitivity range ($200 - 800$ nm) emission of filament is $\sim$ 50 times more intense than the emission of streamer. The streamer zone can hardly be seen at 35 kV due to the high intensity contrast with filaments. At voltage $U = 35$ kV, the filaments have more branches at negative polarity than at positive polarity. At this amplitude of voltage, we can see that each filament channel consists of two parts with different emission intensities. The left part that is closer to the high–voltage electrode has higher emission intensity and less branches while the right part has more branches with lower emission intensity. This gives us the impression that the part with more branches has less emission intensity. However, this is not the only reason for explaining the difference of the emission intensity between two parts. These differences are also caused by the nature of emission of these two parts of channels: the left part of the channel is rich in atomic nitrogen while the right part of the channel mainly consists of second positive system of nitrogen that has the same physical composition as streamers. This will be explained further in chapter 6.

The last column of figure 4.9 shows the well–developed filament structures at $\pm$40 kV. The emission intensity increases with the increase of the amplitude of voltage. The discharge channels propagate further with the increase of amplitude of applied voltage.

4.2 Streamer–to–filament transition of nSDBD on different dielectric surfaces

Streamer–to–filament transition takes place on different dielectric surfaces for the high–pressure high–voltage nanosecond discharges in the gas mixtures containing molecular gases. In this work, the PVC film and ceramic plate were selected as the dielectric materials for the surface discharge to study the transition process. The transitions in this section are observed in a single-shot experiment a few nanoseconds after the start of the discharge. A series of diagrams of the streamer–to–filament transition in a Pressure-Voltage chart is built for the experiments on both PVC and dielectric surfaces. The disc electrode was used for all the transition experiments in this section. The camera gate was fixed to 12 ns to catch the discharge propagation during the first half pulse. Time-integrated single–shot images of the discharge were taken at constant pressure increasing and decreasing the voltage. It should be pointed out here that no hysteresis was observed by changing the voltage up and down or *vise versa*.

4.2.1 Transition curves on PVC surface

Typical ICCD images of the streamer-to-filament transition are presented in figure 4.10. The images were taken for nSDBDs on PVC surface of negative polarity in nitrogen by varying the applied voltage and pressure. The relatively low voltage of -19.2 kV at the high-voltage electrode initiates a streamer nSDBD. It can be seen clearly from the lowest raw of figure 4.10 that at the same voltage level, with the increase of pressure, the ring of streamer zone become smaller and smaller. This indicates that streamer propagates faster at lower pressures.

When only a few (typically $3-5$) filaments are observed during first 12 ns of the discharge, this voltage is considered as a transition one (like the second raw image in figure 4.10). It should be noted that (i) from experiment to experiment, the filaments appear at different points on the high-voltage electrode, they are not associated with the defects on the electrode; (ii) the duration of the transition in the developed filamentary mode, that is the time between the first filament appears and when a regular filamentary pattern is observed (similar to the image at -46 kV in figure 4.10), is equal to $1-2$ ns.

The experiments were conducted at N_2/O_2 mixtures with different oxygen fraction, 0 (pure N_2), 1%, 2%, 5%, 10% and 20% (synthetic air). The gas mixtures with different oxygen fractions were achieved by adding different amount of nitrogen to synthetic air. For example, when adding 0.5 bar synthetic air and 9.5 bar N_2 into the

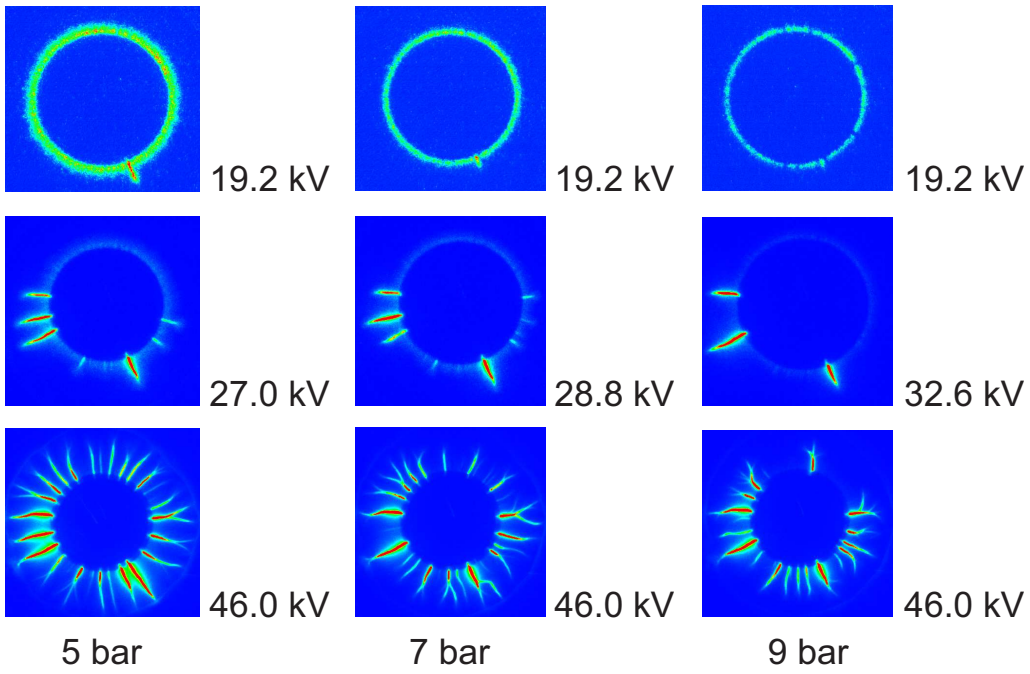

Figure 4.10: Images of streamer surface discharge, transitive discharge and developed filamentary discharge on PVC surface at three given pressures (5 bar, 7 bar and 9 bar). Nitrogen, applied voltage varying from $U = -19.2$ kV to $U = -46$ kV. Camera gate is 12 ns. The diameter of the high–voltage electrode (circle at the center of each image) is equal to 20 mm.

discharge chamber, one can get the 10 bar N_2/O_2 mixture with 1% oxygen fraction. More O_2 fraction cases can be seen in table 4.1.

Table 4.1: Composition of synthetic air and N_2 for a 10 bar gas mixtures.

O_2 fraction	air/bar	N_2/bar
1%	0.5	9.5
2%	1	9
5%	2.5	7.5
10%	5	5

The most significant difference observed for the filamentary discharge at negative and positive polarities is the behavior of the transition curve. The pressure-voltage charts for both polarities for the discharge on PVC surface obtained as described above are given by figure 4.11. Zones marked as *I* and *II* represent streamer and filament zones respectively.

Two set of measurements are compared at each plot in figure 4.11: the solid

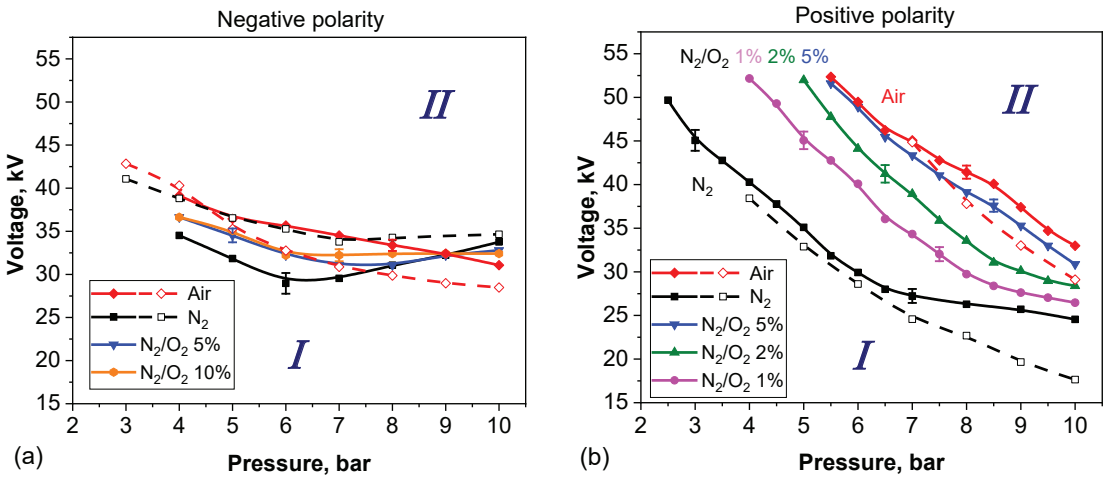

Figure 4.11: Curves of streamer–to–filament transition on the PVC surface taken at the condition that the transition happens during first 12 ns of the discharge for (a) negative and (b) positive polarity of voltage on the high-voltage electrode.

lines represent the results of the present work, where the overall thickness of the PVC layer and the glue layer is 0.7 mm, and the dashed lines show the previous measurements [122], taken at 0.5 mm of the overall dielectric thickness. The voltage measurement error is less than 1 kV.

For negative polarity the streamer–to–filament transition happens almost simultaneously for all observed gases: the difference between air and pure nitrogen is about 5 kV in comparison to tens of kilovolts for positive polarity. There is a point of intersection of curves corresponding to different gas composition, this is especially clearly seen for the data set with four different percentages of oxygen in the mixture. The intersection point seems to be a function of the overall dielectric layer thickness.

For positive polarity, the effect of molecular oxygen addition is extremely strong: 1% of oxygen at 4 bar increases the transition voltage from 41 kV to 52 kV. This dependence seems to disappear with oxygen concentration rising: at 6 bar, the transition voltages for pure nitrogen and mixtures with 1%, 2%, 5% and 20% of oxygen are equal to 30, 40, 44, 48.5 and 49.5 kV respectively. This phenomenon can cause from the photoionization of oxygen [123–126].

4.2.2 Transition curves on ceramic surface

To be sure that (i) streamer–to–filament transition does not appear because of degradation of PVC; (ii) filaments can propagate over the surface of dielectric with different dielectric permittivities, a special series of experiment was performed with ceramics as a dielectric.

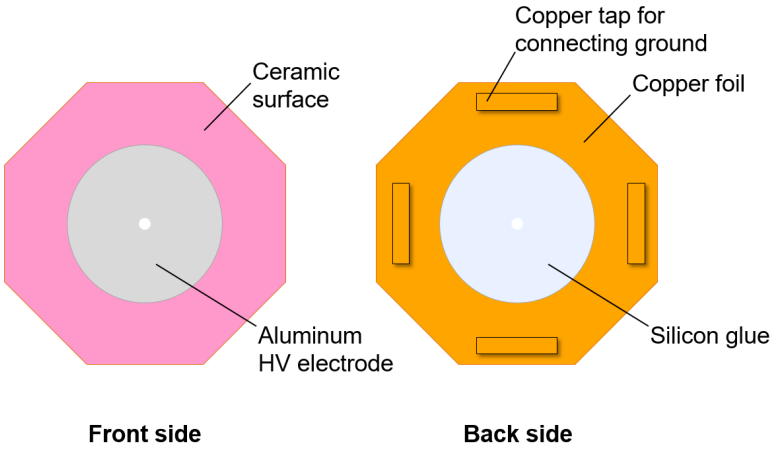

Figure 4.12: (a) Front side and (b) back side view of an aluminum high-voltage (HV) electrode on the ceramic surface.

The high–voltage (HV) electrode glued on the surface of ceramic dielectric material and its connection the the ground electrode are displayed in figure 4.12. From the front view, a thin disc aluminum HV electrode, 20 mm in diameter, was glued in the center of an octagonal ceramic plate ($\epsilon = 10.4$) with the thickness of 1 mm. The silicon glue ($\epsilon = 3.2$) was applied exactly in the region of HV electrode on the other side of the ceramic plate. It should be noted that although a layer of silicon glue efficiently decreased summary permittivity ϵ_Σ of the dielectric and this should be taken into account. For example, when doing numerical modeling, it was important for us to check if there is qualitatively the same streamer–to–filament transition on ceramic surface.

A summary permittivity ϵ_Σ of the resulted dielectric can be estimated using dielectric permittivity of ceramics, $\epsilon_{cer} = 10.4$ and silicon, $\epsilon_{sil} = 3.2$, and thickness of ceramics, $d_{cer} = 1$ mm and silicon layer, $d_{sil} = 0.2$ mm. Considering ceramics and silicon layer as two capacitors of the same area connected in parallel, the summary capacitance C_Σ can be calculated as:

$$\frac{1}{C_\Sigma} = \frac{1}{C_{cer}} + \frac{1}{C_{sil}} \tag{4.3}$$

$$\frac{d_\Sigma}{\epsilon_\Sigma} = \frac{d_{cer}}{\epsilon_{cer}} + \frac{d_{sil}}{\epsilon_{sil}} \tag{4.4}$$

Finally, the summary permittivity ϵ_Σ can be represented as:

$$\epsilon_\Sigma = \frac{d_\Sigma}{\frac{d_{cer}}{\epsilon_{cer}} + \frac{d_{sil}}{\epsilon_{sil}}} = 7.6 \tag{4.5}$$

The rest of the area except the silicon glue area was covered by the conductive

copper foil. Four rectangular copper taps were glued to the copper foil for keeping the good contact between the copper foil and ground electrode.

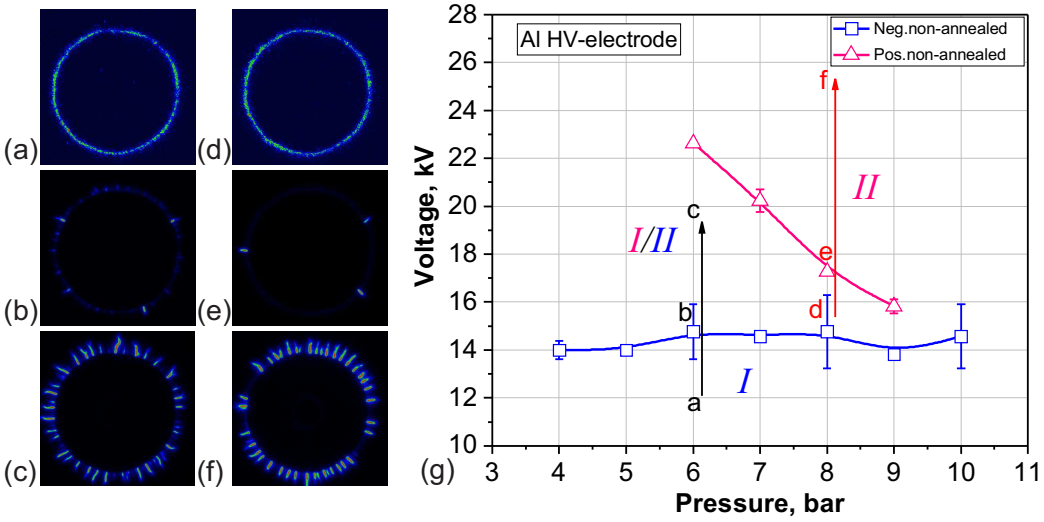

Figure 4.13: Images of (a)(d) streamer surface discharge, (b)(e) transitive discharge and (c)(f) developed filamentary discharge on ceramic surface at two selected pressures (6 bar and 8 bar) in air at both (a)(b)(c) negative and (d)(e)(f) positive polarities. Camera gate is 12 ns. The diameter of the high–voltage electrode (circle at the center of each image) is equal to 20 mm. (g) Curves of streamer–to–filament transition on ceramic surface taken at the condition that the transition happens during first 12 ns of the discharge for the negative polarity of voltage on a non–annealed aluminum high-voltage electrode in synthetic air. Region I is for streamers, region II is for filaments, region I/II is for streamers for positive polarity and filaments for negative polarity.

The images of streamer surface discharge, transitive discharge and developed filamentary discharge on ceramic surface are displayed in figure 4.13 (a)(b)(c) for negative polarity and (d)(e)(f) for positive polarity. The experimental conditions (pressures and voltages) for these six selected images are marked in the transition chart in figure 4.13 (g). The transition chart gives the streamer–to–filament transition curves on a non–annealed Al HV electrode. Below the blue transition curves is the streamer regime while above the curves is the developed filament regime. The experiment was conducted in synthetic air by decreasing the pressure from 10 bar to 4 bar.

It can be seen by comparing the ICCD images in figure 4.13 that there is no significant difference between different polarities or at different pressures (6 bar and 8 bar). The propagation velocity of nSDBD on ceramic surfaces is much slower

than on PVC surfaces, in complete agreement with the predictions in [117]. The length of the discharge channels in the transition mode is shorter than in the filamentary regime for discharge on ceramic surfaces while on PVC surfaces, the length of discharge channels in both transition and filamentary mode are closer.

Figure 4.13 (g) shows the dependencies of the threshold voltage values on the gas pressure for both polarities. It can be seen that for the negative pulse polarity, filamentation occurs at much lower voltage values. The transition voltage keeps stable between $14-15$ kV and shows less dependence on the pressure. Transition curve at positive pulse polarity is characterized by a much stronger pressure dependence. At pressure $p = 9$ bar, the transition happens when the voltage is over 16 kV while at pressure $p = 6$ bar, the transition voltage increased up to 22.5 kV. It should be noted that the error of measured transition voltage at negative polarity $(2-3$ kV) is higher than positive polarity (1 kV).

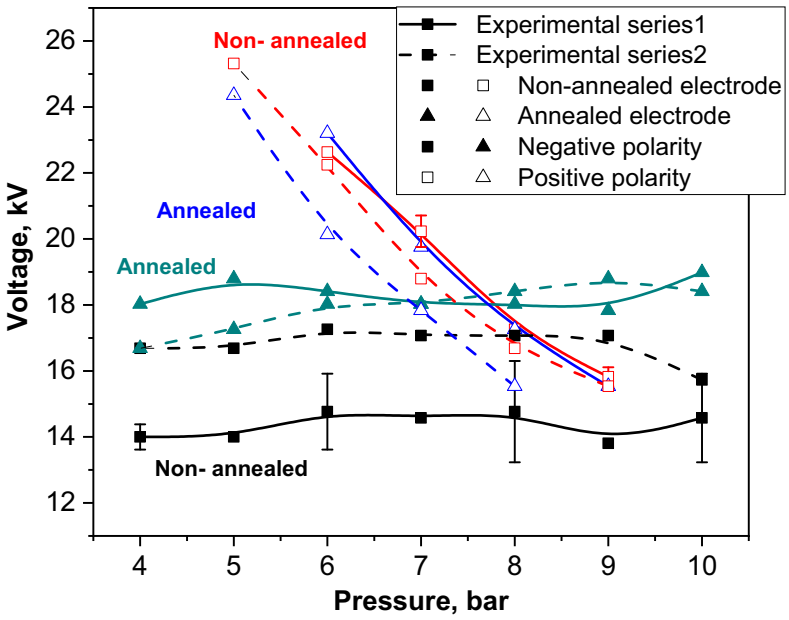

Figure 4.14: Curves of streamer–to–filament transition on ceramic surface taken at the condition that the transition happens during first 12 ns of the discharge for both negative and positive polarities of voltage on both annealed and non–annealed aluminum high-voltage electrodes in air. This graph contains two separated experimental series 1 (solid lines) and 2 (dash lines) with the same experimental condition.

Streamer–to–filament transition curves on ceramic surface on both annealed and non–annealed aluminum high-voltage electrodes are displayed in figure 4.14. The

annealed aluminum HV electrodes are the ones covered by about 2 μm oxide layer at the edge of HV electrode. This graph contains two independent experiments on identical ceramic dielectric electrodes with same experimental condition and operation. Results from two experiment sets, although different in absolute values, show the same tendency of filamentary thresholds between non–annealed and annealed electrodes and between both negative and positive polarities. The difference between these two experiment sets is within $2-3$ kV for both polarities.

As is indicated above, transition curves at negative pulse polarity show less pressure dependence than at positive polarity. It can also been revealed from figure 4.14 that the filamentation thresholds are affected by the presence of oxide layer on the edge of the electrode. At negative polarity, the required transition voltage is higher on the annealed electrode than on non–annealed electrode. On the contrary, for positive polarity, the required transition voltage on the annealed electrode is slightly lower than on the non–annealed electrode. The difference in threshold voltage for annealed and non–annealed electrode, about $1-2$ kV, is low comparing to difference between two polarities.

4.3 Streamer–to–filament transition of nSDBD using electrode synthesized with carbon nanomaterials

To check further the influence of the nature of electrode on the transition, the experiments with carbon nanomaterials deposited on the high–voltage electrode have been performed. They are joint experiments with a team from the Laboratory of Engineering Profile at Al-Farabi Kazakh National University and from the Kazakh-British Technical University (Yerassyl Yerlanuly, Maratbek Gabdullin, Didar Batryshev, Tlekkabul Ramazanov).

The idea behind the experiments was that carbon nanomaterials are known as excellent emitters. If the threshold voltage depends upon electrons emission from the high–voltage electrode, we expected significant changes in the threshold voltage for negative polarity.

Three different carbon nanomaterials were synthesized on the surface of the copper electrode. They are the composite material based on graphite and carbon nanotubes (CNTs), graphite and carbon nanofibers (CNFs) and carbon nanowalls (CNWs). The experiments of streamer–to–filament transition were conducted by applying the high voltage on the electrode synthesized with (or without) carbon nanomaterials.

4.3.1 Carbon nanomaterials synthesized on copper electrode

Composite materials based on the graphite and carbon nanotubes were synthesized on the HV electrode by a Chemical Vapor Deposition (CVD) [127]. A nickel layer with the thickness of 1.5 nm was sprayed onto the surface of the substrate using a magnetron discharge. This method is intended for avoiding the sorption of carbon by copper that is the material of the HV electrode. The synthesis of composite nanomaterials was carried out in a CVD horizontal furnace at a temperature of 1000 °C. This process was conducted at atmospheric pressure of hydrogen with a flow of 50 sccm and methane with a flow of 40 sccm for the duration of 30 minutes.

Figure 4.15(a) and (b) show the results of Raman spectroscopy and scanning electron microscopy (SEM) of the composite material based on graphite and carbon nanotubes (CNTs). The Raman spectrum characterizes a graphite–like structure but SEM results indicate that the samples have CNTs.

The synthesis of composite materials based on the graphite and carbon nanofibers on the HV electrode was carried out by the same synthesis method (CVD) as graphite and CNTs. The difference to graphite and CNTs is that the thickness of nickel layer for spraying is 3 nm instead of 1.5 nm. Figure 4.15(c) and (d) show the results of Raman spectroscopy and SEM of composite material based on graphite and carbon nanofibers. The Raman spectrum shows a graphite–like structure but SEM results indicate that the samples have CNFs. The appearance of carbon nanofibers can be explained as follows: larger nano–clusters appear on the substrate and carbon absorption helps the growth of nanofibers, which contributes to a thicker catalytic nickel layer in the sample.

Carbon nanowalls (CNWs) were synthesized on the HV electrode by the Plasma Enhanced Chemical Vapor Deposition (PECVD) method [128–130]. The synthesis was conducted with a radio–frequency discharge power of 11 W in the gas mixture of argon and methane with the pressure of $1.3-1.8$ Torr. The Raman spectroscopy and SEM of CNWs are shown in figure 4.15(e) and (f). The Raman spectrum completely characterizes the CNWs, in particular, peak D' is the distinguishing trait CNWs from other graphene–like nanostructures. The scanning electron microscope image also shows the well defined CNWs.

4.3.2 Transition curves on electrode synthesized with carbon nanomaterials

The experiments of streamer-filamentary transition were carried out on four disc electrode with or without carbon nanomaterials. The diameter of the central high voltage copper electrode was kept constant as 20 mm. The experiments are per-

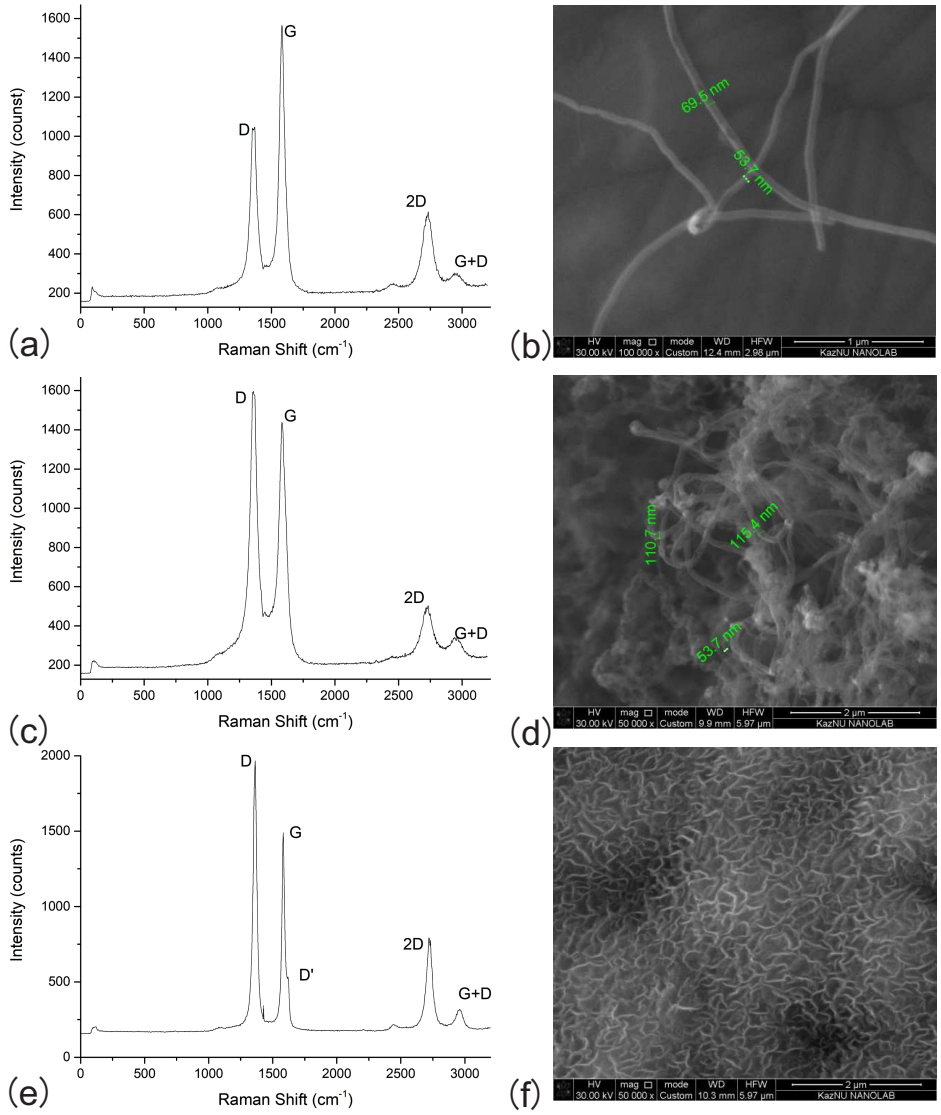

Figure 4.15: Raman spectrum and scanning electron microscope image of (a)(b) composite material based on graphite and carbon nanotubes, (c)(d) graphite and carbon nanofibers and (e)(f) carbon nanowalls.

formed in both nitrogen and synthetic air at both polarities. The transition moment was selected with the ICCD gate of 12 ns as the time instant of $2-3$ filaments appearing near the high-voltage electrode.

The integrated ICCD images at different transition moment are displayed in figure 4.16((a) to (f)). The experiment was done in nitrogen on the high voltage electrode synthesized with carbon nanowalls (CNWs) and the experimental conditions of selected ICCD images are marked by letters (a to f) in figure 4.16(g). Figure 4.16(a)(b)(c) show the transition from streamer to filament at positive po-

larity at 5 bar and figure 4.16(d)(e)(f) give the transition at negative polarity at 9 bar. It can be seen that when the voltage is equal, both filaments and streamers propagate faster at lower pressures. The discharge in the filament mode tends to have more branches at higher pressures. Figure 4.16(g) shows that the transition at positive polarity (red curve) has strong dependence on the pressure while at negative polarity the required transition voltage remain at the same level (38 ± 2 kV) when pressure decreases from 10 bar to 4 bar. Qualitatively, the picture is similar to the electrode system with copper high–voltage electrode containing PVC as a dielectric (figure 4.10) and to the electrode system with annealed/nonannealed Aluminium high–voltage electrode containing ceramics as a dielectric (figure 4.13).

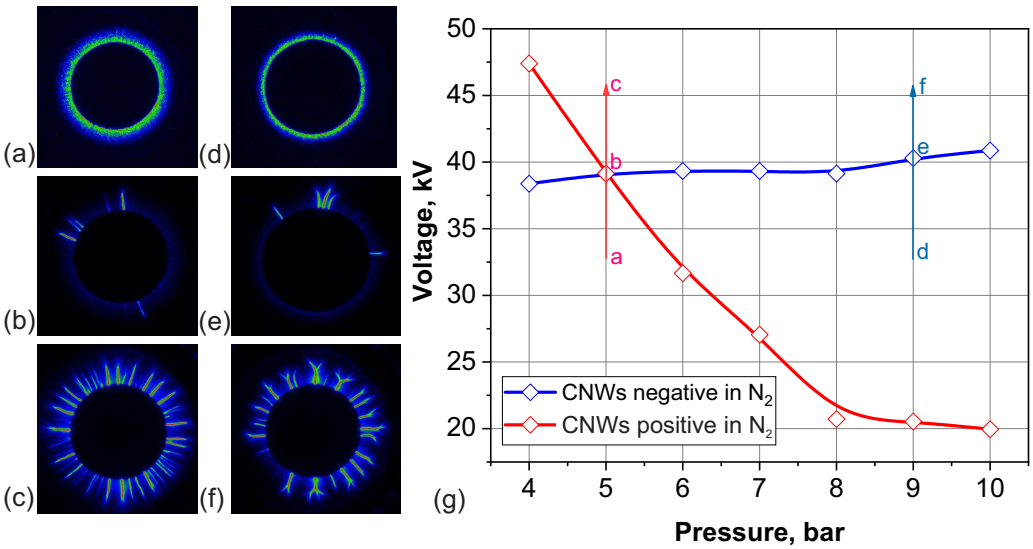

Figure 4.16: Images of (a)(d) streamer surface discharge, (b)(e) transitive discharge and (c)(f) developed filamentary discharge on ceramic surface at two selected pressures (5 bar and 9 bar) in nitrogen at both (a)(b)(c) positive and (d)(e)(f) negative polarities. Camera gate is 12 ns. The diameter of the high–voltage electrode (circle at the center of each image) is equal to 20 mm. (g) Curves of streamer–to–filament transition on electrode synthesized with CNWs taken at the condition that the transition happens during first 12 ns of the discharge.

To study the effects of using different HV electrodes synthesized with carbon nanomaterials on the streamer–to–filament transition behavior, transition curves on electrodes synthesized with different carbon nanomaterials in both air and nitrogen at both negative and positive polarities are displayed in figure 4.17. Generally, the transition curves keep the same tendency as the transition curves on ceramic surfaces that the transition curves have less pressure dependence at negative polarity but strong dependence at positive polarity.

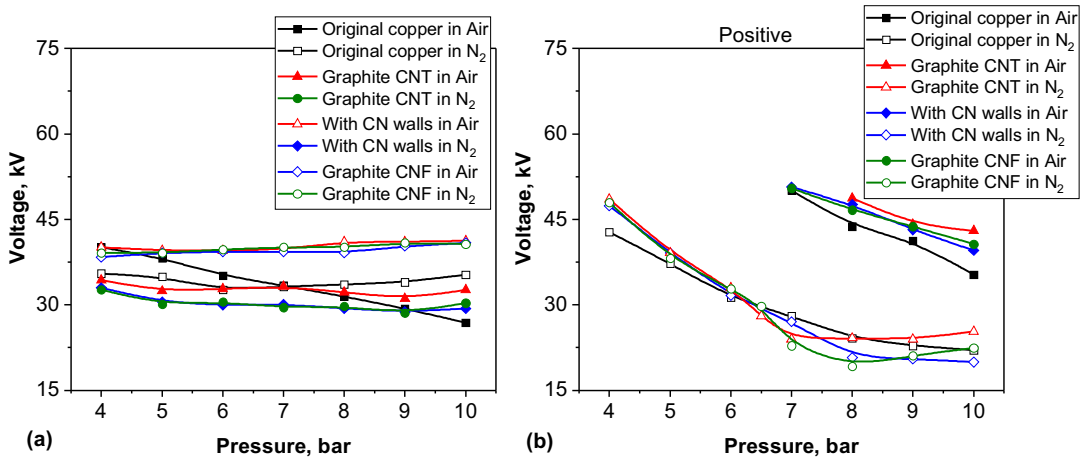

Figure 4.17: Curves of streamer–to–filament transition taken at the condition that the transition happens during first 12 ns of the discharge for both (a) negative and (b) positive polarities of voltage on a copper electrode synthesized with (or without) carbon nanomaterials in both nitrogen and air.

It can be seen from figure 4.17(a) that in air, streamer-filamentary transition for negative polarity happens at lower voltages for the electrodes with carbon nanomaterials at lower pressures while in nitrogen, the transition at negative polarity happens at higher voltage for the electrodes with carbon nanomaterials at whole pressure ranges. For the transition at positive polarity (figure 4.17(b)), there is no noticeable difference of the transitions happen between the electrode sybthesized with or without carbon nanomaterials in nitrogen. In air, carbon nanomaterials slightly increased the required transition voltages at high pressures (over 7 bar).

It can be conclude that the synthesis of the carbon nanomaterials makes the impact on the streamer–to–filament transition mostly at negative polarity. It highly increases the required transition voltages for the discharges in nitrogen and it decrease the dependence of transition voltages on the pressures for the discharges in air. There is no distinctive difference of the transition among which type of nanomaterial was synthesized on the high–voltage electrodes. In another word, carbon nanomaterials synthesized on the HV electrode have limited impact on the streamer–to–filament transition process at both negative and positive polarities.

4.4 Conclusion

In this chapter, parameters of streamer–to–filament transition of nanosecond surface dielectric barrier discharges at high pressures are analysed experimentally. The transition happens similarly in all observed experimental conditions. At low

voltages and pressures, the streamer discharge starts from the edge of the high–voltage electrode. With the increase of voltage on the electrode and/or gas pressure, the discharge channels are constricted and a few filamentary channels appear on the edge of the high–voltage electrode, propagating in the radial direction towards the ground electrode. There is no distinctive difference of the transition process between negative and positive polarities but the transition thresholds are totally different.

For negative polarity high–voltage pulse, the threshold voltage almost does not change with pressure, staying for the pressure range $3 - 12$ bar, within a "corridor" of voltages $30 - 40$ kV for PVC and $14 - 18$ kV for ceramics as a dielectric. For positive polarity high–voltage pulse, the threshold voltage changes dramatically: it drops down from 55 to 20 kV as pressure increases from 3 to 12 bar for PVC as a dielectric and from 26 to 15 kV as pressure increases from 5 to 9 bar for ceramics as a dielectric.

Significant difference is observed at positive polarity when changing gas mixture composition: at 8 bar, the threshold voltage in air is twice higher than the threshold voltage in nitrogen. More than that, adding 1% of molecular oxygen to pure nitrogen leads to sharp increase of the threshold voltage: at 4 bar, the threshold voltage increases from 41 kV to 52 kV.

Modifications of material/structure of the high–voltage electrode (annealed or non–annealed, copper or copper covered with carbon nanomaterials) causes only minor influence. The major difference in the threshold voltage as a function of polarity, gas mixture composition and dielectric permittivity of the surface in the proximity of plasma leads to the conclusion that streamer–to–filament transition can be a consequence of severe transformation of plasma parameters as far as properties of surface streamers are known, we decide to focus on studying of plasma properties in the filaments.

Chapter 5

Plasma properties in the filaments

This chapter contains a series of experiments dedicated to analysis of plasma properties in filamentary nanosecond surface dielectric barrier discharge (nSDBD). The optical emission spectroscopy in the micrometer scale was used to analyse the change in spectral composition of optical emission during the streamer–to–filament transition. The electron temperature, electron density and the specific deposited energy were measured for a wide range of pressures and voltages. Hydrodynamic pertubations caused by discharge are illustrated with the help of the Particle Image Velocimetry (PIV) technique. A model suggested by Dr. Nicolay Popov [41] explaining plasma properties in filamentary nanosecond discharges and the role of excited species in streamer–to–filament transition is discussed in the end of this chapter.

5.1 Optical emission spectroscopy of filamentary discharge

Optical emission spectroscopy (OES), especially the measuring of the atomic emission, is a widely used experimental method for determining the elemental composition of plasma in many kind of discharges. The N^+ atomic line of nitrogen was measured for analysing the electron temperature. The electron density was determined by using the hydrogen and nitrogen atomic line broadening.

5.1.1 Changing of the spectra in filament generation process

In this chapter, we focus on study of spectral composition of plasma during the streamer–to–filament transition process. Because the transition happens in a few nanosecond after the start of discharge and takes place in a small region, the long distance microscope (LDM) was used for taking the time–resolved spectra in the micro–scale.

The scheme of the experimental apparatus used for micro spectroscopy is displayed in figure 5.1(a). The LDM was aligned between the slit of spectrometer and the quartz window of the discharge cell. The slit of the spectrometer was adjusted to let in a single tooth of the gear electrode, as shown in figure 5.1(b). The gratings of the spectrometer were set to zero order for taking the images and adjusting the focal plane during the calibration process. The dielectric material used in this experiment is PVC film with thickness of 0.3 mm. It was treated for over thousands shots for fixing the filament channel in the slit of spectrometer.

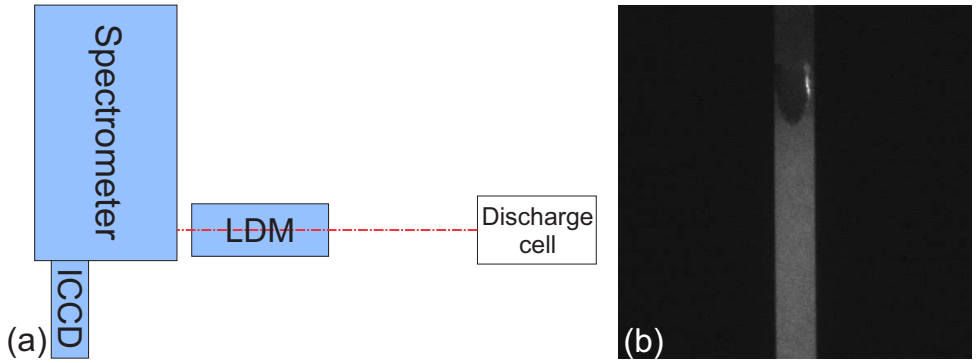

Figure 5.1: (a) Scheme of the experimental apparatus for micro–spectroscopy. (b) Electrode tooth image in the slit of spectrometer (zero order). Resolution of the optical system is 7.6 μm/px.

The discharge propagates from the high–voltage (HV) electrode along the grounded electrode covered with dielectric. In this section, as the tooth of the HV electrode has been put at the top of the slit, the discharge propagates vertically, from the top of vision to the bottom. The experiments were performed in 6 bar nitrogen at negative polarity ($U = -25$ kV). Four specific moments (t =4, 7, 10 and 16 ns) were selected for comparing the changes in spectral composition during the streamer–to–filament transition. At time $t = 4$ ns, it is a pure streamer regime while at $t = 7$ ns, a protrusion appears which is a sign of starting the transition process. At time $t = 10$ ns, this is the end of the transition process and also the early stage of the filamentary regime. At time $t = 16$ ns, a well–defined filament is generated and it contains whole information of the filamentary discharge in a single shot mode.

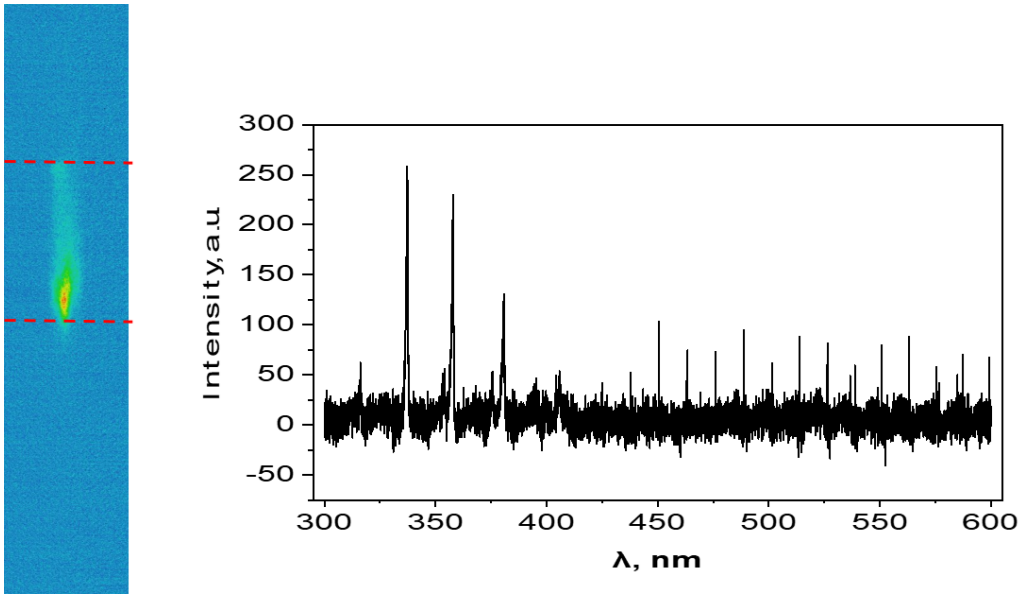

Figure 5.2: ICCD image from zero order of spectrometer at time $t = 4$ ns as well as spectrum of a single discharge channel in the wavelength range of 300–600 nm. Resolution of the optical system is 7.6 μm/px. Not corrected to the spectral sensitivity of the optical system.

An integrated ICCD image taken from zero order of spectrometer at time $t = 4$ ns is displayed on left of figure 5.2. The spectrum of one discharge channel at the same moment in the wavelength range of 300–600 nm is shown on the right. As indicated above and shown in the ICCD image, the discharge at this moment is the surface streamer discharge. The spectrum contains second positive system of nitrogen (SPS N_2: $C^3\Pi_u \rightarrow B^3\Pi_g$) with the highest peak at wavelength λ =337 nm. The spectrum in the wavelength range over 450 nm does not give any information but showing the electrical and optical noise.

Figure 5.3 shows the ICCD image from zero order of spectrometer at time $t = 7$ ns on the left as well as spectrum of single discharge channel acquired at same instant in the wavelength range of 300–600 nm. It can be seen clearly from the image on the left that the protrusion appears in the region further to the HV electrode (marked as region *II*). There are still a bright spot and thin channel with less brightness in region near the electrode (region *I*).

Two spectra on the right show the same spectral composition for both *I* and *II* regions. As in the spectrum for $t = 4$ ns, the second positive system of nitrogen is still the only composition in the spectrum. The difference is that due to the increase of emission intensity in region *II*, we can identify more bands of second positive system of nitrogen in the spectrum.

A few bands of SPS N_2: $C^3\Pi_u \rightarrow B^3\Pi_g$ are marked in the spectrum of region *II*

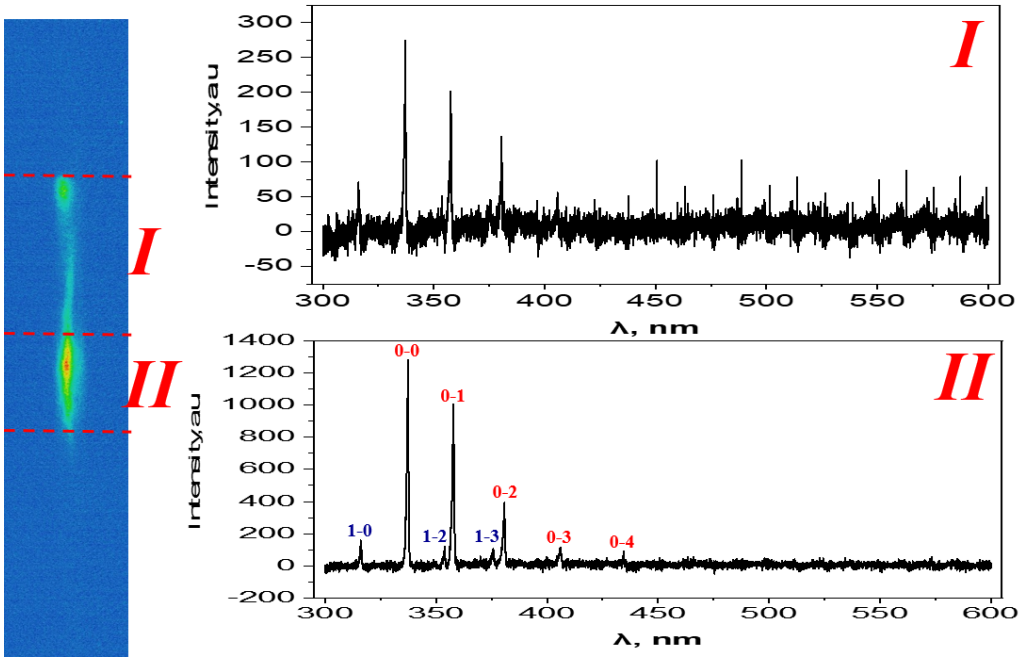

Figure 5.3: ICCD image from zero order of spectrometer at time $t = 7$ ns as well as two spectra of single discharge channel in the wavelength range of 300–600 nm. Each line is identified by two numbers where the first one corresponds to vibrational level in state $C^3\Pi_u$ and the second one to the vibrational level in state $B^3\Pi_g$. Resolution of the optical system is 7.6 μm/px. Not corrected to the spectral sensitivity of the optical system.

in figure 5.3. The following transition process are identified in the discharge at $t = 7$ ns:

$$N_2\left(C^3\Pi_u, v' = 0, 1\right) \rightarrow N_2\left(B^3\Pi_g, v'' = 0, 1, 2, 3, 4\right) + h\nu \tag{5.1}$$

where v' and v'' are the vibrational excitation levels, and $h\nu$ is the energy of an emitted photon during the excitation process.

This is the first time that we see the discharge with "filament" structure containing only the formation of second positive system of nitrogen rather than the continuous wave (cw) spectrum or N^+ atomic lines. Thus we can draw the conclusion that the perturbation generated in the process of streamer–to–filament transition has the same spectral composition identical to a streamer discharge. This means that the chemical excitation process in the discharge should be similar in these two regimes.

At time $t = 10$ ns, the perturbation and the bright spot near the electrode have just been connected via a discharge channel with same diameter as shown in figure 5.4 on the left. From the spectrum on the right, although the spectrum is noisy, we still can find that the spectrum contains three components: second positive

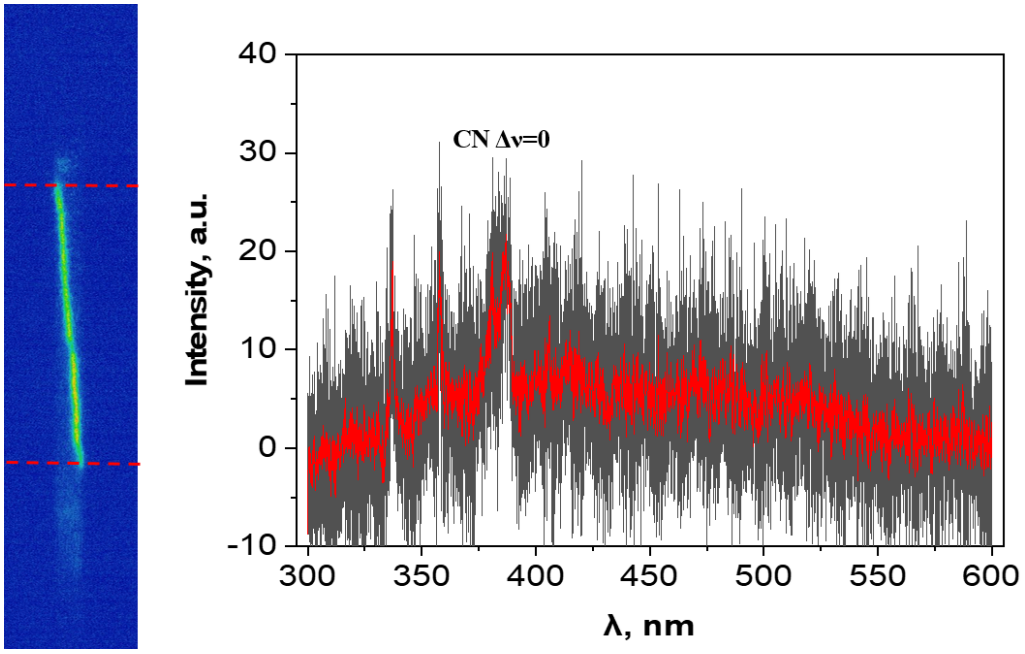

Figure 5.4: ICCD image from zero order of spectrometer at time $t = 10$ ns as well as spectrum of single discharge channel in the wavelength range of 300–600 nm. CN molecular emission of violet system ($B^2\Sigma^+ - X^2\Sigma^+$) of the sequence $\Delta v = 0$ is marked. Resolution of the optical system is 7.6 μm/px. Not corrected to the spectral sensitivity of the optical system.

system of nitrogen, CN molecular emission of violet system and the continuous wave *cw* spectrum. SPS of nitrogen is the sign of a streamer discharge. Three molecular bands of $C^3\Pi_u \rightarrow B^3\Pi_g, 0-0, 0-1$ and $0-2$ can be clearly seen from the spectrum.

Will note that CN molecular band of a violet system is present in the spectra of the filaments of the negative polarity discharge. This observation is true both for integrated over all the filaments spectra [96] and for the micro–image presented here. The admixtures of carbon are due to non–perfumer pumping and due to partial ablation of the surface of dielectric. Indeed, the earth atmosphere contains trace amounts of Ar and CO_2 (78.08% N_2 : 20.95% O_2 : 0.04% CO_2 : 0.93% Ar by mole), and the PVC (polyvinyl chloride) contains C–atoms, the chemical formula of PVC is $-[CH_2 - CHCl]_n-$.

Carbon atoms connect with nitrogen in the following reactions:

$$\begin{aligned} C + N + M &\rightarrow CN + M \\ C + N_2 &\rightarrow CN + N \end{aligned} \tag{5.2}$$

Presence of CN molecular emission of the violet system ($B^2\Sigma^+ - X^2\Sigma^+$) at 388 nm leads to conclusion that atomic nitrogen should be present in the filaments.

At $t = 16$ ns, the well–developed filament has been formed (see figure 5.5 on the

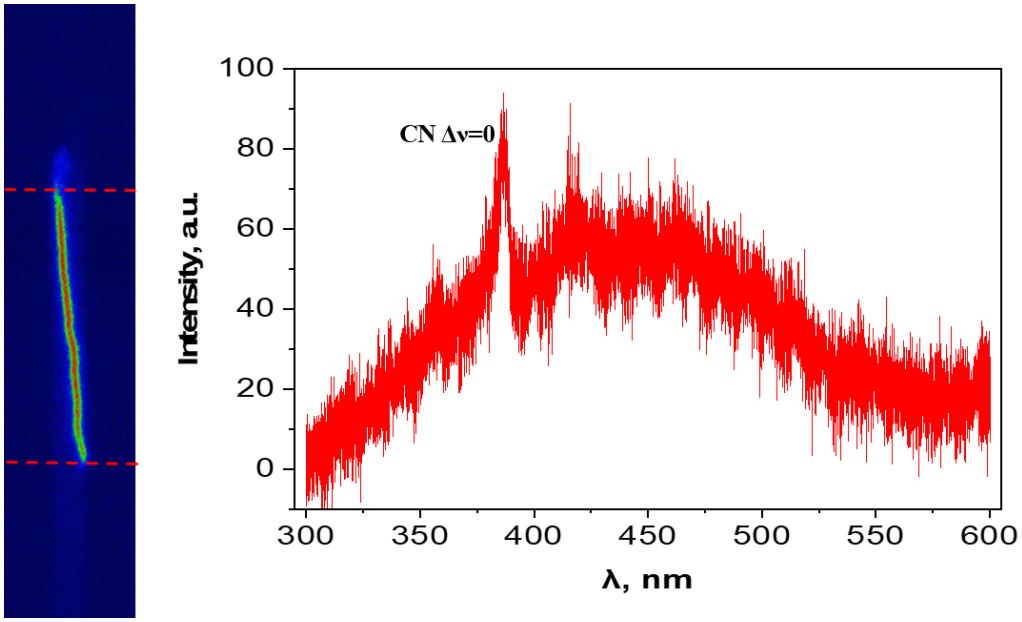

Figure 5.5: ICCD image from zero order of spectrometer at time $t = 16$ ns as well as spectrum of a single discharge channel in the wavelength range of 300–600 nm. CN molecular emission of violet system ($B^2\Sigma^+ - X^2\Sigma^+$) of the sequence $\Delta v = 0$ is marked. Resolution of the optical system is 7.6 μm/px. Not corrected to the spectral sensitivity of the optical system.

left). The filament has a constant diameter along the discharge channel. There is a thin bright core in the channel with higher intensity compared with surroundings. The spectrum on the right of the figure gives the information of CN molecular emission of violet system and the continuous wave *cw* spectrum. Compared with the spectrum at $t = 10$ ns, there is no second positive system of nitrogen any more at $t = 16$ ns. This can be due to two reasons: (a) sharp decrease of E/N and so, no enough energy to excite $N_2(C^3\Pi_u)$ state; (b) complete dissociation of N_2; and this can be a combination of considered cases (a) and (b).

Similar experiments were carried out at positive polarity 25 kV in 6 bar nitrogen (figures are presented in Appendix). Second positive system of nitrogen can be seen clearly at the streamer and transition moments. The tip of filament channel with less emission intensity also mainly contains SPS of N_2. In the well–developed filament channel, the continuous wave cw spectrum at positive polarity is not as obvious as spectrum at negative polarity, which is in correlation to the previous work in the our group [42]. The time and spatial resolved emission spectra at positive polarity are shown in appendix.

5.1.2 Electron temperature measurements using N^+ atomic lines

As far as optical emission from the filament contains cw spectra and atomic lines, it is logical to use the observed atomic lines emission to measure the electron temperature and electron density synchronised in time.

To understand the behavior of the electron temperature evolution in the filamentary discharge and in the near afterglow, the emission of atomic nitrogen ions N^+ in the wavelength range $\lambda = 400 - 800$ nm was analysed. The experiments were performed in the positive polarity discharge in nitrogen at the pressure of 6.75 bar at the pulse amplitude $U = 47$ kV on the high–voltage (HV) electrode. The data were taken with the ICCD camera gates equal to 5 ns. The raw spectrum were corrected to the spectral sensitivity of the system; the background corresponding to the continuum wavelength (cw) emission was subtracted.

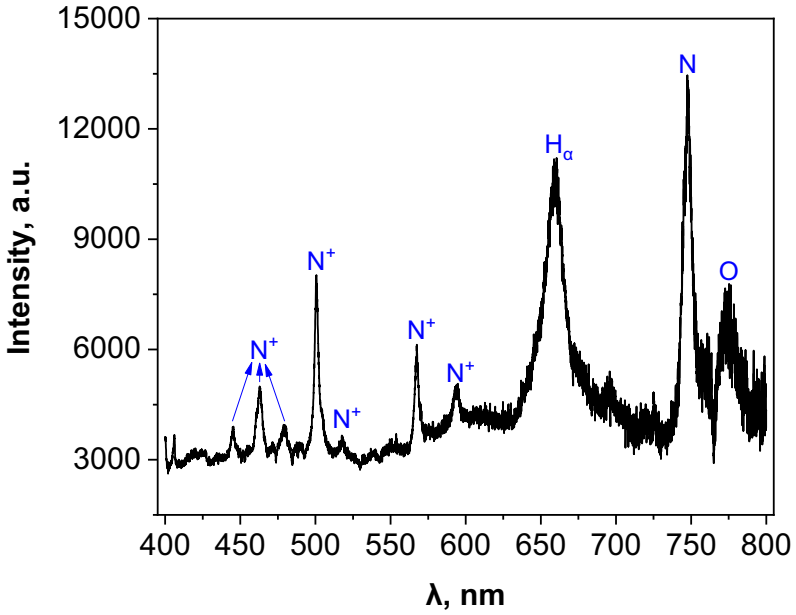

Figure 5.6: Emission spectrum of the positive polarity nanosecond dielectric barrier discharge in 6 bar nitrogen. Applied voltage $U = +47$ kV. The spectrum was corrected to the sensitivity function of the optical system.

The treated spectrum after subtracting the background is shown in figure 5.6. The N^+ as well as H_α, N and O atomic lines can be clearly identified from the plot. In addition, it can be found that the N^+ atomic lines for determining the electron temperature are mainly concentrated in the spectral range with wavelengths below 600 nm.

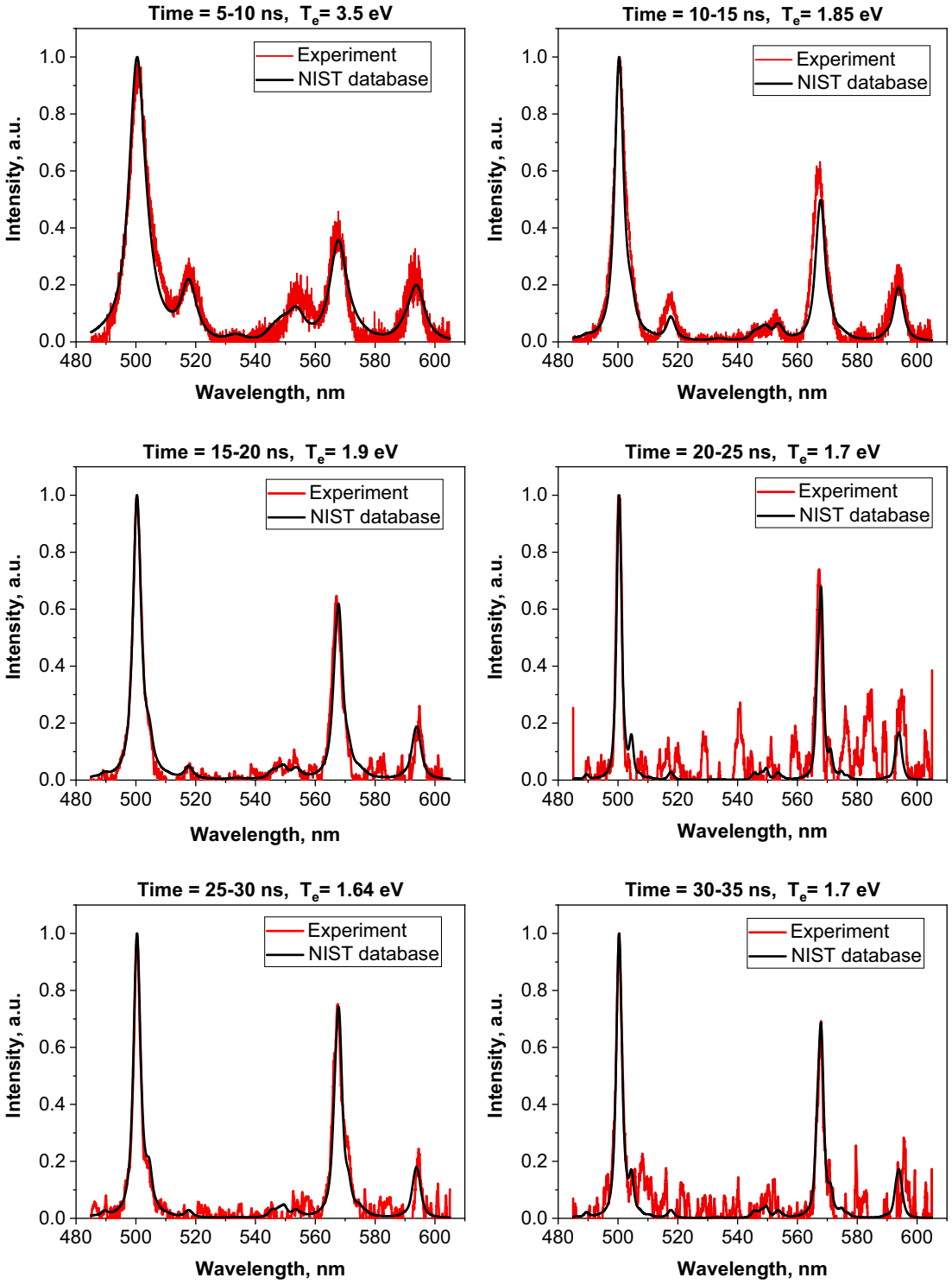

Figure 5.7: Emission spectra of N^+ lines from time= 5 ns to 35 ns. Camera gate is 5 ns. Nitrogen, positive polarity, $U = +47$ kV, $P = 6.75$ bar. The cw background is subtracted.

The spectra in the wavelength range $\lambda = 485 - 605$ nm were modelled by using NIST database [56] of atomic nitrogen ions N^+ with taking the electron temperature T_e as a parameter. A good correlation between the experimental spectra (red curves) and NIST modelling data (dark curves) can be seen clearly from figure 5.7.

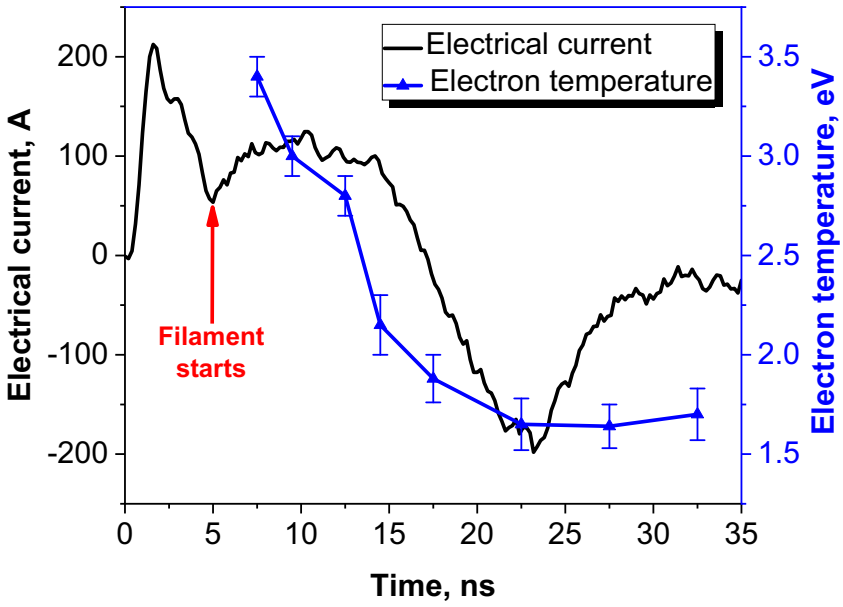

Figure 5.8: Synchronized electrical current and electron temperature measurements. Discharge in nitrogen at positive polarity of the high–voltage pulse, $U = +47$ kV.

Synchronized electrical current through the discharge and electron temperature are presented in figure 5.8. The accuracy of the synchronization, provided by the BCS technique, is 0.5 ns. Streamer–to–filament transition happens at $t \approx 7$ ns. The blue curve in figure 5.8 shows that the electron temperature in the beginning of the filamentary discharge is $T_e = 3 - 3.5$ eV, falling below 2 eV within 10 ns in the discharge. When the discharge is off, the electron temperature decreases to $T_e = 1.6 - 1.7$ eV and stays at this level at least first 10 ns of the afterglow.

5.1.3 Electron density measurements using hydrogen and nitrogen atomic line broadening

Electron density in the afterglow was determined on the basis of the Stark broadening effect of H_α line (656.3 nm) and nitrogen atomic line (746.8 nm) independently. Meanwhile, spectra broadening of other effects, especially Van der Waals broadening and instrumental broadening are also taken into consideration. The experiments were performed in the positive polarity discharge in nitrogen at the pressure of 6 bar

at the pulse amplitude $U = 45$ kV on the high–voltage (HV) electrode. The data were taken with the ICCD camera gate equal to 5 ns. The raw spectra were corrected to the spectral sensitivity of the optical system and the time–resolved corrected spectra in the afterglow are shown in figure 5.9. In this figure, it can be seen clearly that in the near afterglow ($t < 15$ ns) there still exist N^+ atomic lines while start from 15 ns in the afterglow, N^+ atomic lines disappear. But H_α line (656.3 nm) and nitrogen atomic line (746.8 nm) still present in the further afterglow. This is the reason why we can calculate the electron density in the further afterglow rather than the electron temperature.

For all atoms, FWHM of Stark effect can be written as follow [131]:

$$FWHM : \Delta\lambda_{Stark}\ (nm) = 2\omega_e(T_e)\cdot[1+1.75(1-6.7425\times10^{-2}n_e^{-\frac{1}{6}}T_e^{-\frac{1}{2}})\cdot\alpha_e(T_e)]10^{-16}n_e \tag{5.3}$$

where ω_e is electron impact parameter and α_e is the ion broadening parameter. Both of them are affected by electron temperature T_e that is assumed to be 20000 K (1.72 eV according to the experimental results, see figure 5.8). For nitrogen (746 nm), when T_e is equal to 20000 K, the ω_e and α_e are equal to 6.28×10^{-3} and 0.028 respectively [71].

For H_α Stark broadening, Gigosos *et al.* [132] suggested that when the electron density is over 5×10^{14} cm^{-3}, one can filter out the dependence of electron temperature T_e and gas temperature and T_g, if calculating electron density using full width half area (FWHA). However, this equation was mistyped in the original paper and Nikiforov *et al.* made the correction in [133]:

$$FWHA : \Delta\lambda_{Stark}\ (nm) = 1.098\ nm \cdot \left(\frac{n_e}{10^{17}\ cm^{-3}}\right)^{0.67965} \tag{5.4}$$

The width of Van der Waals broadening is calculated from following equation given by Van der Horst et al [48]. For H_α Van der Waals broadening:

$$\Delta\lambda_{VdWaals}\ (nm) = 0.10 \cdot \frac{p}{(T_g/300)^{0.7}} \tag{5.5}$$

For nitrogen (746 nm) Van der Waals broadening:

$$\Delta\lambda_{VdWaals}\ (nm) = 0.037 \cdot \frac{p}{(T_g/300)^{0.7}} \tag{5.6}$$

In our case, the pressure is 6 bar and the gas temperature T_g is assumed as 2000 K. Eventually, Van der Waals broadening for H_α and nitrogen (746 nm) are 0.25 nm and 0.09 nm respectively. In addition, instrumental broadening width

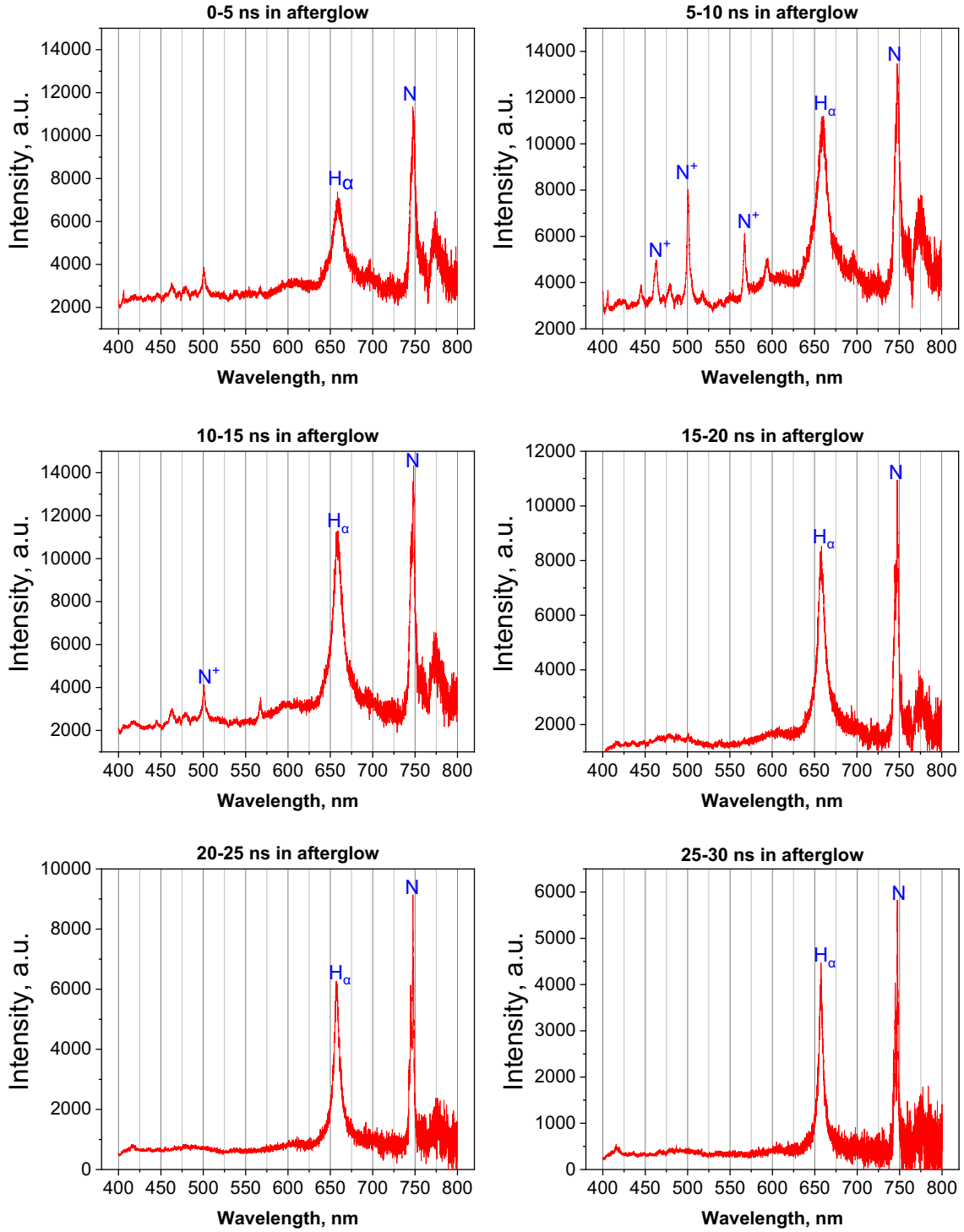

Figure 5.9: Emission spectra of H_α and N atomic lines from time= 0 ns to 30 ns in the afterglow. Camera gate is 5 ns. Nitrogen, positive polarity, $U = +45$ kV, $P = 6$ bar. The spectra are corrected to the spectral sensitivity of the optical system.

$\Delta\lambda_i$ was calculated from parameters of spectrometer (Princeton Instruments Acton-SP2500i) whose linear dispersion is 1.52 nm/mm. Combining with the width of entrance slit (0.2 mm), $\Delta\lambda_i$ can be determined as 0.3 nm.

As mentioned above, to determine n_e from Stark broadening of nitrogen (746 nm), it's necessary to subtract contribution of other effects from measured broadening width $\Delta\lambda_m$. According to equation (3.31), the width contributed only by Stark effect is

$$\Delta\lambda_{Stark} = \frac{(\Delta\lambda_m)^2 - (\Delta\lambda_i)^2}{\Delta\lambda_m} - \Delta\lambda_{VdWaals} \tag{5.7}$$

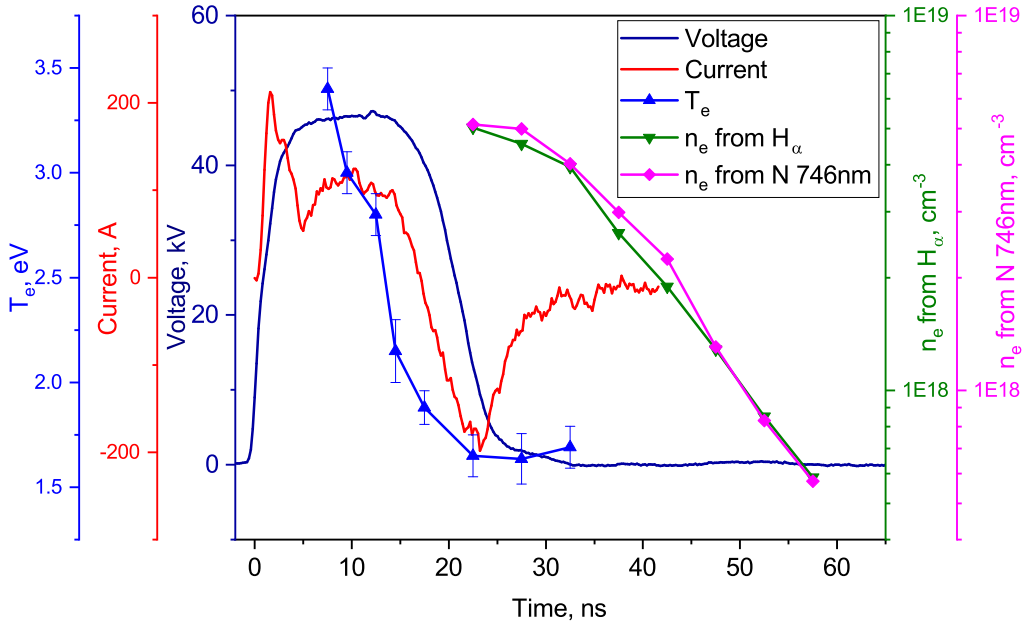

Figure 5.10: Synchronized electrical current and electron density measurements. Discharge in nitrogen at positive polarity of the high–voltage pulse, $U = +45$ kV.

The result of electron density n_e is shown in figure 5.10. And we can see the trend of electron density determined from both H_α (green curve) and atomic nitrogen (pink curve) agree well. It drops slowly in the near afterglow, starting from $n_e \approx 5 \times 10^{18}$ cm^{-3} and decreases to $n_e \approx 5 \times 10^{17}$ cm^{-3} after 40 ns in afterglow.

5.2 Particle Image Velocimetry (PIV) measurement

To study the hydrodynamic and thermal effects of filamentary nanosecond surface dielectric barrier discharge, particle image velocimetry (PIV) experiments were conducted. LaVision Flow Master PIV system was used for the measurements. The experiments were performed in the configurations shown in figure 5.11, two vertical laser sheets, 0.5 mm in thickness, were perpendicularly projected on the discharge surface. Laser frequency was equal to the discharge repetitive frequency of 7 Hz. The laser pulse was synchronized with discharge with a certain delay, the typical delay between the laser pulses (inter–frame delay) was varied from 0.2 to 100 μs depending of the stage of the flow evolution.

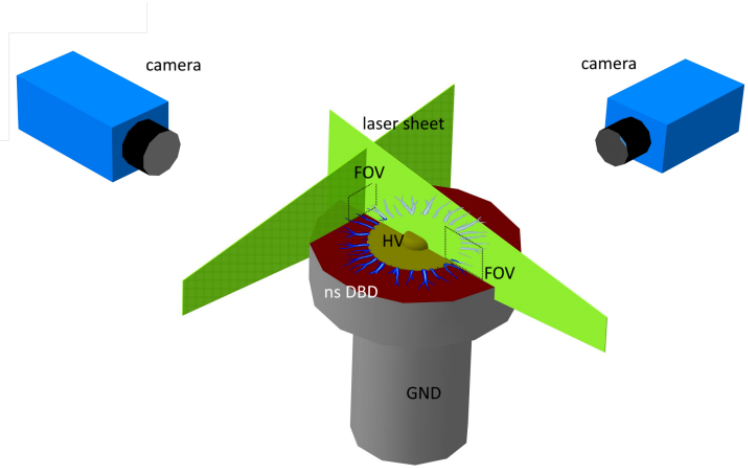

Figure 5.11: Optical assembly for PIV measurements.

The particle images were captured by a camera from Lavision (Imager sCMOS CLHS, 4Mpx, 16 bit) with the lens central line being normal to the laser sheet. Two flows were imaged in two normal planes: with laser sheet set in radial direction or being tangent to the circles concentric with the electrode. The typical linear size of the imaged region was $10 - 15$ mm and the resolution of the vector fields was 100 μm.

The mean velocity distribution was obtained as a result of averaging 70 instantaneous vector fields from the individual measurements. Three-dimensional vector fields were acquired by shifting the discharge cell in the direction normal to the laser sheet and by combining the data from the two views. Cross–correlation was calculated in 32×32 px windows with 50% overlap, consequent signal–to–noise and smoothing filters were applied.

5.2.1 Hydrodynamic perturbations analysis of the filamentary propagation

The disc electrode, 20 cm in diameter, was used as high–voltage electrode in the experiments. The electrode was placed in the high pressure chamber. At the beginning of each experiment, the chamber was seeded by oil mist. Flow seeding was performed by 1 μm oil droplets with a typical dynamic relaxation time 2 μs at 1 atm.

Figure 5.12 displays the typical ICCD images of filamentary discharge in 6 and 11 bar in air at both negative and positive polarities with the amplitude of 43 kV. It can be seen that the filaments at 11 bar have more branches than at 6 bar. The discharge propagates faster at lower pressure.

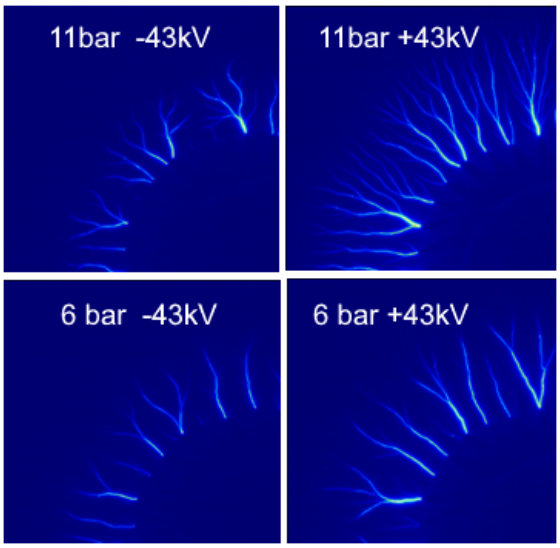

Figure 5.12: Typical ICCD images of filamentary discharge in air at both negative and positive polarities of the high–voltage pulse, $U = \pm 43$ kV.

Energy deposited in discharge channels leads to the formation of shock waves. The shock waves are clearly seen on the particle images as a result of laser light diffraction on the density gradient near the shock front (figure 5.13a). Analysis of the shock waves propagation velocity shows that it is rather weak and decays into an acoustic wave in 5 μs after the pulse. The cylindrical blast waves from the filaments slightly (within parts of mm) outstrip the plane shock from the streamer discharge. This is caused by higher energy release density in the constricted channels, and, consequently, higher wave velocity at first mm.

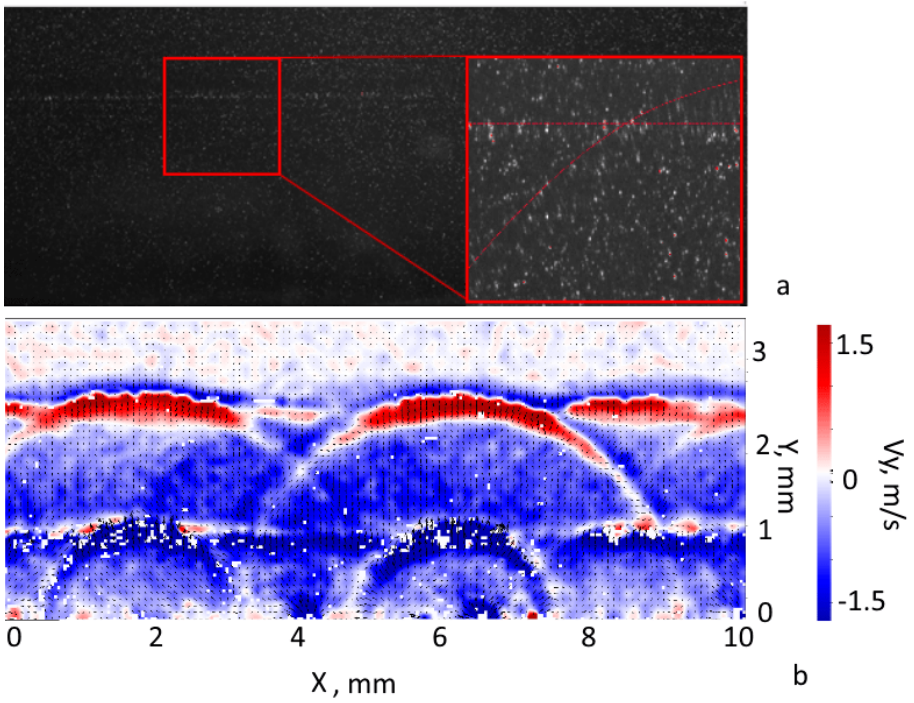

Figure 5.13: (a) Particles images near the discharge–induced shock waves; (b) Pressure waves visualization due to the aero–optical effect. Inter–frame delay is 20 μs.

5.2.2 Velocity measurement of the compression wave

The structure of the flow after the shock propagation stage was studied in a similar optical configuration. Long after the pulse, the density gradients are much lower than during the shock propagation stage, thus the aero–optical error is assumed to be insignificant at this stage. The flow structure induced after the streamer discharge is shown in figure 5.14. One can see that a single vortex is formed above the exposed electrode at a typical time 100 μs. The velocity magnitude in the vortex is $0.2-0.5$ m/s. In a circular electrode configuration, this corresponds to the formation of a toroidal vortex.

To analyse the flow induced by a constricted discharge, the electrode system was modified. The ground electrode was manufactured of a single, 2 mm wide strip of the metal foil to stabilize a position of the discharge channel (although some fluctuations in the filament geometry were still present). Constriction of the discharge leads to the formation of the three-dimensional flow structures with a typical scale of $1-2$ mm (figure 5.15). The perturbation are present along the whole length of the filament. A typical velocity magnitude in the given cross–section varies from pulse to pulse, but never exceeds the value of 0.5 m/s.

The flow was also viewed in the direction normal to the discharge propagation.

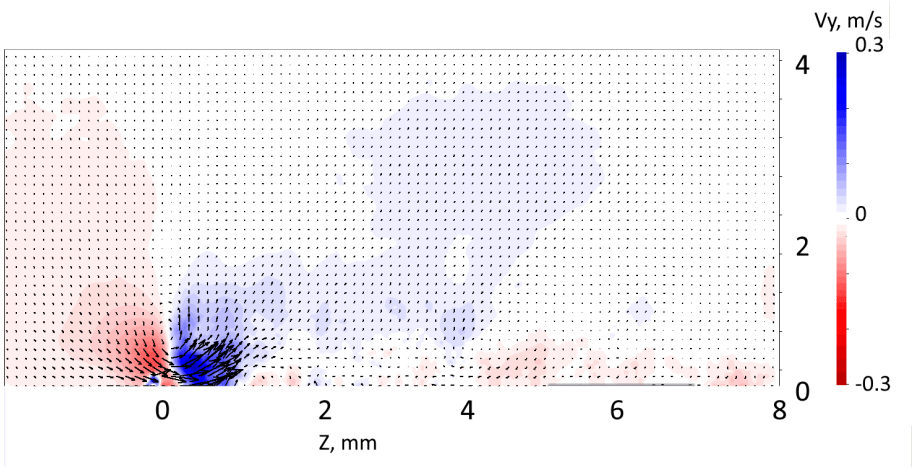

Figure 5.14: Flow velocity vector map in the plane along the discharge propagation direction (X–Y) (P = 11 bar) in the afterglow, t = 100 μs. Discharge in air at positive polarity of the high–voltage pulse, U = +43 kV.

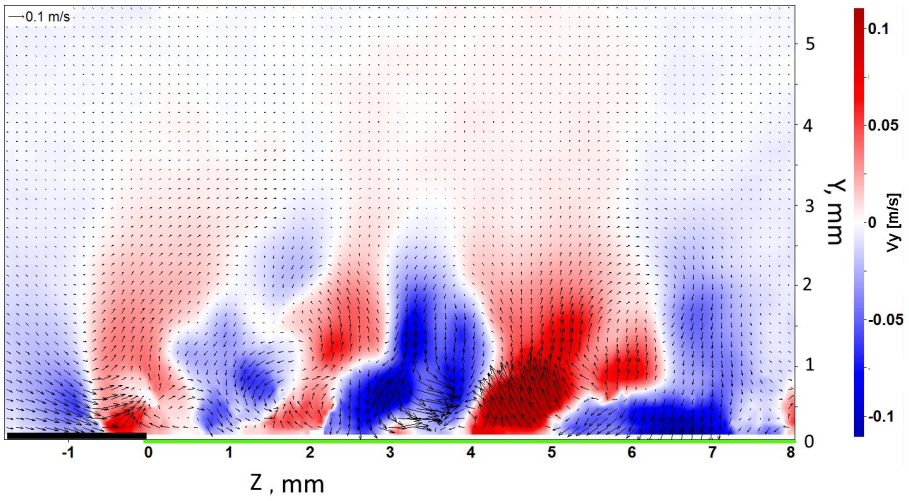

Figure 5.15: Flow velocity vector map in the plane along the discharge propagation direction (X–Y) (P = 11 bar) in the late afterglow, t = 3000 μs. Discharge in air at positive polarity of the high–voltage pulse, U = +43 kV.

From figure 5.16, One can also see a well–recognizable turbulent structures in the vicinity of the filamentary discharges. A typical scale of the vortices is within 1-2 mm, the instantaneous velocity magnitude can be as high as 0.5 m/s. It was found that at an equal voltage magnitude the turbulence intensity drops when the gas pressure increases.

The general structure of the flow around a single filament was extracted from the flow field, averaged over 20 separate measurements with a fixed delay from the voltage pulse. The various cross–sections of the averaged flow are shown in

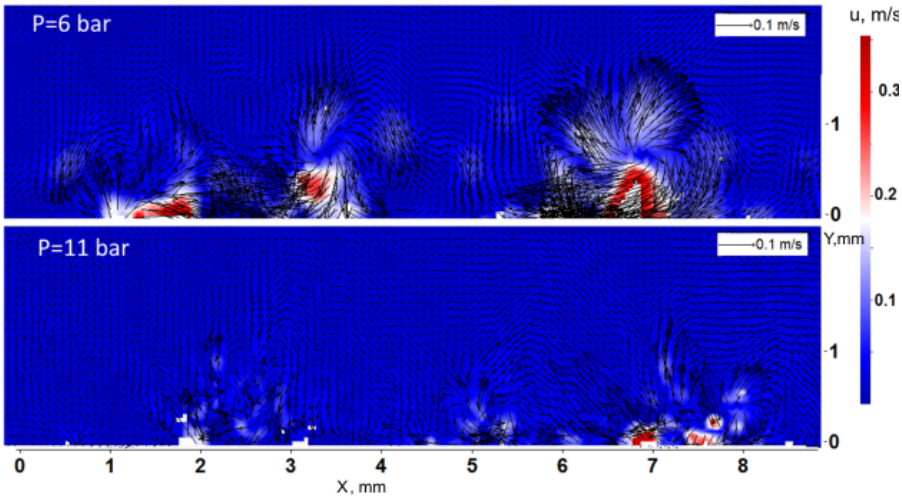

Figure 5.16: Flow velocity vector map in the plane normal to the discharge propagation direction ($P = 6$ and 11 bar) in the late afterglow, $t = 3000$ μs. Discharge in air at positive polarity of the high–voltage pulse, $U = +43$ kV.

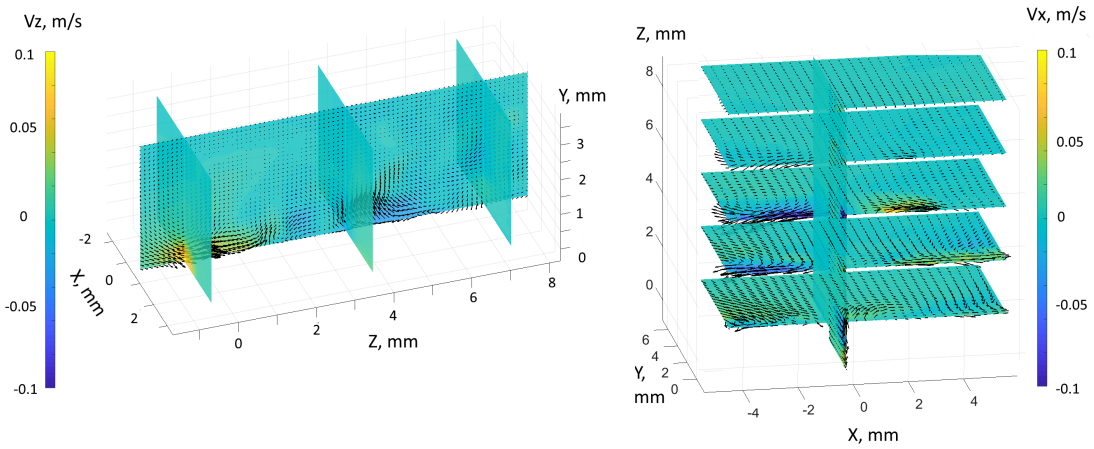

Figure 5.17: Averaged flow–fields induced by a single filament in nSDBD delay 400 μs. ($P = 11$ bar). Discharge in air at positive polarity of the high–voltage pulse, $U = +43$ kV.

figure 5.17. The main large–scale structures observed are the jets near the channel ends, and the pair of vortices with the axes aligned with the filament. Typical velocities of the averaged flow are $0.1 - 0.2$ m/s.

It can be seen that the averaged flow images does not include the turbulent structures that are clearly seen in the immediate filament vicinity in instantaneous snapshots. This can obviously be attributed to the variability of the filament shape from pulse to pulse, leading to the randomization of the flow velocity in this region. It was observed that pulse voltage polarity does not influence the averaged flow

structure; still, the intensity of the instantaneous turbulence is somehow higher for the positive pulse. The latter fact can be related to the more "winding" shape of the filament at the positive polarity of the pulse.

5.3 Mechanism of obtaining high n_e and T_g in the filaments

Theoretical consideration, described below, explaining how to get electron temperatures of the order of $n_e \sim 10^{19}$ cm^{-3} and gas temperatures T_g about 15 kK in high pressure nitrogen–containing molecular gas. To get a solid ground for theoretical explanations, a specific deposited energy in the filaments is measured experimentally.

5.3.1 Propagation of filamentary discharge in air at both polarities

To analyse the specific deposited energy, namely the deposited energy per molecule, it is necessary to estimate a total volume of the filaments. So-called $x-t$ diagrams were used to quantify the propagation of the filaments. To build $x-t$ diagrams, the length of the filaments was analysed statistically and the length of propagation x at the time instant t was put on the plot.

Figure 5.18 (a) presents the filamentary discharge propagation length at a constant voltage ($U = -40$ kV) at three different pressures (5, 8 and 11 bar) as well as the shape of the voltage pulse coming to the electrode. It can be seen that the velocity of the filaments at constant voltage propagation is slightly higher at lower pressure condition. Different values of the first x points for $P = 5$, 8 and 11 bar demonstrate that before the transition, streamers cover a longer distance in the case of lower pressure. The velocity of the filament propagation before slowing down is about 0.4 mm/ns. On the trailing edge of the voltage pulse, at $t > 15$ ns, the velocity of the filaments decreases. To some extent, it is possible to increase the length of the filaments by increasing the duration of the pulse. A typical length of filaments propagation, comprising $5-10$ mm at pressures up to ten bars, is an interesting issue for plasma–assisted combustion: it was mentioned in [122] that the filamentary regime, providing a regular grid of tens of plasma channels with high temperature and high density of O–atoms, results in efficient and stable ignition of combustible mixtures. Longer filaments will result in larger region of ignition.

When the pressure is fixed and the voltage amplitude is changed (see figure 5.18 (b)), the velocity of filaments changes significantly: increase of the voltage amplitude from

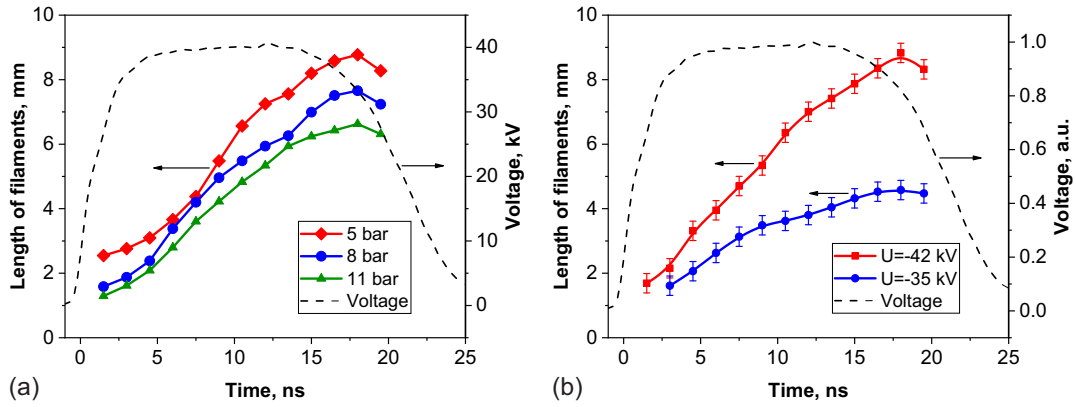

Figure 5.18: x-t diagrams of propagation of filaments for discharge in air at negative polarity: (a) for different pressures; the applied voltage amplitude is $U = -40$ kV; (b) for different voltages; the pressure is $P = 8$ bar.

$U = -35$ kV to $U = -42$ kV leads to acceleration of the filaments from 0.3 mm/ns to 0.5 mm/ns. The regime with pronounced difference in the velocity of filaments, constant pressure $P = 8$ bar and the voltage amplitude changing between $U = -33$ kV and $U = -43$ kV was selected to study the specific deposited energy.

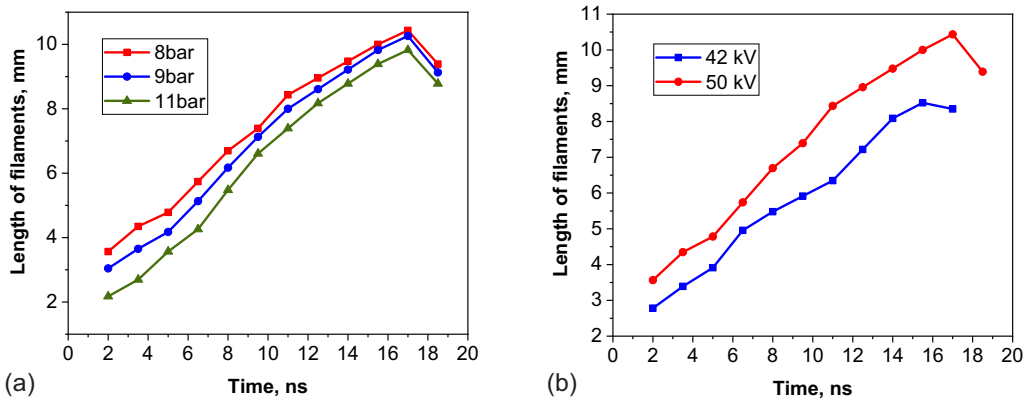

Figure 5.19: x-t diagrams of propagation of filaments for discharge in air at negative polarity: (a) for different pressures; the applied voltage amplitude is $U = +50$ kV; (b) for different voltages; the pressure is $P = 8$ bar.

The same experiments were done at positive polarity and the $x - t$ diagrams at positive polarity are shown in figure 5.19. The velocity of the filaments at constant voltage practically does not depend upon pressure, similar to negative polarity. Different values of the first x points for $P = 8$, 9 and 11 bar demonstrate that before the transition, streamers cover a longer distance in the case of lower pressure.

Being moved at the same initial point, the $x-t$ diagrams for different pressures will follow almost the same way; the velocity of the filament propagation before slowing down is about 0.4 mm/ns.

When the pressure is fixed and the voltage amplitude is changed (see figure 5.19 (b)), the velocity of filaments is not constant any more: increase of the voltage amplitude from $U = +42$ kV to $U = +50$ kV leads to acceleration of the filaments from 0.4 mm/ns to 0.6 mm/ns. The regime with pronounced difference in the velocity of filaments, constant pressure $P = 8$ bar and the voltage amplitude changing between $U = +42$ kV and $U = +52$ kV was selected to study the specific deposited energy.

It can be concluded from the analysis above that for both negative and positive polarities, the amplitude of applied voltage has greater impact on filaments propagation velocity than the pressure has. The pressure condition affects more the propagation velocity of streamers than of the filaments.

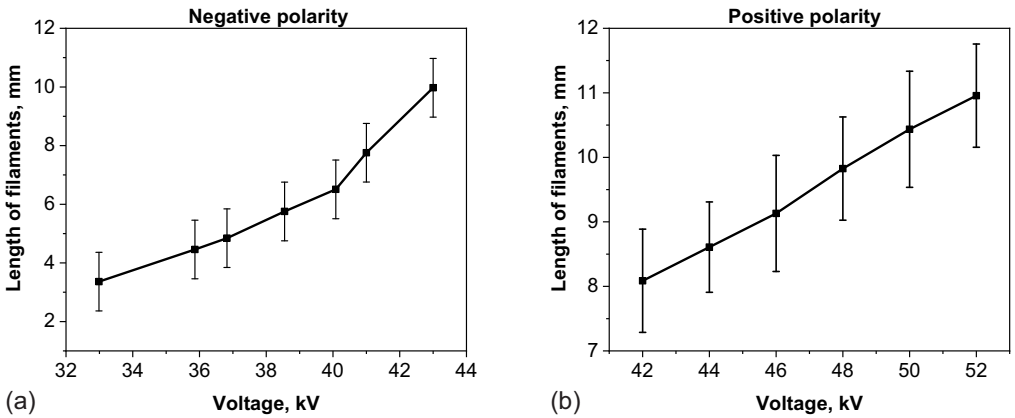

Figure 5.20: A maximum length of the filaments propagation as a function of the voltage amplitude at (a) negative polarity and (b) positive polarity of the pulse. Air, $P = 8$ bar.

The maximum length of the filaments propagation at different voltage amplitudes at both negative and positive polarities are presented in figure 5.20. For negative polarity, when the amplitude of applied voltage increases from $U = -33$ kV to $U = -43$ kV, the maximum length of filaments propagation changes significantly, from 2.7 mm to 10 mm. At positive polarity, the length of propagation of filaments increases from 8.1 mm at $U = +42$ kV to 11 mm at $U = +52$ kV.

5.3.2 Energy deposition in the filaments

Figure 5.21 presents the total deposited energy measured from the waveforms obtained by the back current shunt (BCS) as described in chapter 3. For both

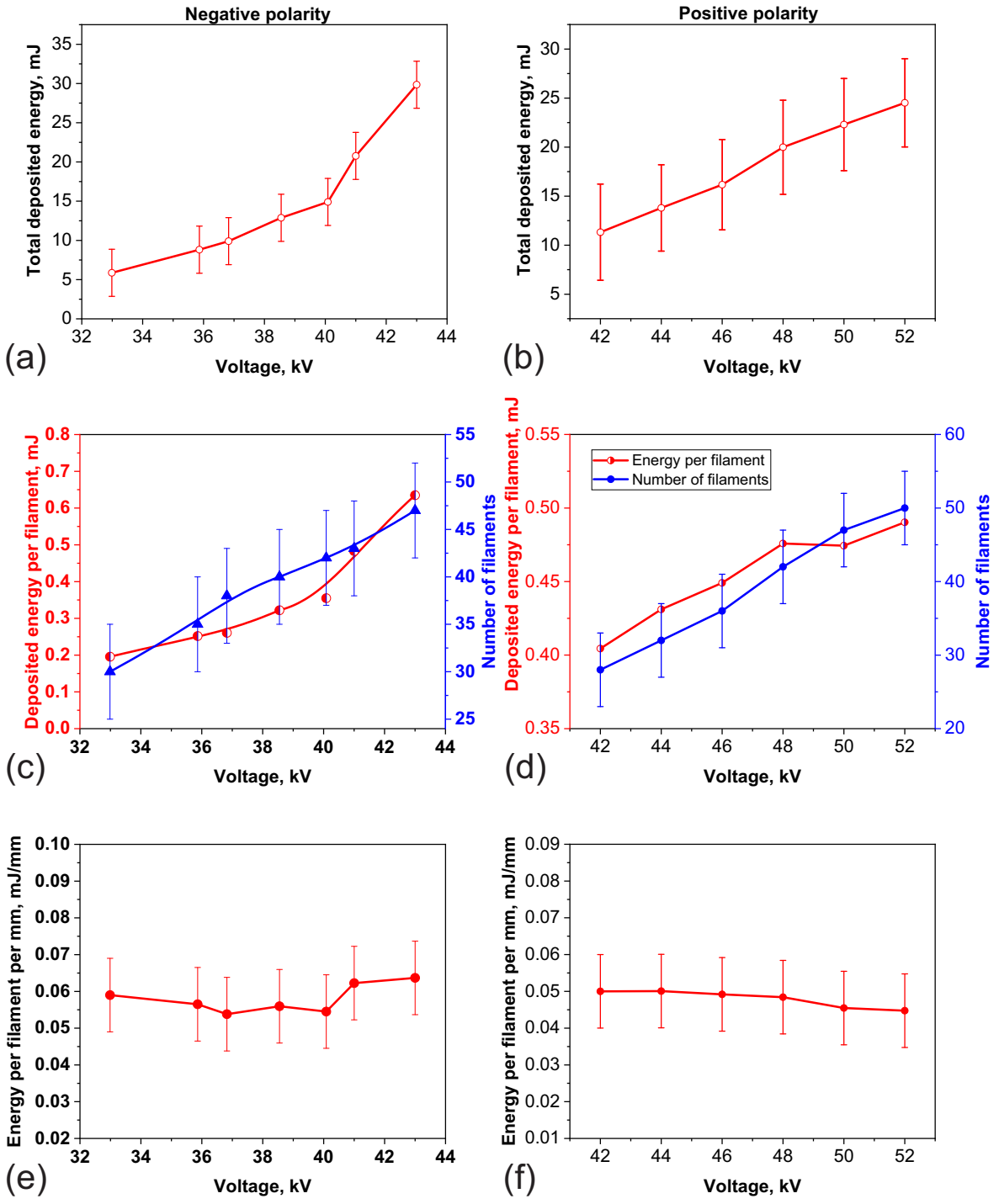

Figure 5.21: Total deposited energy (a) and (b); number of filaments and the deposited energy per filament (c) and (d); the energy per filament per mm (e) and (f) as a function of the voltage amplitude. Left column (a)(c)(e) negative polarity; right column (b)(d)(f) positive polarity of the pulse, air, $P = 8$ bar.

polarities, the total deposited energy increases with voltage, from 6 mJ at $U = -33$ kV to almost 30 mJ at $U = -43$ kV and from 12 mJ at $U = +42$ kV to 24 mJ at $U = +52$ kV (figure 5.21 (a) and (b)). One more parameter to be taken into account to calculate the specific deposited energy is the number of filaments increasing from 30 at $U = -33$ kV to 47 at $U = -43$ kV and from 28 at $U = +42$ kV to 50 at $U = +52$ kV (figure 5.21 (c) and (d)).

Assuming that the energy is equally distributed between the filaments, one can obtain that the energy changes at negative polarity from 0.20 to 0.64 mJ per filament with voltage changing from $U = -33$ to -43 kV and at positive polarity 0.41 to 0.49 mJ per filament with voltage changing from $U = +42$ to $+52$ kV. Finally, assuming that the energy is distributed uniformly along the filament, and dividing the energy per filament by the filament length, will get the plot presented in figure 5.21 (e) and (f). It is clearly seen that in spite of strong dependence of parameters on voltage, the energy per unit length is almost constant for all voltage amplitudes under study at both negative and positive polarities.

To calculate the specific deposited energy, it is necessary to know the cross section of the filament. The diameter of the filament can be estimated from the filtered ICCD macro–images presented in [41]. It reports that the filament captured with no filter can be represented as a thin bright core along the axis of the filament; the core is surrounded by a less bright shell. The diameter of the core calculated as the full width at half maximum (FWHM) of the emission at 480 ± 5 nm is equal to 18 ± 2 μm while the diameter of the entire structure is around $200 - 300$ μm. The bright core is a region where from the *cw* radiation is observed [42, 96].

In assumption that almost all the delivered energy is spent in the core of the filament, 18 ± 2 μm diameter, will estimate the energy per molecule at taking the number of molecules to be equal to the number of molecules at $P = 8$ bar and $T = 300$ K. For the energy per unit length ~ 0.06 mJ/mm as obtained for the conditions of the present work figure 5.21 (e) and (f), will obtain the specific delivered energy $\omega_- \approx 7.4$ eV/particle for negative polarity and $\omega_+ \approx 6.4$ eV/particle for positive polarity.

5.3.3 Analysis of plasma properties in the filaments

As talked above (see figure 5.10), high values of electron density, $n_e = 10^{18} - 10^{19}$ cm^{-3} exist during at least $5 - 10$ ns in the afterglow. Based on this data, let us estimate the heat release in the reactions of electron–ion recombination. The main ions responsible for recombination at sub–nanosecond times scale are molecular ions N_2^+ and O_2^+. Until the fraction of the molecules in the gas is low enough, recombination happens mainly in the following reactions:

$$e + O_2^+ \rightarrow O\left(^3P\right) + O\left(^1D\right) \tag{5.8}$$

$$e + N_2^+ \rightarrow N\left(^4\,S\right) + N\left(^2D\right) \tag{5.9}$$

The recombination is fast, a typical time of the processes 5.8 and 5.9 at $n_e = 2\times10^{18}$ cm^{-3} is $\tau_{rec} \approx 0.4$ ns. Each elementary process results in severe heat release: 5 eV in the reaction (5.8) and 2.25 eV in the reaction (5.9) respectively [134]; and the additional heat will be produced due to the quenching of excited O(^{1}D) and N(^{2}D) atoms. Only due to the heat release in the reactions (5.8) and (5.9) the gas temperature during 1 ns increases up to $15-20$ kK. Increase of gas temperature ΔT_g at constant electron density n_e can be estimated as

$$\Delta T_g = (\gamma - 1)\cdot(n_e^2\beta)\cdot 5eV\cdot\tau/N \tag{5.10}$$

where $\gamma = 1.3$ is a specific heat ratio [135], $\beta = 3\times10^{-8}$ cm^3/s is a recombination coefficient, τ is time interval and N is a gas number density. Indeed, at $P = 6$ bar and $\tau = 1$ ns will obtain that the heat release in recombination is equal to $\Delta T_g = 14-22$ kK for $n_e = (2-2.5)\times10^{18}$ cm^{-3}. Thus the consequence of a fast recombination at high electron density, on the level of $n_e \geq 2\times10^{18}$ cm^{-3}, is increase of gas temperature and approaching of plasma to the local thermodynamic equilibrium (LTE), with the gas temperature T_g close to the electron temperature T_e.

The electron-ion collision frequency ν_{ei} increases with the electron density [136]:

$$\nu_{ei} = \frac{n_e\cdot e^4\cdot ln\Lambda}{18\sqrt{2}\pi\cdot\varepsilon_0^2\cdot\sqrt{m_e}\cdot(T_e)^{3/2}}, \tag{5.11}$$

Here $ln\Lambda$ is the Coulomb logarithm, m_e and e are the mass and the charge of the electron respectively, ε_0 is the dielectric constant.

At the conditions that plasma is strongly ionized and the electron-ion collisions dominate, the conductivity σ_{ei} is calculated as

$$\sigma_{ei} = \frac{n_e\cdot e^2}{m_e\cdot\nu_{ei}}. \tag{5.12}$$

For a typical electron density $n_e = 3\cdot10^{18}$ cm^{-3} and electron temperature $T_e = 3$ eV, the value of the Coulomb logarithm is $ln\Lambda = 5.05$, and so the conductivity $\sigma_{ei} \approx 180\ \Omega^{-1}\cdot$cm^{-1} [136]. In this case, for the electric current density $j_f \leq 3\cdot10^5$ A/cm^2, the electric field in the filaments does not exceed $E_f = 1700$ V/cm. Such a low field in the constricted channels is one of the main reasons for the sharp decrease in the emission intensity of the second positive system of molecule nitrogen, which has been discussed in chapter 4. It should be noted that as far as the field in the

filaments is low, their propagation length is defined by the duration of the pulse (see figure 5.10), and so, using longer pulses, it is possible to obtain longer filament length.

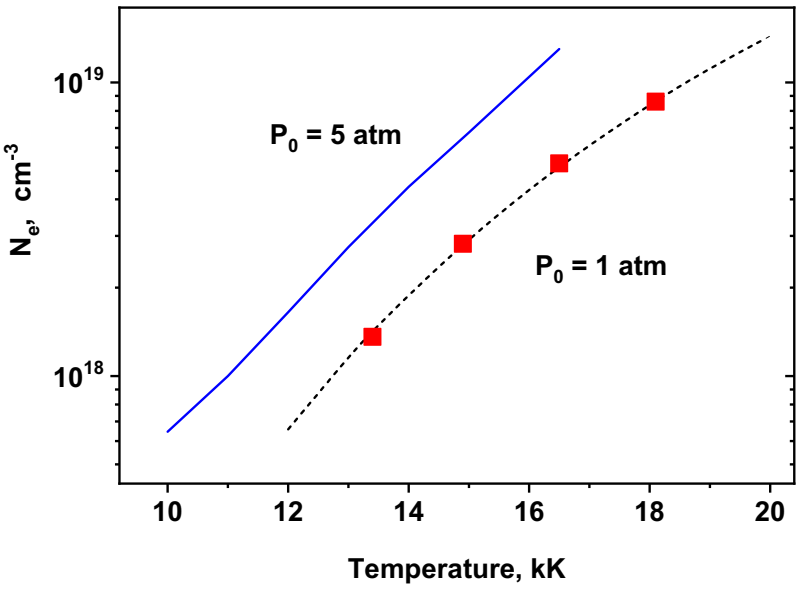

Figure 5.22: Calculated electron density as a function of gas temperature [41] for $P = 1$ bar at the initial gas number density $N_0 = 2.5 \times 10^{19}$ cm^{-3}, and for $P = 5$ bar at the initial gas number density $N_0 = 1.2 \times 10^{20}$ cm^{-3}. Symbols are the experimental data from [137].

The equilibrium electron density calculated as a function of gas temperature is presented in figure 5.22 for two cases: pressure $P = 1$ bar and initial gas number density $N_0 = 2.5 \times 10^{19}$ cm^{-3}; pressure $P = 5$ bar and initial gas number density $N_0 = 1.2 \times 10^{20}$ cm^{-3}. The calculations were carried out by Dr. Nicolay Popov using the model [138] in isochoric approximation. The approximation is valid because the time of filamentation, a few nanoseconds, is much shorter than a typical hydrodynamic time; the gas expansion does not occur and the particle density remains approximately constant, increasing only due to the dissociation of mixture molecules. It follows from the figure that at $P = 5$ bar, the equilibrium electron density $n_e = (2 - 3) \times 10^{18}$ cm^{-3} is reached at a gas temperature equal to $T_g = 13 \pm 0.6$ kK.

Decay of the electron density from $n_e = 5 \times 10^{18}$ cm^{-3} to $n_e = 6 \times 10^{17}$ cm^{-3} during a few tens of nanoseconds at $P = 5$ bar can be explained by gas cooling from $T_g = 14$ kK to $T_g = 10$ kK. Estimates of gas cooling via thermal conductivity using a coefficient of heat conductivity taken from [136] result in typical time tens of nanoseconds at a typical radius of channel equal to 10 μm. It should be noted

that the cooling associated with the gas–dynamic expansion of the channel was not taken into account in the estimates.

Let us consider the processes that allow obtaining the high values of electron density, reached experimentally, $n_e > 10^{18}$ cm^{-3} at $P = 5 - 6$ atm during a sub-nanosecond time. Figure 5.23 presents calculated kinetic curves of the main components and the evolution of the gas temperature in molecular nitrogen at initial pressure $P_0 = 6$ bar, for the initial gas temperature $T_0 = 300$ K and initial reduced electric field $(E/N)_0 = 230$ Td, which corresponds to the measured electron temperature in the discharge, $T_e = 3 - 3.5$ eV. The initial electron density was taken to be 10^{15} cm^{-3} corresponding to electron density in streamers at $P \approx 6$ bar [40]. The calculations were carried out in isochoric approximation; rates of ionization and excitation of nitrogen atoms and molecules by electron impact were calculated using BOLSIG+ software [139]. The self-consistent sets of the cross-sections for elastic and inelastic electron collisions were taken from [140, 141] for N_2 molecules and from [142] for nitrogen atoms. The cross–sections of ionization and dissociation of $N_2(A^3\Sigma_u^+, B^3\Pi_g, C^3\Pi_u)$ molecules by electron impact, as well as cross-sections of the transitions between these states were taken from [143].

At short time period, $t < 0.15$ ns, the density of electronically excited nitrogen molecules, $N_2(B^3\Pi_g, C^3\Pi_u)$ increases proportionally to the density of electrons. At $n_e > 3 \times 10^{16}$ cm^{-3}, quenching of electronically excited $N_2(A^3\Sigma_u^+, B^3\Pi_g, C^3\Pi_u)$ states by electrons dominates above quenching by nitrogen molecules. A significant part of dissociation at these conditions goes *via* dissociation of electronically excited states by electron impact:

$$e + N_2\left(A^3\Sigma_u^+, B^3\Pi_g, C^3\Pi_u\right) \rightarrow e + N\left(^4S\right) + N\left(^2D\right) \tag{5.13}$$

Similar, ionization of electronically excited states by electron impact is important under the present conditions:

$$e + N_2\left(B^3\Pi_g, C^3\Pi_u\right) \rightarrow 2e + N_2^+\left(X^2\Sigma_g^+, A^2\Pi_u\right) \tag{5.14}$$

At $E/N = 230$ Td, ionization from excited states is equal to ionization from the ground state starting from $[N_2(B^3\Pi_g, C^3\Pi_u)]/[N_2] \geq 10^{-3}$. As a result, already at $t > 0.15$ ns, the main ionization takes place from the electronically excited levels. To underline the role of ionization from the excited states at high electric field and high deposited energy, the dashed curve in figure 5.23 presents the electron density calculated without the reaction (5.14). It is clearly seen that the electron density calculated with the stepwise ionization (5.14) at $t = 0.35$ ns is about 15 times higher than the electron density obtained *via* ionization from the ground state only.

Gas temperature presented in figure 5.23 increases dramatically at sub–nanosecond

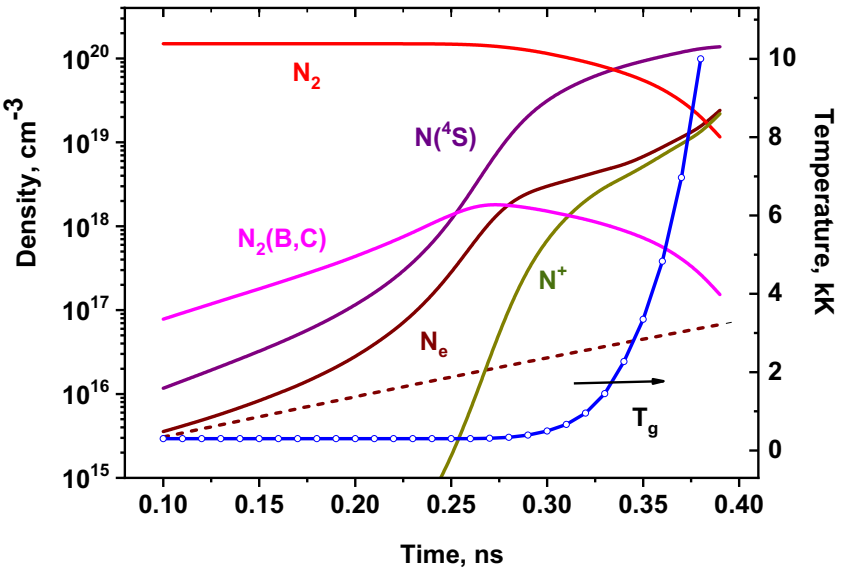

Figure 5.23: Calculated kinetic curves of main species and gas temperature in discharge in nitrogen at $P = 6$ bar, $T_0 = 300$ K, $(E/N)_0 = 230$ Td and $(n_e)_0 = 10^{15}$ cm^{-3} [41].

time scale. The temperature was calculated under the assumption that the difference between the specific delivered energy at the given time instant, $\omega(t)$, and the specific energies spent for dissociation, ω_{diss}, ionization, ω_{ion} and electronic excitation of atoms and molecules, ω_{exc}, $\Delta\omega = \omega - \omega_{diss} - \omega_{ion} - \omega_{exc}$, instantaneously transforms into the heat. Necessary thermodynamic functions were taken from [135].

The ratio of the frequency of electron–ion collisions to the frequency of electron–neutral collisions, ν_{ei}/ν_{en}, increases with the ionization degree, $n_e/[\mathrm{N_2}]$. As a result, the electron temperature, and the rates of gas ionization and excitation decrease. At $t > 0.28$ ns the rates of increase of electron density and of nitrogen atoms density slow down. The electron density at $t = 0.33$ ns is equal to $n_e = 5.3 \times 10^{18}$ cm^{-3}, the density of nitrogen atoms is equal to $[\mathrm{N}(^4\mathrm{S})] \approx 7 \times 10^{19}$ cm^{-3}, and the gas temperature is equal to $T_g \approx 12 - 14$ kK. At this time instant, the specific delivered energy is equal to $\omega \approx 8.8$ eV/molecule. Later in time, the system will approach to the equilibrium state at corresponding gas temperature.

To summarize, the high electron density in the beginning of the filamentation, appearing in reactions of ionization from electronically excited states, leads to significant increase in electric current density. Increase of the density of the electric current, leads to increase in the specific delivered energy and severe heat release on the time scale of parts of nanoseconds. Approaching to the state close to the LTE explains the anomalously slow plasma decay, tens of nanoseconds, observed experi-

mentally: the decay of electron density follows the dynamics of the gas cooling.

It should be noted that in [144], it is assumed that the discharge constriction is the result of magnetic compression of plasma channel. The magnetic pressure P_m is a function of the discharge current I and of the filament radius R_f:

$$P_m = \frac{10^{-7} \cdot \mu I^2}{16\pi^2 R_f^2}. \tag{5.15}$$

Will demand that the magnetic pressure P_m is equal to the gas pressure P_g inside the filament. In assumption that at $P_0 = 6$ atm the gas temperature will reach the value of 15 kK during parts of nanosecond (see figure 5.23), the gas pressure in the channel on this stage is equal to 300 atm. At discharge current 1 A per filament, the magnetic pressure P_m will be equal to gas pressure P_g for the radius of filaments as small as $R_f < 0.015$ μm. Thus, the magnetic compression is not important under conditions of the nanosecond surface discharge considered in the present work.

To answer the question of initiation of the filament, the near–electrode processes should be considered, for example development of the field emission instability of the cathode layer [145]. At high pressures, this instability should be efficient because of high value of the electric field near the cathode, which leads to significant decrease of the cathode work function [136] and increase of the secondary electron emission current.

5.3.4 Near–electrode process

Recent numerical calculations of a cathode layer in a pulsed nanosecond discharge in helium at high pressure [146] demonstrated a possibility of a high electron density generation near the cathode. The calculations were carried out using 1D self–consistent Particle–in–Cell Monte Carlo collisions model. High densities of electrons, $n_e > 10^{18}$ cm^{-3}, were obtained as a result of secondary electron emission from the cathode surface. The account of field emission resulted in shorter time of formation of the cathode layer. Under the conditions of [146], the electron density reached a maximum value n_e^{max} at $t < 2$ ns, and the current density of the field emission was as high as $j_{fe} > 10^8$ A/cm^2.

In [147] the initial stage of nanosecond discharge at atmospheric pressure was studied with extra-high spatial ($3 - 4$ μm) and temporal (70 ps) resolution. The authors demonstrated that nanosecond breakdown initiated by 4 ns rise time 25 kV amplitude voltage pulse in 3 mm pin–to–plane gap starts from a dense spot of electrons near the cathode, with a density $n_e^0 > 10^{20}$ cm^{-3} and a typical size of ~ 10 μm. The authors [147] remark that the nature of the observed electron cloud is still under discussion.

In nanosecond surface dielectric barrier discharges, for both polarities of the high-voltage electrode the filaments start from the edge of the HV electrode and propagate to the bulk of the streamer plasma. In the case of the cathode a reason of formation of the high electron density near the electrode can be a field emission instability, similar to the case described in [146]. A question about the instability of the anode layer and possible formation of anode spots in high pressure SDBD remains open. We assume that the region with a high electron density is formed near the HV electrode. The potential on the front of this region is significantly higher than the potential of the streamer plasma at this point. The sharp gradient of electrical potential near the electrode initiates so-called fast ionization waves (FIW) or the waves of a gradient of the electrical potential [148]. As a result, the surface streamers formed at the head of filaments [96] additionally charge the surface of the dielectric.

It should be noted that in nSDBDs, unlike to pin–to–pin electrode systems, the density of the electrical current increases not only because of contraction: the additional increase is connected to decrease of the number of plasma channels at the moment of the streamer–to–filament transition. In abnormal mode of the discharge, increase of the current density in the micro–channels near the cathode results in rise of the electric field near the cathode, E_c. High electric fields E_c lead to increase of the current density due to the field emission and to development the instability of cathode layer.

It is observed experimentally that in nanosecond surface dielectric barrier discharge, the filaments formed near the high-voltage electrode propagate to the periphery of the discharge with a typical velocity of a parts of millimeters per nanosecond, and the velocity is almost independent of the length of the filament. According to [148], so high propagation velocities are typical for the fast ionization waves. Will estimate a possible speed of FIW under the considered conditions. A necessary condition for the existence of FIW is that the formation of the next element of plasma channel behind the front of the ionization wave is faster than the polarization of plasma before the front of FIW:

$$\tau_{FIW} = R_f / V_{FIW} << \tau_{pol}, \tag{5.16}$$

here R_f is a characteristic filament radius, V_{FIW} is the velocity of the filament. Otherwise, a rapid broadening of the front of ionization wave will be observed.

The polarization time τ_{pol} of a plasma channel of length L and radius R is [136]

$$\tau_{pol} = \frac{1}{4\pi\sigma} \cdot \left(\frac{L}{2R}\right) / ln\left(\frac{L}{R}\right), \tag{5.17}$$

where σ is the conductivity of the channel. Under the domination of electron-neutral

collisions over electron-ion collisions, $\sigma \sim n_e/N$ [136].

At $P = 5$ atm and the following parameters of the streamer channel: the length $L = 2$ mm, the radius $R = 100$ μm and the electron number density $n_e \approx 5 \times 10^{14}$ cm^{-3} [40], we obtain the polarization time of such a channel $\tau_{pol} \approx 0.3$ ns. Therefore, to prevent the broadening of the front of the filament when the filament propagates as a fast ionization wave (FIW) over the streamer channels, the velocity of the wave should be $V_{FIW} \gg 3 \times 10^6$ cm/s, in agreement with the experimental data on velocity of the filaments.

5.4 Conclusion

In this chapter, optical emission spectroscopy was used for studying the changing of the spectra composition during the streamer–to–filament transition process. It is found that the transition happens with the changing of spectra from second positive system of molecule nitrogen to continuum spectra as well as atomic lines. The continuum spectra appear at the moment when the filament channel is well developed after the constriction of the streamers.

Particle image velocimetry (PIV) method was used to study the dynamics of the flow induced by a nanosecond surface dielectric barrier in a constricted mode. It is shown that the discharge constriction leads to the formation of large-scale turbulent structures with typical scales $1 - 2$ mm and velocity magnitude of 0.5 m/s.

It was found that the specific deposited energy in the filamentary plasma measured from experiment can be as high as $\omega_- \approx 7.4$ eV/particle for negative polarity and $\omega_+ \approx 6.4$ eV/particle for positive polarity.

Calculation results show that high electric fields during a short period of time, less than 1 ns, in the front of the filament, are responsible for efficient ionization. Stepwise ionization and dissociation from electronically excited states of molecular nitrogen leads to fast increase of the electron density, dissociation degree and gas heating. Approaching to the state close to the LTE explains the anomalously slow plasma decay in the afterglow, tens of nanoseconds: the electron density corresponds to the value of gas temperature at the given time instant, so the dynamics of plasma decay is determined mainly by gas cooling.

Chapter 6

Detailed study of streamer–to–filament transition in the near–electrode region with spatial resolution 7.6 μm/px

This chapter represents an attempt to observe experimentally the origin of the filament. From the previous chapter, we can conclude that a streamer–to–filament transition is a transition from nonequilibrium streamer plasma (electron density $n_e \simeq 10^{15}$ cm^{-3}, electron temperature T_e is a few electronvolts, gas temperature T_g is close to the ambient temperature) to equilibrium or almost equilibrium plasma ($n_e \simeq 10^{19}$ cm^{-3}, $T_e \approx T_g \approx 15 - 20$ kK). The transform happens in a single–short regime at high pressures and high voltage amplitude. High electric fields at high specific deposited energies can result in efficient and fast ($< 1\ ns$) multiple ignition and dissociation via electronically excited triplet states of molecular nitrogen.

An open question is how and why the diameter of a streamer plasma channel decreases, what are the processes leading to fast change of the plasma channel diameter from $150 - 200$ μm to $15 - 20$ μm? To do this, we concentrated on detailed study of streamer–to–filament transition in the vicinity of the high–voltage electrode. High special resolution of the optical system, 7.6 μm/px, was used.

6.1 Observation on the discharge channels from the micro scale

As was discussed in chapter 4, the streamer–to–filament transition is strongly affected by the applied voltage and pressure. In this chapter, we intentionally selected the condition when the transition process happens as slow as possible. Namely, relatively low amplitude of voltage is used in this chapter. Thus, it can give us more detailed information about the transition process.

6.1.1 backward emission and protrusions

The micro–scale images of filamentary discharge at $U = -25$ kV in N_2 at 6 bar at time instants $t = 2, 5, 7, 8, 9$ and 11 ns are presented in figure 6.1. From the first image, $t = 2$ ns, we can see the propagation of streamer discharge starting from the edge of the high–voltage (HV) electrode, indicated as the yellow dash arc in the image. The grey dash arc shows the front of the streamer propagation.

At $t = 5$ ns, the protrusion generates in the region far to HV electrode and passed through the streamer front. The pink dash arc indicates the place of the protrusion tip. At $t = 7$ ns, the protrusion propagates further and we can see that there is an emission propagating backwards in radial direction from protrusion to HV electrode. We call this "backward emission". In figure 6.1, the blue dash arcs in images of $t = 5, 7, 8, 9$ and 11 ns show the propagation of backward emission. We can see the backward emission propagates as time goes from $t = 5$ to $t = 11$ ns. At $t = 11$ ns, the backward emission almost reaches the edge of HV electrode.

Similar images but at positive polarity $U = +25$ kV are presented in figure 6.2. Different to the discharge at negative polarity, emission of positive streamers start to disappear during their propagation process. The protrusion develops from a dark region 2 mm away from the HV electrode. The backward emission, starting at $t = 8$ ns, propagates towards the HV electrode in radial direction. Similar to negative polarity, at $t = 11$ ns, the backward emission at positive polarity almost reaches the edge of HV electrode.

Figure 6.3 presents x-t diagrams obtained from the ICCD images shown in the figures 6.1 and 6.2. The propagation length of a streamer front (black curve), protrusion tip (red curve) and backward emission (blue curve) are plotted for both negative and positive polarities. The absolute values of propagation velocities for streamers, protrusions and backward emission are presented near the plots in mm/ns units.

It can be seen that at same experimental conditions ($|U| = 25$ kV, 6 bar nitrogen), negative polarity protrusion propagates faster than positive one while the backward

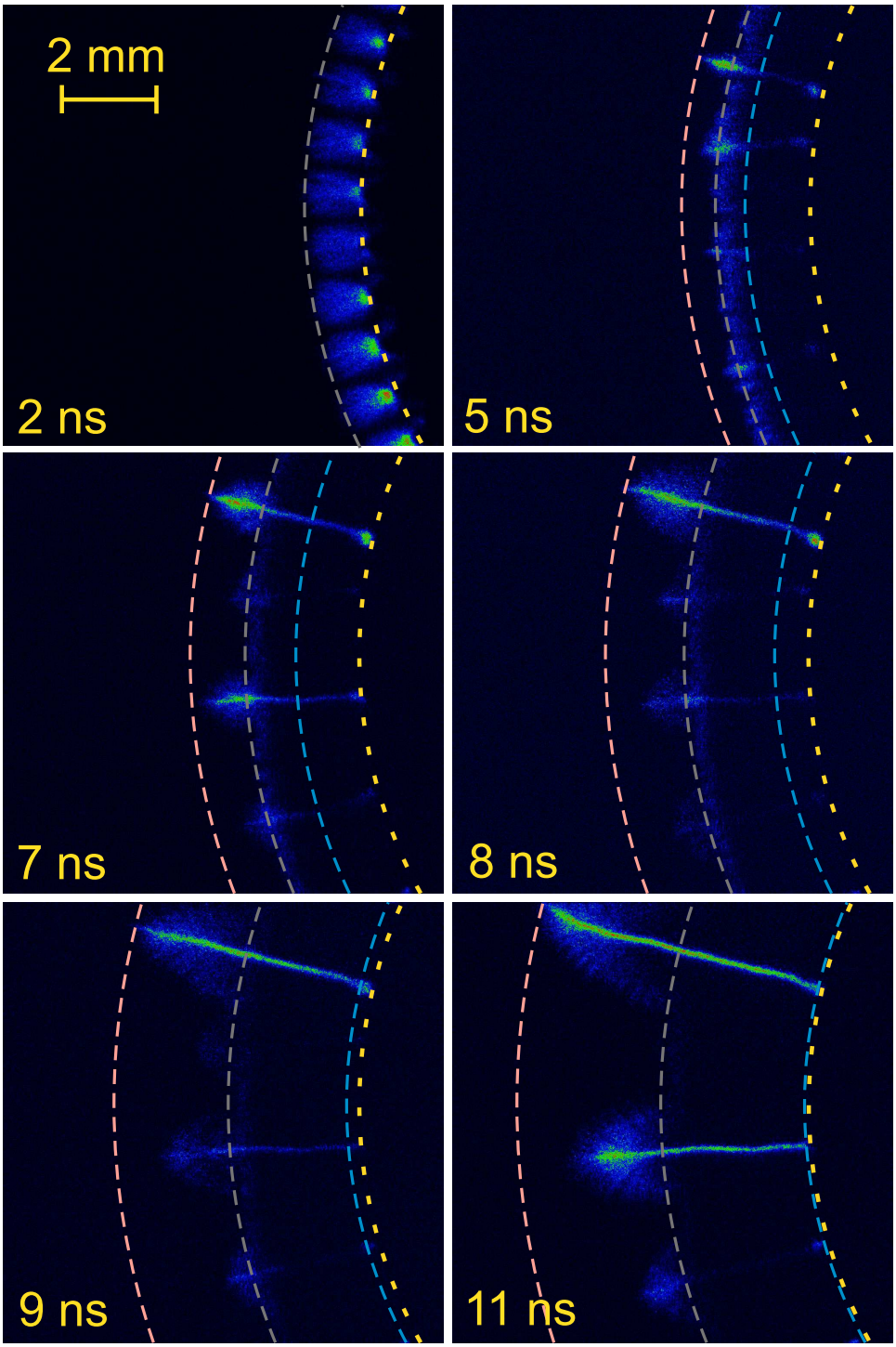

Figure 6.1: Length of protrusions (pink dash), streamer front (grey dash) and backward emission (blue dash) measured from ICCD images of discharge at $U = -25$ kV in N_2 at 6 bar at time $t = 2, 5, 7, 8, 9$ and 11 ns. Camera gate is 1 ns. Resolution of the optical system is 7.6 μm/px. The yellow dash arc indicates the edge of the HV electrode.

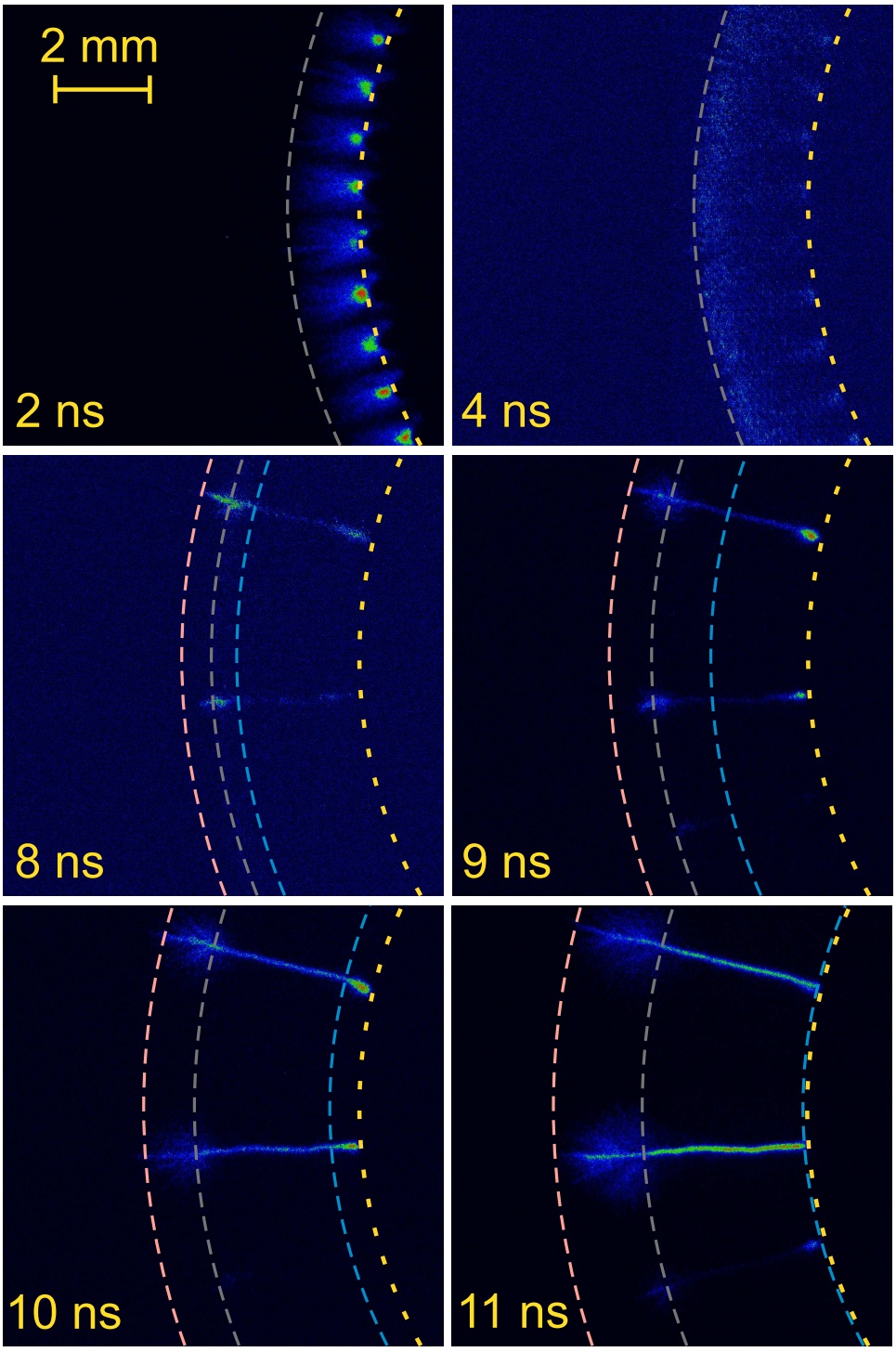

Figure 6.2: Length of protrusions (pink dash), streamer front (grey dash) and backward emission (blue dash) measured from ICCD images of discharge at $U = +25$ kV in N_2 at 6 bar at time $t = 2, 4, 8, 9, 10$ and 11 ns. Camera gate is 1 ns. Resolution of the optical system is 7.6 μm/px. The yellow dash arc indicates the edge of the HV electrode.

emission propagates much slower at negative polarity. Positive polarity streamer propagates faster at the beginning, and later, during the extinction, has almost the same velocity as the negative polarity streamer. At the same time $t = 11$ ns, streamers at both polarities stop to propagate meanwhile the backward emission reaches the HV electrode.

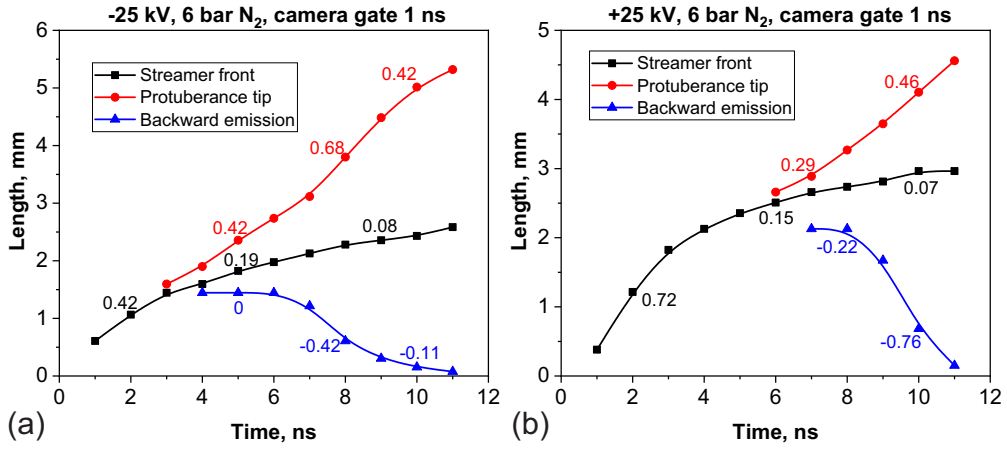

Figure 6.3: X-t diagrams of streamer front, protrusions and backward emission at (a) $U = -25$ kV and (b) $U = +25$ kV. Nitrogen, 6 bar. The propagation velocity is marked in the plots as numbers in unit mm/ns.

It can also been seen from figure 6.3 that the separation of protrusion and backward emission appears earlier at negative polarity ($t = 3 - 4$ ns) than at positive polarity ($t = 6 - 7$ ns).

Similar experiments were performed at higher pressure (7 bar) and higher amplitude of applied voltage ($U = -35$ kV and $U = +33$ kV) with the same gas composition (pure nitrogen). The discharge images at both negative and positive polarities are presented in figure 6.4. The propagation lengths of streamer front (dark curve), protrusion tip (red curve) and backward emission (blue curve) are shown in figure 6.5.

It can be seen from figure 6.4 and 6.5 that at higher pressure and higher amplitude of applied voltage, the protrusion appear much faster (within 0.5 ns) and the backward emission reaches the HV electrode within 1 ns at negative polarity and even faster for positive polarity. Figure 6.5 (b) has not shown the propagation of backward emission for the reason that it propagates too fast to measure.

From the comparison illustrated above, the experimental conditions of $U = \pm 25$ kV, 6 bar nitrogen was selected for detailed study of the streamer–to–filament transition.

Will note that structure of the discharge presented at x-t diagrams (figure 6.3 and

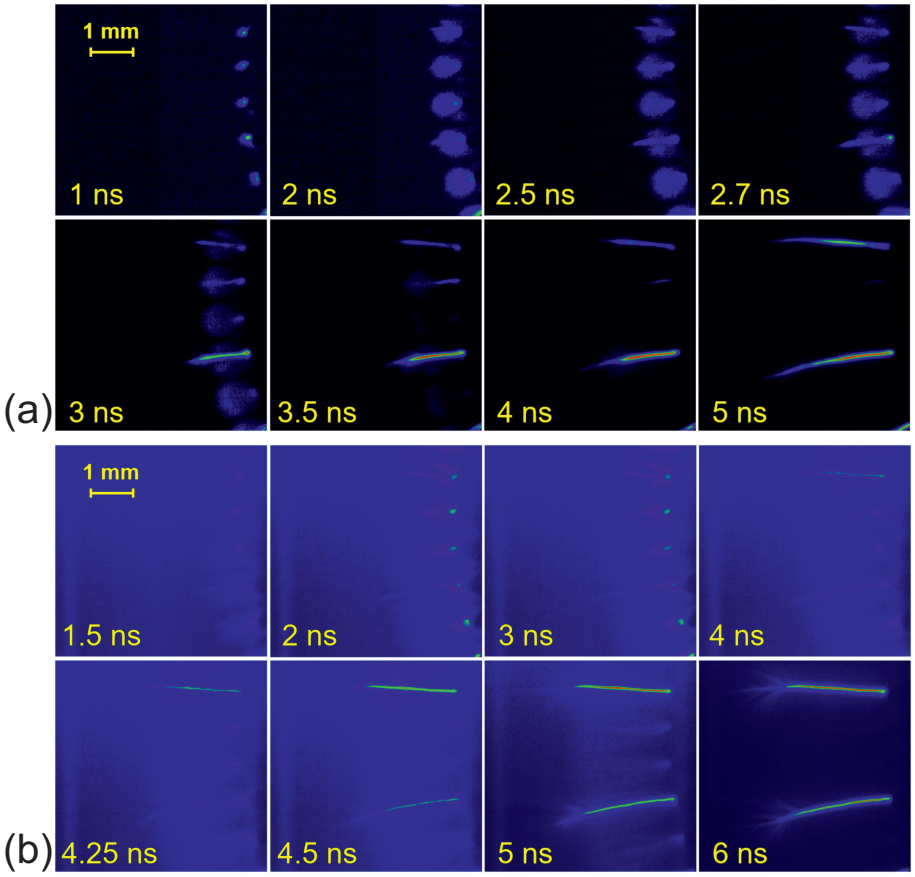

Figure 6.4: Micro–images of discharge propagation at selected moments at (a) $U = -35$ kV, camera gate is 1 ns and (b) $U = +33$ kV, camera gate is 2 ns. Nitrogen, 7 bar. Resolution of the optical system is 7.6 μm/px.

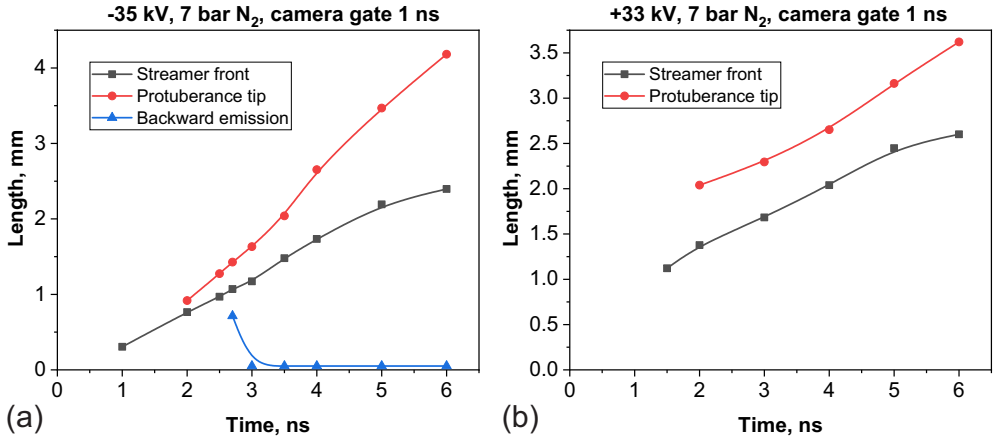

Figure 6.5: X-t diagrams of streamer front, protrusions and backward emission at (a) $U = -35$ kV and (b) $U = +33$ kV. Nitrogen, 7 bar.

6.5) reminds so called Boy's patterns of the lightning ([136], page373). If we replaced a term "protrusions" by a "stem" and "backward emission" by "return stroke", we would be able to suggest some analogy between the observed nanosecond surface dielectric barrier discharge at high pressure and lightning, saying that nSDBD is a "lightning in miniature". We deliberately do not do this: there are similarities and there is some difference between these two discharges.

A lightning flash lasts, on the average, about 200 ms. It consists of several pulses 10 ms each separated by about 40 ms. The first pulse is different from the others, but each pulse starts from the leader channel growing form the cloud to the ground. The leader transports negative charge; the current is about 100 A, almost no emission is observed at this stage. The leader channel consist of a stem (a single channel) and a streamer corona ahead of the stem. When the leader reaches the ground, or collides with a counter–leader, a return wave (highly luminous wave) starts to travel towards the cloud. The velocity of the return wave (the return stroke, the main stage of the lightning discharge) is $0.1 - 0.3$ of the speed of light. The current at this stage reaches hundreds of kA ($\sim$ 100 kA). Will also note that the optical emission spectra at this stage are quite similar to the OES spectra of filamentary nSDBD [54, 149–152].

The protrusion's morphology is similar to the morphology of a propagating leader: a "stem" with the streamer corona on the head of the protrusion (see figure 4.5 and 4.7). The backward emission is the emission of a streamer character (containing molecular bands of N_2). Transformation of spectra from molecular bands of nitrogen to cw and atomic spectra at the end of the backward emission are due to the increase of specific deposited energy. Increase of specific deposited energy is caused by decrease of the diameter of the plasma channel when passing from a streamer stage to a protrusion. Will study how the diameter of the plasma channel changes in space and in time.

6.1.2 Diameter of discharge channels

The diameter of discharge channels, "full width at half maximum" (FWHM) of emission intensity is an essential parameter for estimating the plasma properties. Two sets of experiments were done at both $U = \pm 25$ kV, 6 bar and $U = \pm 35$ kV, 7 bar in nitrogen. It is intended for explaining how the experimental conditions (pressure, amplitude and polarity of applied voltage) affect the diameter of discharge channels.

The micro–images at selected moments ($t = 3, 7, 10$ and 12 ns) are displayed in figure 6.6. The yellow lines show different positions along the discharge channel. The emission intensity distribution along these yellow lines was measured by an

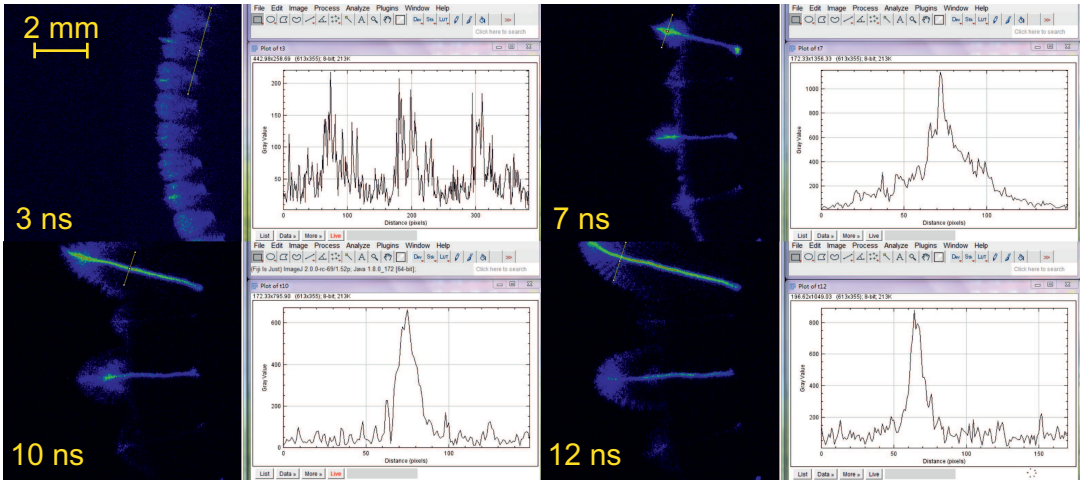

Figure 6.6: Micro ICCD images of discharge at $U = -25$ kV in N_2 at 6 bar at time $t = 3, 7, 10$ and 12 ns as well as the emission intensity distribution along the yellow line in images measured by "Fiji". Camera gate is 1 ns. Resolution of the optical system is 7.6 μm/px.

open–source software called "Fiji" [153] as shown on the right of each image.

Full width at half maximum (FWHM) of emission intensity of plasma channel observed by ICCD camera as a function of time is plotted in figure 6.7 for $U = -25$ kV, 6 bar discharge in nitrogen. The data are presented for different distances from the high–voltage electrodes taken as a parameter. The range of positions of measurements is between 160 μm $-$ 4 mm from the HV electrode.

Preliminary spectral measurements, similar to the measurements presented in Chapter 5 (figure 5.2–5.5), show that the emission from the discharge is a streamer–like emission with the second positive system of molecular nitrogen bands at $t <$ 8 ns, and a filament-like emission containing mainly cw spectra at $t > 9 - 10$ ns. Schematically, a grey rectangle in figure 6.7 separates the interval with a streamer emission and the interval with a filament emission.

For the convenience of description, we will use a variable "d" to refer to the distance from HV electrode. In the streamer emission zone, at the positions which are close to the HV electrode ($d = 160$ and 300 μm), the discharge channels experiences an expansion from $200 - 300$ μm up to 550 μm which is due to the propagation of a streamer discharge. Starting from $t = 2$ ns, the discharge channels start to shrink and the diameters decreases to less than 200 μm at $t = 5$ ns. This can be explained by the protrusions appearing in the middle of the streamer front.

At $t = 8$ ns, filaments generate from the ionized channel that connects the protrusions and HV electrode. In the filament zone shown in figure 6.7, the diameters at different positions of discharge channel stay at the small value, lower than 100 μm.

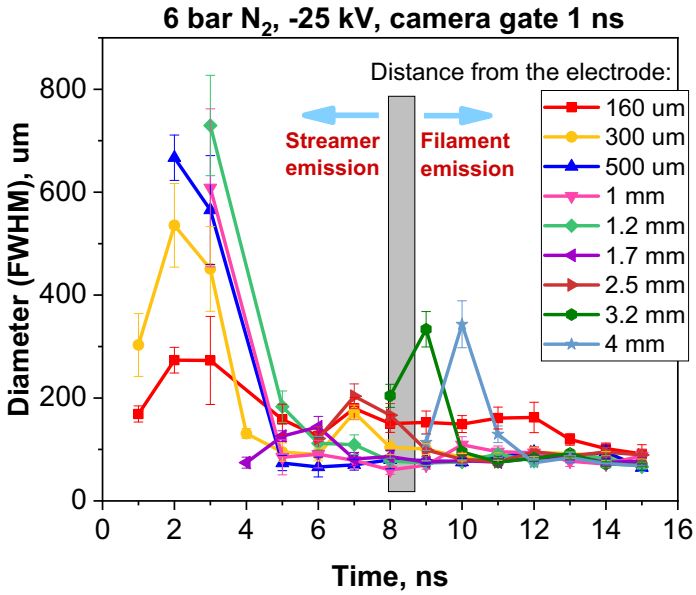

Figure 6.7: Full width at half maximum (FWHM) of discharge channels at different positions from the HV electrode. $U = -25$ kV, 6 bar, N_2.

There are two exceptions: at the position, $d = 160$ μm to HV electrode, there is a bright spot with a diameter of 150 μm and at the positions faraway from the HV electrode, $d = 3.2$ and 4 mm, the peaks at $t = 9$ and 10 ns still show the diameter of the propagating protrusion tips.

To estimate the impact of amplitude of applied voltage, camera gate and experimental frequency on the diameter of measured discharge channels, two additional sets of experiments with different camera gates and frequencies were done by varying the amplitude of applied voltages. As shown in figure 6.8, the diameter of a plasma channel with a camera gate 20 ns in a single shot mode is almost two times larger comparing to the diameter with a camera gate 1 ns and images accumulated for 50 times. It can be seen from the figure that the diameter of discharge channel practically does not depend on the amplitude of applied voltages.

We consider measurements in a single shot regime as a physical limit for the measurements of the diameter: error is possible because of slightly different development of a plasma channel from pulse to pulse. Knowing that maximum possible error at 50 times averaging is almost a factor of 2, we will continue measurements with 50 accumulations with a camera gate 1 ns to get the information about the temporal dynamics of the transition.

Similar to the data for 6 bar nitrogen and $U = -25$ kV, micro ICCD images of filamentary discharge at $U = -35$ kV in N_2 at 7 bar at time $t = 2.7, 3, 7$ and 10 ns were processed by "Fiji" for measuring the diameter of discharge channels. Emission

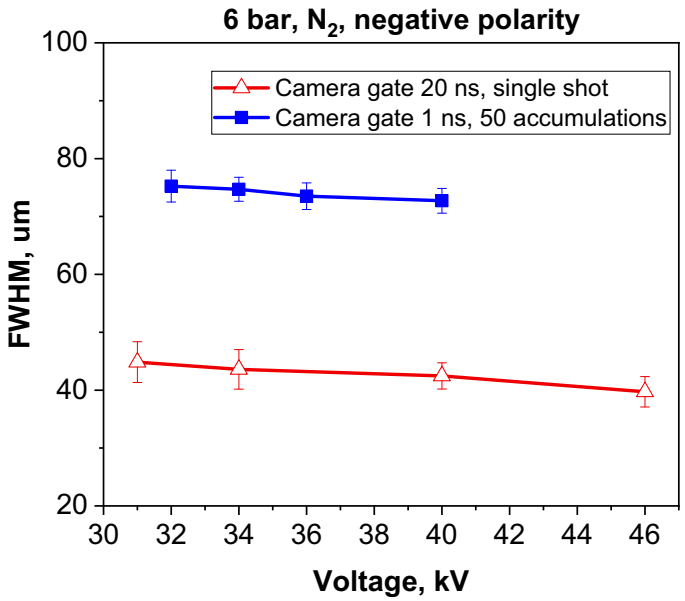

Figure 6.8: Full width at half maximum (FWHM) of discharge channels with different amplitude of applied voltage, camera gate and frequency. Negative polarity, 6 bar, nitrogen.

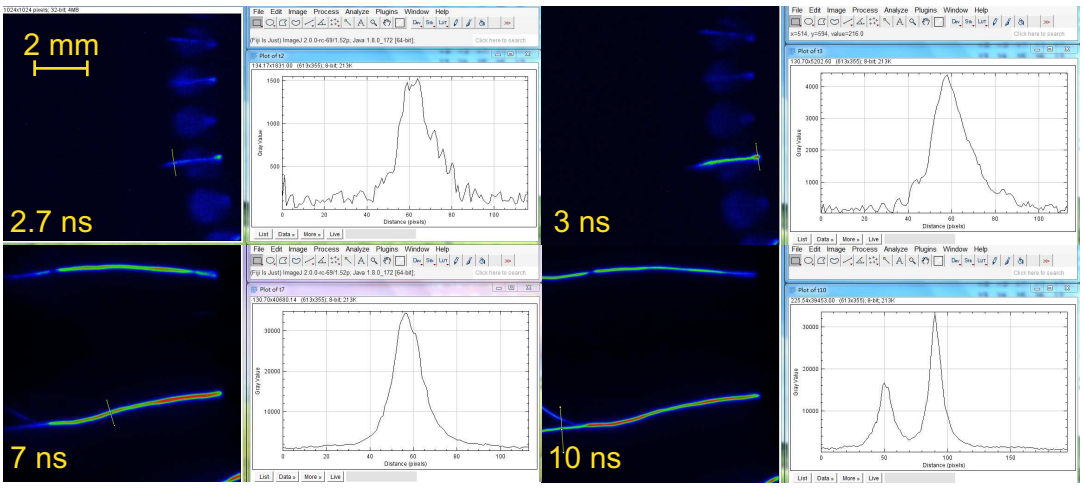

Figure 6.9: Micro ICCD images of discharge at $U = -35$ kV in N_2 at 7 bar at time $t = 2.7, 3, 7$ and 10 ns as well as the emission intensity distribution along the yellow line in images measured by "Fiji". Camera gate is 1 ns. Resolution of the optical system is 7.6 μm/px.

taken by ICCD camera at different time instants is presented at the left hand side of the frames in figure 6.9. Profiles of emission intensity distribution along the yellow line of each frame are presented at the right hand side of figure 6.9. Will note that the intensity distribution curves are less noisy at $U = -35$ kV than at $U = -25$ kV

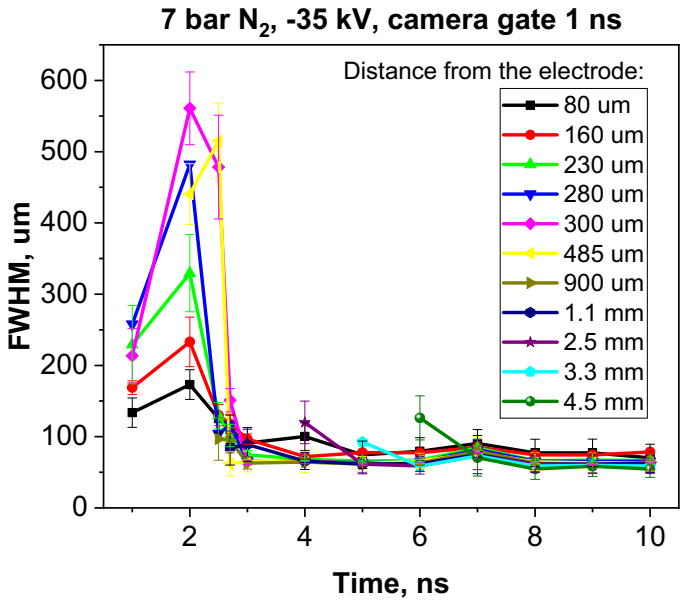

Figure 6.10: Full width at half maximum (FWHM) of emission intensity of discharge channels at different positions from the HV electrode. $U = -35$ kV, 7 bar, nitrogen.

due to the higher emission intensity at higher voltage. It can also be seen that at $U = -35$ kV, 7 bar in N_2 the protrusion is formed at $t = 2.7$ ns and well developed at $t = 3$ ns.

Figure 6.10 shows full width at half maximum (FWHM) of plasma channels at $U = -35$ kV, 6 bar in N_2 at different positions from the HV electrode. At the distances less than 500 μm from the electrode, all the curves experience the same trend. The diameters of the plasma channel increase due to the expansion of streamer phase and then significantly shrink to less than 100 μm at $t = 2 - 3$ ns. At time after $t = 4$ ns, nearly everywhere along the plasma channel, the diameter is less than 100 μm. Diameter less than 100 μm during a long time, $2 - 10$ ns, is a sign of forming the filament.

Full width at half maximum (FWHM) of plasma channels at positive polarity ($U = +25$ kV, 6 bar and $U = +33$ kV, 7 bar) in N_2 as a function of time at different positions from the electrode is displayed in figure 6.11. At $U = +25$ kV, 6 bar, due to the homogeneous expansion and the disappearing emission of streamer discharge, high diameters of a streamer discharge channel can hardly be seen. Instead, the protrusions generating at $t = 2 - 3$ ns with the diameter of $200 - 300$ μm can be clearly seen from figure 6.11 (a). At $U = +25$ kV, 6 bar, the diameters start at a high value (580 μm at the position $d = 280$ μm to the HV electrode) and then decrease to about 50 μm after $4 - 5$ ns.

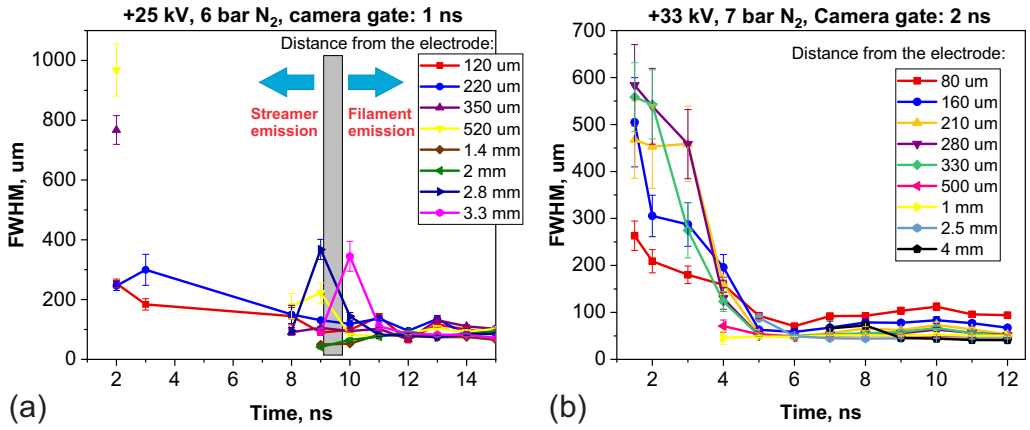

Figure 6.11: Full width at half maximum (FWHM) of emission intensity of discharge channels at positive polarity at different positions from the HV electrode. (a) $U = +25$ kV, 6 bar, (b) $U = +33$ kV, 7 bar, nitrogen.

6.1.3 Emission intensity along discharge channels

As described above, the diameter of discharge channel changes at different positions from the HV electrode during the discharge propagation. The emission intensity along the discharge channels also vary upon time. Figure 6.12 shows the measurement process of emission intensity along the discharge channel at specific moments at both negative and positive polarities. Each four time moments were selected differently from negative and positive polarities according to their different discharge propagation behavior.

By using the methods described in figure 6.12, we can get the diagram of emission intensity distribution along discharge channel at $U = \pm 25$ kV in N_2 at 6 bar with the camera gate 1 ns (figure 6.13). The color bars in the figure have been unified for both polarities in order to make a better comparison. From figure 6.13 (a), we can see that at negative polarity the protrusion appear at $t = 4$ ns. At $t = 5$ ns, there is a spot with high emission intensity appearing in the region near the HV electrode. Starting from this moment, the emission intensity is mainly separated into two zones, one region close to the HV electrode and the other one is protrusion. For $t = 5$ to 7 ns, we can clearly see the increase of emission intensity of protrusion and its propagation further from the HV electrode. At the same time, we observe propagation of a wave of emission from the protrusion head back to the high–voltage electrode. This wave corresponds to the blue curves (backward emission) in the figure 6.3(a).

If to consider a fixed point, e.g. 0.8 mm from the HV electrode, the emission intensity increases in the period $\Delta t = 4 - 7$ ns due to the passage of the back wave. When the backward emission approaches the HV electrode ($t = 9$ ns), the

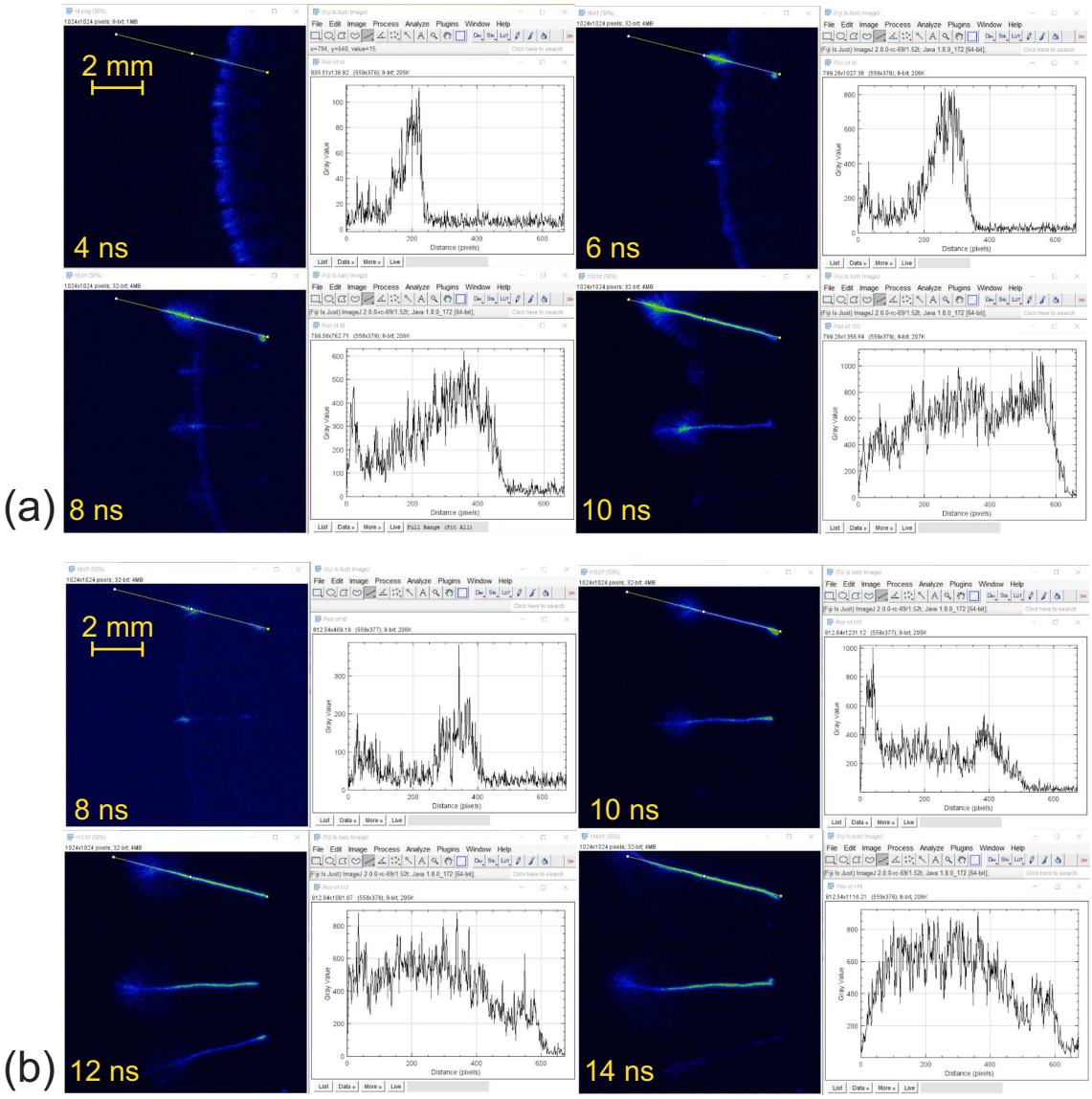

Figure 6.12: Micro ICCD images of discharge at (a) $U = -25$ kV at time instants $t = 4, 6, 8$ and 10 ns and (b) $U = +25$ kV at time instants $t = 8, 10, 12$ and 14 ns in N_2 at 6 bar as well as the emission intensity distribution along the discharge channel measured by "Fiji". Camera gate is 1 ns. Resolution of the optical system is 7.6 μm/px.

bright spot near the electrode decays. No two separate emission zones are observed any more. Starting from $t = 9$ ns, the intensity along the whole discharge channel increase as the discharge propagates; it is exactly the moment when streamer–like spectra change to the cw and atomic lines spectra.

At positive polarity discharge with the same amplitude of applied voltage, figure 6.13 (b) shows similar trends as at negative polarity. The intensity of the spot near the electrode is even higher than the intensity of protrusion. There is a jump

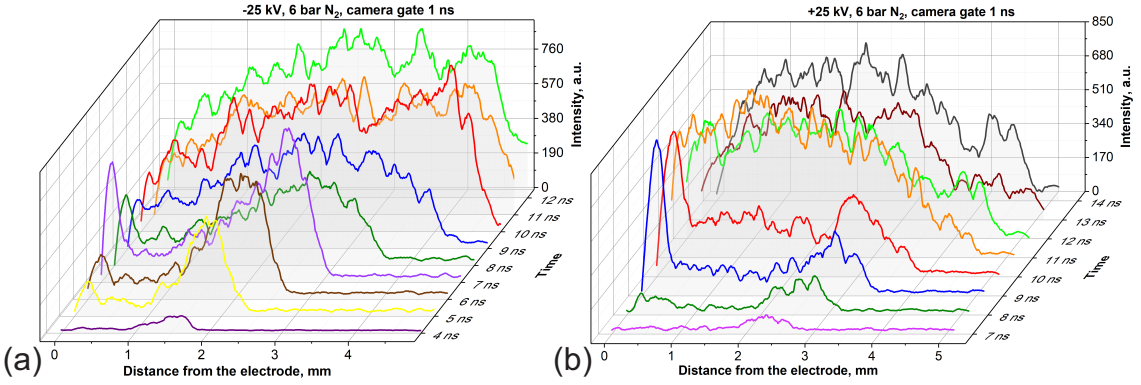

Figure 6.13: 3D diagram of emission intensity distribution along discharge channel at (a) $U = -25$ kV from time $t = 4$ to 12 ns and (b) $U = +25$ kV at time $t = 7$ and 14 ns in N_2 at 6 bar. The same colors mean the same time delay from the beginning of the discharge emission.

between $t = 10$ and 11 ns which is exactly the moment when the backward emission propagates until the HV electrode. Starting from $t = 11$ ns, the intensity along the whole discharge channel increases sharply to a high value and stays the same as the discharge propagates.

6.2 Micro–scale spectral measurement

As described in chapter 5, the streamer–to–filament transition generally happens with the changing of the spectra composition: from second positive system of molecule nitrogen in streamer regime to continuum wavelength and atomic lines in filamentary regime.

For studying the streamer–to–filament transition in detail, the spectroscopy experiments were done with the resolution 7.6 μm/px. The aim of these detailed experiments was to find, in time and space, a point where the cw spectrum and the high electron density appear, on the "point of origin" of the filament.

We decided to focus onto two spectral features: (i) H_α emission and (ii) CN emission. H_α emission at 656.3 nm was used to study the electron density behavior in time and space. In these experiments, 5% admixture of molecular hydrogen to N_2 was used. As indicated in chapter 5, at negative polarity on the HV electrode, the CN molecular band of violet system ($B^2\Sigma^+ - X^2\Sigma^+$) in wavelength range of $382 - 389$ nm is always observed at the same as cw spectrum. The origin of CN emission is from amount of C–atoms in the system. Assuming that time–resolved CN behavior is the same as time–resolved behavior of the cw emission, we analysed

CN emission in time and space.

6.2.1 H_α and CN intensity

Time–resolved micro–images for the period $t = 2 - 12$ ns were obtained using zero order of diffraction gratings. It can be seen from figure 6.14 that starting from $t = 5$ ns, the discharge channel starts to constrict and the protrusion appears. At $t = 9 - 10$ ns, the filamentary channel is almost formed. We intentionally used the same geometry for ICCD imaging through the slit of the spectrometer, and then for taking spectra keeping the entrance slit as narrow as possible at the condition that filament is not cut by the slit. Will note that to get a spectrum, we had to collect ~ 1000 accumulations.

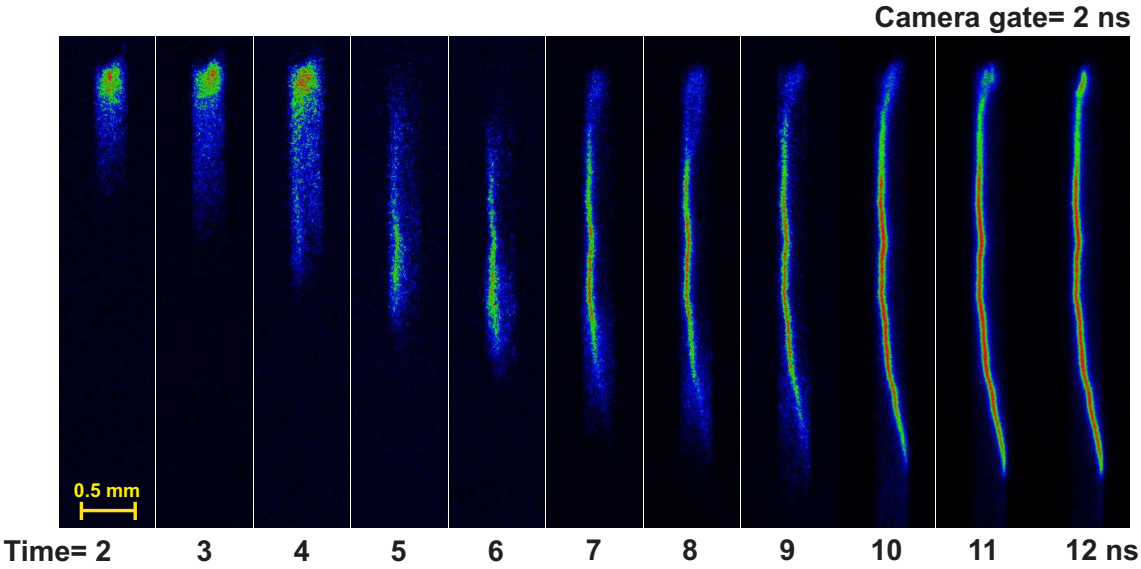

Figure 6.14: Time–resolved micro–images of discharge propagation from $t = 2-12$ ns measured by zero order of gratings from the slit of spectrometer. $U = -32$ kV, 6 bar, N_2/H_2 (5%), ICCD camera gate 2 ns and 10 accumulations for each image.

Figure 6.15(a) presents x-t diagrams obtained from the ICCD images shown in the figures 6.14. The propagation length of a streamer front (black curve), protrusion tip (red curve) and backward emission (blue curve) are plotted for the negative filamentary discharge at $U = -32$ kV in 6 bar N_2/H_2 (5%) mixtures. Full width at half maximum (FWHM) of emission intensity of plasma channel as a function of time is plotted in figure 6.15(b) for the same experimental condition. The data are presented for different distances from the high–voltage electrodes taken as a parameter. Different from the curves presented in figure 6.7 and figure 6.10, the diameter of streamer emission in figures 6.14 in time period $\Delta t = 2 - 4$ ns cannot

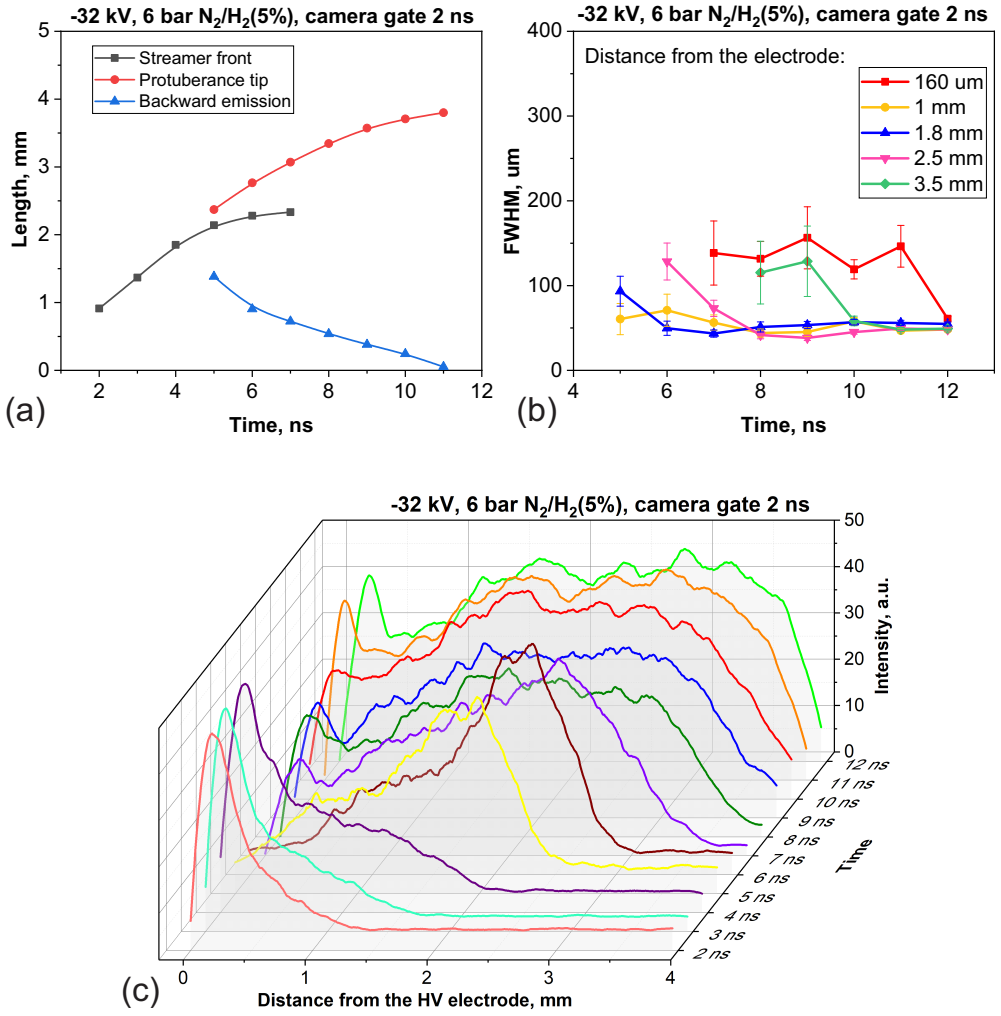

Figure 6.15: (a) X-t diagrams of streamer front, protrusions and backward emission; (b) full width at half maximum (FWHM) of plasma channels at different positions from the HV electrode; (c) 3D diagram of emission intensity distribution along plasma channel. $U = -32$ kV, 6 bar, N_2/H_2 (5%), ICCD camera gate 2 ns and 10 accumulations for each image.

be obtained due to the limitation of slit of spectrometer (~ 250 μm). Figure 6.15(c) shows the 3D diagram of emission intensity distribution along plasma channel.

Time–resolved H_α spectra is shown in figure 6.16 containing the integration of whole discharge region. It can be seen that at $t = 5$ and 6 ns, no H_α emission is observed. Instead, the second order of SPS system of molecular nitrogen which peaks at 337 nm can be seen from the spectra. Starting from $t = 7$ ns, the H_α peak begins to appear and the intensity of emission increases progressively. At $t = 9$ ns, the H_α peak is well defined and the second order of SPS system of nitrogen disappears. Combining observed spectra with the discharge images shown in figure 6.14, one

can find that the time interval $\Delta t = 7 - 10$ ns is the interval where the backward emission propagates from the protrusion head to the high–voltage electrode.

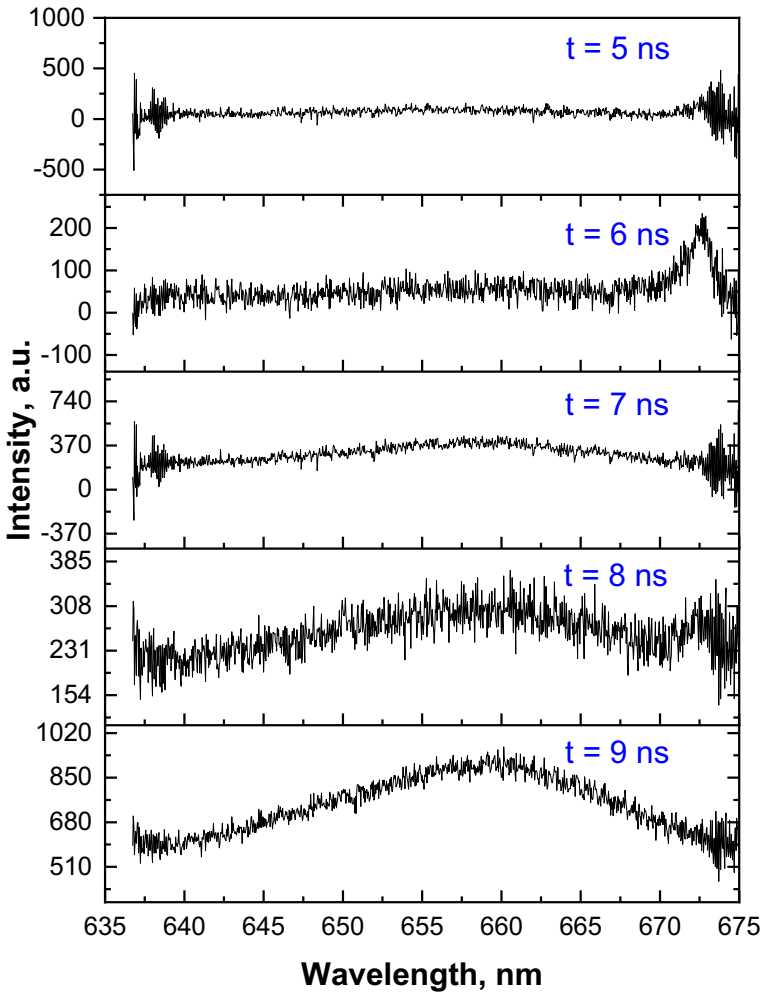

Figure 6.16: Time–resolved H_α line emission integrated in space from $t = 5$ to $t = 9$ ns in the process of streamer–to–filament transition. $U = -32$ kV, 6 bar, N_2/H_2 (5%), ICCD camera gate 2 ns and 1000 accumulations per frame.

Further, the spectra of discharges from $t = 7$ to 10 ns were analysed for different distances (d) from the HV electrode. The spatial–resolved spectra accompanied by the micro images of discharge channels at $t = 7 - 10$ ns are presented in figure 6.17. The HV electrode is on the top of each image and the discharge propagates downwards to the ground electrode on the bottom. Each image is divided into 5 regions, marked as region I, II, III, IV and V. From top to the bottom, the distance from the HV electrode d equals to $0 - 0.8$ mm, $0.8 - 1.6$ mm, $1.6 - 2.4$ mm, $2.4 - 3.2$ mm and $3.2 - 4$ mm.

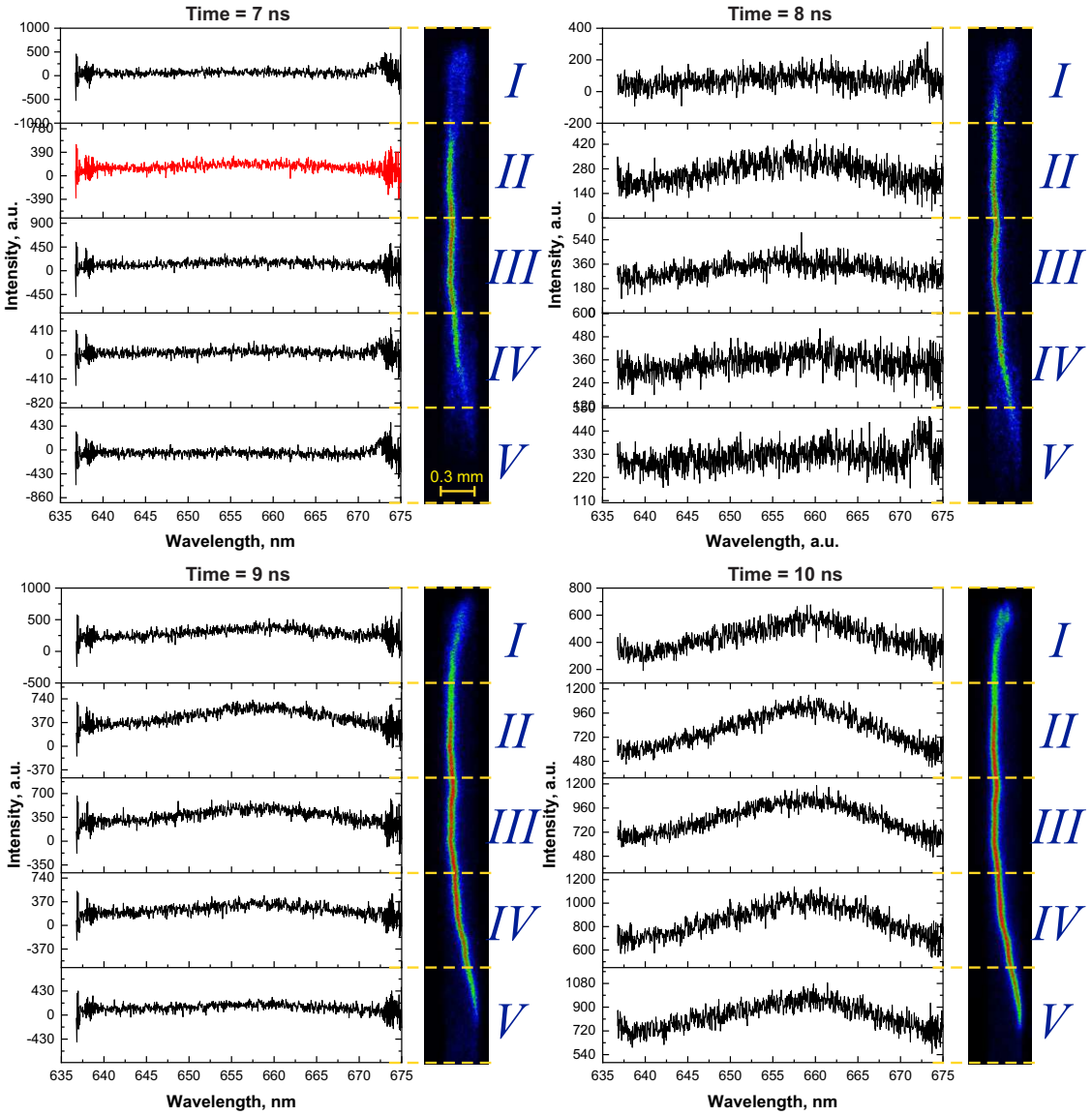

Figure 6.17: Spatial–resolved H_α lines from $t = 7$ to $t = 10$ ns in the process of streamer–to–filament transition. $U = -32$ kV, 6 bar, N_2/H_2 (5%), ICCD camera gate 2 ns and 1000 accumulations per frame.

It can be seen that for the very first time, H_α emission appears at $t = 7$ ns in the region II, $d = 0.8 - 1.6$ mm from the electrode (see the red curve in figure 6.17). At $t = 8$ ns, the H_α peaks spread in both directions, appearing in region II, III and IV. At $t = 9$ ns, the H_α line emission is observed in the whole region. At $t = 10$ ns, the H_α line increases in intensity, designating a well–developed filament.

Intensities of H_α lines from region I to V were compared in figure 6.18 at $t = 8, 9$ and 10 ns. These peaks were normalized to the top as shown on the right. The sharp peak at 674 nm at $t = 8$ ns in figure 6.18(b) is the second order of SPS of molecule

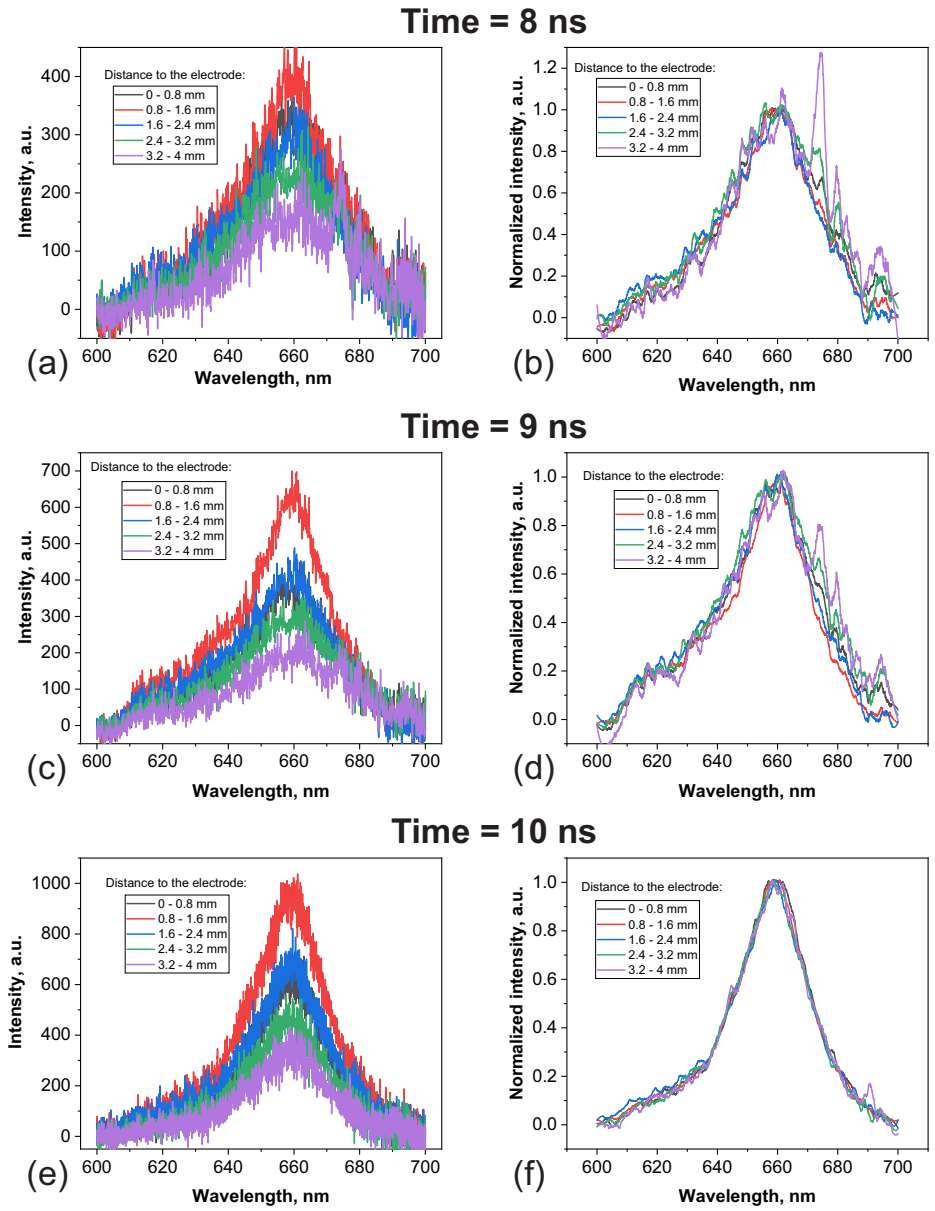

Figure 6.18: Spatial–resolved H_α intensity at different position from the HV electrode at $t = 8, 9$ and 10 ns and their normalized intensity in the process of streamer–to–filament transition. $U = -32$ kV, 6 bar, N_2/H_2 (5%), ICCD camera gate 2 ns and 1000 accumulations per frame.

nitrogen. At $t = 10$ ns, the SPS of molecule nitrogen disappears.

The height of H_α peaks can be drawn for the different positions from the HV electrode. Peak emission intensities for H_α and CN emission as a function of distance from the high–voltage electrode for the time interval $\Delta t = 8 - 10$ ns is presented in figure 6.19(a) and figure 6.19(b) respectively. As time goes from $t = 8$ to $t = 11$ ns, the emission intensities of both H_α line and CN band increase. The highest emission

intensity of H_α line appears in region II, $0.8-1.6$ mm from the HV electrode, while the CN band has the maximum intensity in the region III, at the position 2 mm from the HV electrode.

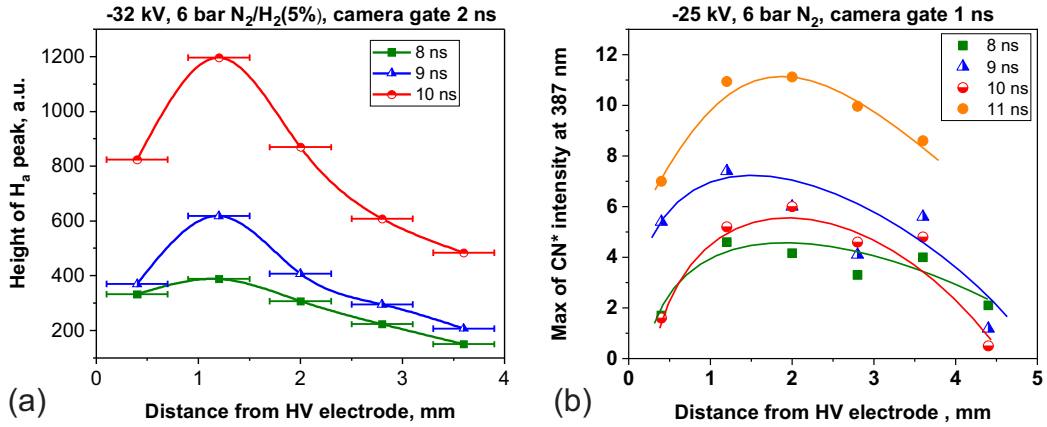

Figure 6.19: Maximum intensity of H_α lines from $t = 8$ to $t = 10$ ns and CN bands at 387 nm from $t = 8$ to $t = 11$ ns in the process of streamer–to–filament transition.

It is important to note that we observe the origin of H_α and CN emission (and so, a start point of streamer–to–filament transition) at significant, $1-2$ mm distance from the HV electrode. The first stage of transition is a shrinking of a streamer channel and formation of a protrusion (and so, increasing of the current density), and the second stage is a propagation of the backwave. The region $1-2$ mm is actually a region between two maxima of emission (see figure 6.15), namely near–electrode region and a head of the protrusion.

Intensity of H_α line measured for different regions (I to V) is different but the FWHM values are identical which indicates the same electron density appearing along the whole discharge channel.

6.2.2 Electron density measurement

The electron density was measured by the same method as described in 5.1.3. The normalized H_α line emission at $t = 8, 9$ and 10 ns in regions I, II and III are shown in figure 6.20. It can be seen that the FWHM of H_α lines have a small drop from $t = 8$ ns to $t = 10$ ns. This trend does not depend on the distance from the HV electrode.

The results of the measured electron density are displayed in figure 6.21. It can be found from the chart that the electron density stays at the value of 10^{19} cm^{-3} and decrease slightly from $t = 8$ ns to $t = 10$ ns. There is no big difference among different positions from the HV electrode.

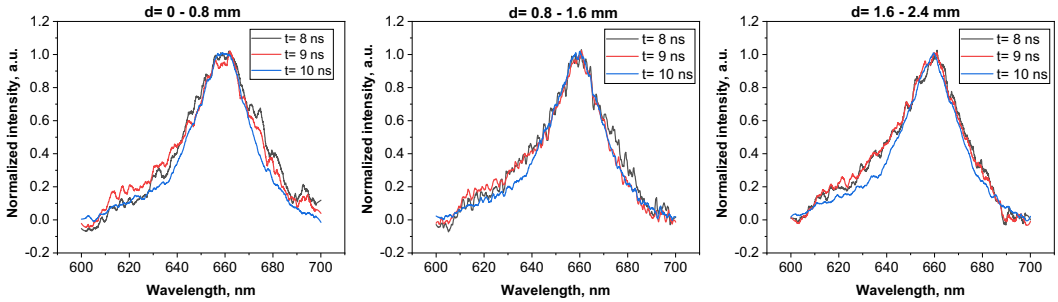

Figure 6.20: Normalized H_α lines at $t = 8, 9$ and 10 ns in region I, II and III. $U = -32$ kV, 6 bar, N_2/H_2 (5%), ICCD camera gate 2 ns and 1000 accumulations per frame.

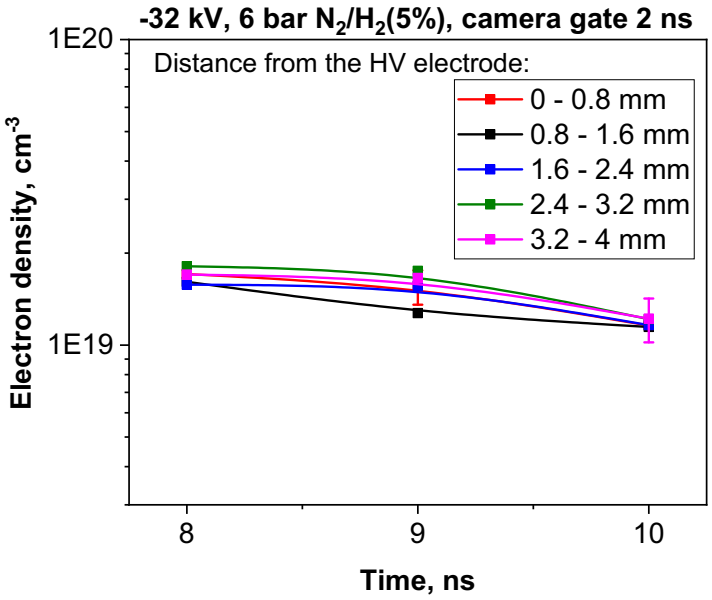

Figure 6.21: Spatial–resolved electron density measured from H_α lines at $t = 8, 9$ and 10 ns in the process of streamer–to–filament transition. $U = -32$ kV, 6 bar, N_2/H_2 (5%), ICCD camera gate 2 ns and 1000 accumulations per frame.

To summarize, time–, spatial– and wavelength–resolved micro–imaging show the following: both for negative and positive polarities of the high–voltage pulse, streamer–to–filament transition consists of a several sequential stages: first, a flat or quasi–flat front of a streamer plasma transforms to a set of protrusions. Some of them survive and some not, forming a set of equidistant plasma channels. In spite of significant increase of current density, plasma in the protrusions stays nonequilibrium: the spectrum of the protrusion consists mainly of molecular bands of nitrogen. Backward emission, propagating from a protrusion head back to the high–

voltage electrode, demonstrates appearance of H_α and cw emission first in the bulk of plasma, $1-2$ mm away from the HV electrode.

Experimentally obtained voltage–pressure charts (figure 4.11) show dramatical influence of small additions of O_2 to N_2 on the voltage and pressure of transition at positive polarity of the discharge. The next section contains numerical analysis of changes of a streamer morphology at different amplitudes of applied voltage when adding different percentage of O_2 to nitrogen.

6.3 Numerical modeling of oxygen admixtures on the streamer morphology

As discussed in chapter 4, the threshold voltage of streamer–to–filament transition at elevated pressures at positive polarity is function of oxygen fraction in N_2/O_2 gas mixtures. The discharge in simulation is represented by a series of isolines of the electron density and the electric field. Unfortunately, until now there is not any calculation model can simulate streamer–to–filament transition and filamentary stage of the nanosecond surface discharge at high pressure.

In this section, we use the modified PASSKEy code provided by Dr. Yifei Zhu [117] to calculate positive surface streamers in gas mixtures with different oxygen fraction. To keep the same photoionization model, we did not considered discharge in pure N_2. Two mixtures, $N_2/O_2(1\%)$ and synthetic air ($N_2/O_2(20\%)$), were selected for comparison. Three amplitudes of voltage ranging from 35 to 55 kV were applied on the HV electrode.

6.3.1 Plasma properties simulation at positive polarity: emission intensity, electron density and electric field

This section presents very preliminary results of calculations of dynamics of high-pressure streamers.

The evolution of calculated electron density in unit /cm^3 for positive discharge at 6 bar in N_2/O_2 mixtures with two different oxygen fractions (1% and 20% of oxygen) is compared at three amplitudes of applied voltages (35, 45 and 55 kV) in figure 6.22. The point $(0,0)$ corresponds to the so–called triple point, a junction of the metal of electrode, dielectric and gas mixture. The horizontal scale is $0-6$ mm and the vertical scale is $0-0.4$ mm. To facilitate comparison, we kept the same scale for all plots within each figure.

The electron density in the left column, having larger value than the result on the right, is the result calculated in the gas mixtures of N_2/O_2 with 1% of oxygen.

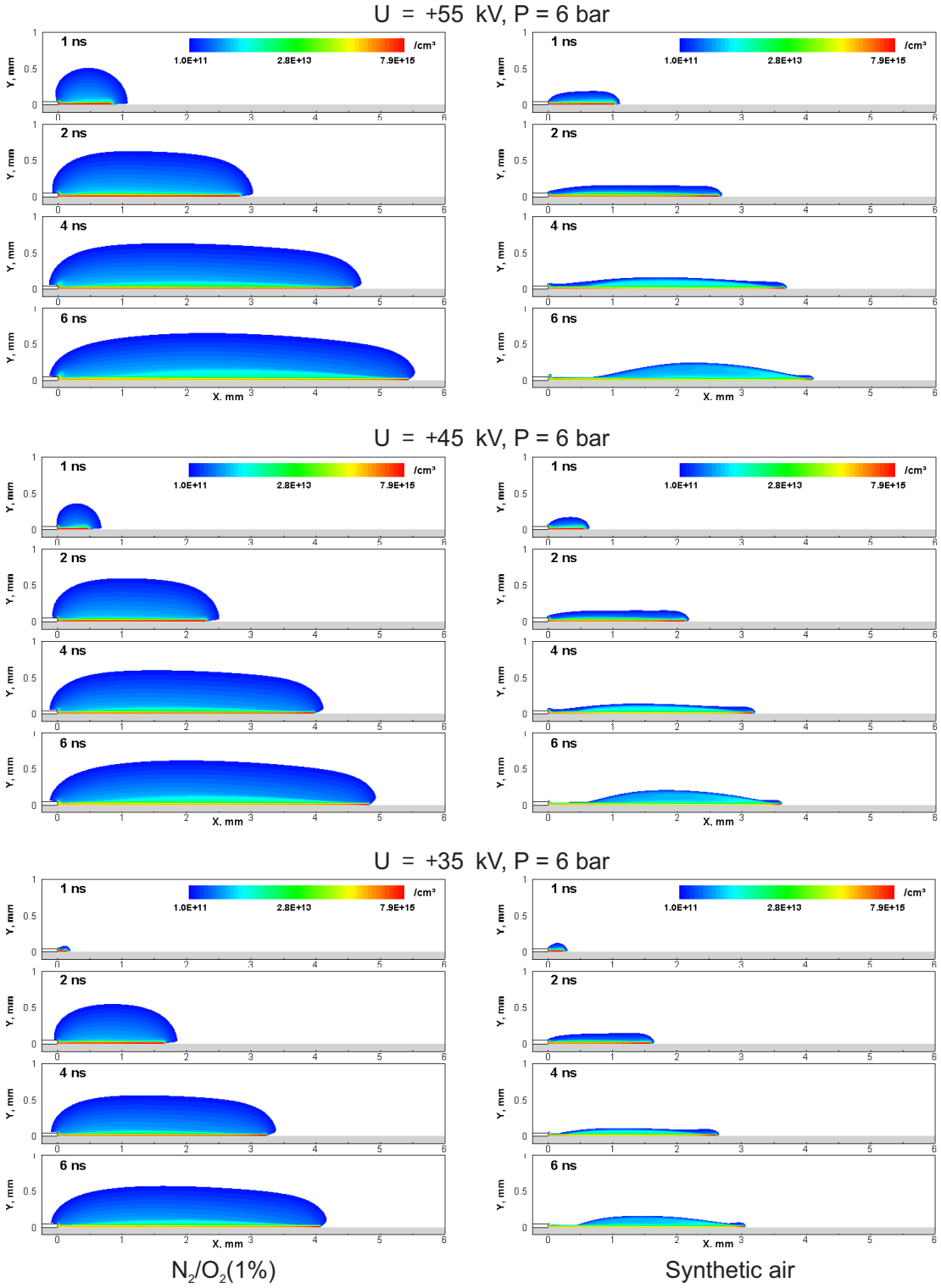

Figure 6.22: The evolution of calculated electron density in unit /cm^3 for positive discharge channel. Time instants are 1, 2, 4 and 6 ns. The scale on OX–axis is $0-6$ mm. The scale on OY–axis is $0-1$ mm.

The maximum electron density appears in the region near the dielectric surface and propagates towards the streamer head. Higher amplitude of applied voltage can support the discharge propagate further and faster. The electron density distributes homogeneously along the streamer channel.

Spatial distribution of the electron density is different for N_2/O_2 mixture with 1% of oxygen and for air. In particular, streamer is more volumetric for the mixture with 1% of oxygen: a typical radius of the streamer defined by $n_e = 10^{11}$ cm^{-3} isoline is around 500 μm in $N_2/O_2 = 99/1$ mixture, and about 100 μm in air. Velocity of propagation at the same voltage is also higher in $N_2/O_2 = 99/1$ mixture.

To compare the behavior of emission of nitrogen molecular bands, it is necessary to get the information about the electron density and electric field. The evolution of the absolute value of the electric field in the positive streamers at time instants of 1, 2, 4 and 6 ns is shown in figure 6.23. For both gas mixtures, high values of electric field are observed in the positive streamer head. The maximum value of electric field as shown in red in figure 6.23 corresponds to approximatively 720 kV/cm (450 Td at pressure $P = 6$ bar). Lower oxygen fraction condition shows smaller electric field value in the region near the HV electrode but higher electric field value in the head of positive streamers.

The evolution of calculated $N_2(C^3\Pi_u)$ density in unit /cm^3 for positive discharge channel at high pressure (6 bar) in N_2/O_2 mixtures with two different oxygen fractions is compared at different amplitudes of applied voltages in figure 6.24. The left column shows the results in the gas mixtures of N_2/O_2(1%) while the right column gives the evolution of $N_2(C^3\Pi_u)$ density in synthetic air.

The emission is proportional to the $N_2(C^3\Pi_u)$ density at the given moment of time (both production and quenching are taken into accounted by the code) and at the given point in space. Although we do not pretend to provide a quantitative comparison, qualitatively these are peculiarities which would be interesting to observe in the experiments for validation of results of numerical modeling.

In particular, the $N_2(C^3\Pi_u)$ emission always decreases in vertical (OY) direction. The emission pattern in $N_2/O_2 = 99/1$ mixture is always bigger than in air. The emission from the streamer head almost does not change the shape in the process of streamer propagation; the radius of emission in the streamer head does not change with voltage between +35 kV and +55 kV, but decreases significantly when passing from $N_2/O_2 = 99/1$ mixture to air. Similar to the electron density, the $N_2(C^3\Pi_u)$ emission propagates faster in both radial (OX in figure 6.24) and vertical (OY) directions. Finally, well–defined "cloud" of $N_2(C^3\Pi_u)$ emission appears near the high–voltage electrode when the voltage increases from +35 kV to +55 kV. A typical diameter of the "cloud" is $1 - 2$ mm. Between the near–electrode "cloud" and the streamer head, a kind of waist (decreasing diameter of the channel) is clearly seen.

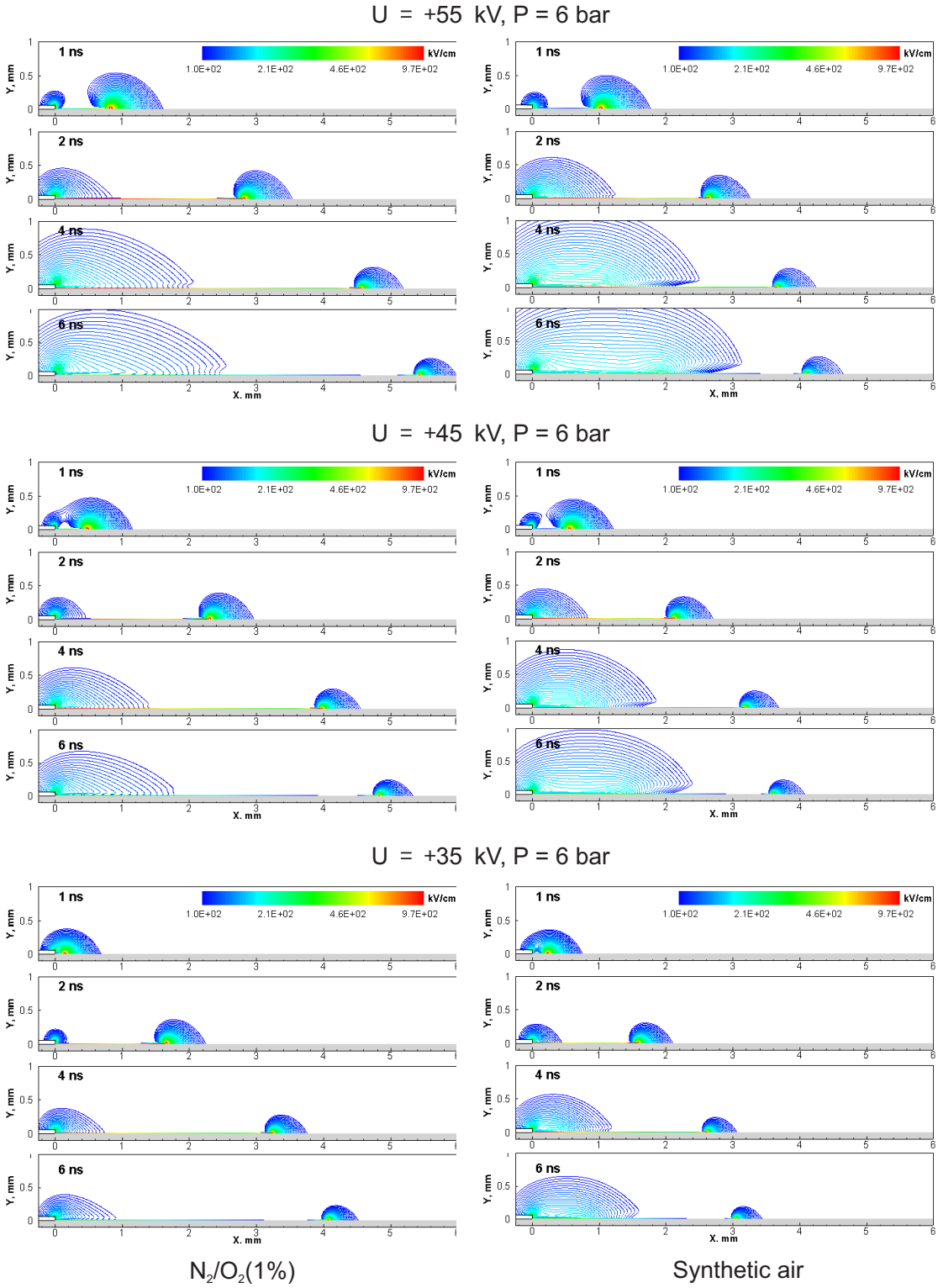

Figure 6.23: The evolution of the absolute value of electric field in unit kV/cm for positive discharge channel. Time instants are 1, 2, 4 and 6 ns. The scale on OX–axis is $0-6$ mm. The scale on OY–axis is $0-1$ mm.

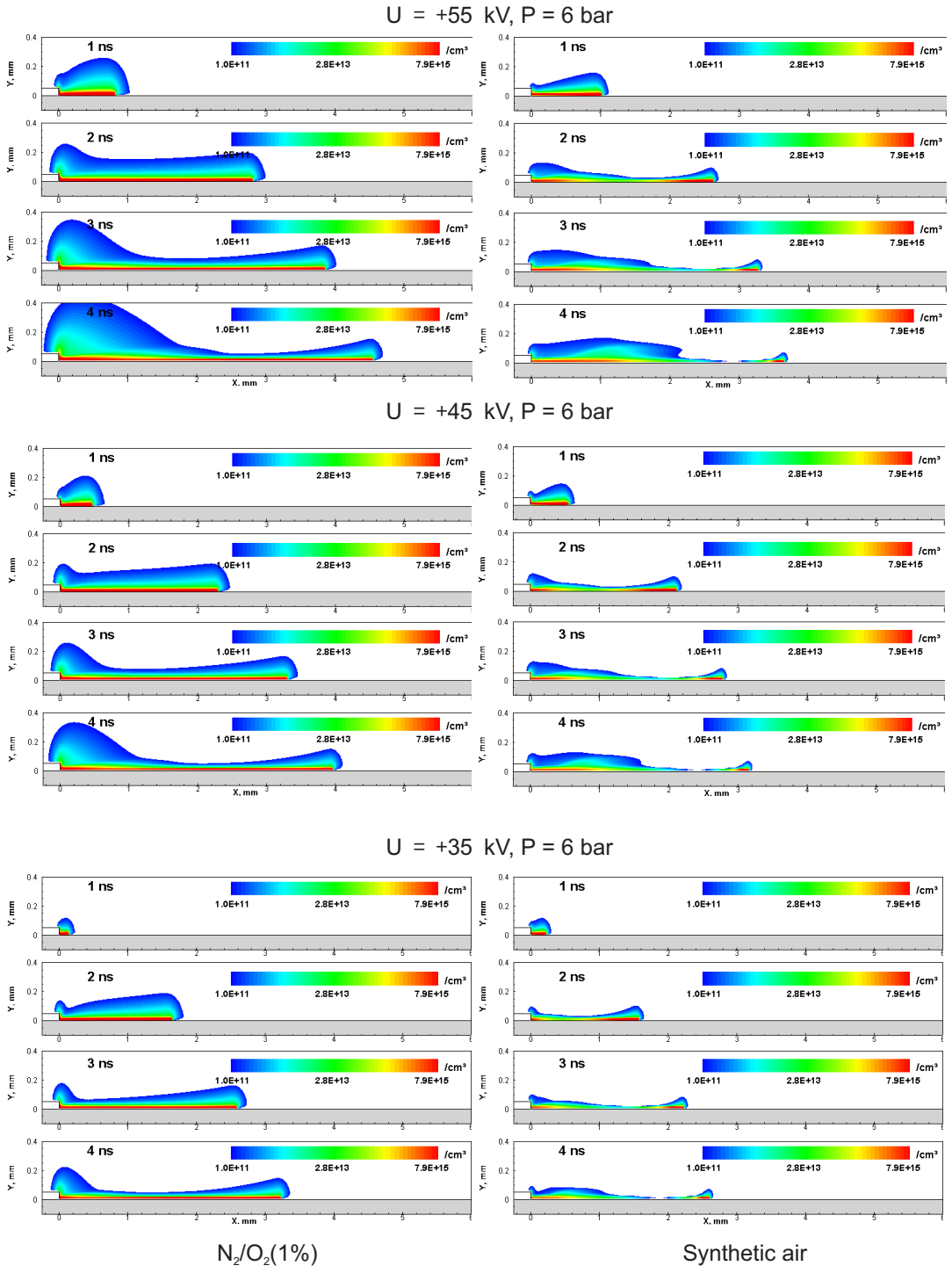

Figure 6.24: The evolution of calculated $N_2(C^3\Pi_u)$ density in unit /cm^3 for positive discharge channel. Time instants are 1, 2, 3 and 4 ns. The scale on OX–axis is $0-6$ mm. The scale on OY–axis is $0-0.4$ mm. Note that in the experiment, at positive polarity $p = 6$ bar pressure the transition happened at $U_{tr} \approx 40$ kV for $N_2/O_2(1\%)$ mixture, and at $U_{tr} \approx 49.5$ kV for air

To make a deeper analysis of the discharge channel, a point at $x = 1$ mm, $y = 0.02$ mm was selected as a probe for calculating the electron density and electric field at 6 bar positive polarity. The reasons to take a point $(x, y) = (1, 0.02)$ mm are the following: (i) 1 mm is a characteristic distance where the waist in the streamer emission is observed; (ii) 20 μm is a characteristic diameter of the filament. Will remind that streamer–to–filament transition was observed experimentally with a camera gate corresponding to 12 first nanoseconds of the discharge, the instant when the $N_2(C^3\Pi_u)$ discharge emission appearing for the first time was considered as $t = 0$ instant. At positive polarity $p = 6$ bar pressure the transition happened at $U_{tr} \approx 40$ kV for $N_2/O_2 = 99/1$ mixture, and at $U_{tr} \approx 49.5$ kV for air.

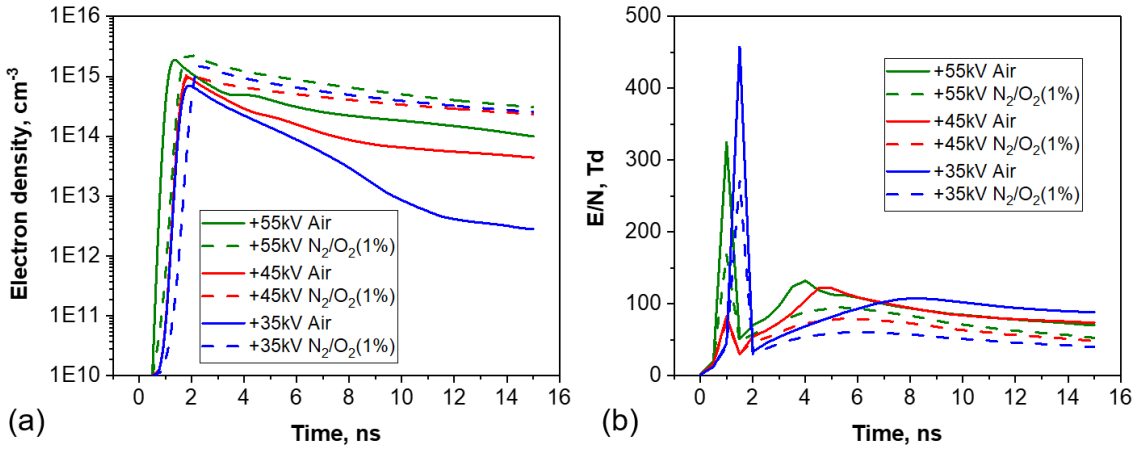

Figure 6.25: The evolution of (a) electron density (b) electric field at the point probe ($x = 1$ mm, $y = 0.02$ mm) for positive polarity.

No dramatical change is observed in streamer behavior between 35 and 45 kV for $N_2/O_2 = 99/1$ mixture or between 45 and 55 kV for air. The electron density at time instant of $1 - 15$ ns and electric field at three different amplitudes of applied voltage in both air and $N_2/O_2 = 99/1$ gas mixtures are shown in figure 6.25.

In $N_2/O_2(1\%)$ gas mixture, the electron density is almost one order higher than in synthetic air and has less dependency on the amplitude of applied voltage. In air, the evolution of electron density is strongly affected by the amplitude of applied voltages. For +35 kV on the HV electrode, the electron density has a faster decay than at the higher voltage. It can be seen from figure 6.25 (b) that the reduced electric field (E/N) in discharge in $N_2/O_2(1\%)$ gas mixture at $(x, y) = (1, 0.02)$ mm is lower than in synthetic air.

The evolution of total deposited energy at the point probe ($x = 1$ mm, $y = 0.02$ mm) for positive polarity is shown in figure 6.26. The total deposited energy in air is much lower than in $N_2/O_2(1\%)$ gas mixture for all amplitudes of applied voltage conditions.

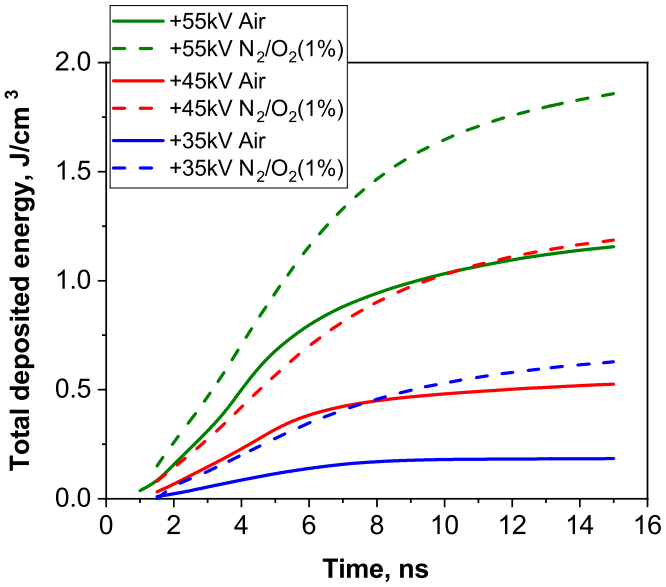

Figure 6.26: The evolution of total deposited energy at the point probe ($x = 1$ mm, $y = 0.02$ mm) for positive polarity.

Coming back to figure 6.25(a), the difference in decay of the electron density can be explained by a few reasons: at 6 bar in air, the reactions of attachment are very important. A characteristic time of transforming e to O_2^- is less than 1 ns:

$$e + O_2 + O_2 \rightarrow O_2^- + O_2 \qquad k = 2 \times 10^{-29}(300/T_e)\ \mathrm{cm^6 s^{-1}} \tag{6.1}$$

The decay of the electron density in air is mainly by attachment to oxygen, and it is faster than recombination. In addition, the main ion in air at $p = 6$ bar is O_4^+, due to the fast conversion of O_2^+ into O_4^+ with participation of N_2 and O_2 [125]:

$$O_2^+ + N_2 + N_2 \rightarrow O_2^+N_2 + N_2 \qquad k = 9 \times 10^{-31}\ \mathrm{cm^6 s^{-1}} \tag{6.2}$$

$$O_2^+N_2 + N_2 \rightarrow O_2^+ + N_2 + N_2 \qquad k = 4.3 \times 10^{-10}\ \mathrm{cm^3 s^{-1}} \tag{6.3}$$

$$O_2^+N_2 + O_2 \rightarrow O_4^+ + N_2 \qquad k = 10^{-9}\ \mathrm{cm^3 s^{-1}} \tag{6.4}$$

$$O_2^+ + O_2 + M \rightarrow O_4^+ + M \qquad k = 2.4 \times 10^{-30}\ \mathrm{cm^6 s^{-1}} \tag{6.5}$$

In $N_2/O_2(1\%)$ gas mixture the role of O_4^+ will be less pronounced, and the recombination rate is much higher for O_4^+ [125]:

$$e + O_4^+ \rightarrow O_2 + O_2 \qquad k = 1.4 \times 10^{-6}(300/T_e)^{1/2}\ \mathrm{cm^3 s^{-1}} \tag{6.6}$$

$$e + O_2^+ \rightarrow O + O \qquad k = 2 \times 10^{-7}(300/T_e)\ \mathrm{cm^3 s^{-1}} \tag{6.7}$$

Finally, additional production of electrons in $N_2/O_2(1\%)$ gas mixture can be due to associative ionization [154].

The considerations above explain why the decay of the electron density in air is much faster than in $N_2/O_2(1\%)$ gas mixture. Lower electron densities, and so lower electrical current, provide lower delivered energies at similar electric fields.

Will underline that the radius of a streamer (both defined from calculated electron density and from $N_2(C^3\Pi_u)$ emission) is higher in $N_2/O_2(1\%)$ gas mixture. Nevertheless, decay of electron density is much higher in air, and, as a consequence, higher current in $N_2/O_2(1\%)$ gas mixture (in more uniform–initially situation) will lead to a local heat due to relaxation of electronically excited and ionized species (fast gas heating [155]) and to instability leading to streamer–to–filament transition.

6.4 Conclusion

In this chapter, streamer–to–filament transition in the vicinity of the high–voltage electrode with a high special resolution of the optical system, 7.6 μm/px, was studied in detail. It was found that the diameter of discharge channel decreases from a few hundreds of micrometers to a few tens of micrometers right before the streamer–to–filament transition happens.

The backward emission and the protrusions were found during the streamer–to–filament transition at moderate amplitude of the applied voltage in nitrogen. Transition to cw spectra, so to filaments happens when the backward emission reaches the high–voltage electrode. At the same experimental condition (pressure and amplitude of applied voltage), negative protrusion propagates faster than positive ones while the backward emission propagates much slower at negative polarity. Positive streamer propagates faster at the beginning and then stays at the same value as negative streamer during its extinction process. The separation of protrusion and backward emission appears earlier at negative polarity than at positive polarity.

The micro–scale spectral results show that H_α line emission appears at $t = 7$ ns, slightly before the backward emission reaches the high–voltage electrode, and has the strongest intensity in the region 1.2 mm from the high–voltage electrode. High electron density, over 10^{19} cm^{-3}, is evenly distributed throughout the discharge channel.

2D PASSKEy code was used to calculate the discharge at high pressure. The results show that at positive polarity, the discharge in $N_2/O_2(1\%)$ mixture produces higher electron density and total deposited energy than in air with the same amplitude of applied high voltage.

Chapter 7

General conclusions

7.1 Contributions of the present work

This work was focused on the experimental study of a single–shot pulsed nanosecond surface dielectric barrier discharge (nSDBD) at elevated pressure. The conditions and parameters of streamer–to–filament transition in the pressure range $1 - 12$ bar for N_2/O_2 gas mixtures containing $0, 1, 2, 5, 10$ and 20% of oxygen for both negative and positive polarities were investigated.

The streamer–to–filament transition happens similarly in all observed experimental conditions. At low voltages and pressures, the streamer discharge starts from the edge of the high–voltage electrode. With the increase of voltage on the electrode and/or gas pressure, the discharge channels are constricted and a few filamentary channels appear on the edge of the high–voltage electrode, propagating in the radial direction towards the ground electrode. There is no distinctive difference of the transition process between negative and positive polarities but the transition thresholds are totally different.

For negative polarity high–voltage pulse, the threshold voltage almost does not change with pressure. During first 12 ns of discharge, streamer–to–filament transition happened within a "corridor" of voltage amplitudes $30 - 40$ kV for PVC and $14 - 18$ kV for ceramics as a dielectric. For positive polarity high–voltage pulse, the threshold voltage changes dramatically: it drops down from 55 to 20 kV as pressure increases from 3 to 12 bar for PVC as a dielectric and from 26 to 15 kV as pressure increases from 5 to 9 bar for ceramics as a dielectric.

Significant difference is observed at positive polarity when changing gas mixture composition: at 8 bar, the threshold voltage in air is twice higher than the threshold voltage in nitrogen. Adding 1% of molecular oxygen to pure nitrogen leads to sharp increase of the threshold voltage: at 4 bar, the threshold voltage increases from 41 kV to 52 kV.

Modifications of material/structure of the high–voltage electrode (annealed or non–annealed, copper or copper covered with carbon nanomaterials) causes only minor influence.

The major difference in the threshold voltage as a function of polarity, gas mixture composition and dielectric permittivity of the surface in the proximity of plasma leads to the conclusion that streamer–to–filament transition can be a consequence of severe transformation of plasma parameters.

Plasma parameters in the filaments were studied with the help of electrical measurements, optical emission spectroscopy, Particle Image Velocimetry (PIV) and kinetic modeling. It was found that the specific deposited energy in the filamentary plasma can be as high as $6 - 7$ eV/particle for both polarities of the high–voltage pulse. High specific deposited energy in the filaments was confirmed by PIV measurements demonstrating formation of large–scale turbulent structures at the place of the filaments at the time scale of 0.3 ms.

Synchronized measurements of voltage on the electrode, discharge optical emission spectra and electron density showed that (i) cw spectra appear together with the broadened atomic lines; (ii) electron density decay is slow, tens of nanosecond; (iii) electron temperature in the near afterglow stays high, a few electronvolts.

Numerical modeling proves a possibility to get via stepwise ionization and dissociation from electronically excited states of molecular nitrogen, plasma with high electron density ($\sim 10^{19}$ cm^{-3}), almost complete dissociation and gas temperature T_g close to electron temperature T_e. Time scale of increase of gas temperature to the value close to the electron temperature (to get the state close to local thermodynamic equilibrium (LTE)) is 0.2 ns in nitrogen at pressure $p = 6$ bar and initial reduced electric field $(E/N)_0 = 230$ Td.

To link two observed states of plasma in nSDBD, a streamer with $T_g \ll T_e$ and a filament with plasma close to LTE, the transition was studied by ICCD imaging and optical emission spectroscopy combined with microscopy. It was found that before the transition, thin channels with streamer–like plasma are formed stochastically in the bulk of plasma. These channels are the "prototypes" of future filaments, we call them "protrusions", their diameter is almost 10 times smaller than the diameter of a streamer. Time– and space–resolved measurements showed that the cw emission starts when a wave of emission (a "backward" emission) passes from the head of protrusion to a distance about 1 mm from the high–voltage electrode. Then cw

emission and high electron density appear, first at the point $\sim$ 1 mm apart from the electrode, and being observed along all the filament the next nanosecond. Performed numerical modeling confirm that a reason of different threshold voltages for streamer–to–filament transition can be linked to difference in deposited energy because of different kinetics of recombination/attachment as a function of gas mixture composition.

7.2 Perspectives and future work

The results of streamer–to–filament transition presented in the current thesis enrich the knowledge about nSDBD at elevated gas pressures. However, several questions such as the mechanism of discharge channel constriction, dependence of plasma parameters (electron temperature T_e and electron density n_e) upon polarity of applied high voltage and gas composition, the effect of photoionization and kinetics of recombination on the streamer–to–filament transition and the suitable numerical model for calculating the transition remain open.

As continuation of this thesis, a parametric study of time–resolved electron density and electron temperature for both polarities in different gas mixtures can be performed. For streamer–to–filament transition, suggested and developed in this thesis cylindrical electrode can be used as a setup for laser diagnostics.

Taking into account that the process of transition is extremely fast (H_α emission provides simultaneous appearance of high electron density along $\sim$ 3 mm filament during $\sim$ 1 ns), a picosecond TALIF can provide O and N–atoms measurements resolved in time and space. Picosecond laser electric field induced second harmonic generation (E–FISH) can be used for 2D–mapping of the electric field in transitory regime.

Finally, 2D numerical modeling including streamer kinetics can be improved by implementing main reactions corresponding to LTE plasma and used to better understand how the critical parameter of plasma distributed in time and space. 2D time–resolved electron density, electric field, $N_2(C^3\Pi_u)$ emission and H_α emission can be considered as markers for analysis of streamer–to–filament transition.

Appendix

A.1 Filamentary sDBD on cylindrical electrode

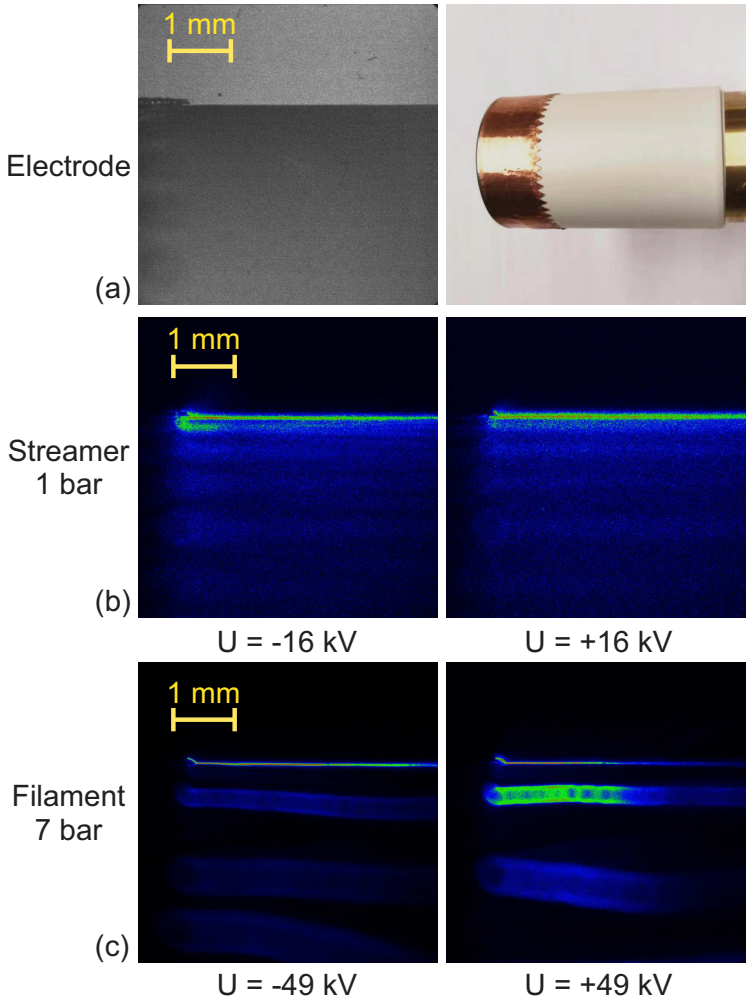

Figure 1: ICCD images of (a) cylindrical electrode; (b) streamer discharge in atmospheric air at $U = \pm 16$ kV; (c) filamentary discharge in 7 bar air at $U = \pm 49$ kV. ICCD camera gate is 20 ns. Resolution of the optical system is 1 μm/px.

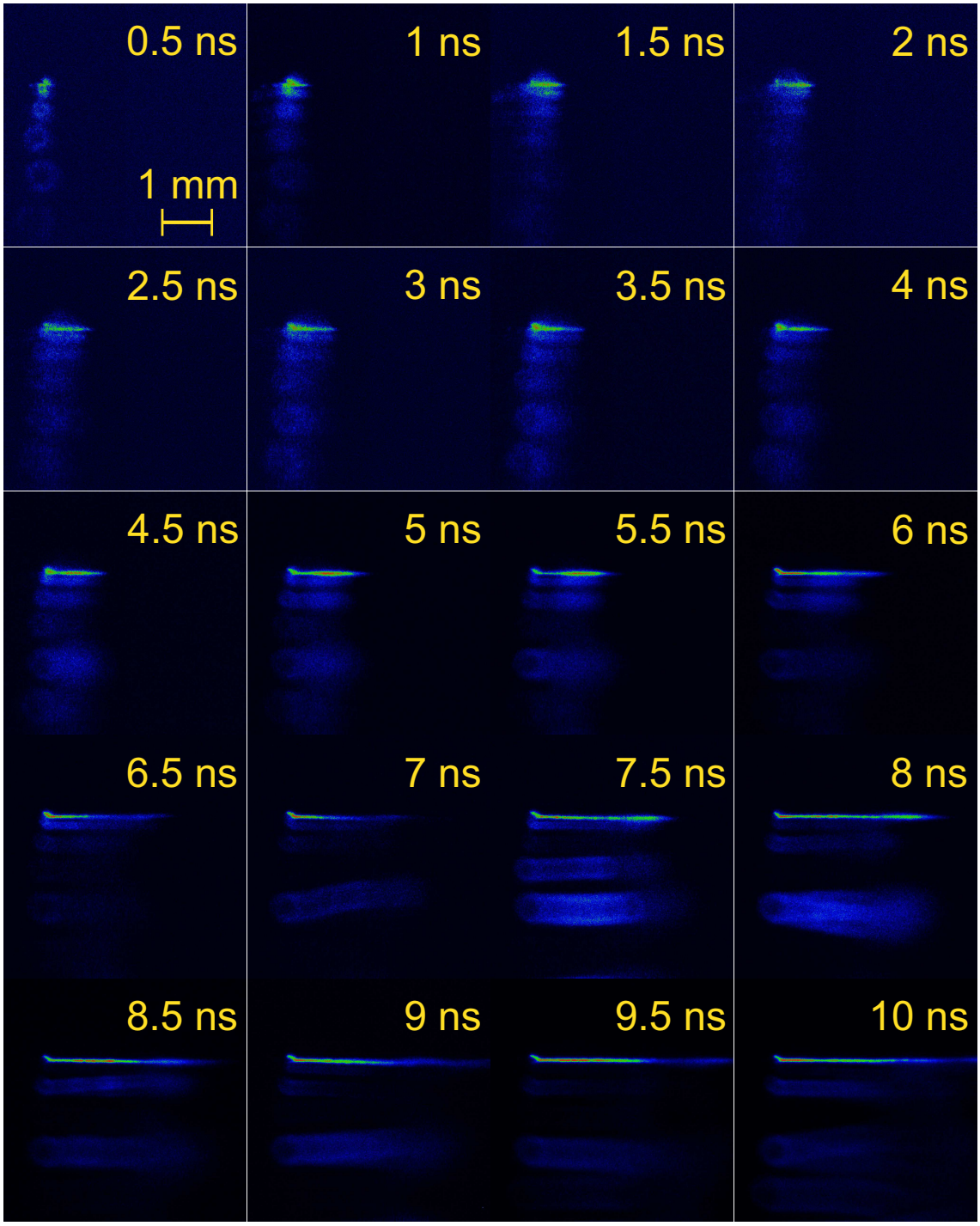

Figure 2: Micro–images of discharge propagation on cylindrical electrode in 7 bar air at negative polarity. Voltage $U = -49$ kV. Camera gate is 0.5 ns. Resolution of the optical system is 1 μm/px. Time instant is marked with yellow in each frame.

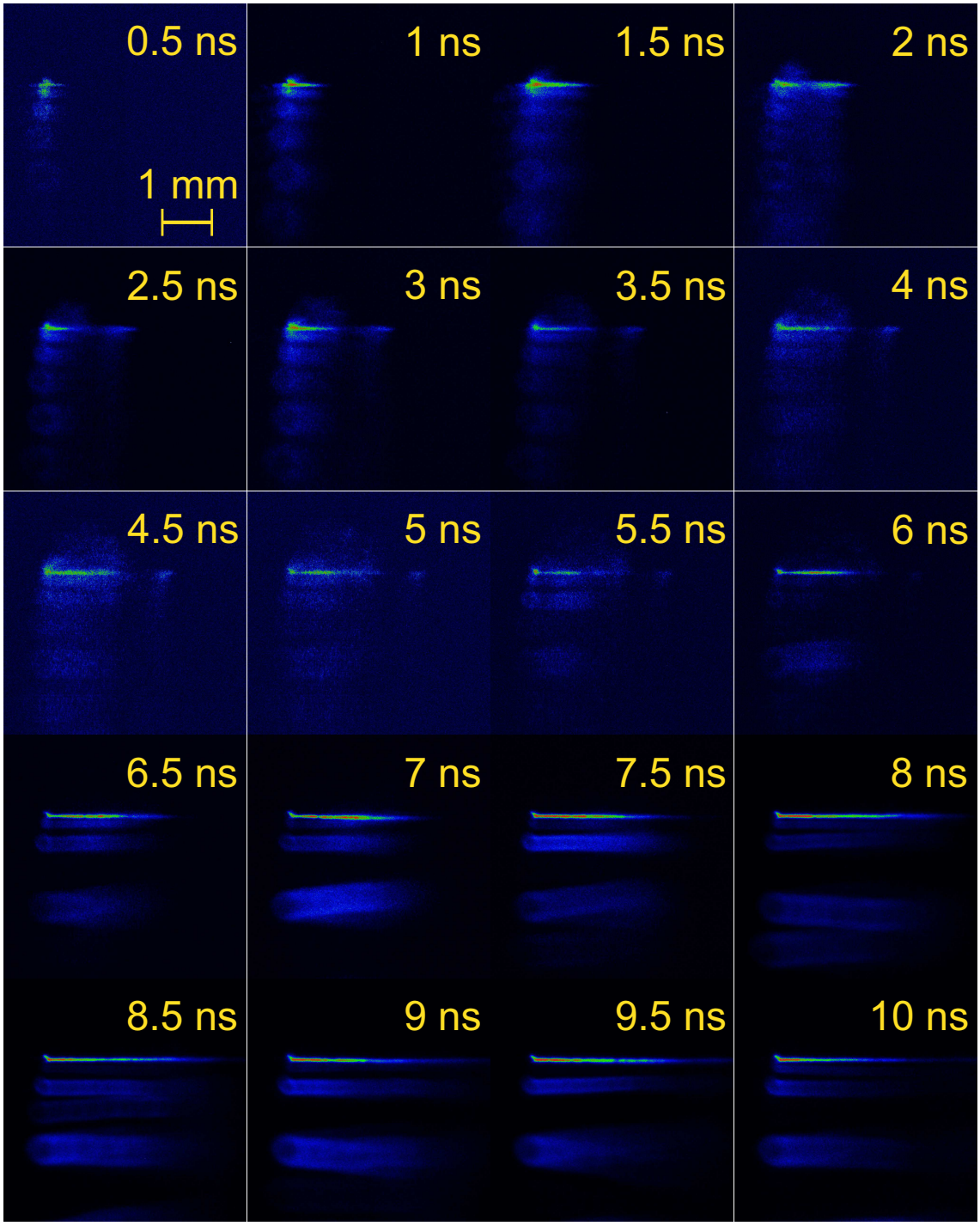

Figure 3: Micro–images of discharge propagation on cylindrical electrode in 7 bar air at positive polarity. Voltage $U = +49$ kV. Camera gate is 0.5 ns. Resolution of the optical system is 1 μm/px. Time instant is marked with yellow in each frame.

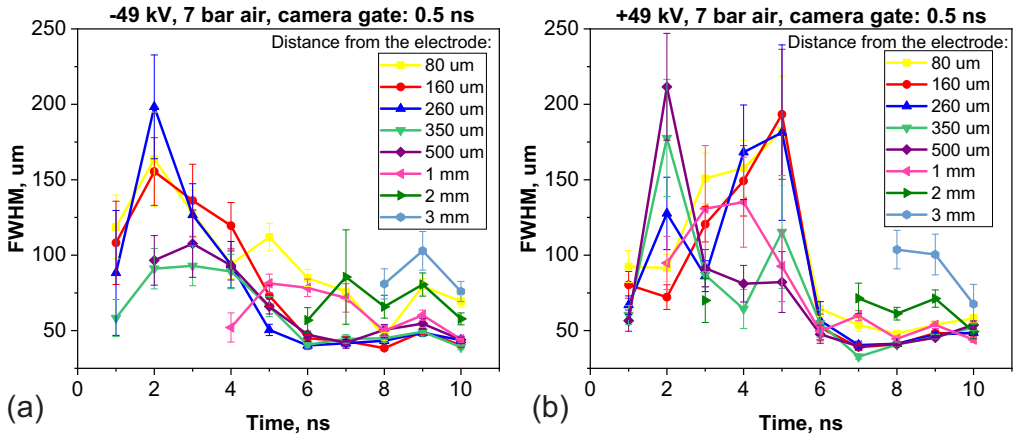

Figure 4: Full width at half maximum (FWHM) of filamentary plasma channels at different positions from the high–voltage electrode. $U = \pm 49$ kV, 7 bar, air. Resolution of the optical system is 1 μm/px.

A.2 Spectra of filamentary sDBD at positive polarity

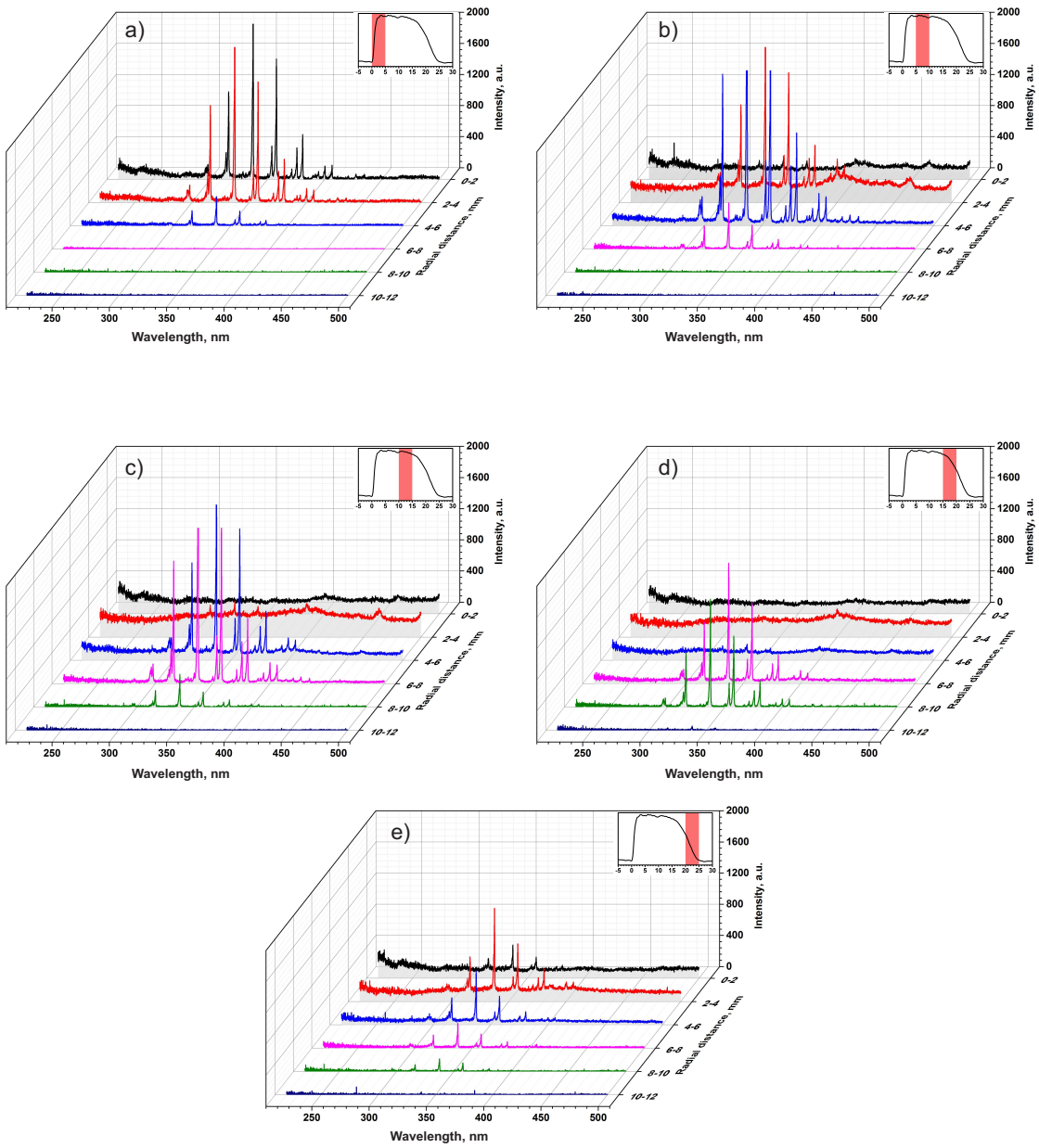

Figure 5: Emission spectra of the positive polarity discharge in air. $U = +50$ kV, 6 bar. The spectra are corrected to the sensitivity function of the optical system. The figure is taken from [95].

A.3 ICCD images and energy deposition of filamentary sDBD at both negative and positive polarities in nitrogen and air

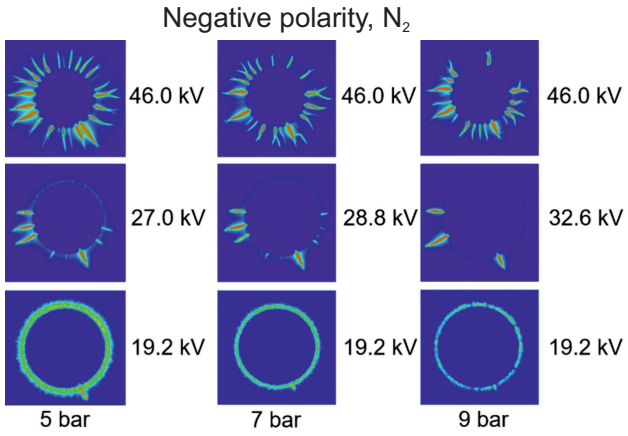

Figure 6: ICCD images of streamer surface discharge, transitive discharge and developed filamentary discharge on PVC surface at three given pressures (5 bar, 7 bar and 9 bar). Nitrogen, applied voltage varying from $U = -19.2$ kV to $U = -46$ kV. Camera gate is 12 ns. The diameter of the high–voltage electrode (circle at the center of each image) is equal to 20 mm.

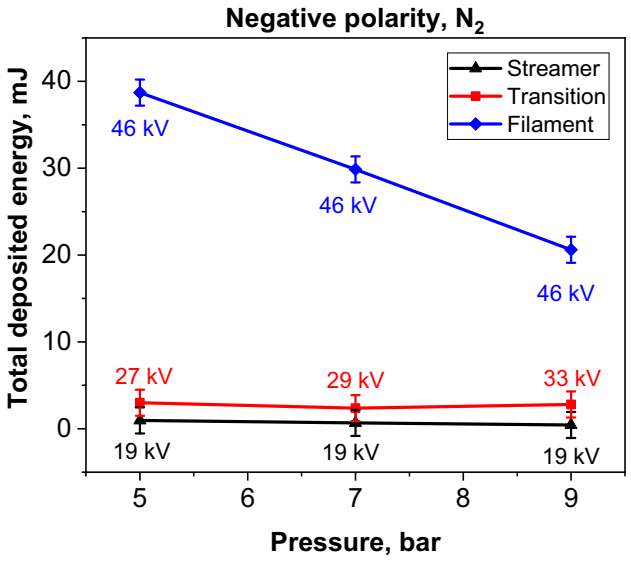

Figure 7: Total deposited energy of streamer, transitive and filamentary discharge at negative polarity in nitrogen as a function of pressure.

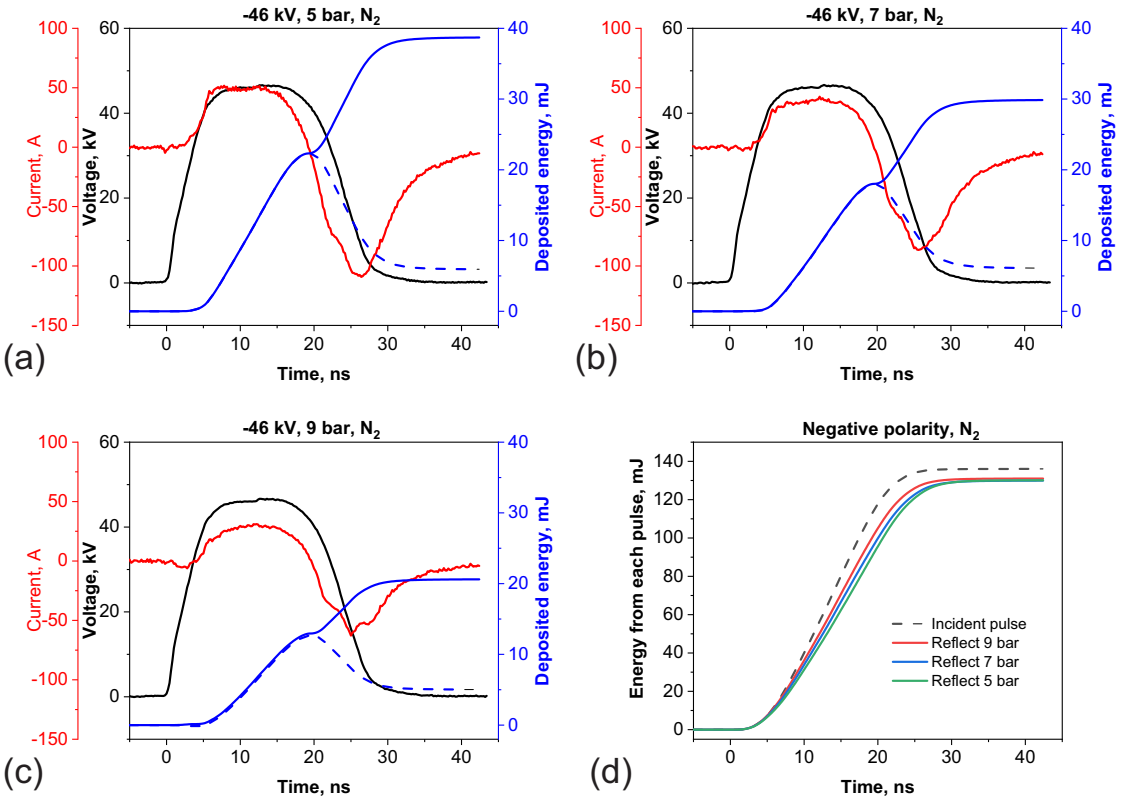

Figure 8: Measured voltage, current, and energy deposition at negative polarity in (a) 5 bar; (b) 7 bar; (c) 9 bar nitrogen. (d) Energy deposition of both incident and reflected pulses.

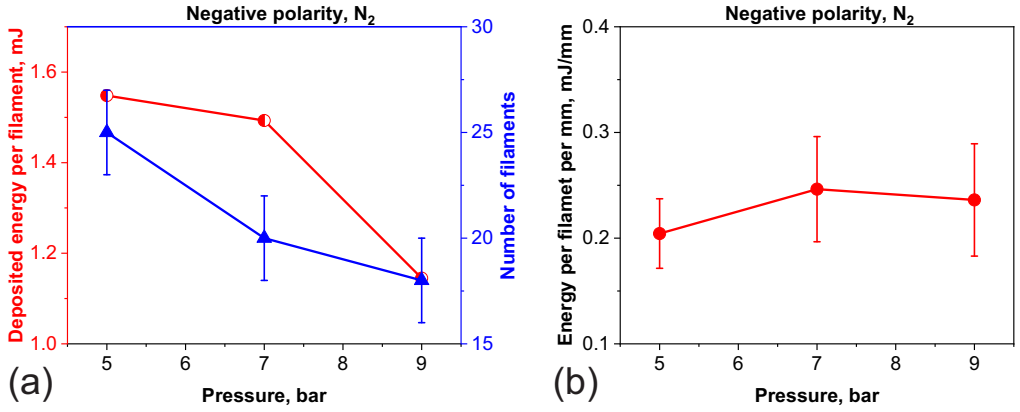

Figure 9: (a) Number of filaments and the deposited energy per filament; (b) the energy per filament per mm of the discharge at negative polarity in nitrogen as a function of pressure.

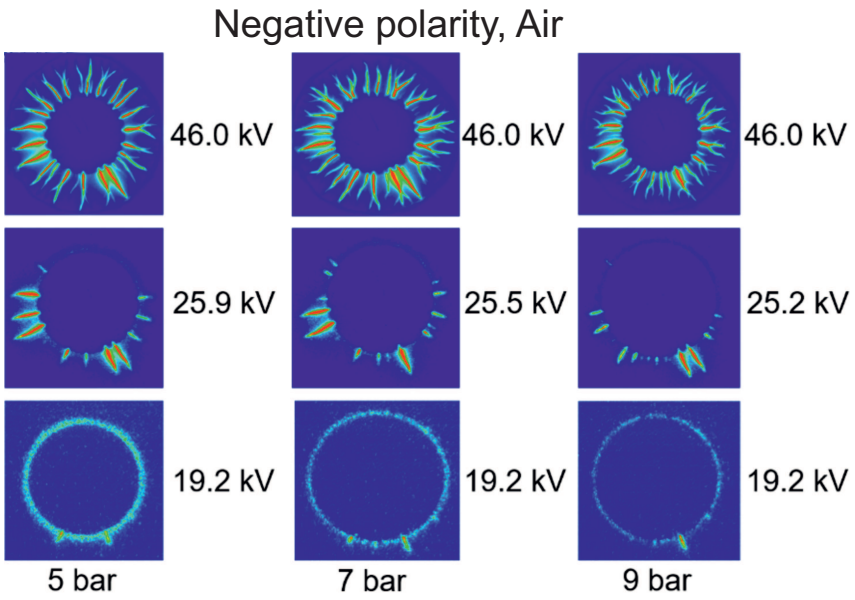

Figure 10: ICCD images of streamer surface discharge, transitive discharge and developed filamentary discharge on PVC surface at three given pressures (5 bar, 7 bar and 9 bar). Air, applied voltage varying from $U = -19.2$ kV to $U = -46$ kV. Camera gate is 12 ns. The diameter of the high–voltage electrode (circle at the center of each image) is equal to 20 mm.

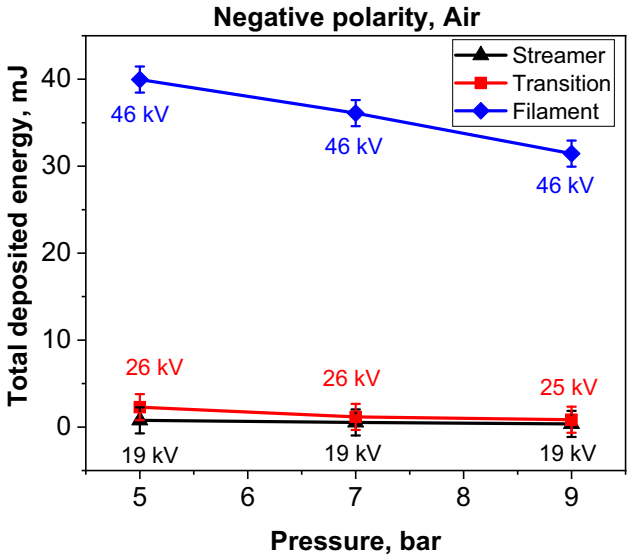

Figure 11: Total deposited energy of streamer, transitive and filamentary discharge at negative polarity in air as a function of pressure.

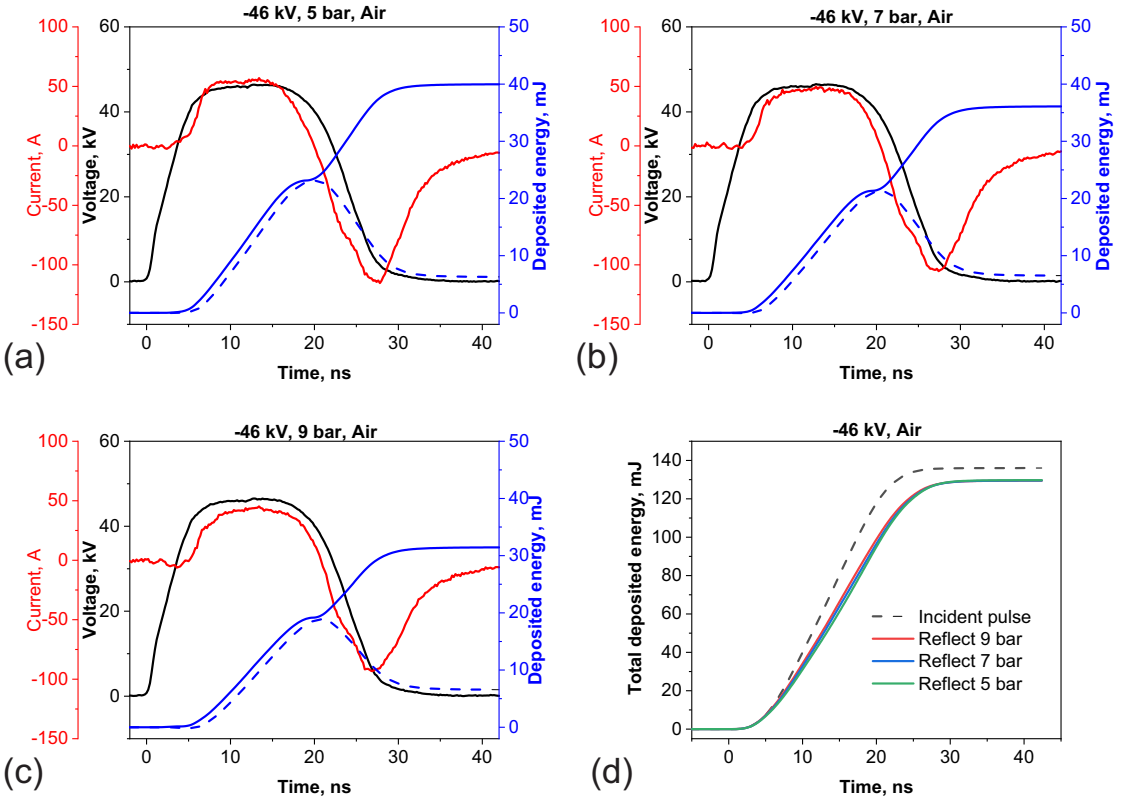

Figure 12: Measured voltage, current, and energy deposition at negative polarity in (a) 5 bar; (b) 7 bar; (c) 9 bar air. (d) Energy deposition of both incident and reflected pulses.

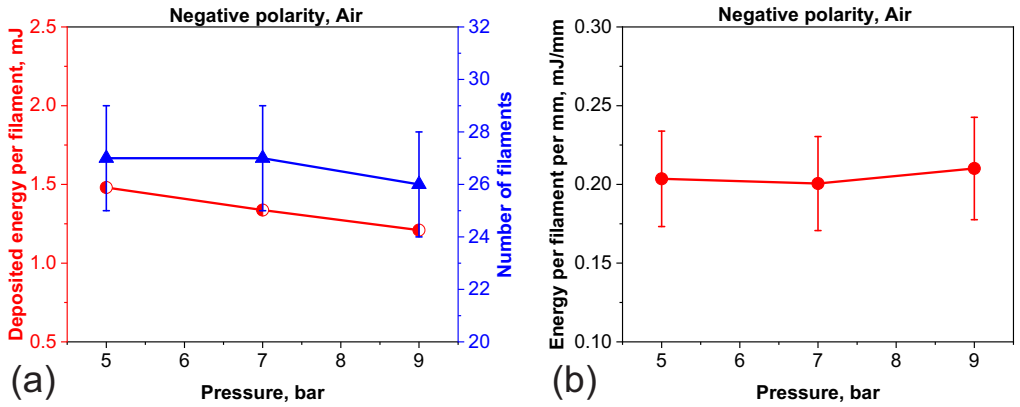

Figure 13: (a) Number of filaments and the deposited energy per filament; (b) the energy per filament per mm of the discharge at negative polarity in air as a function of pressure.

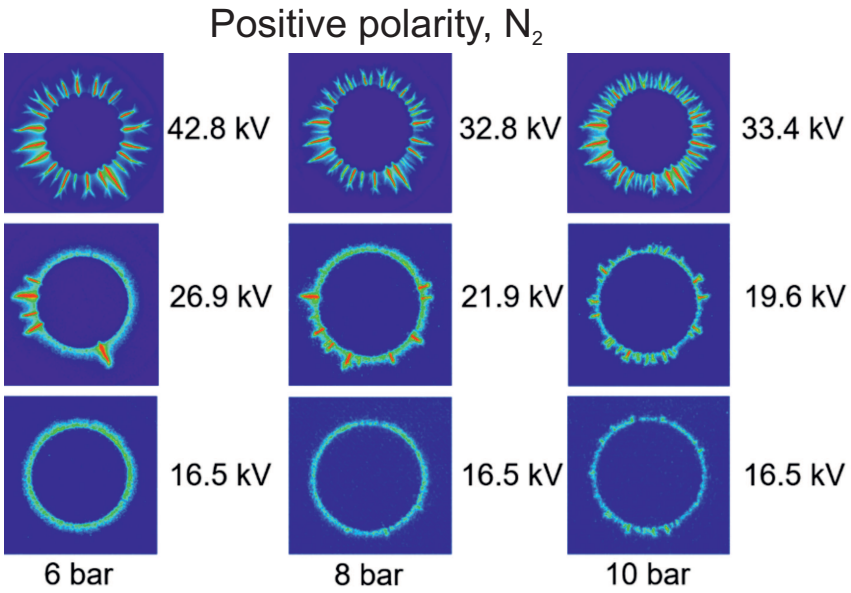

Figure 14: ICCD images of streamer surface discharge, transitive discharge and developed filamentary discharge on PVC surface at three given pressures (6 bar, 8 bar and 10 bar). Nitrogen, applied voltage varying from $U = +16.5$ kV to $U = +42.8$ kV. Camera gate is 12 ns. The diameter of the high–voltage electrode (circle at the center of each image) is equal to 20 mm.

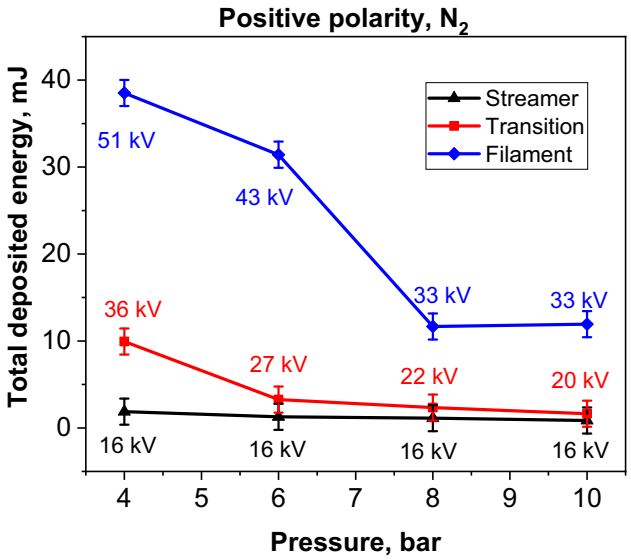

Figure 15: Total deposited energy of streamer, transitive and filamentary discharge at positive polarity in nitrogen as a function of pressure.

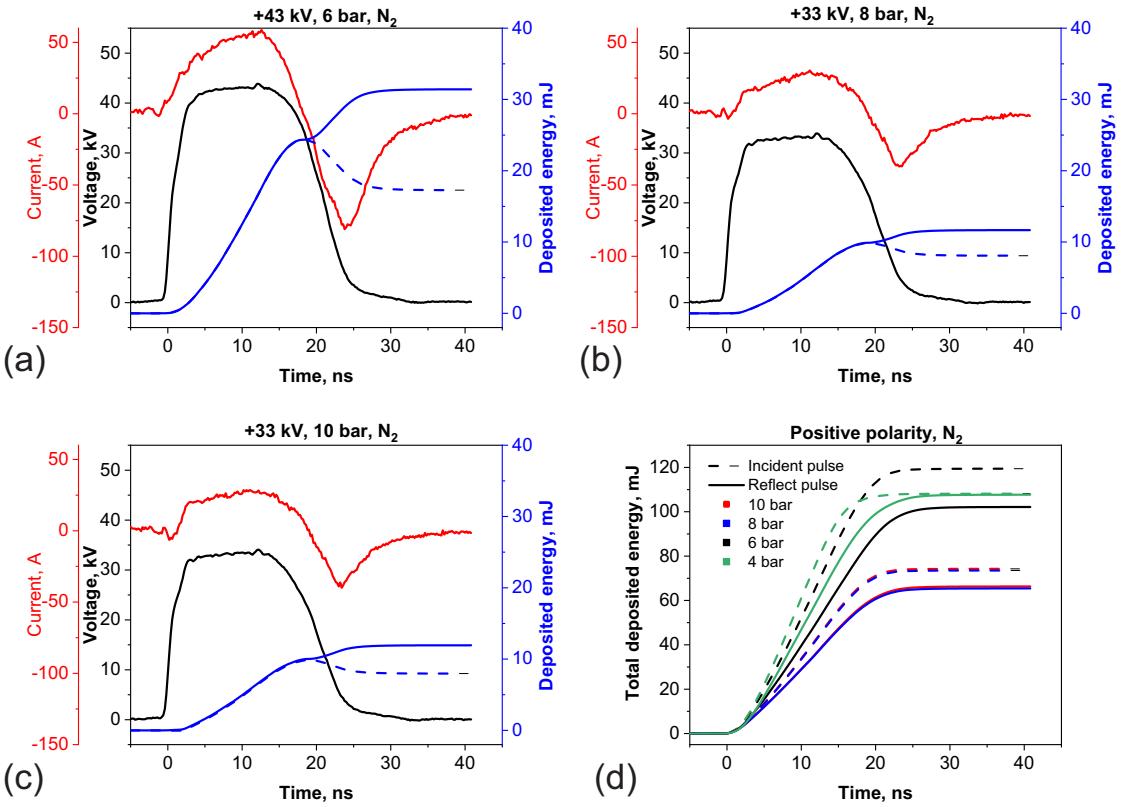

Figure 16: Measured voltage, current, and energy deposition at positive polarity in (a) 6 bar; (b) 8 bar; (c) 10 bar nitrogen. (d) Energy deposition of both incident and reflected pulses.

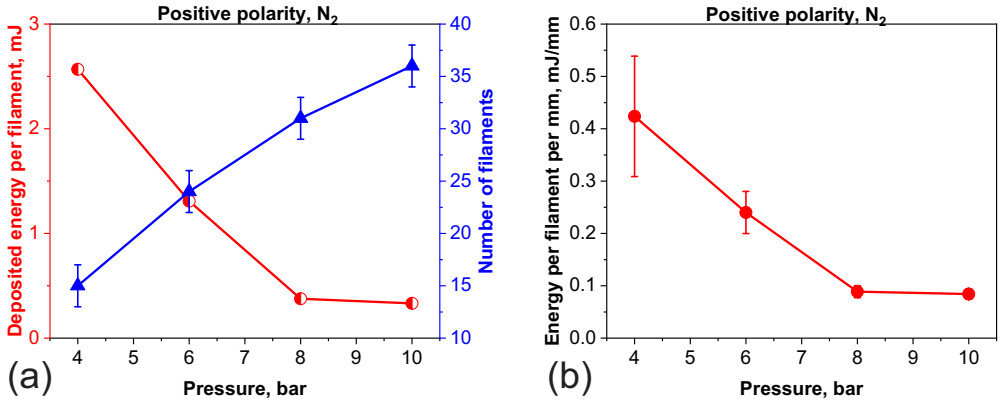

Figure 17: (a) Number of filaments and the deposited energy per filament; (b) the energy per filament per mm of the discharge at positive polarity in nitrogen as a function of pressure.

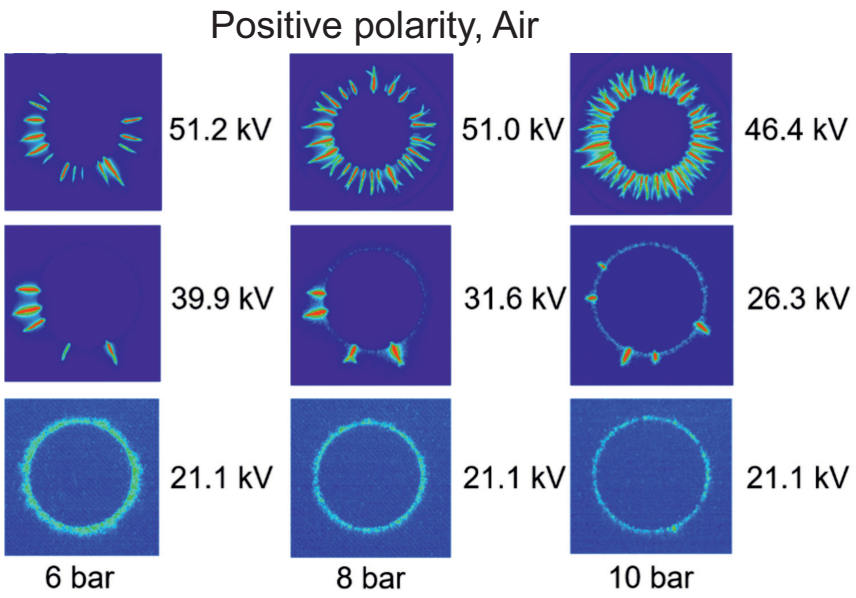

Figure 18: ICCD images of streamer surface discharge, transitive discharge and developed filamentary discharge on PVC surface at three given pressures (6 bar, 8 bar and 10 bar). Air, applied voltage varying from $U = +21.1$ kV to $U = +51.2$ kV. Camera gate is 12 ns. The diameter of the high–voltage electrode (circle at the center of each image) is equal to 20 mm.

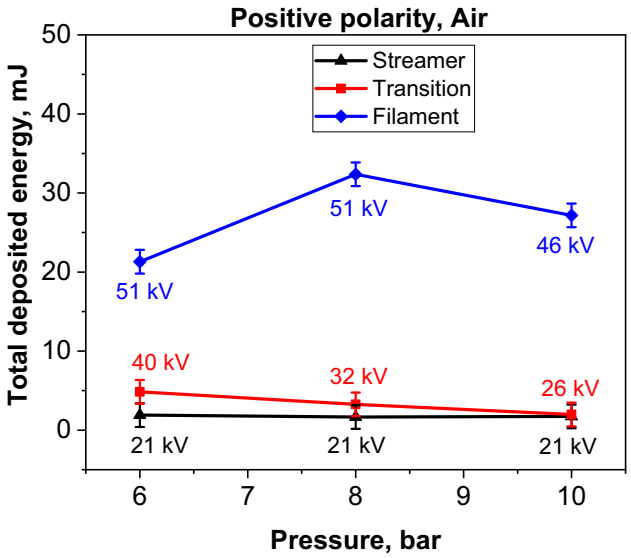

Figure 19: Total deposited energy of streamer, transitive and filamentary discharge at positive polarity in air as a function of pressure.

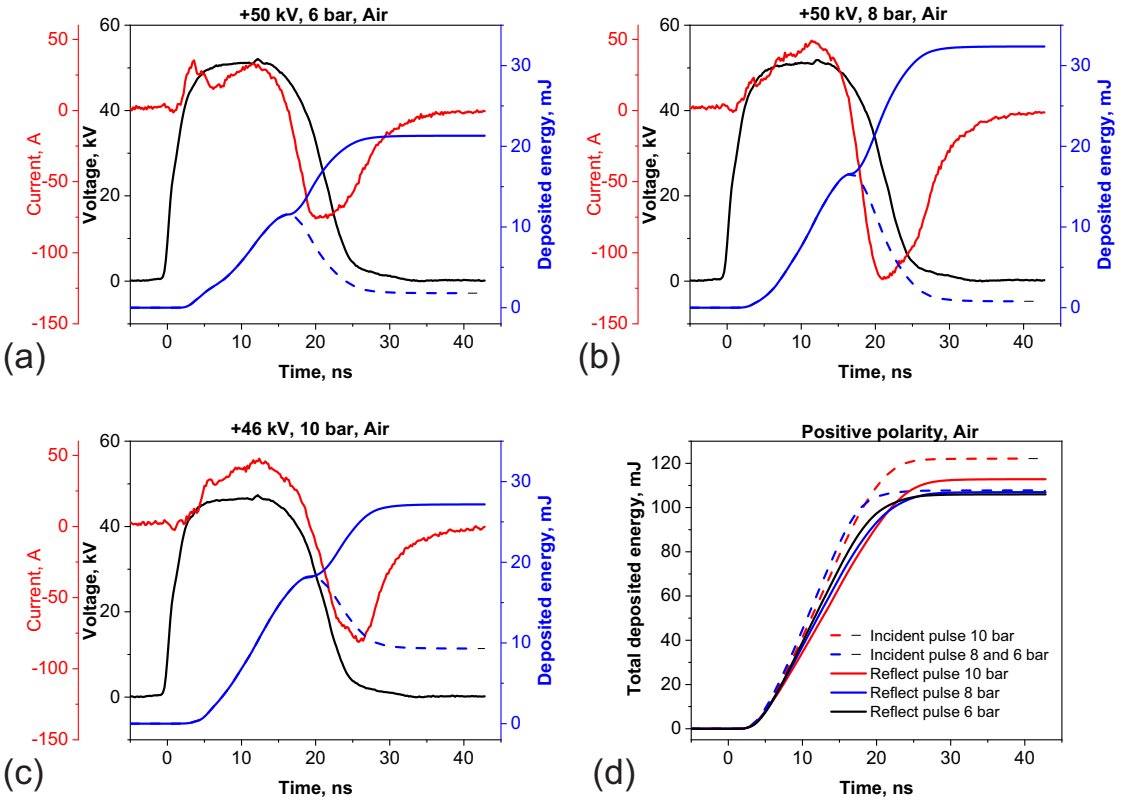

Figure 20: Measured voltage, current, and energy deposition at positive polarity in (a) 6 bar; (b) 8 bar; (c) 10 bar air. (d) Energy deposition of both incident and reflected pulses.

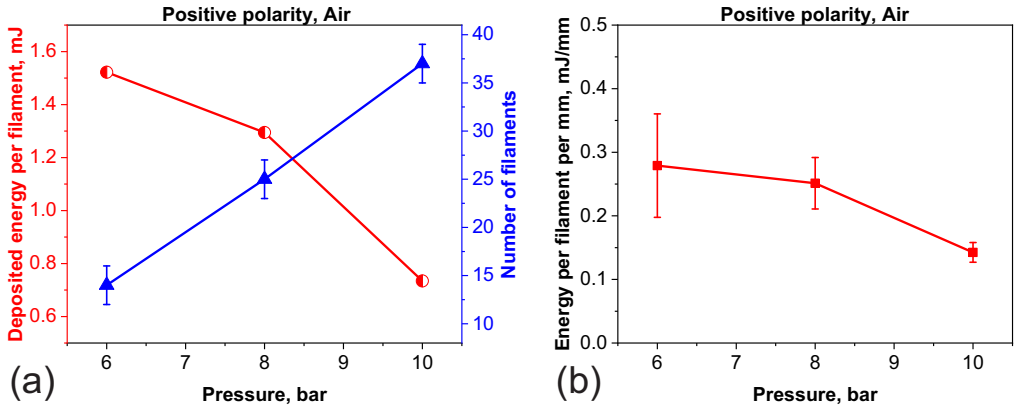

Figure 21: (a) Number of filaments and the deposited energy per filament; (b) the energy per filament per mm of the discharge at positive polarity in air as a function of pressure.

List of Figures

List of Publications

Publications in reviewed journals

1. Ding, C., Khomenko, A.Y., Shcherbanev, S.A. and Starikovskaia, S.M.. Filamentary nanosecond surface dielectric barrier discharge. Experimental comparison of the streamer-to-filament transition for positive and negative polarities. *Plasma Sources Science and Technology* 2019, 28(8), p.085005.

2. Shcherbanev, S.A., Ding, C., Starikovskaia, S.M. and Popov, N.A.. Filamentary nanosecond surface dielectric barrier discharge. Plasma properties in the filaments. *Plasma Sources Science and Technology* 2019, 28(6), p.065013.

3. Chng, T.L., Ding, C., Naphade, M., Goldberg, B.M., Adamovich, I.V. and Starikovskaia, S.M.. Characterization of an optical pulse slicer for gas-phase electric field measurements using field-induced second harmonic generation. *Journal of Instrumentation* 2020, 15(03), p.C03005.

4. Selivonin, I., Ding, C., Starikovskaia, S. and Moralev, I.. The effect of the exposed electrode oxidation on the filamentation thresholds of a nanosecond DBD. *Journal of Physics: Conference Series* 2020, 1698(1), p. 012028.

Conference proceedings

1. Ding, C., Shcherbanev, S.A. and Starikovskaia, S.M., Time-resolved electron temperature OES measurement in filamentary discharge. *24th Europhysics Conference on Atomic and Molecular Physics of Ionized Gases (ESCAMPIG XXIV)* July 2018, Glasgow, Scotland.

2. Ding, C., Shcherbanev, S.A., Chng, T.L., Popov, N.A. and Starikovskaia, S.M.. Streamer–to–filamentary transition and electron temperature measurement in positive polarity nanosecond surface discharge between 1 and 10 bar. *AIAA*

Scitech 2019 Forum Jan 2019, San Diego, California, United States. p.AIAA 2019-0462.

3. Ding, C., Shcherbanev, S.A. and Starikovskaia, S.. Oxygen effects in the transition process of streamer–to–filament nanosecond surface dielectric barrier discharge. *13th Frontiers in Low-Temperature Plasma Diagnostics (FTLDP) and 1st Frontiers in Low-Temperature Plasma Simulations (FTLPS)* May 2019, Bad Honnef, Germany.

4. Ding, C., Shcherbanev, S.A. and Starikovskaia, S.. Measurement of electron temperature and electron density in filamentary nanosecond surface dielectric barrier discharge. *24th International Symposium on Plasma Chemistry (ISPC XXIV)* June 2019, Naples, Italy.

5. Ding, C., Jean, A., Shcherbanev, S., Selivonin, I., Moralev, I., Popov, N.A. and Starikovskaia, S.. Experimental study of energy delivered to the filaments in high pressure nanosecond surface discharge. *AIAA Scitech 2020 Forum* Jan 2020, Orlando, Florida, United States. p.AIAA 2020-1662.

6. Ding, C., Yerlanuly, Y., Gabdullin, M., Batryshev, D., Ramazanov, T. and Starikovskaia, S.M., Experiments on the streamer–filamentary transition using carbon nanomaterial electrodes. *25th Europhysics Conference on Atomic and Molecular Physics of Ionized Gases (ESCAMPIG XXV)* July 2020, Paris, France.

7. Ding, C., Jean, A., Popov, N.A. and Starikovskaia, S.M.. Spectral micro–scale measurements of the initial stage of streamer–to–filament transition in high pressure nanosecond surface dielectric barrier discharge. *AIAA Scitech 2021 Forum* Jan 2021, Virtual event. p.AIAA 2021-1699.

Bibliography

[1] W. Siemens, "Ueber die elektrostatische induction und die verzögerung des stroms in flaschendrähten," *Annalen der Physik*, vol. 178, no. 9, pp. 66–122, 1857.

[2] T. Andrews and P. G. Tait, "On the volumetric relations of ozone, and the action of the electrical discharge on oxygen and other gases," *philosophical transactions of the royal society*, vol. 150, no. 7, pp. 113–131, 1860.

[3] U. Kogelschatz, "Dielectric-barrier discharges: their history, discharge physics, and industrial applications," *Plasma chemistry and plasma processing*, vol. 23, no. 1, pp. 1–46, 2003.

[4] K. Buss, "Die elektrodenlose entladung nach messung mit dem kathodenoszillographen," *Archiv für Elektrotechnik*, vol. 26, no. 4, pp. 261–265, 1932.

[5] U. Kogelschatz, "Advanced ozone generation," in *Process technologies for water treatment*, pp. 87–118, Springer, 1988.

[6] R. Brandenburg, "Dielectric barrier discharges: progress on plasma sources and on the understanding of regimes and single filaments," *Plasma Sources Science and Technology*, vol. 26, no. 5, p. 053001, 2017.

[7] E. Moreau, "Airflow control by non-thermal plasma actuators," *Journal of physics D: applied physics*, vol. 40, no. 3, p. 605, 2007.

[8] M. Forte, J. Jolibois, J. Pons, E. Moreau, G. Touchard, and M. Cazalens, "Optimization of a dielectric barrier discharge actuator by stationary and non-stationary measurements of the induced flow velocity: application to airflow control," *Experiments in fluids*, vol. 43, no. 6, pp. 917–928, 2007.

[9] N. Benard and E. Moreau, "Electrical and mechanical characteristics of surface ac dielectric barrier discharge plasma actuators applied to airflow control," *Experiments in Fluids*, vol. 55, no. 11, p. 1846, 2014.

[10] M. Černák, I. Hudec, D. Kováčik, A. Zahoranová, *et al.*, "Diffuse coplanar surface barrier discharge and its applications for in-line processing of low-added-value materials," *The European Physical Journal Applied Physics*, vol. 47, no. 2, p. 22806, 2009.

[11] B. Eliasson and U. Kogelschatz, "Modeling and applications of silent discharge plasmas," *IEEE transactions on plasma science*, vol. 19, no. 2, pp. 309–323, 1991.

[12] X. Tu and J. Whitehead, "Plasma-catalytic dry reforming of methane in an atmospheric dielectric barrier discharge: Understanding the synergistic effect at low temperature," *Applied Catalysis B: Environmental*, vol. 125, pp. 439–448, 2012.

[13] H.-H. Kim, "Nonthermal plasma processing for air-pollution control: a historical review, current issues, and future prospects," *Plasma Processes and Polymers*, vol. 1, no. 2, pp. 91–110, 2004.

[14] A. Mizuno, "Industrial applications of atmospheric non-thermal plasma in environmental remediation," *Plasma Physics and Controlled Fusion*, vol. 49, no. 5A, p. A1, 2007.

[15] J. Chang, "Physics and chemistry of plasma pollution control technology," *Plasma Sources Science and Technology*, vol. 17, no. 4, p. 045004, 2008.

[16] R. Brandenburg, H. Barankova, L. Bardos, A. G. Chmielewski, M. Dors, H. Grosch, M. Hołub, I. Jogi, M. Laan, J. Mizeraczyk, *et al.*, "Plasma-based depollution of exhausts: principles, state of the art and future prospects," in *Monitoring, control and effects of air pollution*, pp. 229–254, InTech, 2011.

[17] M. Schmidt, I. Jõgi, M. Hołub, and R. Brandenburg, "Non-thermal plasma based decomposition of volatile organic compounds in industrial exhaust gases," *International journal of environmental science and technology*, vol. 12, no. 12, pp. 3745–3754, 2015.

[18] Y. Tanaka, "Continuous emission spectra of rare gases in the vacuum ultraviolet region," *JOSA*, vol. 45, no. 9, pp. 710–713, 1955.

[19] U. Kogelschatz, H. Esrom, J.-Y. Zhang, and I. Boyd, "High-intensity sources of incoherent uv and vuv excimer radiation for low-temperature materials processing," *Applied Surface Science*, vol. 168, no. 1-4, pp. 29–36, 2000.

[20] G. Borcia, C. Anderson, and N. Brown, "Dielectric barrier discharge for surface treatment: application to selected polymers in film and fibre form," *Plasma Sources Science and Technology*, vol. 12, no. 3, p. 335, 2003.

[21] G. Borcia, C. Anderson, and N. Brown, "Surface treatment of natural and synthetic textiles using a dielectric barrier discharge," *Surface and Coatings Technology*, vol. 201, no. 6, pp. 3074–3081, 2006.

[22] D. Mariotti, T. Belmonte, J. Benedikt, T. Velusamy, G. Jain, and V. Švrček, "Low-temperature atmospheric pressure plasma processes for "green" third generation photovoltaics," *Plasma Processes and Polymers*, vol. 13, no. 1, pp. 70–90, 2016.

[23] M. Heise, W. Neff, O. Franken, P. Muranyi, and J. Wunderlich, "Sterilization of polymer foils with dielectric barrier discharges at atmospheric pressure," *Plasmas and polymers*, vol. 9, no. 1, pp. 23–33, 2004.

[24] S. K. Pankaj, C. Bueno-Ferrer, N. Misra, L. O'Neill, A. Jiménez, P. Bourke, and P. Cullen, "Characterization of polylactic acid films for food packaging as affected by dielectric barrier discharge atmospheric plasma," *Innovative Food Science & Emerging Technologies*, vol. 21, pp. 107–113, 2014.

[25] R. Matthes, C. Bender, R. Schlüter, I. Koban, R. Bussiahn, S. Reuter, J. Lademann, K.-D. Weltmann, and A. Kramer, "Antimicrobial efficacy of two surface barrier discharges with air plasma against in vitro biofilms," *PloS one*, vol. 8, no. 7, p. e70462, 2013.

[26] G. Fridman, M. Peddinghaus, M. Balasubramanian, H. Ayan, A. Fridman, A. Gutsol, and A. Brooks, "Blood coagulation and living tissue sterilization by floating-electrode dielectric barrier discharge in air," *Plasma Chemistry and plasma processing*, vol. 26, no. 4, pp. 425–442, 2006.

[27] N. Y. Babaeva and M. J. Kushner, "Intracellular electric fields produced by dielectric barrier discharge treatment of skin," *Journal of Physics D: Applied Physics*, vol. 43, no. 18, p. 185206, 2010.

[28] K.-d. Weltmann, R. Brandenburg, S. Krafczyk, M. Stieber, and T. Von Woedtke, "Device for the plasma treatment of human, animal or plant surfaces, in particular of skin or mucous membrane areas," July 30 2019. US Patent 10,363,429.

[29] S. Starikovskaia, "Plasma assisted ignition and combustion," *Journal of Physics D: Applied Physics*, vol. 39, no. 16, p. R265, 2006.

[30] I. Kosarev, V. Khorunzhenko, E. Mintoussov, P. Sagulenko, N. Popov, and S. Starikovskaia, "A nanosecond surface dielectric barrier discharge at elevated pressures: time-resolved electric field and efficiency of initiation of combustion," *Plasma Sources Science and Technology*, vol. 21, no. 4, p. 045012, 2012.

[31] S. Starikovskaia, "Plasma-assisted ignition and combustion: nanosecond discharges and development of kinetic mechanisms," *Journal of Physics D: Applied Physics*, vol. 47, no. 35, p. 353001, 2014.

[32] M. I. Boulos, P. Fauchais, and E. Pfender, *Thermal plasmas: fundamentals and applications*. Springer Science & Business Media, 1994.

[33] A. Fridman, *Plasma chemistry*. Cambridge university press, 2008.

[34] V. N. Ochkin, *Spectroscopy of low temperature plasma*. John Wiley & Sons, 2009.

[35] D. Z. Pai, G. D. Stancu, D. A. Lacoste, and C. O. Laux, "Nanosecond repetitively pulsed discharges in air at atmospheric pressureвЂ"the glow regime," *Plasma Sources Science and Technology*, vol. 18, no. 4, p. 045030, 2009.

[36] D. Z. Pai, D. A. Lacoste, and C. O. Laux, "Transitions between corona, glow, and spark regimes of nanosecond repetitively pulsed discharges in air at atmospheric pressure," *Journal of Applied Physics*, vol. 107, no. 9, p. 093303, 2010.

[37] R. Brandenburg, Z. Navrátil, J. Jánskỳ, P. St'Ahel, D. Trunec, and H.-E. Wagner, "The transition between different modes of barrier discharges at atmospheric pressure," *Journal of Physics D: Applied Physics*, vol. 42, no. 8, p. 085208, 2009.

[38] L. B. Loeb and J. M. Meek, "The mechanism of spark discharge in air at atmospheric pressure. i," *Journal of applied physics*, vol. 11, no. 6, pp. 438–447, 1940.

[39] L. B. Loeb and J. M. Meek, "The mechanism of spark discharge in air at atmospheric pressure. ii," *Journal of applied physics*, vol. 11, no. 7, pp. 459–474, 1940.

[40] S. Stepanyan, A. Y. Starikovskiy, N. Popov, and S. Starikovskaia, "A nanosecond surface dielectric barrier discharge in air at high pressures and different polarities of applied pulses: transition to filamentary mode," *Plasma Sources Science and Technology*, vol. 23, no. 4, p. 045003, 2014.

[41] S. Shcherbanev, C. Ding, S. Starikovskaia, and N. Popov, "Filamentary nanosecond surface dielectric barrier discharge. plasma properties in the filaments," *Plasma Sources Science and Technology*, vol. 28, no. 6, p. 065013, 2019.

[42] C. Ding, A. Y. Khomenko, S. Shcherbanev, and S. Starikovskaia, "Filamentary nanosecond surface dielectric barrier discharge. experimental comparison of the streamer-to-filament transition for positive and negative polarities," *Plasma Sources Science and Technology*, vol. 28, no. 8, p. 085005, 2019.

[43] P. Stritzke, I. Sander, and H. Raether, "Spatial and temporal spectroscopy of a streamer discharge in nitrogen," *Journal of Physics D: Applied Physics*, vol. 10, no. 16, p. 2285, 1977.

[44] H. Albrecht, W. Bloss, W. Herden, R. Maly, B. Saggau, and E. Wagner, "New aspects on spark ignition," tech. rep., SAE Technical Paper, 1977.

[45] M. Lomaev, D. Rybka, D. Sorokin, V. Tarasenko, and K. Y. Krivonogova, "Radiative characteristics of nitrogen upon excitation by volume discharge initiated by runaway electron beam," *Optics and Spectroscopy*, vol. 107, no. 1, pp. 33–40, 2009.

[46] T. Shao, V. F. Tarasenko, C. Zhang, M. I. Lomaev, D. A. Sorokin, P. Yan, A. V. Kozyrev, and E. K. Baksht, "Spark discharge formation in an inhomogeneous electric field under conditions of runaway electron generation," *Journal of Applied Physics*, vol. 111, no. 2, p. 023304, 2012.

[47] N. Minesi, S. Stepanyan, P. Mariotto, G. D. Stancu, and C. O. Laux, "Fully ionized nanosecond discharges in air: the thermal spark," *Plasma Sources Science and Technology*, 2020.

[48] R. Van der Horst, T. Verreycken, E. Van Veldhuizen, and P. Bruggeman, "Time-resolved optical emission spectroscopy of nanosecond pulsed discharges in atmospheric-pressure N_2 and N_2/H_2O mixtures," *Journal of Physics D: Applied Physics*, vol. 45, no. 34, p. 345201, 2012.

[49] B. Du, N. Sadeghi, T. V. Tsankov, D. Luggenhölscher, and U. Czarnetzki, "Temporally resolved optical emission spectroscopic investigations on a nanosecond self-pulsing micro-thin-cathode discharge," *Plasma Sources Science and Technology*, vol. 21, no. 4, p. 045015, 2012.

[50] M. Janda, V. Martišovitš, K. Hensel, L. Dvonč, and Z. Machala, "Measurement of the electron density in transient spark discharge," *Plasma Sources Science and Technology*, vol. 23, no. 6, p. 065016, 2014.

[51] A. Lo, A. Cessou, C. Lacour, B. Lecordier, P. Boubert, D. Xu, C. Laux, and P. Vervisch, "Streamer-to-spark transition initiated by a nanosecond overvoltage pulsed discharge in air," *Plasma Sources Science and Technology*, vol. 26, no. 4, p. 045012, 2017.

[52] M. A. Uman, R. E. Orville, and L. E. Salanave, "The density, pressure, and particle distribution in a lightning stroke near peak temperature," *Journal of Atmospheric Sciences*, vol. 21, no. 3, pp. 306–310, 1964.

[53] M. A. Uman, R. E. Orville, and L. E. Salanave, "The mass density, pressure, and electron density in three lightning strokes near peak temperature," *Journal of Geophysical Research*, vol. 69, no. 24, pp. 5423–5424, 1964.

[54] H. Xu, P. Yuan, J.-Y. Cen, and G.-S. Zhang, "The changes on physical characteristics of lightning discharge plasma during individual return stroke process," *Physics of Plasmas*, vol. 21, no. 3, p. 033512, 2014.

[55] N. Minesi, S. A. Stepanyan, P. B. Mariotto, G.-D. Stancu, and C. O. Laux, "On the arc transition mechanism in nanosecond air discharges," in *AIAA Scitech 2019 Forum*, p. 0463, 2019.

[56] A. Kramida, Yu. Ralchenko, J. Reader, and and NIST ASD Team. NIST Atomic Spectra Database (ver. 5.6.1), [Online]. Available: `https://physics.nist.gov/asd` [2018, March 25]. National Institute of Standards and Technology, Gaithersburg, MD., 2018.

[57] T. Belmonte, H. Kabbara, C. Noël, and R. Pflieger, "Analysis of zn i emission lines observed during a spark discharge in liquid nitrogen for zinc nanosheet synthesis," *Plasma Sources Science and Technology*, vol. 27, no. 7, p. 074004, 2018.

[58] P. Bårmann, S. Kröll, and A. Sunesson, "Spectroscopic measurements of streamer filaments in electric breakdown in a dielectric liquid," *Journal of Physics D: Applied Physics*, vol. 29, no. 5, p. 1188, 1996.

[59] P. Šunka, "Pulse electrical discharges in water and their applications," *Physics of plasmas*, vol. 8, no. 5, pp. 2587–2594, 2001.

[60] T. Namihira, S. Sakai, T. Yamaguchi, K. Yamamoto, C. Yamada, T. Kiyan, T. Sakugawa, S. Katsuki, and H. Akiyama, "Electron temperature and electron density of underwater pulsed discharge plasma produced by solid-state pulsed-power generator," *IEEE transactions on plasma science*, vol. 35, no. 3, pp. 614–618, 2007.

[61] W. An, K. Baumung, and H. Bluhm, "Underwater streamer propagation analyzed from detailed measurements of pressure release," *Journal of applied physics*, vol. 101, no. 5, p. 053302, 2007.

[62] M. Šimek, M. Člupek, V. Babickỳ, P. Lukeš, and P. Šunka, "Emission spectra of a pulse needle-to-plane corona-like discharge in conductive aqueous solutions," *Plasma Sources Science and Technology*, vol. 21, no. 5, p. 055031, 2012.

[63] I. Marinov, S. Starikovskaia, and A. Rousseau, "Dynamics of plasma evolution in a nanosecond underwater discharge," *Journal of Physics D: Applied Physics*, vol. 47, no. 22, p. 224017, 2014.

[64] B. Pongrác, M. Šimek, M. Člupek, V. Babickỳ, and P. Lukeš, "Spectroscopic characteristics of h α/oi atomic lines generated by nanosecond pulsed corona-like discharge in deionized water," *Journal of Physics D: Applied Physics*, vol. 51, no. 12, p. 124001, 2018.

[65] S. Bodrov, V. Bukin, M. Tsarev, A. Murzanev, S. Garnov, N. Aleksandrov, and A. Stepanov, "Plasma filament investigation by transverse optical interferometry and terahertz scattering," *Optics express*, vol. 19, no. 7, pp. 6829–6835, 2011.

[66] X.-M. Zhu, J. L. Walsh, W.-C. Chen, and Y.-K. Pu, "Measurement of the temporal evolution of electron density in a nanosecond pulsed argon microplasma: using both stark broadening and an oes line-ratio method," *Journal of Physics D: Applied Physics*, vol. 45, no. 29, p. 295201, 2012.

[67] B.-D. Huang, K. Takashima, X.-M. Zhu, and Y.-K. Pu, "The influence of the repetition rate on the nanosecond pulsed pin-to-pin microdischarges," *Journal of Physics D: Applied Physics*, vol. 47, no. 42, p. 422003, 2014.

[68] B.-D. Huang, X.-M. Zhu, K. Takashima, and Y.-K. Pu, "The spatial–temporal evolution of the electron density and temperature for a nanosecond microdischarge," *Journal of Physics D: Applied Physics*, vol. 46, no. 46, p. 464011, 2013.

[69] M. Janda, T. Hoder, A. Sarani, R. Brandenburg, and Z. Machala, "Cross-correlation spectroscopy study of the transient spark discharge in atmospheric pressure air," *Plasma Sources Science and Technology*, vol. 26, no. 5, p. 055010, 2017.

[70] A. W. Houpt and S. B. Leonov, "Charge transfer in constricted form of surface barrier discharge at atmospheric pressure," *Journal of Thermophysics and Heat Transfer*, vol. 31, no. 1, pp. 145–153, 2016.

[71] T. Orrière, E. Moreau, and D. Z. Pai, "Ionization and recombination in nanosecond repetitively pulsed microplasmas in air at atmospheric pressure," *Journal of Physics D: Applied Physics*, vol. 51, no. 49, p. 494002, 2018.

[72] T. Orrière, *Confinement microméetrique de déecharges pulsées nanosecondes dans l'ais a pression atmosphérique et effets électro-aérodynamiques.* PhD thesis, University of Poitiers, France, 2018. (in French).

[73] E. Parkevich, M. Medvedev, G. Ivanenkov, A. Khirianova, A. Selyukov, A. Agafonov, P. A. Korneev, S. GusвЂ™kov, and A. Mingaleev, "Fast fine-scale spark filamentation and its effect on the spark resistance," *Plasma Sources Science and Technology*, vol. 28, no. 9, p. 095003, 2019.

[74] E. Parkevich, M. Medvedev, A. Khirianova, G. Ivanenkov, A. Selyukov, A. Agafonov, K. Shpakov, and A. Oginov, "Extremely fast formation of anode spots in an atmospheric discharge points to a fundamental ultrafast breakdown mechanism," *Plasma Sources Science and Technology*, vol. 28, no. 12, p. 125007, 2019.

[75] E. Johnson and L. Malter, "A floating double probe method for measurements in gas discharges," *Physical Review*, vol. 80, no. 1, p. 58, 1950.

[76] F. F. Chen, J. D. Evans, and W. Zawalski, "Electric probes," in *In Plasma Diagnostic Techniques, edited by Huddlestone, RH and Leornard, SL*, Citeseer, 1965.

[77] M. Hopkins and W. Graham, "Langmuir probe technique for plasma parameter measurement in a medium density discharge," *Review of scientific instruments*, vol. 57, no. 9, pp. 2210–2217, 1986.

[78] A. P. Paranjpe, J. P. McVittie, and S. A. Self, "A tuned langmuir probe for measurements in rf glow discharges," *Journal of Applied Physics*, vol. 67, no. 11, pp. 6718–6727, 1990.

[79] F. F. Chen, "Langmuir probe diagnostics," in *Mini-Course on Plasma Diagnostics, IEEEICOPS meeting, Jeju, Korea*, 2003.

[80] R. L. Merlino, "Understanding langmuir probe current-voltage characteristics," *American Journal of Physics*, vol. 75, no. 12, pp. 1078–1085, 2007.

[81] N. Sewraj, N. Merbahi, J. Gardou, P. R. Akerreta, and F. Marchal, "Electric and spectroscopic analysis of a pure nitrogen mono-filamentary dielectric barrier discharge (mf-dbd) at 760 torr," *Journal of Physics D: Applied Physics*, vol. 44, no. 14, p. 145201, 2011.

[82] M. Šimek, "Optical diagnostics of streamer discharges in atmospheric gases," *Journal of Physics D: Applied Physics*, vol. 47, no. 46, p. 463001, 2014.

[83] D. Babankova, S. Civiš, L. Juha, M. Bittner, J. Cihelka, M. Pfeifer, J. Skála, A. Bartnik, H. Fiedorowicz, J. Mikolajczyk, *et al.*, "Optical and x-ray emission spectroscopy of high-power laser-induced dielectric breakdown in molecular gases and their mixtures," *The Journal of Physical Chemistry A*, vol. 110, no. 44, pp. 12113–12120, 2006.

[84] P. Bruggeman, D. Schram, M. Á. González, R. Rego, M. G. Kong, and C. Leys, "Characterization of a direct dc-excited discharge in water by optical emission spectroscopy," *Plasma Sources Science and Technology*, vol. 18, no. 2, p. 025017, 2009.

[85] C. O. Laux, "Radiation and nonequilibrium collisional-radiative models," *von Karman Institute Lecture Series*, vol. 7, 2002. www.specair-radiation.net.

[86] J. Boeuf, Y. Lagmich, T. Unfer, T. Callegari, and L. Pitchford, "Electrohydrodynamic force in dielectric barrier discharge plasma actuators," *Journal of Physics D: Applied Physics*, vol. 40, no. 3, p. 652, 2007.

[87] S. Roy, "Flow actuation using radio frequency in partially ionized collisional plasmas," *Applied Physics Letters*, vol. 86, no. 10, p. 101502, 2005.

[88] A. V. Likhanskii, M. N. Shneider, S. O. Macheret, and R. B. Miles, "Modeling of dielectric barrier discharge plasma actuators driven by repetitive nanosecond pulses," *Physics of plasmas*, vol. 14, no. 7, p. 073501, 2007.

[89] T. Unfer and J. Boeuf, "Modelling of a nanosecond surface discharge actuator," *Journal of physics D: applied physics*, vol. 42, no. 19, p. 194017, 2009.

[90] A. Y. Starikovskii, A. Nikipelov, M. Nudnova, and D. Roupassov, "SDBD plasma actuator with nanosecond pulse-periodic discharge," *Plasma Sources Science and Technology*, vol. 18, no. 3, p. 034015, 2009.

[91] V. Soloviev and V. Krivtsov, "Surface barrier discharge modelling for aerodynamic applications," *Journal of Physics D: Applied Physics*, vol. 42, no. 12, p. 125208, 2009.

[92] V. Soloviev, V. Krivtsov, S. Shcherbanev, and S. Starikovskaia, "Evolution of nanosecond surface dielectric barrier discharge for negative polarity of a voltage pulse," *Plasma Sources Science and Technology*, vol. 26, no. 1, p. 014001, 2016.

[93] N. Y. Babaeva, D. V. Tereshonok, and G. V. Naidis, "Fluid and hybrid modeling of nanosecond surface discharges: effect of polarity and secondary electrons emission," *Plasma Sources Science and Technology*, vol. 25, no. 4, p. 044008, 2016.

[94] N. Y. Babaeva, G. V. Naidis, C. Ding, and S. Starikovskaia, "Positive nanosecond surface discharge at high pressures and voltages," in *24th International Symposium on Plasma Chemistry (ISPC 24)*, 2019.

[95] S. Shcherbanev, *Filamentary nanosecond surface dielectric barrier discharge at elevated pressures. Streamer-to-filamentary transition and application for plasma assisted combustion.* Theses, Université Paris Saclay (COmUE), Dec. 2016.

[96] S. Shcherbanev, A. Y. Khomenko, S. Stepanyan, N. Popov, and S. Starikovskaia, "Optical emission spectrum of filamentary nanosecond surface dielectric barrier discharge," *Plasma Sources Science and Technology*, vol. 26, no. 2, p. 02LT01, 2016.

[97] I. Grekhov and G. A. Mesyats, "Nanosecond semiconductor diodes for pulsed power switching," *Physics-Uspekhi*, vol. 48, no. 7, p. 703, 2005.

[98] I. Grekhov, V. Efanov, A. Kardo-Sysoev, and S. Shenderey, "Power drift step recovery diodes (dsrd)," *Solid-State Electronics*, vol. 28, no. 6, pp. 597–599, 1985.

[99] A. Kardo-Sysoev, V. Efanov, and I. Chashnikov, "Fast power switches from picosecond to nanosecond time scale and their application to pulsed power," in *Digest of Technical Papers. Tenth IEEE International Pulsed Power Conference*, vol. 1, pp. 342–347, IEEE, 1995.

[100] V. Brylevsky, V. Efanov, A. Kardo-Sysyev, and I. Tchashnicov, "Power nanosecond semiconductor opening plasma switches," in *Proceedings of 1996 International Power Modulator Symposium*, pp. 51–54, IEEE, 1996.

[101] A. Kardo-Sysoev, S. Zazulin, N. Efanov, O. Lelitov, and A. Kriklenko, "High repetition frequency power nanosecond pulse generation," in *Digest of Technical Papers. 11th IEEE International Pulsed Power Conference (Cat. No. 97CH36127)*, vol. 1, pp. 420–424, IEEE, 1997.

[102] N. Anikin, S. Starikovskaia, and A. Y. Starikovskii, "Study of the oxidation of alkanes in their mixtures with oxygen and air under the action of a pulsed volume nanosecond discharge," *Plasma physics reports*, vol. 30, no. 12, pp. 1028–1042, 2004.

[103] L. M. Vasilyak, E. I. Asinovskii, A. V. Kirillin, and V. V. Markovets, "Emission from a pulsed discharge in helium," *Teplofizika vysokikh temperatur*, vol. 13, no. 1, pp. 195–198, 1975.

[104] G. Metzger and J. Vabre, "Transmission lines with pulse excitation," *Academic Press*, 1969.

[105] J. Gregory, "A cassegrainian–maksutov telescope design for the amateur," *Sky & telescope*, vol. 16, p. 236, 1957.

[106] D. Maksutov, "New catadioptric meniscus systems," *JOSA*, vol. 34, no. 5, pp. 270–284, 1944.

[107] C. Wynne, "Maksutov spectrograph cameras," *Monthly Notices of the Royal Astronomical Society*, vol. 153, no. 3, pp. 261–277, 1971.

[108] LaVision, *Product-Manual 1004091 for Long Distance Microscope*. LaVision GmbH, Göttingen.

[109] F. D'A, "The barlow lens," *Nature*, vol. 1, p. 653, 1870.

[110] F. A. Carson, *Basic optics and optical instruments*. Dover Publications, 1969.

[111] H.-J. Kunze, *Introduction to plasma spectroscopy*, vol. 56. Springer Science & Business Media, 2009.

[112] E. E. Whiting, "An empirical approximation to the voigt profile," *Journal of Quantitative Spectroscopy and Radiative Transfer*, vol. 8, no. 6, pp. 1379–1384, 1968.

[113] J. J. Olivero and R. Longbothum, "Empirical fits to the voigt line width: A brief review," *Journal of Quantitative Spectroscopy and Radiative Transfer*, vol. 17, no. 2, pp. 233–236, 1977.

[114] M. Raffel, C. E. Willert, F. Scarano, C. J. Kähler, S. T. Wereley, and J. Kompenhans, *Particle image velocimetry: a practical guide*. Springer, 2018.

[115] H. Du and M.-g. Li, "The study for particle image velocimetry system based on binocular vision," *Measurement*, vol. 42, no. 4, pp. 619–627, 2009.

[116] S. O. Warner and B. L. Smith, "Autocorrelation-based estimate of particle image density for diffraction limited particle images," *Measurement Science and Technology*, vol. 25, no. 6, p. 065201, 2014.

[117] Y. Zhu, S. Shcherbanev, B. Baron, and S. Starikovskaia, "Nanosecond surface dielectric barrier discharge in atmospheric pressure air: I. measurements and 2D modeling of morphology, propagation and hydrodynamic perturbations," *Plasma Sources Science and Technology*, vol. 26, no. 12, p. 125004, 2017.

[118] Y. Zhu and S. Starikovskaia, "Fast gas heating of nanosecond pulsed surface dielectric barrier discharge: Spatial distribution and fractional contribution from kinetics," *Plasma Sources Science and Technology*, vol. 27, no. 12, p. 124007, 2018.

[119] A. Bourdon, V. P. Pasko, N. Liu, S. Célestin, P. Ségur, and E. Marode, "Efficient models for photoionization produced by non-thermal gas discharges in air based on radiative transfer and the helmholtz equations," *Plasma Sources Science and Technology*, vol. 16, no. 3, p. 656, 2007.

[120] A. Luque, U. Ebert, C. Montijn, and W. Hundsdorfer, "Photoionization in negative streamers: Fast computations and two propagation modes," *Applied physics letters*, vol. 90, no. 8, p. 081501, 2007.

[121] S. Pancheshnyi, S. Starikovskaia, and A. Y. Starikovskii, "Measurements of rate constants of the n2 (c3πu, vвЂI= 0) and n2+ (b2σ+ u, vвЂI= 0) deactivation by n2, o2, h2, co and h2o molecules in afterglow of the nanosecond discharge," *Chemical Physics Letters*, vol. 294, no. 6, pp. 523–527, 1998.

[122] S. A. Shcherbanev, N. A. Popov, and S. M. Starikovskaia, "Ignition of high pressure lean H_2: air mixtures along the multiple channels of nanosecond surface discharge," *Combustion and Flame*, vol. 176, pp. 272–284, 2017.

[123] S. Pancheshnyi, S. Starikovskaia, and A. Y. Starikovskii, "Role of photoionization processes in propagation of cathode-directed streamer," *Journal of Physics D: Applied Physics*, vol. 34, no. 1, p. 105, 2001.

[124] S. Pancheshnyi, "Role of electronegative gas admixtures in streamer start, propagation and branching phenomena," *Plasma Sources Science and Technology*, vol. 14, no. 4, p. 645, 2005.

[125] S. Pancheshnyi, M. Nudnova, and A. Starikovskii, "Development of a cathode-directed streamer discharge in air at different pressures: experiment and comparison with direct numerical simulation," *Physical Review E*, vol. 71, no. 1, p. 016407, 2005.

[126] S. Nijdam, F. Van De Wetering, R. Blanc, E. Van Veldhuizen, and U. Ebert, "Probing photo-ionization: experiments on positive streamers in pure gases and mixtures," *Journal of Physics D: Applied Physics*, vol. 43, no. 14, p. 145204, 2010.

[127] K. A. Abdullin, D. G. Batryshev, E. V. Chihray, M. T. Gabdullin, D. V. Ismailov, B. G. Kim, and A. K. Togambaeva, "Obtaining multiwalled and single-walled carbon nanotubes and nanocomposites," *Canadian Journal of Physics*, vol. 92, no. 7/8, pp. 813–818, 2014.

[128] D. Batryshev, Y. Yerlanuly, T. Ramazanov, M. Dosbolayev, and M. Gabdullin, "Elaboration of carbon nanowalls using radio frequency plasma enhanced chemical vapor deposition," *Materials Today: Proceedings*, vol. 5, no. 11, pp. 22764–22769, 2018.

[129] D. Batryshev, Y. Yerlanuly, T. Ramazanov, and M. Gabdullin, "Investigation of synthesis of carbon nanowalls by the chemical vapor deposition method in the plasma of a radio frequency capacitive discharge," *IEEE Transactions on Plasma Science*, vol. 47, no. 7, pp. 3044–3046, 2019.

[130] D. Batryshev, Y. Yerlanuly, B. Alpysbaeva, R. Nemkaeva, T. Ramazanov, and M. Gabdullin, "Obtaining of carbon nanowalls in the plasma of radio-frequency discharge," *Applied Surface Science*, vol. 503, p. 144119, 2020.

[131] H. R. Griem, *Plasma spectroscopy*. New York : McGraw-Hill, 1964. Includes bibliographies.

[132] M. A. Gigosos, M. Á. González, and V. Cardeñoso, "Computer simulated balmer-alpha,-beta and-gamma stark line profiles for non-equilibrium plasmas

diagnostics," *Spectrochimica Acta Part B: Atomic Spectroscopy*, vol. 58, no. 8, pp. 1489–1504, 2003.

[133] A. Y. Nikiforov, C. Leys, M. Gonzalez, and J. Walsh, "Electron density measurement in atmospheric pressure plasma jets: Stark broadening of hydrogenated and non-hydrogenated lines," *Plasma Sources Science and Technology*, vol. 24, no. 3, p. 034001, 2015.

[134] E. Mintoussov, S. Pendleton, F. Gerbault, N. Popov, and S. Starikovskaia, "Fast gas heating in nitrogen–oxygen discharge plasma: II. energy exchange in the afterglow of a volume nanosecond discharge at moderate pressures," *Journal of Physics D: Applied Physics*, vol. 44, no. 28, p. 285202, 2011.

[135] M. Capitelli, G. Colonna, and A. D'Angola, *Fundamental aspects of plasma chemical physics: thermodynamics*, vol. 66. Springer Science & Business Media, 2011.

[136] Y. P. Raizer, *Gas discharge physics*. Verlag Berlin Heidelberg: Springer, 1991.

[137] S. Andreev and T. Gavrilova, "Investigation of a pulsed stabilized discharge in air at a pressure above 100 atm," *High temperature*, vol. 12, no. 6, pp. 1138–1142, 1974.

[138] C. Park, "Review of chemical-kinetic problems of future nasa missions. I-Earth entries," *Journal of Thermophysics and Heat transfer*, vol. 7, no. 3, pp. 385–398, 1993.

[139] G. Hagelaar and L. Pitchford, "Solving the boltzmann equation to obtain electron transport coefficients and rate coefficients for fluid models," *Plasma Sources Science and Technology*, vol. 14, no. 4, p. 722, 2005.

[140] A. Phelps and L. Pitchford, "Anisotropic scattering of electrons by N_2 and its effect on electron transport," *Physical Review A*, vol. 31, no. 5, p. 2932, 1985.

[141] SIGLO database `http://www.lxcat.laplace.univ-tlse.fr` [2013, June 4]. , 2013.

[142] L. Alves, "The ist-lisbon database on lxcat," *Journal of Physics: Conference Series*, vol. 565, no. 1, p. 012007, 2014.

[143] J. Bacri and A. Medani, "Electron diatomic molecule weighted total cross section calculation: III. main inelastic processes for N_2 and N_2^+," *Physica B+C*, vol. 112, no. 1, pp. 101–118, 1982.

[144] A. Khirianova, E. Parkevich, and S. Tkachenko, "Features of interferometry of small-sized plasma channels obtained during nanosecond discharge," *Physics of Plasmas*, vol. 25, no. 7, p. 073503, 2018.

[145] Y. D. Korolev and G. A. Mesyats, *Physics of Pulsed Breakdown in Gases*. Ekaterinburg: Ural Division of the Russian Academy of Science, 1998.

[146] D. Levko and L. L. Raja, "High-voltage microdischarge as a source of extreme density plasma," *Physics of Plasmas*, vol. 25, no. 1, p. 013509, 2018.

[147] E. Parkevich, G. Ivanenkov, M. Medvedev, A. Khirianova, A. Selyukov, A. Agafonov, A. Mingaleev, T. Shelkovenko, and S. Pikuz, "Mechanisms responsible for the initiation of a fast breakdown in an atmospheric discharge," *Plasma Sources Science and Technology*, vol. 27, no. 11, p. 11LT01, 2018.

[148] L. Vasilyak, S. Kostyuchenko, N. Kudryavtsev, and I. Filyugin, "High–speed ionization waves at an electric breakdown," *Phys.–Uspekhi*, vol. 163, pp. 263–286, 1994.

[149] G. Garipov, B. Khrenov, P. Klimov, V. Klimenko, E. Mareev, O. Martines, E. Mendoza, V. Morozenko, M. Panasyuk, I. Park, *et al.*, "Global transients in ultraviolet and red-infrared ranges from data of universitetsky-tatiana-2 satellite," *Journal of geophysical research: atmospheres*, vol. 118, no. 2, pp. 370–379, 2013.

[150] J. Cen, P. Yuan, H. Qu, and T. Zhang, "Analysis on the spectra and synchronous radiated electric field observation of cloud-to-ground lightning discharge plasma," *Physics of Plasmas*, vol. 18, no. 11, p. 113506, 2011.

[151] H. Qu, P. Yuan, T. Zhang, and Z. Chang, "Analysis on the correlation between temperature and discharge characteristic of cloud-to-ground lightning discharge plasma with multiple return strokes," *Physics of Plasmas*, vol. 18, no. 1, p. 013504, 2011.

[152] X. Wang, P. Yuan, J. Cen, J. Liu, and Y. Li, "The channel radius and energy of cloud-to-ground lightning discharge plasma with multiple return strokes," *Physics of Plasmas*, vol. 21, no. 3, p. 033503, 2014.

[153] J. Schindelin, I. Arganda-Carreras, E. Frise, V. Kaynig, M. Longair, T. Pietzsch, S. Preibisch, C. Rueden, S. Saalfeld, B. Schmid, *et al.*, "Fiji: an open-source platform for biological-image analysis," *Nature methods*, vol. 9, no. 7, pp. 676–682, 2012.

[154] N. Lepikhin, *Fast energy relaxation in the afterglow of a nanosecond capillary discharge in nitrogen/oxygen mixtures*. PhD thesis, Université Paris-Saclay (ComUE), 2017.

[155] N. Popov, "Fast gas heating in a nitrogen–oxygen discharge plasma: I. kinetic mechanism," *Journal of Physics D: Applied Physics*, vol. 44, no. 28, p. 285201, 2011.

ECOLE DOCTORALE

Titre : Etude expérimentale des paramètres du plasma dans la décharge filamentaire à barrière diélectrique de surface nanoseconde

Mots clés : Nanoseconde pulsé, décharge filamentaire, paramètre plasma

Résumé : Les décharges de barrière diélectrique de surface nanoseconde (nSDBD) à la pression atmosphérique ont été étudiées de manière approfondie au cours des deux dernières décennies pour le contrôle du débit. Il y a environ dix ans, le nSDBD à haute pression a été suggéré comme source d'allumage assisté par plasma de mélanges combustibles. Au cours des six dernières années, il a été constaté qu'une transformation sévère d'une décharge de flûte de surface nanoseconde à un seul coup est observée à une pression et / ou une tension de gaz croissantes. La présente thèse est consacrée à l'étude de la transition streamer-filament dans une décharge de barrière nanoseconde de surface haute pression à un seul coup dans des gaz non réactifs (azote, oxygène et leurs mélanges). La revue de la littérature présente une analyse détaillée des décharges de banderoles et des étincelles transitoires de nanosecondes largement étudiées au cours des 4 dernières années.
Les résultats sont présentés en trois parties. La première partie montre les paramètres de la transition streamer-filament dans le nSDBD haute pression pour différentes compositions de mélange gazeux. Pour les polarités tant négatives que positives, la transition est fonction de la pression et de l'amplitude de la tension. Pour une polarité positive, l'effet de l'addition d'oxygène moléculaire sur la transition est extrêmement fort. L'influence de différents diélectriques et de différents matériaux d'électrodes sur le début et le développement des filaments est étudiée expérimentalement.
Dans la deuxième partie, les propriétés du plasma dans les filaments sont étudiées à l'aide des mesures d'énergie, de la spectroscopie d'émission optique (OES) et de la vélocimétrie par image de particules (PIV). On trouve que le plasma au stade filamentaire est proche du LTE, ce qui démontre une lente décroissance de la densité électronique (dizaines de nanosecondes) liée à la relaxation de température. Les résultats des mesures sont comparés aux résultats de la modélisation numérique expliquant les principales caractéristiques observées expérimentalement. La troisième partie est consacrée à l'étude détaillée de la transition streamer-filament à la micro-échelle à haute résolution spatiale.

Title : Experimental study of plasma parameters in nanosecond surface dielectric barrier filamentary discharge

Keywords : Nanosecond pulsed, filamentary discharge, plasma parameter

Abstract : Nanosecond surface dielectric barrier discharges (nSDBDs) at atmospheric pressure have been studied extensively over the last two decades for flow control. About ten years ago, the nSDBD at high pressures was suggested as a source for plasma assisted ignition of combustible mixtures. During last six years, it was found that a severe transformation of a single-shot nanosecond surface streamer discharge is observed at increasing gas pressure and/or voltage. The present thesis is devoted to study of streamer-to-filament transition in a single shot high pressure surface nanosecond barrier discharge in non-reactive gases (nitrogen, oxygen and their mixtures). Literature review presents detailed analysis of streamer discharges and of transitory nanosecond sparks widely studied during last 4 years.
The results are presented in three parts. The first part shows the parameters of streamer-to-filament transition in the high pressure nSDBD for different gas mixture composition. For both negative and positive polarities, the transition is a function of pressure and of the voltage amplitude. For positive polarity, the effect of molecular oxygen addition on the transition is extremely strong. The influence of different dielectrics and different electrode materials of the start and development of the filaments is studied experimentally.
In the second part, plasma properties in the filaments are studied with the help of the energy measurements, optical emission spectroscopy (OES) and Particle Image Velocimetry (PIV). Plasma at filamentary stage is found to be close to the LTE demonstrating slow (tens of nanoseconds) electron density decay linked to the temperature relaxation. The results of the measurements are compared with the results of numerical modeling explaining the main experimentally observed features. The third part is devoted to detailed study of streamer-to-filament transition in the micro-scale with high spatial resolution.

Institut Polytechnique de Paris
91120 Palaiseau, France